Molecular plating of thin lanthanide layers with improved material properties for nuclear applications

Dissertation
zur Erlangung des Grades
“Doktor der Naturwissenschaften”
im Promotionsfach Chemie

am Fachbereich Chemie, Pharmazie und Geowissenschaften
der
Johannes Gutenberg-Universität
in Mainz

vorgelegt von

Alessio Vascon
geboren in Padova -Italien-

Mainz 2013

D77

Hiermit versichere ich gemäss § 10 Abs. 3d der Promotionsordnung vom 24.07.2007, dass ich die jetzt als Dissertation vorgelegte Arbeit selbst angefertigt und alle benutzten Hilfsmittel (Literatur, Apparaturen, Material) in der Arbeit angegeben habe.

Mainz, den 26.06.2013

Zusammenfassung

In der vorliegenden Arbeit werden Experimente beschrieben, die zu einem vertieften Verständnis fundamentaler Prozesse bei der elektrochemischen Herstellung von Dünnschichten, sog. Targets, für kernphysikalische und -chemische Studien führten. Targets wurden mittels 'Molecular Plating' (MP) hergestellt, indem eine Elektrodeposition aus organischem Medium in der Regel bei konstantem Strom in Zwei-Elektroden-Zellen. Die Resultate erlaubten, optimierte Herstellungsbedingungen zu ermitteln, welche die Produktion deutlich verbesserter Targets erlaubten.

MP bei konstantem Strom ist ein massentransportkontrollierter Prozess. Der angelegte Strom wird durch einen konstanten Fluss elektroaktiver Spezies zur Kathode – auf der die Schicht wächst – und Anode aufrechterhalten. Die Untersuchungen zeigten, dass das Zellenpotential des Elektrodepositionssystems immer durch den Ohm'schen Spannungsabfall auf Grund des Widerstandes der verwendeten Lösung dominiert wurde. Dies erlaubte die Herleitung einer Beziehung zwischen dem Zellenpotential und der Konzentration der elektroaktiven Spezies. Die Beziehung erlaubt die Erklärung des gemessenen zeitlichen Verlaufs des Zellenpotentials während der Abscheidung als Funktion der Elektrolytkonzentration. Dies dient als Basis, auf der nun ein umfassenderes Bild der Prozesse, die für die charakteristischen Minima im Potentialverlauf einer Abscheidung verantwortlich sind, gewonnen werden kann. Es konnte gezeigt werden, dass die Minima mit der fast vollständigen Entfernung (durch Abscheidung) der aus einem gelösten Salz erzeugten Nd-Ionen korrespondieren. Die abgeschiedene Spezies wurde als Nd^{3+} identifiziert, vermutlich als Carboxylat, Oxid oder Hydroxid, was auf Grund der hohen negative Werte des Standardredoxpotentials der Lanthanide verständlich erscheint.

Von den vorliegenden elektroaktiven Spezies tragen die Nd^{3+} Ionen nur zu knapp 20% zum Gesamtstrom bei. Durch Elektrolyse tragen auch die Lösungsmittelkomponenten zu diese Strom bei. Die Gegenwart von elektrolysiertem Lösungsmittel wurde in Analysen der Dünnschichten bestätigt. Diese waren immer mit chemi- und physisorbierten Lösungsmittelmolekülen bedeckt.

Die Analyse der Dünnschichten zeigte, dass die Oberflächen von einem furchenartiges Netz durchzogen waren, und dass diese während des Trocknen der Schichten nach dem MP entstanden. Ob die Schichten an Luft oder in inerter Atmosphäre trockneten, hatte keinen Einfluss. Es wurden Experimente mit mehreren Lösungsmitteln durchgeführt, die sich deutlich in ihren physikalischen Eigenschaften, v.a. dem Siedepunkt, unterschieden. Furchenfreie Dünnschichten konnten insbesondere bei MP in N,N-dimethylformamide (DMF) erzeugt werden. Die Verwendung von DMF in Kombination mit einer Abscheidung auf sehr glatten Substraten erlaubte die Produktion von sehr homogenen, glatten und defektfreien Schichten. Diese waren vermutlich geringeren inneren Spannungen während des Trocknens ausgesetzt, als Schichten auf raueren Substraten oder solche, die aus flüchtigeren Lösungsmitteln hergestellt wurden. Die Oberflächenrauigkeit des Substrats und das gewählte Lösungsmittel wurden so als Schlüsselfaktoren für die Produktion hochqualitativer Schichten identifiziert. Es konnte gezeigt werden, dass mit MP eine sehr effiziente Methode zur Herstellung homogener Schichten mit exzellenter Ausbeute ist.

In weiteren Experimenten mit dem primordialen α-Emitter ^{147}Sm als Modellisotop wurde die Eignung solcher Schichten als α-Quelle untersucht. Sowohl die Energieauflösung als auch der Anteil der α-Teilchen, die den Detektor erreichten, waren von den Quelleneigenschaften abhängig. Die Effekte wurden verschiedenen Variablen der Dünnschicht zugeordnet, welche die α-Spektren beeinflussten. Dominant war die Wahl des Lösungsmittels und die Rauigkeit des Substrats. Dies beeinflusste Schichtdicke und -morphologie sowie die Art des Schichtwachstums und veränderte die Detektionseffizienz in α-Messungen bis zu 15%. Nur homogene, ebene Schichten, die aus DMF auf glatten Substraten abgeschieden wurden, eignen sich optimal als α-Quelle.

Die gewonnenen Ergebnisse erlauben die optimierte Herstellung nuklearer Targets durch MP. Künftige Anwendungen beinhalten insbesondere die Herstellung von Targets für neutroneninduzierte Spaltexperimente und untergrundarme α-Messungen sehr kleiner Aktivitäten.

Summary

This work describes experiments to gain an improved understanding of the processes associated with the electrochemical production of thin lanthanide layers for nuclear science investigations, i.e., nuclear targets. Nd, Sm, and Gd layers were prepared by means of the so-called molecular plating (MP) technique, where electrodeposition from an organic medium is usually performed in the constant current mode using two-electrode cells. The obtained results allowed the identification of optimized production conditions, which led to a significantly improved layer quality.

Constant current density MP is a mass-transport controlled process. The applied current is maintained constant by constant fluxes of electroactive species towards the cathode – where the layer is grown – and the anode. The investigations showed the cell potentials of the electrodeposition systems to be always dominated by the ohmic drop produced by the resistance of the solutions used for the studies. This allowed to derive an expression relating cell potential with concentration of the electroactive species. This expression is able to explain the trends recorded with different electrolyte concentrations and it serves as a basis to get towards a full understanding of the reasons leading to the characteristic minima observed in the evolution of the cell potential curves with time. The minima were found to correspond to an almost complete depletion of the Nd ions obtained by dissolution of the model salt used for the investigations. Nd was confirmed to be deposited at the cathode as derivatives of Nd^{3+} – possibly as carboxylate, oxide or hydroxide. This fact was interpreted on the basis of the highly negative values of the standard redox potentials typical for lanthanide cations.

Among the different electroactive species present in the complex MP solutions, the Nd^{3+} ions were found to contribute to less than 20% to the total current. Because of electrolysis, also the mixed solvent contributed to the applied costant current as an electroactive species. The presence of electrolyzed solvent was confirmed by the analysis of the produced deposits, which were always covered by both chemisorbed and physisorbed solvent molecules.

Target characterizations showed the surfaces of the layers to present severe cracks, which were found to form during the drying time after completion of the MP. Different drying environments, i.e., air or Ar, did not affect the deposits. The drying-related nature of cracking and the solvent composition of the produced layers suggested to perform constant current density MPs using solvents with significantly different physical properties, most notably the boiling point. N,N-dimethylformamide (DMF), i.e., the highest boiling point solvent, proved to be very effective for the production of crack-free surfaces. DMF, in combination with the use of very smooth deposition substrates, allowed the growth of smooth, defectless layers, which likely underwent smaller stress during drying than the deposits produced by using rougher substrates and more volatile solvents. The roughness of the deposition substrate and the solvent used for the platings proved then to be core factors for the preparation of high quality layers. MP thus showed to be very effective for the production of uniform and homogeneous targets with excellent yield.

Tests of the performance of layers produced by MP as α-particle sources were also carried out. ^{147}Sm was used as model isotope for the α spectroscopy investigations. Both peak resolution and the fraction of α particles reaching the detector were found to be influenced by source effects. These effects were categorized according to different “layer variables”, i.e., variables influencing the α spectra by means of “layer effects”, and were found to be promoted by the plating solvent and the roughness of the deposition substrate used to perform the MPs. These parameters likely affected thickness, morphology, and growth mode of the layers. The layer variables proved to alter the relative detection efficiencies of the α measurements by as much as 15%. Only the uniform and homogeneous layers produced by MP from DMF using the smoothest deposition substrate available turned out to be optimum α-particle sources.

The results obtained from this work open the way to an improved production of nuclear targets by means of molecular plating. Future applications include in particular the preparation of targets to be used in neutron-induced fission experiments and in low-background, low-activity α measurements.

Table of contents

1. Introduction..1

1.1 The TRAKULA project...2

1.1.1 Spent nuclear fuel, the role of partitioning and transmutation, and the physics of transmutation...2
1.1.2 Neutrino science and the SNO+ experiment..5

1.2 Targets for TRAKULA... 6

1.2.1 Targets for fission cross-section measurements...6
1.2.2 Targets for ^{144}Nd half-life determination...8
1.2.2.1 ^{144}Nd and the half-life measurements of long-lived α-particle emitters...9

1.3 Lanthanide and actinide elements..11

1.3.1 Chemistry of the lanthanides...11
1.3.2 Chemistry of the actinides...13

1.4 Target preparation...14

1.4.1 General target requirements and main production techniques.................... 14
1.4.2 Molecular plating...15

1.5 Target characterization techniques...17

1.5.1 Neutron activation analysis and γ-ray spectroscopy...................................17
1.5.2 Radiographic imaging..21
1.5.3 Scanning electron microscopy..22
1.5.4 Atomic force microscopy.. 24
1.5.5 X-ray photoelectron spectroscopy...27

1.6 Outline of the thesis...31

2. Toward large-area targets for "TRAKULA".......................................39

2.1 Introduction..40

2.2 Experimental...42

2.2.1 Target preparation.. 42
2.2.2 Target characterization...43

2.3 Results and discussion... 44

2.3.1 Gd-targets.. 44
2.3.1.1 Comparison between magnetic and ultrasonic stirring at low current density... 44
2.3.1.2 Application of ultrasonic stirring at high current density.............. 46
2.3.2 Nd-targets... 47

2.3.2.1 Application of ultrasonic stirring at low and high current density........ 47
2.3.3 Time-resolved progress of the plating process........ 49

2.4 Layout of the new electrochemical cell........ 53

2.5 Summary........ 54

3. Elucidation of constant current density molecular plating........ 56

3.1 Introduction........ 57

3.2 Experimental details........ 58

3.2.1 Deposition cells........ 58
3.2.2 Molecular plating at constant current density........ 59
3.2.3 Deposition substrates........ 60
3.2.4 Conductivity tests........ 60
3.2.5 Atomic Force Microscopy (AFM) studies........ 61
3.2.6 X-ray Photoelectron Spectroscopy (XPS) studies........ 62
3.2.7 Gamma-ray spectroscopy studies........ 63

3.3 Experimental results and analysis........ 63

3.3.1 Analysis of the conductivity tests........ 63
3.3.2 AFM analysis........ 64
3.3.3 XPS analysis........ 66
3.3.4 Molecular plating performed with Cell A........ 71
3.3.5 Molecular plating performed with Cell B........ 73
3.3.6 Molecular plating on a smaller deposition area in Cell B........ 75
3.3.7 Deposition yield evaluation of the molecular plating realized using Cell B........ 77
3.3.8 Kinetics of molecular plating........ 79
3.3.9 Evaluation of charge consumption for Nd plating........ 80

3.4 Discussion........ 80

3.5 Conclusion........ 84

3.6 Appendix A. Supplementary Material........ 86

4. Fundamental aspects of molecular plating and production of smooth crack-free Nd targets........ 99

4.1 Introduction........ 100

4.2 Experimental........ 101

4.2.1 Target production........ 101
4.2.2 Target characterization........ 102

4.3 Results and discussion........ 103

4.4 Conclusions........ 109

5. Smooth crack-free targets for nuclear applications produced by molecular plating.. 112

5.1 Introduction..113

5.2 Experiments and results.. 114

- 5.2.1 Deposition cell... 114
- 5.2.2 Solvents used for molecular plating..114
- 5.2.3 Deposition substrates.. 115
- 5.2.4 Molecular plating at constant current density.......................... 116
- 5.2.5 Atomic force microscopy (AFM) studies.................................. 116
  - *5.2.5.1 Experiments.. 116*
  - *5.2.5.2 Results...117*
    - *5.2.5.2.1 Layer-growth studies from DMF solution.....................117*
    - *5.2.5.2.2 Influence of the plating solvent and of the drying environment.. 118*
    - *5.2.5.2.3 Influence of the electrolyte concentration......................120*
    - *5.2.5.2.4 Influence of the current density.....................................120*
    - *5.2.5.2.5 Liquid AFM study from IP+IB solution........................ 122*
- 5.2.6 Scanning electron microscopy (SEM) studies........................... 123
  - *5.2.6.1 Experiments.. 123*
  - *5.2.6.2 Results...123*
- 5.2.7 Radiographic imaging (RI) studies.. 124
  - *5.2.7.1 Experiments.. 124*
  - *5.2.7.2 Results...124*
- 5.2.8 X-ray photoelectron spectroscopy (XPS) studies..................... 125
  - *5.2.8.1 Experiments.. 125*
  - *5.2.8.2 Results...127*
    - *5.2.8.2.1 Samples prepared from IP+IB...................................... 127*
    - *5.2.8.2.2 Samples prepared from DMF.......................................129*
    - *5.2.8.2.3 Samples prepared from pyridine.................................. 131*
- 5.2.9 Molecular plating from DMF solution.......................................133
  - *5.2.9.1 Cell potential trends... 133*
  - *5.2.9.2 Kinetics derived from* γ*-ray spectroscopy...................................134*
  - *5.2.9.3 Conductivity measurements..136*
  - *5.2.9.4 Temperature measurements..136*

5.3 Discussion..136

5.4 Conclusion... 140

6. The performance of thin layers produced by molecular plating as α**-particle sources..144**

6.1 Introduction..145

6.2 Sample production and characterization..148

- 6.2.1 Deposition cell... 148
- 6.2.2 Deposition substrates.. 148
- 6.2.3 Molecular plating at constant current density.......................... 149
- 6.2.4 X-ray photoelectron spectroscopy (XPS) studies..................... 150

6.2.4.1 Experiments.. 150
6.2.4.2 Results..151
6.2.4.2.1 Sm samples.. 151
6.2.4.2.2 Sm-free samples...152
6.2.5 Scanning electron microscopy (SEM) studies... 154
6.2.5.1 Experiments.. 154
6.2.5.2 Results..154
6.2.6 Atomic force microscopy (AFM) studies.. 156
6.2.6.1 Experiments.. 156
6.2.6.2 Results..156
6.2.7 Radiographic imaging (RI) studies.. 158
6.2.7.1 Experiments.. 158
6.2.7.2 Results..158
6.2.8 Gamma-ray spectroscopy studies...160
6.2.8.1 Experiments.. 160
6.2.8.2 Results..160

6.3 Alpha-particle spectroscopy investigation.......................................161

6.3.1 Experiments...161
6.3.2 Results...162
6.3.2.1 Experiment A: influence of the plating solvent............................162
6.3.2.2 Experiment B: influence of the roughness of the deposition substrate...163
6.3.2.3 Experiment C: influence of surface cracks in the DMF samples... 164
6.3.2.4 Experiment D: influence of the deposition time used to produce the DMF samples..164

6.4 Discussion...165

6.5 Conclusion... 169

7. Outlook and closing remarks...172

1. Introduction

Lanthanide and actinide thin layers play a central role in nuclear sciences. They are used in both nuclear physics and nuclear chemistry experiments, and they are planned to be key components in future nuclear applications. In experimental nuclear physics and chemistry, lanthanide and actinide layers serve mainly as sources of stationary nuclei, i.e., targets, to be used in several nuclear research fields. In nuclear spectroscopy, for example, targets are frequently used to search for unknown decay branches in different nuclides [1,2] or to evaluate with precision the half-lives of specific isotopes, especially of the very long-lived ones [2,3]. In nuclear reaction studies lanthanide and actinide targets are instead commonly used to measure nuclear data, e.g., nuclear reaction cross sections to improve the existing databases [4,5]. In particular, thin actinide targets have long since found large application in nuclear fusion reaction studies aiming at the production of superheavy elements [6,7].

In recent years, the possible use of thin actinide layers in fields other than the ones of nuclear physics and nuclear chemistry research has aroused much interest [8,9]. For example, theoretical studies have shown that ultra-thin (i.e., < 1 µm [10]) ^{242m}Am ($t_{1/2}$ ~ $1.4 \cdot 10^2$ y [11]) layers may be successfully applied for the future construction of nuclear engines with suitable propulsion for manned deep space travels (e.g., travel to Mars [12]). The same actinide thin layers may also be used for the construction of small-core reactors [13], nuclear batteries [14], and nuclear pumped lasers [14]. Unfortunately, the poor availability of many of the isotopes suitable for nuclear applications and also the lack of effective, well-established techniques for the production of thin layers of such isotopes are among the reasons why the proposed projects have not yet been realized.

1.1 The TRAKULA project

TRAKULA (**tra**nsmutationsrelevante **k**ernphysikalische **U**ntersuchungen **l**anglebiger **A**ktinide, i.e., nuclear physical investigations of long-lived actinides with relevance to transmutation) is a joint research project of the German Federal Ministry of Science and Education (BMBF). The main focus of the project is on the transmutation of radioactive waste to be studied with nuclear physics experiments. Several are the partners of the collaboration: the Helmholtz-Zentrum Dresden-Rossendorf (HZDR), the Technical University of Dresden (TU Dresden), the Johannes Gutenberg University of Mainz (JGU), the Physikalisch Technische Bundesanstalt of Braunschweig (PTB), the Technical University of Munich (TUM), and the University of Cologne [15].

The long-term role of the University of Mainz within the collaboration is to produce actinide and lanthanide targets. Targets of ^{235}U, ^{238}U, and ^{242}Pu will be used by HZDR and PTB to perform transmutation-related studies. Targets of ^{144}Nd will be instead investigated by TU Dresden in low-background measurements relevant to neutrino science.

On the way to the future production of targets for TRAKULA, investigations elucidating the fundamental aspects of one of the most widely applied target production techniques, i.e., molecular plating (MP), have been carried out. The experiments have been performed using the lanthanide elements Nd, Sm, and Gd. Targets of these elements have been characterized with different analytical techniques and the obtained results have been used to improve the properties of the layers themselves. The performance of the produced samples as radioactive sources has also been tested.

The present thesis describes the experiments carried out during this research activity.

1.1.1 Spent nuclear fuel, the role of partitioning and transmutation, and the physics of transmutation

Most of the hazards in dealing with spent fuel stem from isotopes of the following chemical elements: Pu, the so-called minor actinides (MAs) Np, Am, Cm, and some long-lived fission products (FPs) such as I and Tc at concentration levels of kilograms per ton [16]. These radioactive by-products, although present at relatively low concentrations in the spent fuel, are hazardous to life forms when released into the environment. As such, their final disposal requires isolation from the biosphere in stable, deep geological formations for long periods of time. A measure of the hazards of these elements is provided by the toxicity and, in particular, the radiotoxicity arising from their radioactive nature rather than their chemical form [16]. A reference point is the radiotoxicity associated with the raw material used to fabricate one ton of enriched U, including not only the U isotopes, but also all of their radioactive daughter products. The reference radiotoxicity level is reached by spent nuclear fuel only after periods of more than 10^5 years (Figure 1-1 [17]). In more detail, the radiotoxicity of FPs dominates the first 10^2 years after discharge and it decreases to the natural reference level in about $3 \cdot 10^2$ years. However, in the longer term, the main radiotoxicity is that of the transuranics (TRUs, i.e., elements with $Z > 92$), particularly Pu isotopes and the decay products of ^{241}Pu. Approximately 10^2-10^3 years after fuel discharge, the radiotoxicity is dominated by ^{241}Am, the radioactive daughter of ^{241}Pu, and between 10^3 and 10^4 years by ^{240}Pu. Thereafter, ^{239}Pu is the main contributor to radiotoxicity. Beyond 10^5 years the main sources of radiotoxicity come from the descendants of ^{241}Am [16].

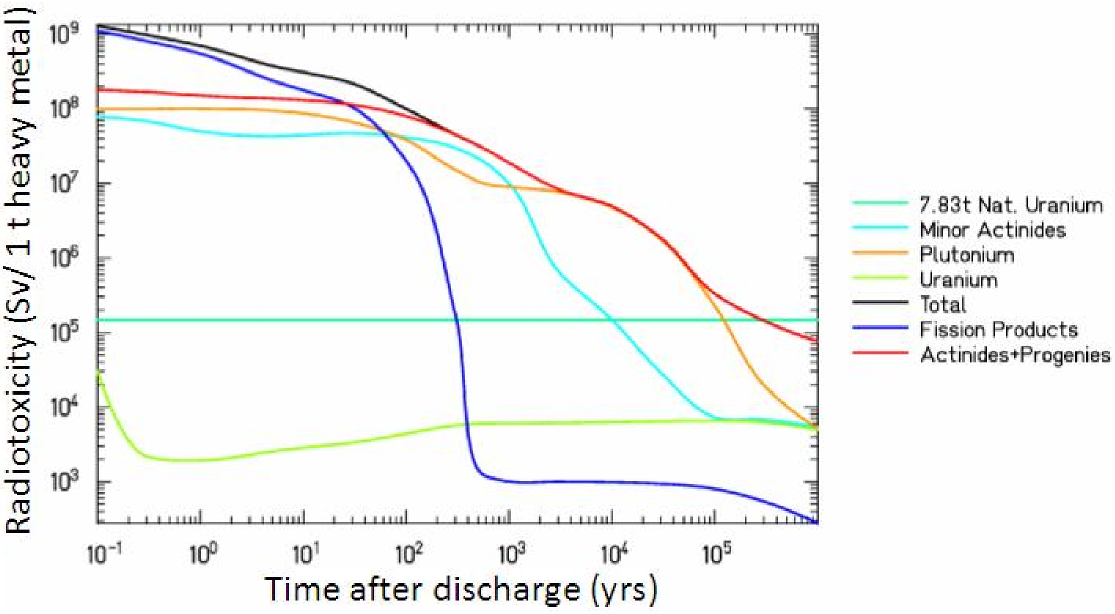

Figure 1-1 Radiotoxicity evolution in time of spent nuclear fuel and its radioactive components [17].

According to the Generation IV initiative, i.e., the international forum on new reactor concepts, partitioning and transmutation (P&T) must be included in the strategies for the development of future nuclear power systems [18]. P&T has indeed been considered as a way of reducing the burden on a geological disposal. As Pu and MAs are mainly responsible for the long-term radiotoxicity, when these nuclides are removed from the waste (partitioning) and then “burned” in a neutron field (transmutation), the remaining waste loses most of its long-term radiotoxicity. The radiotoxicity inventory can be reduced up to a factor of 10 if all the Pu is recycled and burned, and up to a factor of 100 or more if, in addition to Pu, the MAs are transmuted [19].

Any type of transmutation is a function of the neutron cross sections (σ) and their energy dependence [19]. In the transmutation of nuclear waste, the essential mechanism is to transform the TRUs via fission into much shorter-lived or even stable FPs. However, the fission process is always in competition with other processes, in particular with neutron capture, which yields heavier β^--decaying isotopes leading to the build-up of higher activities [16]. The competition between the capture and fission processes is then of high relevance. From the inspection of ratios $\alpha = \overline{\sigma_c}/\overline{\sigma_f}$ of the average capture and fission cross section of different isotopes (Table 1-1 [19]), it is obvious that fast neutron spectra give smaller α values than thermal neutron spectra as delivered from pressurized water reactors (PWRs).

Table 1-1 Average fission and capture cross sections and corresponding α values for different isotopes in both thermal (PWR) and fast neutron spectra [19].

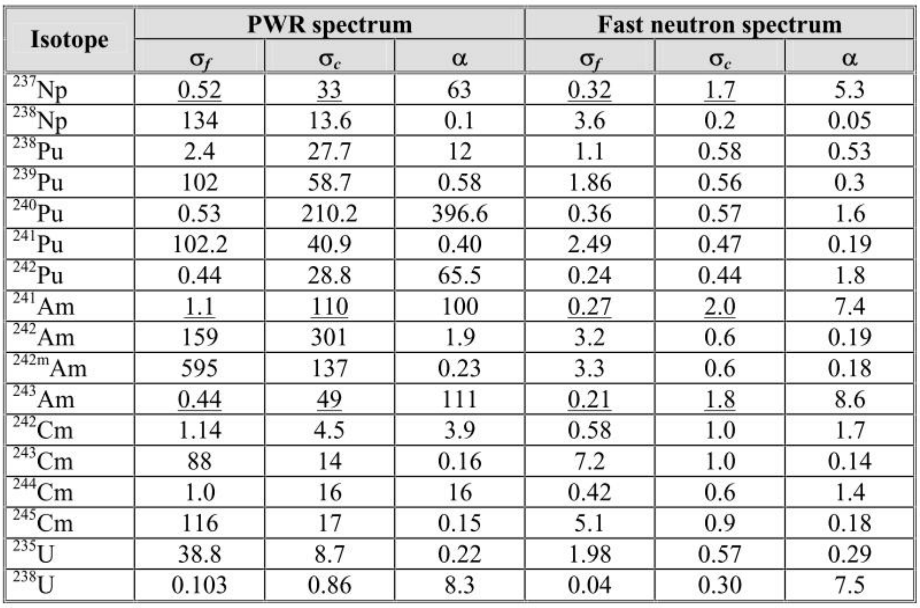

Isotope	PWR spectrum			Fast neutron spectrum		
	σ_f	σ_c	α	σ_f	σ_c	α
^{237}Np	0.52	33	63	0.32	1.7	5.3
^{238}Np	134	13.6	0.1	3.6	0.2	0.05
^{238}Pu	2.4	27.7	12	1.1	0.58	0.53
^{239}Pu	102	58.7	0.58	1.86	0.56	0.3
^{240}Pu	0.53	210.2	396.6	0.36	0.57	1.6
^{241}Pu	102.2	40.9	0.40	2.49	0.47	0.19
^{242}Pu	0.44	28.8	65.5	0.24	0.44	1.8
^{241}Am	1.1	110	100	0.27	2.0	7.4
^{242}Am	159	301	1.9	3.2	0.6	0.19
^{242m}Am	595	137	0.23	3.3	0.6	0.18
^{243}Am	0.44	49	111	0.21	1.8	8.6
^{242}Cm	1.14	4.5	3.9	0.58	1.0	1.7
^{243}Cm	88	14	0.16	7.2	1.0	0.14
^{244}Cm	1.0	16	16	0.42	0.6	1.4
^{245}Cm	116	17	0.15	5.1	0.9	0.18
^{235}U	38.8	8.7	0.22	1.98	0.57	0.29
^{238}U	0.103	0.86	8.3	0.04	0.30	7.5

Therefore, in a fast spectrum actinides are preferentially fissioned, not transmuted into higher actinides. This implies that fast systems are more “efficient” – from the point of view of neutron economy – in destroying actinides because fewer neutrons are lost to capture reactions before eventual fission.

Fast neutron fields can be provided by either fast fission reactors, i.e., breeder reactors, or accelerator-driven systems (ADS) [19]. In the first case, fast neutrons sustain the fission chain reaction without the use of a neutron moderator. In the second case, an accelerator delivers a high energy proton beam (0.6-1.6 GeV) which strikes a target, e.g., of liquid lead producing spallation neutrons. These neutrons are then multiplied to achieve high flux values in the surrounding fissionable fuel. Both irradiation systems can be loaded with fuels with potentially very different mixtures of Pu and MAs, according to the chosen approach and the objective of the P&T strategy.

1.1.2 Neutrino science and the SNO+ experiment

SNO+ is a deep underground facility focused on the study of neutrino physics. It is based on a kilo-tonne scale liquid scintillator detector primarily filled with linear alkylbenzene, which is used as scintillating solvent. SNO+ is meant to detect neutrinos when they interact with electrons and nuclei in the detector to produce charged particles which, in turn, create light as they pass through the scintillator. The flash of light is then detected by an array of photomultiplier tubes [20].

One of the most important open questions in the field of neutrino physics which SNO+ tries to answer is the following: are neutrinos so-called Majorana or Dirac particles? In the latter case, particles are distinct from antiparticles, whereas for Majorana particles the opposite is true. Attempts to detect the (possible) Majorana nature of neutrinos focus around the double-β decay processes. We describe here as one example the case of double-β^- decay, where two neutrons in the same nucleus decay simultaneously to emit two antineutrinos and two electrons:

$$^{A}Z_{N} \rightarrow {}^{A}(Z+2)_{N-2} + 2e^{-} + 2\overline{\nu_{e}} + Q \qquad (1)$$

If neutrinos are Majorana particles, the antineutrino emitted by one of the neutrons can be absorbed as a neutrino by the other. The resulting process, in which no neutrinos are emitted, is called neutrinoless double-β decay [20]:

$$^{A}Z_{N} \rightarrow {}^{A}(Z+2)_{N-2} + 2e^{-} + Q \qquad (2)$$

Analogue scenarios occur for double-β^+ and double-EC decays [21,22].

If neutrinoless double-β decay was observed, it would not only prove that neutrinos are Majorana particles, but it would also provide a measurement of the neutrino mass, since the rate of neutrinoless double-β decay is related to the square of the neutrino mass [23].

In case (1) the energy spectrum from the two electrons has similar features to that from single-β decay: a continuous spectrum ending at a well-defined end point determined from the *Q* value of the reaction. In case (2) the summed energy of the two emitted electrons is exactly equal to the *Q* value of the reaction [24]. The SNO+ experimental concept is then to observe an isotope capable of decaying via double-β decay and to search for a peak at the end point of the spectrum [24]. Among the several candidate isotopes to perform this experiment, ^{150}Nd has been regarded as the most appropriate one (Figure 1-2 [25]).

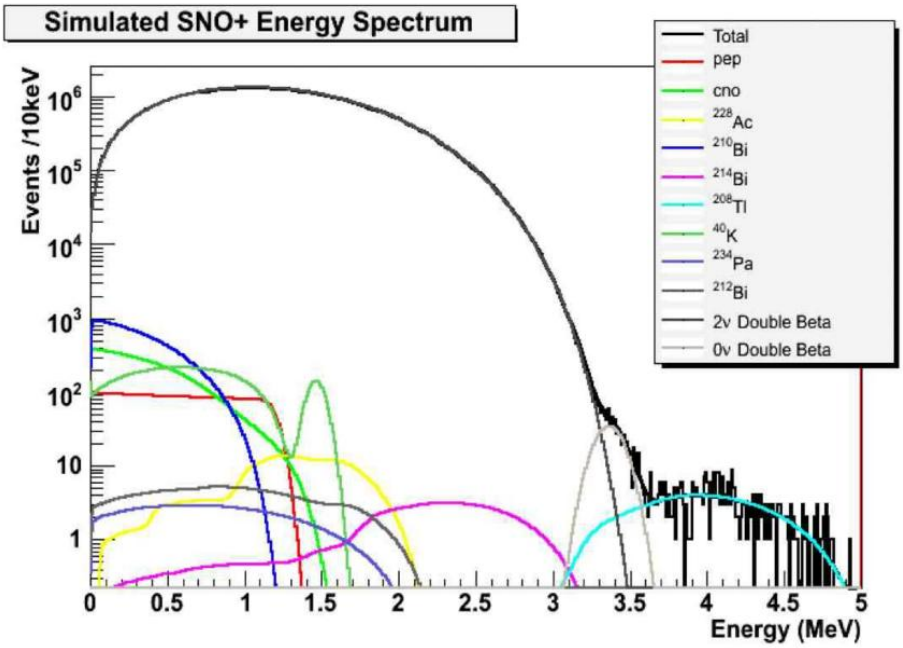

Figure 1-2 Simulated SNO+ energy spectrum for ^{150}Nd. The double-β decay dominates at low energies, while the neutrinoless double-β decay is present as a small peak at the high-energy end of the spectrum. Further shown are expected backgrounds from solar pep neutrinos [26, see chapter 12], CNO neutrinos [26, see chapter 12], and the natural decay chains (U, Th). No Nd-related background components are included [25].

1.2 Targets for TRAKULA

1.2.1 Targets for fission cross-section measurements

Both reliable predictions of the nuclear physical processes relevant to transmutation and the optimization of the fast nuclear energy systems (i.e., fast reactors and ADS) depend on the availability of accurate values of neutron-induced cross sections. While these cross sections are well-known in the energy range of the thermal neutrons ($E_n < 0.05$ eV), in the range of the fast neutrons ($0.1 < E_n < 10$ MeV) the inaccuracy is significant.

Recently, two major sources of the uncertainty impact have been identified [27]: (i) uncertainties of the neutron-induced fission cross sections of Pu isotopes and MAs, and (ii) uncertainties of the inelastic scattering cross sections of fast neutrons on structural and cooling materials of the reactors (e.g., Fe, Pb, Na). Consequently, a set of the highest priority target accuracies for fast reactors has been defined in order to improve the existing databases (Table 1-2 [27]).

Table 1-2 Summary of the highest priority target accuracies for fast reactors (where SFR = sodium-cooled fast reactor, GFR = gas-cooled fast reactor, LFR = lead-cooled fast reactor, ABTR = advanced breeder test reactor, and EFR = European fast reactor) [27].

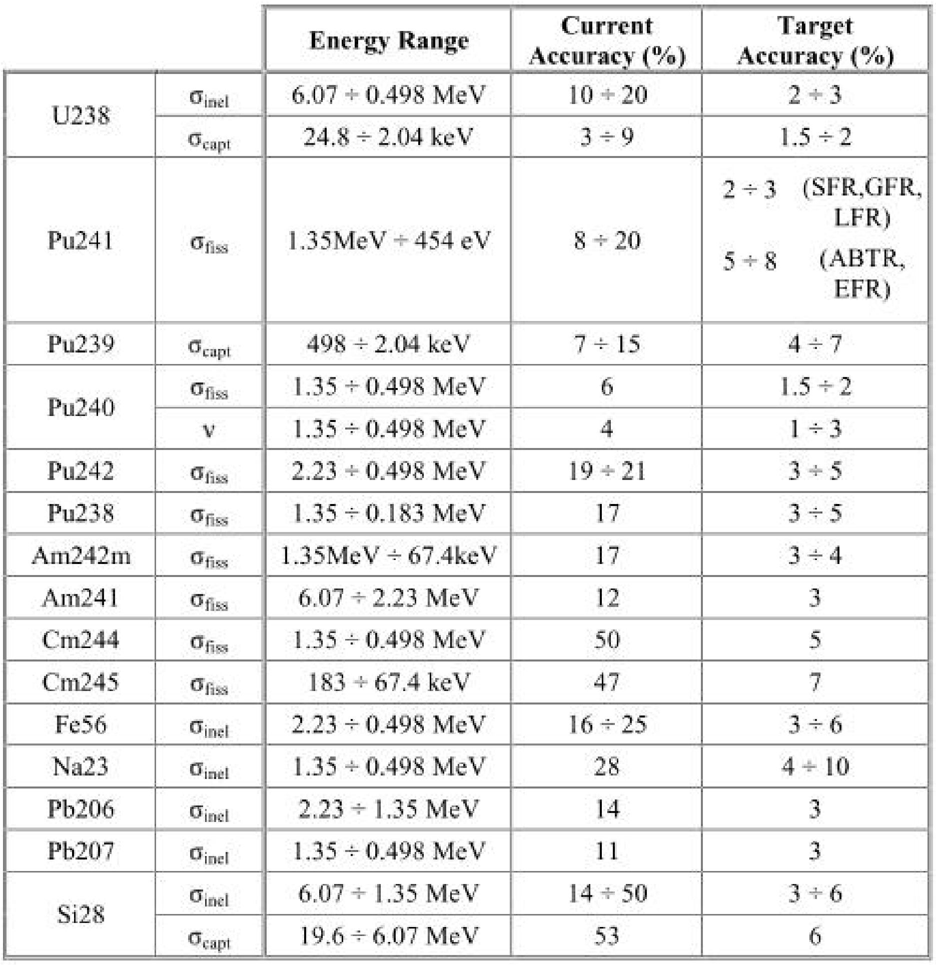

		Energy Range	Current Accuracy (%)	Target Accuracy (%)
U238	σ_{inel}	6.07 ÷ 0.498 MeV	10 ÷ 20	2 ÷ 3
	σ_{capt}	24.8 ÷ 2.04 keV	3 ÷ 9	1.5 ÷ 2
Pu241	σ_{fiss}	1.35MeV ÷ 454 eV	8 ÷ 20	2 ÷ 3 (SFR,GFR, LFR) 5 ÷ 8 (ABTR, EFR)
Pu239	σ_{capt}	498 ÷ 2.04 keV	7 ÷ 15	4 ÷ 7
Pu240	σ_{fiss}	1.35 ÷ 0.498 MeV	6	1.5 ÷ 2
	ν	1.35 ÷ 0.498 MeV	4	1 ÷ 3
Pu242	σ_{fiss}	2.23 ÷ 0.498 MeV	19 ÷ 21	3 ÷ 5
Pu238	σ_{fiss}	1.35 ÷ 0.183 MeV	17	3 ÷ 5
Am242m	σ_{fiss}	1.35MeV ÷ 67.4keV	17	3 ÷ 4
Am241	σ_{fiss}	6.07 ÷ 2.23 MeV	12	3
Cm244	σ_{fiss}	1.35 ÷ 0.498 MeV	50	5
Cm245	σ_{fiss}	183 ÷ 67.4 keV	47	7
Fe56	σ_{inel}	2.23 ÷ 0.498 MeV	16 ÷ 25	3 ÷ 6
Na23	σ_{inel}	1.35 ÷ 0.498 MeV	28	4 ÷ 10
Pb206	σ_{inel}	2.23 ÷ 1.35 MeV	14	3
Pb207	σ_{inel}	1.35 ÷ 0.498 MeV	11	3
Si28	σ_{inel}	6.07 ÷ 1.35 MeV	14 ÷ 50	3 ÷ 6
	σ_{capt}	19.6 ÷ 6.07 MeV	53	6

At HZDR the neutron-time-of-flight source nELBE produces neutrons by means of a liquid lead radiator. The electron beam of the superconducting electron accelerator ELBE hits the lead radiator creating intense bremsstrahlung, which generates neutrons in (γ,n) reactions inside the lead [28]. As the kinetic energy of the released neutrons ranges from few tens of keV to some MeV, nELBE is suitable for neutron-induced cross section measurements relevant to transmutation research.

Within the frame of the TRAKULA project, large-area targets (i.e., ca. 40 cm^2) of ^{235}U, ^{238}U, and ^{242}Pu are needed to set up ionization chambers for fission cross section measurements relevant to the development of fast reactors. ^{238}U is feasible as test material to develop fission chambers because of its relatively low specific activity. ^{235}U, whose fission cross section for both thermal and fast neutrons is very well known, can instead be used as a standard to build reference ionization chambers. These chambers will be built at both HZDR and PTB. At PTB measurements with reference neutron fields will allow the determination of the density of the ^{235}U targets. The knowledge of this value will permit the calibration of the neutron beam intensity of the nELBE source of HZDR. After calibration, the Pu targets will be used to set up a parallel-plate fission chamber at HZDR for the neutron-induced fission cross section measurement of ^{242}Pu, which is an important isotope for transmutation research as shown in Table 1-2.

1.2.2 Targets for ^{144}Nd half-life determination

Even if neutrinoless double-β decay is allowed, it occurs at only a small fraction of the rate of two neutrino double-β decay. One of the main challenges of the double-β decay searches, then, is to distinguish the small number of monoenergetic electron pairs produced by neutrinoless double-β decay from the large continuum of electron pairs produced by two neutrino double-β decay. In order to ensure that these signals can be separated, good energy resolution and statistics are demanding. If on the one hand the resolution achievable with a scintillator detector cannot be high, on the other hand the amount of Nd isotope that can be suspended in the SNO+ scintillator is very large, this assuring good statistics. Indeed, as the natural abundance of ^{150}Nd is 5.6%, just 1% natural Nd-loading in the 1000 t of the scintillator would correspond to 560 kg of this isotope [25]. However, at the same time the 1% Nd-loading in the scintillator system would also correspond to 2380 kg of ^{144}Nd (natural abundance 23.8%) [25]. As ^{144}Nd is a long-lived α emitter it may contribute to the background of the SNO+ experiment both directly and via (α,n) reactions, hence requiring a good understanding of the background radiation produced from its decay. To infer its contribution to the background, the activity produced by ^{144}Nd has to be known, which requires a very precise knowledge of the half-life ($t_{1/2}$) of this isotope.

For this reason, TU Dresden, which is partner in the SNO+ collaboration, needs small-area, i.e., ca. 9 cm^2, ^{144}Nd targets within the frame of the TRAKULA project. Because of the long half-life ($t_{1/2} \sim 2.7 \cdot 10^{15}$ y [3]) and corresponding low specific activity of ^{144}Nd, the measurement of the targets will be performed in the low-background environment of the underground laboratory "Felsenkeller" in Dresden. There measurements using an ionization chamber monitoring for alpha particles emitted by a sample containing a well-defined number of ^{144}Nd atoms will be performed to evaluate the half-life of ^{144}Nd.

1.2.2.1 *^{144}Nd and the half-life measurements of long-lived α-particle emitters*

Alpha decay occurs via the emission of a fully ionized He nucleus (i.e., an α particle) from a radioactive nuclide:

$$^{A}Z_{N} \rightarrow {}^{A-4}(Z-2)_{N-2} + \alpha + Q \qquad (3)$$

The energies of α particles emitted by radioactive nuclides range from 1.8 MeV (^{144}Nd) to 11.7 MeV (^{212}Po^{m}), and most of them lie between 4 and 8 MeV. This relatively small range in energies is associated with an enormous range in half-lives, from about 10^{-7} s (^{213}At) [29] to 10^{19} y (^{209}Bi) [30], a factor of over 10^{33}.

In its simplest form, the dependence of the half-life on the α-decay energy is expressed by the empirical Geiger-Nuttall law:

$$\log t_{1/2} = a + \frac{b}{\sqrt{Q_\alpha}} \qquad (4)$$

where a and b are constants and Q_α is the α-particle decay energy, which always exceeds the kinetic energy of the α particle by the recoil energy of the product nucleus [26]. Equation (4) shows the existence of an inverse relationship between the logarithm of the half-life of an α-emitting nucleus and the square root of the α-particle decay energy. This expression, originally formulated as a quantitative relation between decay constant and range in air of α particles, and later theoretically explained by Gamow, Gurney and Condon using quantum mechanical tunneling [29], gives a good explanation as to why ^{144}Nd is a very long-lived α emitter. Because of the very small α-particle kinetic energy (only 0.1 MeV smaller than the Q_α value), ^{144}Nd must have a very long half-life, which is in fact $(2.65 \pm 0.37) \cdot 10^{15}$ y according to the most recent determination [3].

If the half-life has to be experimentally evaluated for a very long-lived radioactive substance, the counting rate $C = \varepsilon \cdot \lambda \cdot N$, where ε is the detection efficiency, λ the decay constant, and N the number of radioactive nuclei, may not change measurably over the time available for observation. In this case λ (hence $t_{1/2}$, as $\lambda = \ln 2/t_{1/2}$) may be found from the relation $\lambda N = -dN/dt = C/\varepsilon$, provided -dN/dt, i.e., the activity, may be determined in an absolute way (through knowledge of ε) and N is known or can be calculated. This method, which is essentially a measurement of specific activity, is usually performed with low background and high efficiency detectors. For low-level α-particle counting, the choice is generally between gas-filled ionization chambers, semiconductor or liquid scintillation detectors. In the case of gas-filled ionization chambers and semiconductor detectors the counting efficiency is usually approaching 50%, with backgrounds of approximately 3-4 counts per minute (cpm) and 0.5 counts per hour (cph), respectively. In the case of liquid scintillation detectors, instead, the counting efficiency can approach 100%, and the background rates range from 10 to 100 cpm [26]. As regards the attainable energy resolution, semiconductor detectors are the best choice as in this case the energy required for the formation of an electron-hole pair is small, e.g., ca. 3.5 eV in silicon. This energy is approximately one tenth that needed for producing an ion pair in a gas, and one hundredth the energy that gives rise to one photoelectron at the photocathode of a scintillation counter, which is thus the detector with the worst resolution [29]. However, liquid scintillation counters have the advantage of easy preparation of the samples, which have just to be dissolved or uniformly dispersed in the scintillation liquid. In many cases, the number of atoms – N – can be determined very precisely prior to insertion into the detector by means of well-established spectrometric techniques like, e.g., inductively coupled plasma optical emission spectrometry (ICP-OES) [31], inductively coupled plasma mass spectrometry (ICP-MS) or atomic absorption spectroscopy (AAS). A small error on N, essential for the high precision determination of the half-life of an isotope, is instead not easily achievable in the case of gas-filled ionization chambers [3] and semiconductor detectors, where the samples usually need more complex preparations, which cause the starting number of detectable radioactive nuclei to vary. For measurements with these detectors, sample preparation techniques like, e.g., molecular plating, are frequently applied to produce thin and homogeneous solid deposits, which should be almost weight-less in order to avoid spreading and tailing of the α lines of interest. Critical issues associated with thickness, homogeneity, sample's geometrical arrangement, and the like could be avoided by adopting the relatively new scintillating bolometer technique [32]. This technique has been recently applied to determine, e.g., the half-life of the extremely long-lived α-particle emitter ^{209}Bi – $t_{1/2} = (1.9 \pm 0.2) \cdot 10^{19}$ y – with both high energy resolution and high detection efficiency (100%) [30]. Unfortunately, the bolometer technique can be applied only if a massive crystal containing the element of interest is made available by specific production methods.

As regards the half-life determination of ^{144}Nd, several have been the measurements performed in the past using different detection techniques. Here, the most recent one dates back to more than twenty-five years ago (Table 1-3).

Table 1-3 Literature values of the half-life of ^{144}Nd and corresponding applied methods of detection.

Reference	Year of publication	Method	Half-life (y)
[33]	1954	Nuclear emulsion	$1.5 \cdot 10^{15\,*}$
[34]	1954	Nuclear emulsion	$5 \cdot 10^{15\,*}$
[35]	1956	Nuclear emulsion	$2.2 \cdot 10^{15\,*}$
[36]	1959	Liquid scintillation counter	$2 \cdot 10^{13\,*}$
[37]	1960	Ionization chamber	$2.1 \cdot 10^{15\,*}$
[2]	1961	Ionization chamber	$(2.4 \pm 0.3) \cdot 10^{15}$
[38]	1965	Ionization chamber	$(2.1 \pm 0.4) \cdot 10^{15}$
[3]	1987	Ionization chamber	$(2.65 \pm 0.37) \cdot 10^{15}$

* Error bar not reported in the original publication.

The analysis of the data listed in Table 1-3 clearly shows a significant spread among the determined half-life values. Precision is therefore lacking. A new measurement of the ^{144}Nd half-life is thus irrevocable to achieve the goals established within the SNO+ collaboration [20].

The use of an ionization chamber for the future determination of ^{144}Nd activity is consistent with the choices made in the last fifty years of measurements of this isotope. Nonetheless, as stated above, this method of detection requires thin and uniform targets, possibly weight-less, not easy to produce. The preparation of the targets plays then a central role in the half-life evaluation of ^{144}Nd.

1.3 Lanthanide and actinide elements

Targets for TRAKULA consist of lanthanide and actinide elements. The chemistry of these elements is briefly reviewed.

1.3.1 Chemistry of the lanthanides

When analyzing the chemistry of the lanthanide series, which ranges from Ce to Lu – see Figure 1-3 – the following main properties stand out [39-41]:

- The lanthanides are characterized by the filling of the 4f orbitals after La, a d-block element with the electron configuration [Xe] $6s^2$ $5d^1$.
- The 4f orbitals penetrate the Xe core appreciably. The 4f electrons are then “inside” the 5s and 5p electrons of Xe and are core-like in their behaviour, being shielded from the ligands, and thus taking no part in bonding.
- As the series Ce-Lu is traversed, the 4f orbitals do not shield effectively the 5s and 5p orbitals from the increasing nuclear charge, hence causing a smooth decrease in the atomic radii with increasing Z, which is known as lanthanide contraction.
- The elementhal lanthanides are highly electropositive and easily oxidized, primarily to the +3 state, which is the characteristic state of all lanthanides both in solid compounds and in solutions in water and other solvents. Additional oxidation states are the +4 states in Ce^{4+} and Tb^{4+} because of the stabilizing effects of the noble gas configuration – [Xe] – and of the half-filled configuration – [Xe] $4f^7$ – respectively. Also known are the +2 states in Eu^{2+} and Yb^{2+} because of half-filled – [Xe] $4f^7$ – and filled – [Xe] $4f^{14}$ – configurations, respectively.
- Because of the lanthanide contraction, the radii of the +3 ions are smoothly decreasing while the coordination number, basicity, and ease of oxidation decrease along the series.
- The lanthanide ions exhibit a very wide range of coordination numbers (generally 6-12, but numbers of 2, 3 or 4 are also known).
- Because of the large size, each lanthanide cation has minimized covalent interactions with ligands and reduced electrostatic interactions. This brings to form labile ionic complexes that undergo facile and rapid exchange of ligand (e.g., water). This situation limits the number of isolable lanthanide complexes.
- Both isolable and solution-stable lanthanide complexes are derived from ligands containing oxygen donors.

The lanthanides are then quite unique among the elements of the periodic table (except for the closely similar late actinides). They resemble each other so markedly both in the elemental state and in compounds that changes in properties for a given oxidation state with increasing atomic number are largely changes in degree rather than in kind.

All lanthanide elements but Pm are stable and occur in nature. Some natural lanthanides consist of stable as well as primordial α-decaying isotopes.

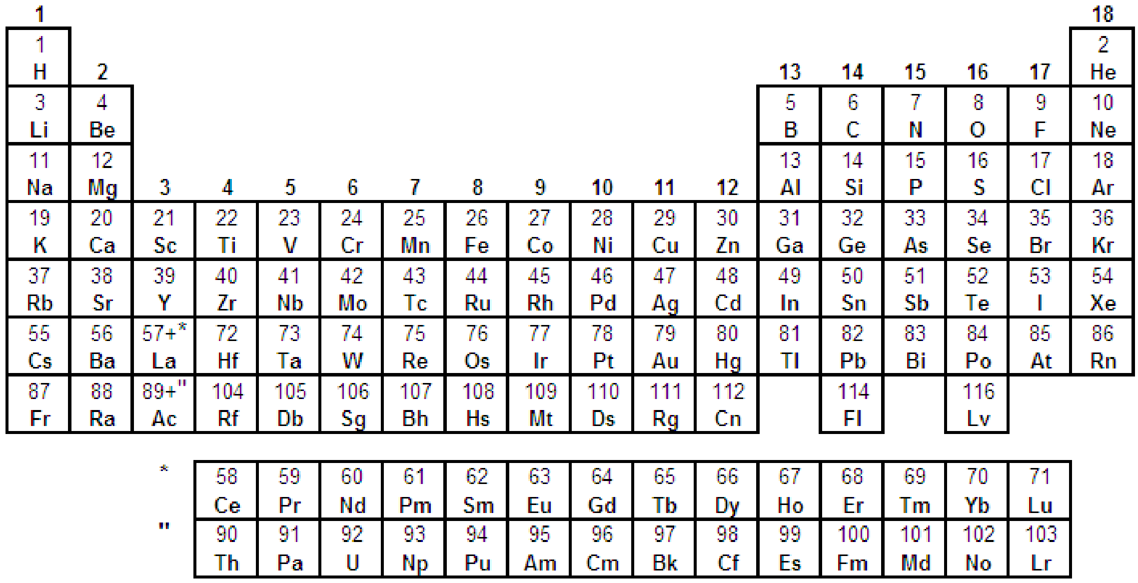

1	2	3	4	5	6	7	8	9	10	11	12	13	14	15	16	17	18
1 H																	2 He
3 Li	4 Be											5 B	6 C	7 N	8 O	9 F	10 Ne
11 Na	12 Mg											13 Al	14 Si	15 P	16 S	17 Cl	18 Ar
19 K	20 Ca	21 Sc	22 Ti	23 V	24 Cr	25 Mn	26 Fe	27 Co	28 Ni	29 Cu	30 Zn	31 Ga	32 Ge	33 As	34 Se	35 Br	36 Kr
37 Rb	38 Sr	39 Y	40 Zr	41 Nb	42 Mo	43 Tc	44 Ru	45 Rh	46 Pd	47 Ag	48 Cd	49 In	50 Sn	51 Sb	52 Te	53 I	54 Xe
55 Cs	56 Ba	57+* La	72 Hf	73 Ta	74 W	75 Re	76 Os	77 Ir	78 Pt	79 Au	80 Hg	81 Tl	82 Pb	83 Bi	84 Po	85 At	86 Rn
87 Fr	88 Ra	89+" Ac	104 Rf	105 Db	106 Sg	107 Bh	108 Hs	109 Mt	110 Ds	111 Rg	112 Cn		114 Fl		116 Lv		

*	58 Ce	59 Pr	60 Nd	61 Pm	62 Sm	63 Eu	64 Gd	65 Tb	66 Dy	67 Ho	68 Er	69 Tm	70 Yb	71 Lu
"	90 Th	91 Pa	92 U	93 Np	94 Pu	95 Am	96 Cm	97 Bk	98 Cf	99 Es	100 Fm	101 Md	102 No	103 Lr

Figure 1-3 The periodic table of the elements as known today.

1.3.2 Chemistry of the actinides

As regards the chemistry of the actinide series, which ranges from Th to Lr – see Figure 1-3 – the following main properties stand out [39,41,42]:

- The actinides result from the successive addition of electrons to the empty 5f orbitals of Ac, a d-block element with the electron configuration [Rn] $7s^2$ $6d^1$.
- Early in the actinide series, the 6d orbitals are lower in energy than the 5f orbitals, which start being filled only at Pa. This is different from what happens in the case of the early lanthanides, where the 4f orbitals are lower in energy than the 5d ones. The energy gap between the $5f^n$ $7s^2$ and the $5f^{n-1}$ 6d $7s^2$ configurations is smaller than in the corresponding lanthanides, and Pa, U, and Np electrons occupy both 5f and 6d orbitals. From Pu onwards, in the ground state, the 6d orbitals are not occupied, with the exception of Cm and most likely Lr, which has not been measured experimentally.
- Relativistic effects cause the 5f orbitals to expand. Therefore they do not penetrate the Rn core and they are not shielded as efficiently by the filled 6s and 6p subshells as the 4f orbitals of the lanthanides are (by the corresponding 5s and 5p subshells). As a consequence, the 5f orbitals participate in bonding in contrast to the 4f electrons.
- For the earlier actinides the more expanded nature of the 5f orbitals and the near-degeneracy of the 5f, 6d, and 7s electrons mean that more outer-shell electrons can be involved in compound formation. This implies that higher oxidation states are available and, as for the d block, several are often available for each metal.

- As the actinide series is traversed and the atomic number increases, the 5f electrons do not shield each other from the increasing nuclear charge effectively, hence causing a rapid drop of both energies and dimensions (i.e., actinide contraction) of the 5f orbitals. As a consequence, the electronic structure and the ions of the later actinides from Am onwards become like those of the lanthanides, whose chemistry they thus resemble.
- For the elements Th, Pa, and U the most stable oxidation states are the highest possible states, i.e., +4, +5, and +6, respectively, which correspond to the noble gas configuration [Rn]. For the elements Np, Pu, and Am the highest oxidation states are +7, +7, and +6, respectively, but the most stable states are +5, +4, and +3, respectively. From Am to Lr the most stable oxidation state becomes +3, with the exception of No where also the +2 state appears to be extremely stable because of the stabilizing effects of the filled – [Rn] $5f^{14}$ – configuration.
- In compounds of the +2, +3, and +4 oxidation states, the metals – M – are usually present as the simple M^{2+}, M^{3+}, and M^{4+} cations or as species derived from these ions. For the higher oxidation states the most common species from U onwards, both in solid compounds and in aqueous solution, are those formed with anions such as F^- or O^{2-}.

The chemistry of the early actinides therefore is quite different from that of the lanthanides, whereas the late actinides resemble the lanthanides quite well.

All actinide elements are radioactive. Only Th, U, and trace amounts of Np and Pu in U ores – formed in interaction of neutrons with ^{238}U [43] – occur in nature. All the other actinides have half-lives short compared to the age of the earth and thus, if formed in primordial nucleosynthesis, they have decayed.

1.4 Target preparation

1.4.1 General target requirements and main production techniques

Lanthanide and actinide layers to be used as nuclear targets should be thin, homogeneous, chemically/radiochemically pure, crack-free, and structurally rigid (i.e., with a good adherence to the deposition substrate). Moreover, due to the scarcity of most of the used isotopes and – in some cases – their high specific activity, the applied preparation methods should give high deposition yields and should be rather simple in order to allow handling in glove-boxes without too much expense. Finally, an easy and complete recovery of the target material should be possible especially if exotic isotopes are used [44].

All of these requirements are valid for both targets to be used as radioactive sources for, e.g., nuclear spectroscopy investigations and targets to be applied in accelerator experiments. Thickness and homogeneity are important in targets to be used for, e.g., activity measurements in order to reduce scattering and absorption of radiations (i.e., back-scattering, self-scattering, and self-absorption) in the sample and in its support. At the same time, targets to be used in accelerator experiments need to be thin and uniform to allow various charged particles to pass through the deposit without undue energy loss. Chemical and radiochemical purities are of course important as interfering radioactive background has always to be avoided. As regards the cracking of the layers, this usually gains more attention in the case of irradiation experiments as cracks and other aberrations in the target result in an increased tendency to break under the thermal stress of the beam [45]. This can lead to material flaking off the target backing, resulting in dead spots on the target face, the wasting of isotopically pure materials and contamination of the experimental area [45]. Further, the target and its backing experience an increase in temperature due to irradiation, which results in warping and often breaking of the deposited layer [46]. Therefore structural rigidity of the produced targets is another fundamental requirement.

Among the large variety of methods available for target preparation conventional ones include: cold rolling [47], vacuum evaporation [48], molecular plating [49], painting/sedimentation [50], electrodeposition [51], die compaction [52], and more recently polymer-assisted deposition [53]. Each method has advantages and disadvantages with regard to the general target requirements.

1.4.2 Molecular plating

Molecular plating is one of the most widely applied target production methods for radioactive isotopes or isotopically enriched material. This technique is based on the electrodeposition of an element either in the constant current or in the constant voltage mode. It uses two-electrode cells (i.e., cathode and anode) where very small volumes (i.e., tens to hundreds of microliters) of an acqueous solution of the element of interest are inserted and mixed with an organic solvent.

MP was first introduced by Parker and Falk [54] in 1962 as an alternative to electrodeposition from acqueous solutions. The original article introduced the new method as follows:

> “The most significant difference between the method to be described and ordinary electrodeposition is that electrolytic dissociation does not occur to any comparable degree during the passage of current. Also, in the present instance, the same chemical compound, chloride or nitrate as the case may be, is deposited at the cathode as that originally dissolved in the electrolyte. Thus we have coined the name “molecular plating” for this particular method. Other differences are the use of high voltages (50-2000 V) and the use of an organic solution” [54].

Less than ten years after its introduction, MP had already made a name for itself by producing a very wide range of targets: targets of nuclides employed as reference samples for the calibration of detection systems, e.g., ^{137}Cs, ^{60}Co [55], targets of lanthanides [56], and targets of actinides [57-59]. All the targets produced by MP were characterized by common properties: quantitative deposition yields, thinness, homogeneity, and structural rigidity of the produced layers. Moreover, the technique stood for its simplicity. In particular, the comparison with ordinary electrodeposition from acqueous solutions showed that despite quantitative deposition yields attainable with both techniques, MP did not require high current densities (mA/cm^2 instead of A/cm^2), thus avoiding disruption of the layer deposit (or the substrate) by means of hydrogen evolution at the cathode [60].

All these positive features have led MP to become one of the most successfully applied methods for the production of targets to be used in nuclear research fields like, e.g., nuclear spectroscopy [3], nuclear reaction studies [4], and also in the research on the physics and chemistry of the superheavy elements [6,7]. Despite this, little has been the development of the technique over time in terms of both characterization of the produced layers and knowledge of the electrochemical processes underlying plating – the only noteworthy result being that the element of interest is usually not deposited as the original chemical compound [61,62]. Definitely, one of the main disadvantages of working with two-electrode cells without reference electrode is that the working potential of the electrode of interest – usually the cathode – is not known, this implying no information about the processes taking place at that electrode. Moreover, the study of the electrochemistry in non-aqueous solutions has a more recent history than that in aqueous solutions, this being additionally complicated by the unique chemistry of the elements usually involved in target preparation, i.e., lanthanides and actinides, some of which are also poorly available and highly radioactive. All this has caused work to focus mainly on gaining empirical evidence on how to further improve the properties of the produced layers [63].

This situation has recently led Garcia et al. [53] and Ali et al. [46] to doubt the suitability of MP especially for the production of targets to be used with the high intensity beams of future generation accelerators. In the last years there has in fact been a push for higher-intensity (i.e., a tenfold intensity increase) beams to further study nuclear structure, nuclear reactions and nuclear astrophysics [see, e.g., 64-66]. A current question in the nuclear target production and application community is then the following: is MP still the ideal technique for target preparation? One of the aims of the present thesis is to give an answer to this question.

1.5 Target characterization techniques

Several analytical techniques were used to characterize the targets produced by molecular plating. They are: neutron activation analysis (NAA), γ-ray spectroscopy, radiographic imaging (RI), scanning electron microscopy (SEM), atomic force microscopy (AFM), and X-ray photoelectron spectroscopy (XPS). In this section the main theoretical and technical aspects of the different techniques are described in order to allow a full understanding of the experiments described in the following chapters. For clarity, NAA and γ-ray spectroscopy are discussed together as their use was always interdependent. Alpha-particle spectroscopy was also used, but not as a target characterization technique. Therefore, general information on α spectroscopy is not reported here, but can be found in Section 1.2.2.1 and later in Chapter 6.

1.5.1 Neutron activation analysis and γ-ray spectroscopy

The activation analyses are a set of elemental analytical techniques characterized by high sensitivity, selectivity, accuracy and precision. Their main drawback is the lack of speciation information, i.e., no information about the chemical form of the element, any attached ligands, and the like is obtained [67]. These analyses allow determining the amount of a given element contained in some material by means of nuclear reactions [26]. Neutrons are the predominant activation particles and nuclear reactors are frequently used for activation analysis as intense sources of such particles. In many reactors of the so-called swimming pool type, e.g., the TRIGA research reactors (Figure 1-4a), the neutrons are generated inside the reactor core, which is situated at the bottom of a water tank. The neutron spectra of nuclear reactors have always shapes similar to that shown in Figure 1-4b [68], but the ratios between thermal ($E_n < 0.05$ eV), epithermal ($0.05 < E_n < 10^5$ eV), and fast neutrons ($10^5 < E_n < 10^7$ eV) are different and vary even inside a reactor. Thermal neutrons mainly induce (n,γ) reactions in the atoms of the stable elements, i.e., the atom captures a neutron and the new nuclide is generated in an excited state, which generally de-excites by the emission of γ rays or conversion electrons. Most activation analysis is done with thermal neutrons as many elements have high cross sections for the (n,γ) reactions with such neutrons. Moreover, copious fluxes of thermal neutrons ($\varphi \sim 10^{12}$ cm^{-2}s^{-1}) are generally available in nuclear reactors [26].

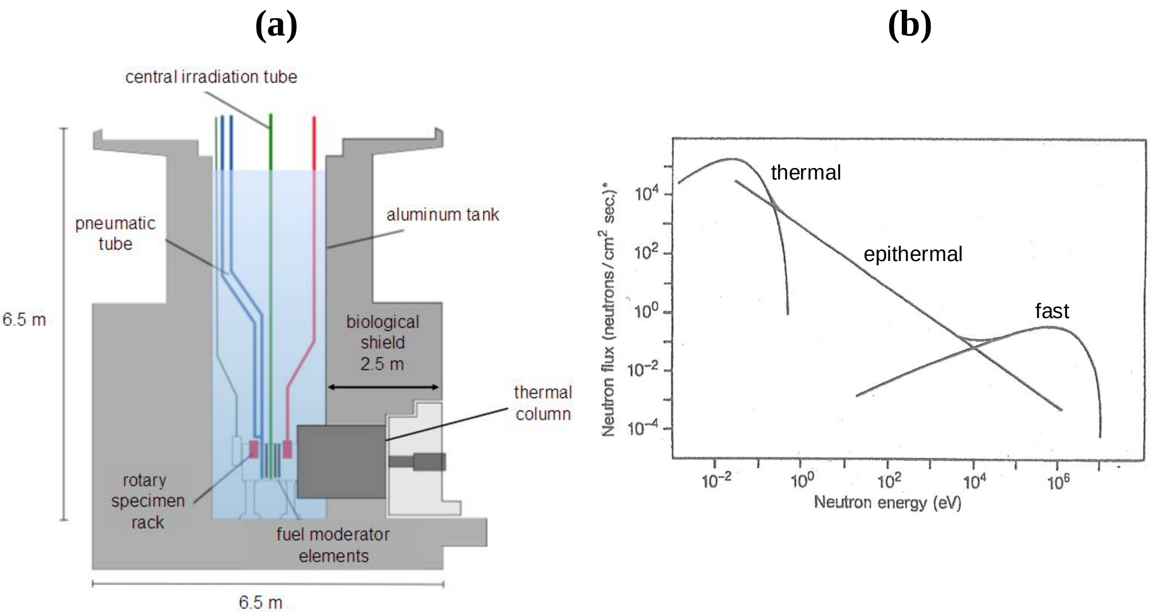

Figure 1-4 Cross-sectional view of the TRIGA Mainz research reactor (a). Typical neutron spectrum in a reactor irradiation facility (b) [68].

NAA offers several methods to determine the amount of an element contained in a certain matrix. Usually, absolute or relative activation analyses are performed, with the relative method being the simplest one. In this case, standards of known amounts of pure material have to be irradiated and counted using the same conditions as the samples being analyzed. The mass of the sample element (m_x) is then calculated as follows [26]:

$$m_x = m_{st} \times \left(\frac{A_x}{A_{st}} \right) \qquad (5)$$

where m_{st} is the mass of the standard, and A_x and A_{st} are the activities of the irradiated sample and standard, respectively.

The first step of a relative activation analysis is the preparation of the standard and the sample, which should have the same size, geometry, composition and homogeneity to ensure that any attenuation of the incoming radiation, or the sample radiation before counting, or any count rate-dependent effects, are exactly the same. The cross section of the (n,γ) reaction, the isotopic abundancy of the target nucleus, and the half-life of the formed isotope should be large enough to allow measurement of the emitted radiation. The irradiation conditions involve the determination of the flux and irradiation duration. The activation analyses performed in the framework of the present thesis always adopted the relative method and used the rotary specimen rack (see Figure 1-4a) as irradiation position inside the reactor, where a thermal neutron flux of $7 \cdot 10^{11}$ $cm^{-2}s^{-1}$ was delivered. The samples were liquid solutions contained in sealed polyethylene test-tubes, which were used because of their purity, low cross section for thermal neutrons, little or no long-lived activity by activation, and resistance to radiation [67]. The isolation of the activity of interest and its counting were always performed without any previous radiochemical treatment. Indeed, a high-purity Ge (HPGe) detector was used to identify the radionuclides in the radioactive sample from the characteristic energies of their delayed γ rays, and the measurement of the corresponding activities could thus be performed.

The HPGe detector is a PIN diode detector where the n-type region is prepared by Li diffusion without drifting and the p-type region is prepared by implanting B ions. The absence of Li drifting allows this detector to be stored at room temperature, and to be cooled only when in use [69]. HPGe detectors are therefore normally housed in vacuum-tight cryostats, which are mounted on liquid nitrogen dewars. To reduce natural background, most γ-ray detectors are operated within a shielded enclosure. A γ-ray spectroscopy system similar to that used for the performed experiments is shown in Figure 1-5.

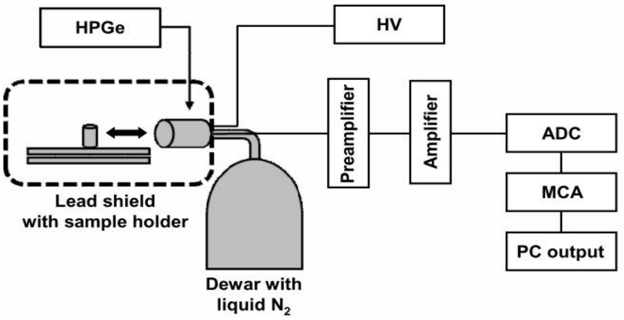

Figure 1-5 Block diagram of a set-up for performing γ-spectroscopy with a high-purity Ge (HPGe) detector.

The sample is always placed at a certain distance from the HPGe detector, which is connected to a high-voltage (HV) power supply. The initial signal is very small and the preamplifier, attached directly to the detector, amplifies this signal. The signal is shaped by the spectroscopy amplifier and then converted from analog to digital by the analog-to-digital converter (ADC). The results are stored in digital form in the multi-channel analyzer (MCA). The output of the analysis is a plot of signal intensity (i.e., number of counts per channel) *vs* channel number, which can be readily converted into signal intensity *vs* γ-ray energy after calibration of the detector.

In the experiments performed with, e.g., Nd-containing samples, the reaction ^{146}Nd(n, γ)^{147}Nd was used to produce ^{147}Nd, which decays by β^- emission to ^{147}Pm. The 91.0 keV γ line is the most intense one [70] and was always used as a reference peak when counting Nd samples after neutron irradiations (Figure 1-6).

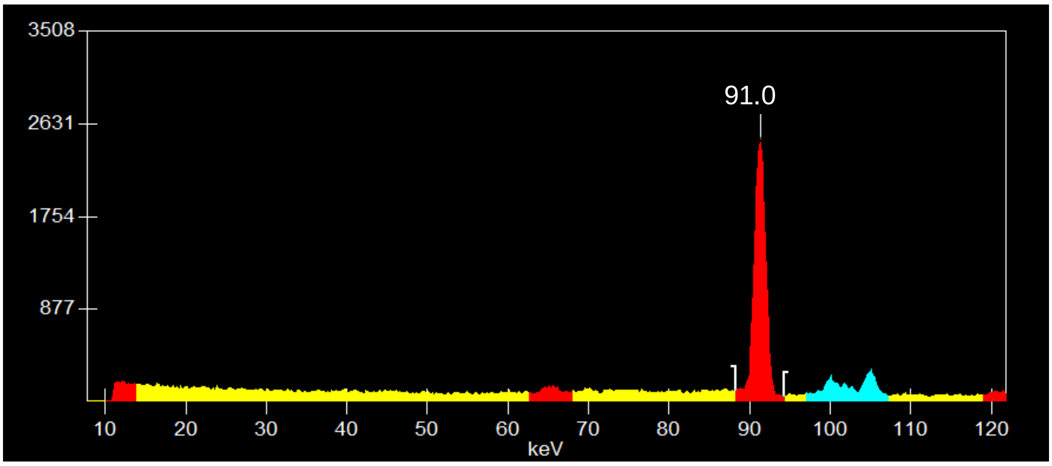

Figure 1-6 The 91.0 keV γ line resulting from the decay of ^{147}Nd produced in the reaction ^{146}Nd(n, γ)^{147}Nd. The spectrum was recorded using the software Genie 2000.

The spectrum for low γ-ray energies – up to several hundred keV, where pair production is not significant – consists of a Compton continuum and photopeaks. The Compton continuum is the continuum of energies corresponding to the Compton scattered electrons, whereas the photopeak corresponds to the electrons originated by photoelectric absorption of the γ ray of interest inside the detector volume. At very low energy (< 100 keV) the Compton continuum may almost disappear [69] – see Figure 1-6 – hence increasing the ratio of the area under the photopeak to that under the entire spectrum. To evaluate the peak areas background subtraction has to be performed, and some shape has to be assumed for the continuum to be removed. Experimentally, the peak areas obtained after counting of, e.g.,^{147}Nd samples were always calculated by subtracting linear or step continuum backgrounds (see [71] for details on peak area calculations). According to (5), these areas were then used to evaluate the amount of the element of interest and hence the deposition yields obtained after the perfomed MP experiments.

1.5.2 Radiographic imaging

Radiographic imaging is based on the effect of photostimulated luminescence (PSL) and the use of an imaging plate (IP), which is a two-dimensional detector of ionizing radiation utilizing a photostimulable phosphor [72]. Powdery materials capable of emitting light when stimulated by, e.g., electromagnetic radiation, are commonly referred to as phosphors. Photostimulated luminescence involves a phosphor, commonly a $BaFX:Eu^{2+}$ (X = Cl, Br, or I) ionic crystal. The crystal is doped with a trace amount of Eu^{2+}, which acts as luminescence center by replacing Ba to create a solid solution. When $BaFX:Eu^{2+}$ is irradiated with ionizing radiation, e.g., γ rays, Eu^{2+} centers become Eu^{3+} and electron-hole pairs are produced, the number of which is proportional to the absorbed radiation energy. These pairs create quasi-stable F-centers, which can be of two types: $F(F^-)$ and $F(X^-)$ [73]. An F-center, or color center, consists of an electron occupying a halogen ion vacancy. The F-centers and corresponding hole traps can thus store energy of absorbed ionizing radiation. The mechanism of the release of this absorbed energy is mainly interpreted according to the theory from Takahashi et al. [72,73], which can be explained as follows: once the F-centers have been formed, the irradiation with a lower-frequency light source, e.g. red light, than that used to create the Eu^{3+} ions raises the trapped electrons to their excited states, where they are thermally excited to the conduction band. At this point, the electrons recombine with holes trapped by Eu^{2+} ions, producing an excited Eu^{2+} ion, which de-excites by emitting light corresponding to the 5d-4f transitions. The light intensity is proportional to the number of trapped electrons, and thus to the absorbed radiation energy. Using two-dimensional position sensitive imaging plates, RI can be applied to investigate the distribution of, e.g., radioactive material on a sample surface. In this work, the surface homogeneity of radioactive targets produced by MP using γ-emitting tracers, e.g., ^{147}Nd, was analyzed by RI. The spatial resolution of the technique was < 200 μm [74]. Experimentally, the RI analyses were carried out as follows: a flexible IP, in which bunches of 5-μm large crystals of $BaFBr:Eu^{2+}$ were uniformly coated on a polyester support film, was exposed for a definite amount of time to the γ radiation emitted from the produced target. The exposed IP was then scanned with a laser beam of red light while being conveyed with high accuracy in a phosphor reader. A bluish purple (400 nm) PSL light, released upon laser excitation, was collected through the light collection guide to the photomultiplier tube (Figure 1-7 [75]). This light was converted to analog electric signals, which were later transformed into digital signals. These signals were saved in a computer and then elaborated to create a 3D radiographic image that reflected the spatial activity distribution and hence the homogeneity of the sample.

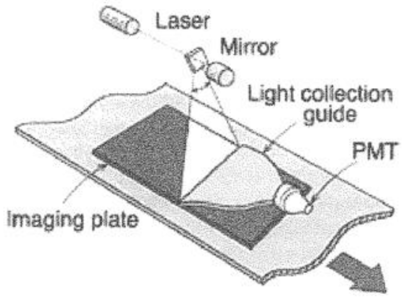

Figure 1-7 The exposed imaging plate, while being conveyed, is scanned with a focused laser beam. The PSL light released upon the laser is collected into the photomultiplier tube through the light collection guide and is converted to electric signals [75].

1.5.3 Scanning electron microscopy

The scanning electron microscope permits the observation and characterization of heterogeneous organic and inorganic materials on a nanometer to micrometer scale [76]. The two major components of a SEM are the electron column and the control system (Figure 1-8 [77]).

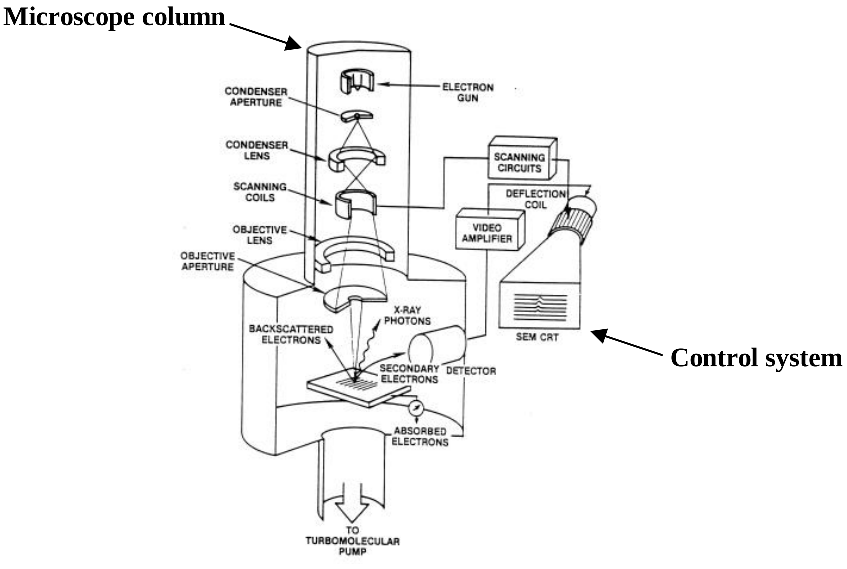

Figure 1-8 The two major parts of the SEM, the electron column and the control system [77].

The electron column consists of an electron gun and two or more electron lenses, which influence the paths of electrons traveling down an evacuated tube. The base of the column is usually taken up with vacuum pumps that produce vacuum of about 10^{-4} Pa. The control system consists of a cathode ray tube (CRT) viewing screen and the knobs and computer keyboard that control the electron beam.

In the electron gun, electrons crated by thermoionic emission from a negatively biased W cathode are accelerated to ground potential at the anode. A hole in the anode allows a fraction of these electrons to proceed down the column. As the spot size from the electron gun is too large to produce a sharp image, electromagnetic lenses are used to focus the electrons into a small (usually less than 10 nm) spot on the specimen. The beam emerges from the final lens into the specimen chamber, where it interacts with the specimen, which must be electrically conductive, at least at the surface, and electrically grounded to prevent the accumulation of electrostatic charge. The scanned image is formed point by point. The deflection system causes the beam to move to a series of discrete locations along a line and then along another line below the first, and so on, until a rectangular raster is generated on the specimen. Simultaneously, the same scan generator creates a similar raster on the CRT viewing screen, hence producing an image whose magnification is the ratio of the length of the raster on the viewing screen to the corresponding length of the raster on the specimen. As the beam electrons enter the specimen, they undergo inelastic and elastic scattering processes, which distribute the electrons over a three-dimensional interaction volume with dimensions in the micrometer range. The sizes of this volume and of the electron spot create serious restrictions on the spatial resolution of SEM, which cannot in fact resolve atomic distances. From the interaction volume various types of radiation emerge, including backscattered and secondary electrons, characteristic X rays, and cathodoluminescence radiation. Among all these types of radiation, backscattered and secondary electrons are the most commonly detected radiations. Backscattered electrons are high-energy beam electrons, which are reflected out of the specimen interaction volume by elastic scattering interactions with specimen atoms. Secondary electrons are instead low-energy (< 50 eV) electrons that are ejected from loosely bound outer shells of the specimen atoms by inelastic scattering interactions with beam electrons. Usually, an Everhart-Thornley detector is used, which collects both secondary and backscattered electrons. As the electrons are accelerated towards a positively biased thin metal coating on the face of a scintillator material, light is emitted and conducted by total internal reflection in a light guide to a photomultiplier, where photons are converted back into electrons and multiplied. The amplified electrical signal is first subjected to analog-to-digital conversion and then displayed and saved as a digital image. Backscattered and secondary electrons are the principal signals used to form images in scanning electron microscopy, because they are capable of carrying information about the specimen in terms of image contrast, which arises when the signal collected from the beam-specimen interaction varies from one location to another. The most frequent application of the SEM is the visualization of the topography of three-dimensional objects. Topographic contrast includes all those effects by which the morphology of the specimen can be imaged. This contrast arises because the number of the detected secondary and backscattered electrons depends on the angle of incidence between the beam and the specimen surface, which varies only according to the local inclination of the specimen. As the angle of incidence increases, the escape distance of one side of the beam will decrease, and more electrons will be emitted. Thus steep surfaces and edges tend to be brighter than flat surfaces, which results in images with a well-defined, three-dimensional appearance.

The SEM experiments performed during the thesis were always dedicated to characterize the morphology of the targets produced by MP.

1.5.4 Atomic force microscopy

Atomic force microscopy is a scanning technique, which produces very high resolution, 3D images of sample surfaces. The AFM physically “feels” the surface with a sharp tip, by which ultrasmall forces (less than 1 nN) present between the AFM tip surface and the sample surface are measured. This technique is most often compared with SEM, as the dimensional range of the two techniques is rather similar, with SEM having a somewhat lower resolution (5 nm) to AFM (0.1 nm) [78]. Nonetheless, because of the AFM’s ability to magnify in the X, Y, and Z axes, maps of the height of the sample surface can be built up, which is not possible with SEM where only two-dimensional projections of the surfaces are recorded. Moreover, AFMs are capable of investigating the surfaces of both conductors and insulators in almost any environment, from vacuum, to gas, to liquid, with the ambient air conditions being the most usually applied ones. With electron beam techniques, instead, only conductive samples and vacuum environments are admitted for measurement. The main limiting characteristic of the AFM is that it is not practical to make measurements on areas greater than about 100 × 100 μm^2, as the scanning of the surface would be too slow.

The main components of an AFM are the microscope stage, the control electronics and a computer. The microscope stage contains the scanner (i.e., piezoelectric transducers), the sample holder and the force sensor. Often, the stage is supported on a vibration isolation platform which reduces noise and increases the obtainable resolution.

The piezoelectric transducers contained in the AFM stage are used for scanning of the sample surfaces. They are electromechanical materials (usually lead barium titanate ceramics) that convert electrical potential into mechanical motion by changes in the crystal structure, with expansion in some directions and contraction in others. The AFM used during the thesis allowed horizontal X-Y scanning (see Figure 1-9 [79]) by means of a plate where two piezo transducers were inserted. Vertical Z scanning was instead performed by a piezo contained in the head of the instrument that permitted also amplitude modulation vibration during tapping mode analysis (see below).

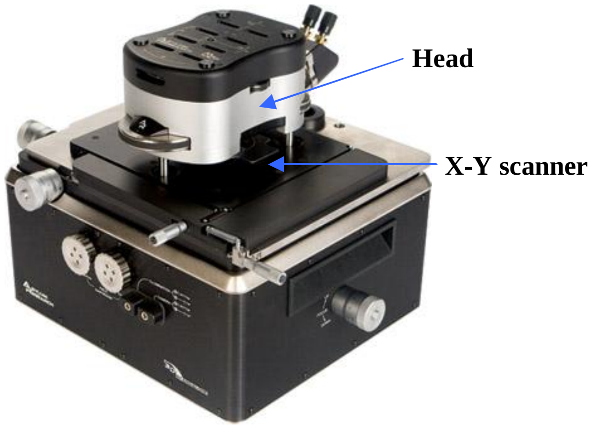

Figure 1-9 An image of the atomic force microscope used for the experiments performed during the thesis [79].

The force sensors of the AFM stage are instead used to sense the force between the tip and the surface of the sample. They are microfabricated silicon or silicon nitride cantilevers with a sharp tip at their end. Usually, a laser beam hits the reflective back side of the cantilever and the light is reflected onto a four-segment photodiode detector (Figure 1-10 [78]). When the tip interacts with the sample surface the reflected light path changes, and the force is then measured by monitoring the change in light detected by the four quadrants of the photodetector.

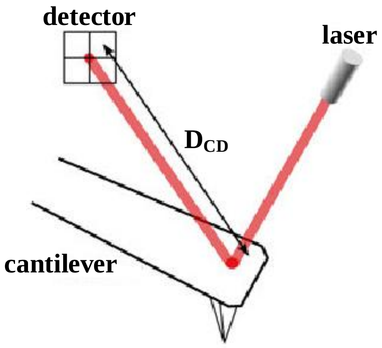

Figure 1-10 Shematic diagram of the force measurement with a force sensor. As the cantilever-detector distance D_{CD} is large, a small movement of the cantilever causes a large change in the laser spot position at the detector [78].

In an AFM, the force between the sample and the tip is used to sense the proximity of the tip to the sample [80]. The AFM can be used either in the static or the dynamic mode. In the static mode, also referred to as contact mode, the sharp tip at the end of the cantilever is brought into contact with the sample surface. During initial contact, the atoms at the end of the tip experience a very weak repulsive force due to electronic orbital overlap with the atoms in the surface of the sample. The force acting on the tip causes the cantilever to deflect, which is measured by the photodetector. In the dynamic mode of operation, also referred to as noncontact imaging mode, the tip is instead brought into close proximity to (within a few nanometers of), but not in contact with, the sample. The cantilever, is deliberately vibrated in either amplitude modulation mode or frequency modulation mode. Very weak van der Waals attractive forces are present at the tip-sample interface and the effect is a damping of the cantilever oscillation, which leads to a reduction in the frequency and amplitude of the oscillation as monitored by the force sensor.

Lateral forces applied at the tip during scanning in the contact mode affect roughness measurements, which are performed by measuring the height variations of the piezoelectric transducers. To minimize the effects of friction and other lateral forces on topography measurements in the contact mode, AFMs can be operated in the so-called tapping or intermittent contact mode. In the tapping mode, during the surface scan, the cantilever/tip assembly is vibrated in amplitude modulation mode by a Z piezo mounted above the assembly, and the oscillating tip slightly taps the surface at the resonant frequency of the cantilever (70-400 kHz) with a constant (20-100 nm) amplitude of vertical oscillation (Figure 1-11 [80]). The oscillating amplitude is kept large enough that the tip passes from the attractive to the repulsive regimes without getting stuck to the sample.

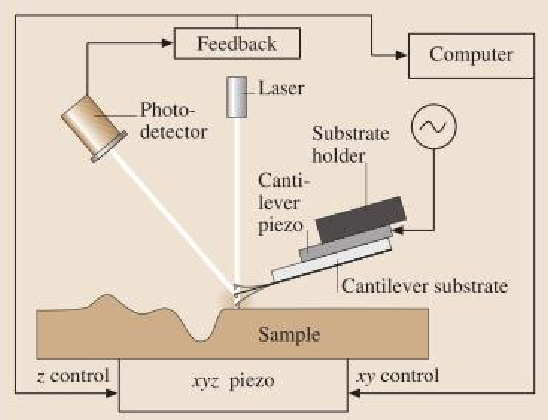

Figure 1-11 Shematic of tapping mode used for surface roughness measurements [80].

The amplitude is reduced by the contact with the sample surface and the change in the oscillation is used in a feedback loop to maintain the probe-sample interaction constant and hence the probe-sample distance fixed. The amount the Z piezoelectric moves up and down to maintain the tip-sample distance fixed is assumed to be equal to the sample topography. In this way, a height image is recorded, and the surface roughness is measured.

Tapping mode analysis allows also amplitude and phase-shift images to be recorded. Amplitude images can be used as an illustration of the shape (morphology) of the sample, while phase images, which depend on the shifts of the phase of the oscillating cantilever due to tip-sample interactions, represent a useful way of distinguishing materials.

During the thesis, mainly tapping mode analyses were performed, which allowed the evaluation of the surface roughness of the produced targets. Topographic images were thus primarily recorded.

1.5.5 X-ray photoelectron spectroscopy

XPS relies on the photoelectric effect. The energy carried by an incoming X-ray photon is absorbed by the target atom, raising it into an excited state from which it relaxes by the emission of a photoelectron. The typical XPS spectrometer consists mainly of a X-ray source, a sample holder providing electrical contact between sample and spectrometer, an electron energy analyzer and a detection system (Figure 1-12 [81]).

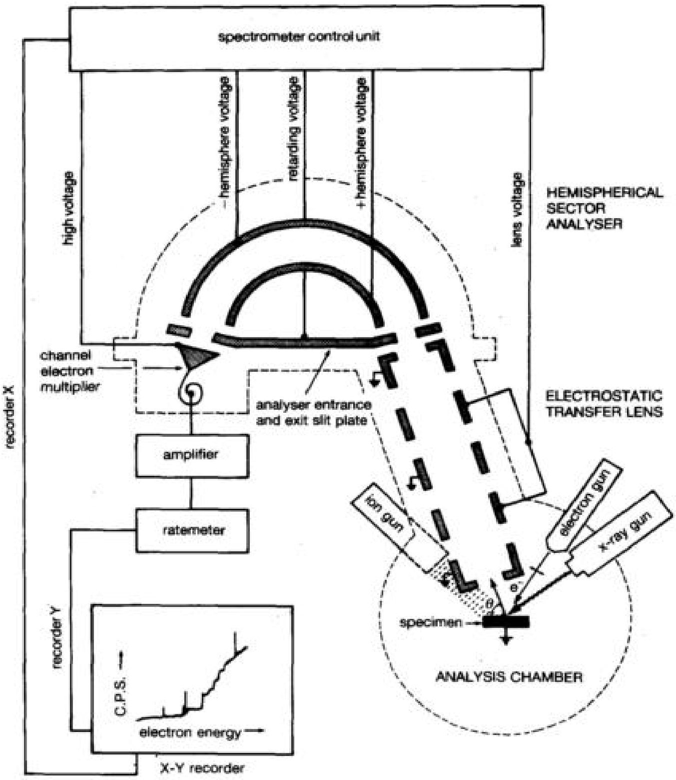

Figure 1-12 Schematic representation of the main components of a XPS spectrometer [81].

In order to avoid any possible interference during the analysis, the spectrometer is always operated in ultra-high vacuum (UHV) conditions, i.e., with pressures around 10^{-6} Pa. In the X-ray source thermoionic electrons emitted from a W filament are accelerated and focused onto water-cooled Mg or Al anodes [82]. The twin-anode design enables to distinguish photoelectron and Auger lines present in the spectra. The impact of the high energy electrons causes the emission of K_α X-rays of characteristic energies: 1253.6 eV for Mg and 1486.6 eV for Al. Other contributions to the X-ray spectrum are due to double ionization phenomena, transitions from the valence band, and bremsstrahlung background. All these contributions lead to “satellite” peaks in the spectra by means of induced photoemission. The peaks are removed by the use of a monochromator, which helps also to enhance the resolution of the analysis by focusing and monochromatizing the K_α X-rays.

Once the K_α X-rays hit the surface of the sample, photoelectrons are emitted from all energy levels (i.e., core and valence levels) of the target atom (Figure 1-13a [81]). As energy is conserved, the following relationship is valid for the emitted photoelectron:

$$\text{K.E.} = h\nu - \text{B.E.} - \phi_{\text{sample}} \qquad (6)$$

where K.E. and B.E. are the kinetic energy and binding energy of the electron, respectively, hν is the photon energy, and ϕ_{sample} is the work function of the solid sample (Figure 1-13b [81]).

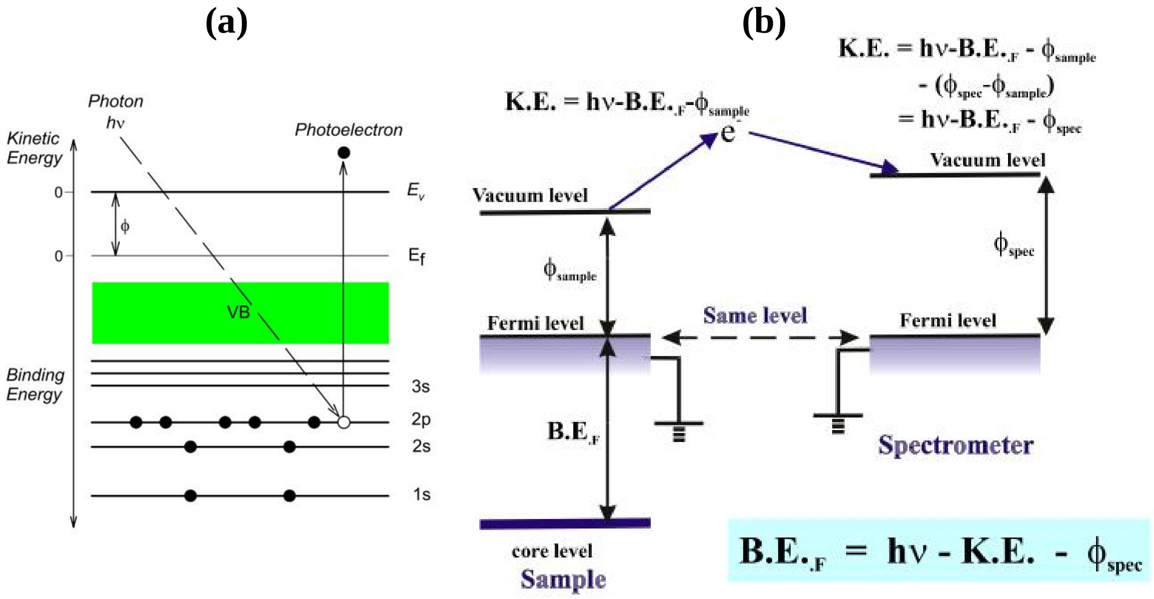

Figure 1-13 The electron transition involved in the photoemission of a 2p electron from a target atom (a) [81]. Energy level diagram for an electrically conductive sample grounded to the spectrometer (b) [81].

Because of the electrical contact, the Fermi levels of both sample and spectrometer are aligned. The K.E. of the photoelectrons can then be measured from the Fermi level of the spectrometer (see Figure 1-13b), hence (6) is always transformed into the following relationship:

$$K.E. = h\nu - B.E. - \phi_{spec} \qquad (7)$$

where all the terms are exactly those of (6) except for ϕ_{spec}, which is the work function of the spectrometer.

The photoelectrons emitted from the surface of the sample with kinetic energy K.E. are collected by the electron energy analyzer. Commonly, this is a hemispherical sector analyzer where electrostatic fields are established to deflect the electrons between two hemispheres in such a way that only those travelling at a defined – frequently constant – energy (the so-called pass energy) arrive at the detector. The detection system is an electron multiplier, usually a channeltron. The output of the analysis is a plot of signal intensity (i.e., number of electrons counted per second – cps –) *vs* K.E. of the electrons. As during a XPS experiment K.E., hν, and ϕ_{spec} are known, the B.E. of an atomic electron can be easily derived. Therefore a XPS spectrum allows inferring the electronic structure of a solid from the valence band to the core electrons.

After X-ray bombardment, the excited electrons may either be emitted from the sample without energy loss, leading to the characteristic (elastic) peaks of the XPS spectrum, or may undergo one or more inelastic scattering processes, which contribute to the background formation. The background rises on the high binding energy side (low kinetic energy) of each peak (Figure 1-14 [83]), as a result of each individual photoemission line acting as a source of additional electrons, which may subsequently undergo scattering events [84].

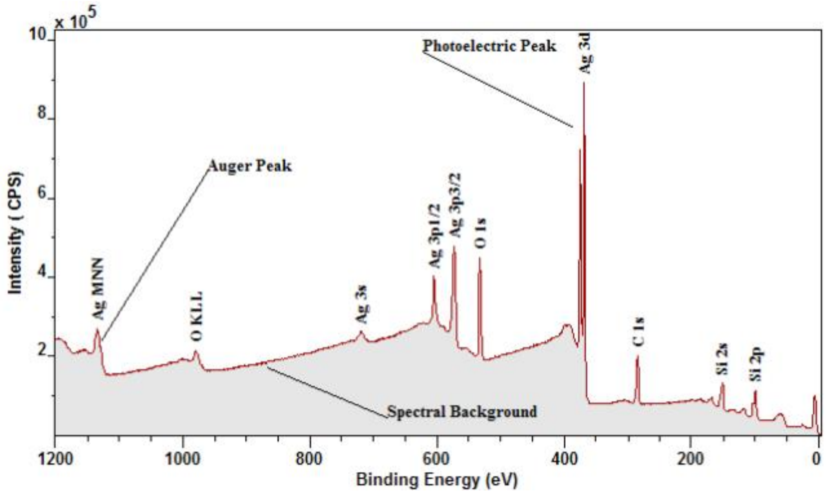

Figure 1-14 An example of a typical XPS survey spectrum taken from a compound sample using Mg K_α radiation. XPS and Auger peaks appear above a background of scattered electrons [83].

To evaluate the area and the exact B.E. position of a XPS peak, a background subtraction has always to be performed. The most common backgrounds to subtract are linear or Shirley backgrounds (for details see [83]). The B.E. of the XPS peak is usually influenced by the formal oxidation state of the atom and its local chemical and physical environment [84]. In general, the more tightly bound the electron is in a particular chemical configuration, the higher will be the B.E. of the corresponding peak in the photoelectron spectrum. The change in energy of the photoelectron line from a certain atom is called its chemical shift. Shifts in peak energies are observed also because of electrostatic charging of the sample during XPS measurement. In such cases, it is common practice to identify a reference peak, note its energy difference from the expected value, and apply the same shift to all other peaks in the spectrum before making any chemical state assignments.

While the Al and Mg K_α radiations normally used for the XPS analyses penetrate into the samples up to some micrometers, only the electrons emitted from the first atomic layers reach the detector without undergoing inelastic scattering. For an electron of intensity I_0 emitted at a depth d below the surface, the intensity is attenuated according to the Beer-Lambert law. Therefore, the intensity I_s of the same electron as it reaches the surface is:

$$I_s = I_0 \exp\left(-\frac{d}{\lambda}\right) \qquad (8)$$

where λ is the inelastic mean free path of an electron in a solid. According to this exponential law, 95% of the photoelectronic signal is made by electrons which have covered a distance smaller than 3λ. In the case of, e.g., Al K_α radiation most λ's are in the range of 1 – 3.5 nm, hence the sampling depth (3λ) for XPS under these conditions is only 3 – 10 nm [84]. For these reasons XPS is widely used as a very sensitive surface analysis technique, which can convey both compositional and quantitative surface information.

In the experiments performed in this thesis, XPS was always used to carry out compositional surface analyses of the targets produced by MP.

1.6 Outline of the thesis

On the way to the production of targets for TRAKULA, first molecular plating experiments using Gd and Nd as test elements were performed. Special focus was on the search for optimal deposition conditions for small-area targets that could be also applicable to the large-area targets needed for the project. In particular, mixing the plating solutions with an ultrasonic stirrer was found to be suitable for the future production of the large-area U and Pu targets. This mixing technique avoids the use of large volumes of solution, which are disadvantageous for the recovery of rare and expensive isotopes in case of incomplete depositions and are difficult to cool down. First attempts to explain the MP process were also made. This work, a contribution to the proceedings of the 25th World Conference of the International Nuclear Target Development Society (INTDS), is published in “Nuclear Instruments and Methods in Physics Research A” and is presented in Chapter 2.

To understand how to produce better quality layers for nuclear science experiments, thorough, systematic investigations of the fundamental aspects of the molecular plating process were carried out. The elucidation of the method required performing constant current density MPs, which used a Nd salt as model electrolyte for the tests and a mixture of isopropanol and isobutanol as plating solvent. Several MP parameters were varied to investigate the process and cell potential curves were recorded to monitor the response of the process to the variables. Different analytical techniques were used to investigate the produced Nd layers and the results of these investigations allowed interpreting the observed behaviours of the MPs. A theoretical description of important basic features of constant current density MP was formulated. This work is published in "Nuclear Instruments and Methods in Physics Research A" and it is presented in Chapter 3.

Chapter 4 resumes the main conclusions reported in Chapter 3 and presents new, preliminary results obtained by changing the plating solvent from the mixture of isopropanol and isobutanol to the low-volatility N,N-dimethylformamide. The use of this solvent and of smooth deposition substrates – suggested by the MP elucidation study and by new layer characterizations – allowed the production of the first smooth and crack-free Nd layers. This work is a contribution to the proceedings of the 26th World Conference of the International Nuclear Target Development Society (INTDS) and it is accepted for publication in "Journal of Radioanalytical and Nuclear Chemistry".

A full account of the experiments with N,N-dimethylformamide and with solvents other than isopropanol/isobutanol, also under conditions beyond the ones described in Chapter 4, is reported in Chapter 5. Here, the core factors playing a decisive role for the production of smooth and crack-free Nd layers by means of molecular plating are outlined and explained. A comparison with the polymer-assisted deposition method [53] is made. This work has been published in "Nuclear Instruments and Methods in Physics Research A".

Towards the future determination of the precise half-life of ^{144}Nd ($t_{1/2} \sim 2.7 \cdot 10^{15}$ y [3]), constant current density MPs were carried out to prepare different ^{147}Sm layers, whose performance as α-particle sources was investigated. ^{147}Sm ($t_{1/2} \sim 1.1 \cdot 10^{11}$ y [31]) was selected as model isotope for the investigations because of its relatively high specific activity. The MP parameters that most significantly affected the quality of the produced α sources were identified, and optimum conditions were determined. This work has been published in "Nuclear Instruments and Methods in Physics Research A" and it is presented in Chapter 6.

Chapter 7 contains concluding remarks and a short outlook.

References

[1] R.F. Sperlein, R.L. Wolke, *A search for alpha instability in* ^{184}*Os*, J. Inorg. Nucl. Chem. **38** (1976) 27-29.

[2] R.D. Macfarlane, T.P. Kohman, *Natural alpha radioactivity in medium-heavy elements*, Phys. Rev. **121** (1961) 1758-1769.

[3] B. Al-Bataina, J. Jänecke, *Half-lives of long-lived alpha emitters*, Radiochim. Acta, **42** (1987) 159-164.

[4] J.E. Evans, R.W. Lougheed, M.S. Coops, R.W. Hoff, E.K. Hulet, *The use of electrodeposition methods to prepare actinide targets for cross-section measurements and accelerator bombardments*, Nucl. Instrum. Methods **102** (1972) 389-401.

[5] H. Sakane, Y. Kasugai, M. Shibata, Y. Ikeda, K. Kawade, *Measurement of the activation cross-sections of (n,np+d) reactions for lanthanide isotopes in the energy range between 13.4 and 14.9 MeV*, Ann. Nucl. Energy **29** (2002) 1209-1224.

[6] K. Eberhardt, M. Schädel, E. Schimpf, P. Thörle, N. Trautmann, *Preparation of targets by electrodeposition for heavy element studies*, Nucl. Instrum. Meth. A **521** (2004) 208-213.

[7] Yu.V. Lobanov, G.V. Buklanov, F.Sh. Abdullin, A.N. Polyakov, I.V. Shirokovsky, Yu.S. Tsyganov, V.K. Utyonkov, *Targets of uranium, plutonium, and curium for heavy-element research*, Nucl. Instrum. Meth. A **397** (1997) 26-29.

[8] G. Chapline, *Fission fragment rocket concept*, Nucl. Instrum. Meth. A **271** (1988) 134-140.

[9] C. Rubbia, *Neutrons in a highly diffusive, transparent medium: an effective neutron storage device,* Emerging Nuclear Energy Systems ICENES'98, Proceedings of the Ninth International Conference on Emerging Nuclear Energy Systems, Herzliya, Israel, Vol. 1(4), June 28-July 2, 1998.

[10] Y. Ronen, E. Shwageraus, *Ultra-thin* ^{242m}*Am fuel elements in nuclear reactors,* Nucl. Instrum. Meth. A **455** (2000) 442-451.

[11] Y.A. Akovali, *Nuclear data sheets for A = 242,* Nucl. Data Sheets **96** (2002) 177-239.

[12] C. Rubbia, *Report of the working group on a preliminary assessment of a new fission fragment heated propulsion concept and its applicability to manned missions to the planet Mars*, Italian Space Agency, Rome, April 1999.

[13] Y. Ronen, M. Aboudy, D. Regev, *A novel method for energy production using* ^{242m}*Am as a nuclear fuel*, Nucl. Technol. **129** (2000) 407-417.

[14] P. Benetti, A. Cesana, L. Cinotti, G.L. Raselli, M. Terrani, *^{242m}Am and its potential use in space applications*, EPS Euroconference XIX Nuclear Physics Divisional Conference, Journal of Physics: Conference Series **41** (2006) 161-168.

[15] TRAKULA website (www.hzdr.de/TRAKULA).

[16] M. Salvatores, G. Palmiotti, *Radioactive waste partitioning and transmutation within advanced fuel cycles: achievements and challenges*, Prog. Part. Nucl. Phys. **66** (2011) 144-166.

[17] A.R. Junghans, *Transmutation of high-level radioactive waste: basics, methods, perspectives*, Nuclear Physics Data for the Transmutation of Nuclear Waste, WE-Heraeus-Seminar, Bad Honnef, Germany, February 25-27, 2013.

[18] *Potential benefits and impacts of advanced nuclear fuel cycles with actinide partitioning and transmutation*, NEA status report 6894, 2011.

[19] *Physics and safety of transmutation systems*, NEA status report 6090, 2006.

[20] C. Kraus, S.J.M. Peeters, *The rich neutrino programme of the SNO+ experiment*, Prog. Part. Nucl. Phys. **64** (2010) 273-277, and SNO+ website (http://snoplus.phy.queenssu.ca).

[21] J. Dawson, R. Ramaswamy, C. Reeve, J.R. Wilson, K. Zuber, *A search for various double beta decay modes of tin isotopes*, Nucl. Phys. A **799** (2008) 167-180.

[22] C. Droese, K. Blaum, M. Block, S. Eliseev, F. Herfurth, E.M. Ramirez, Yu.N. Novikov, L. Schweikhard, V.M. Shabaev, I.I. Tupitsyn, S. Wycech, K. Zuber, N.A. Zubova, *Probing the nuclide ^{180}W for neutrinoless double-electron capture exploration*, Nucl. Phys. A **875** (2012) 1-7.

[23] S.R. Elliott, P. Vogel, *Double beta decay*, Annu. Rev. Nucl. Part. Sci. **52** (2002) 115-151.

[24] J. Dawson, D. Degering, M. Köhler, R. Ramaswamy, C. Reeve, J.R. Wilson, K. Zuber, *Search for double-β decays of tin isotopes with enhanced sensitivity*, Phy. Rev. C **78** (2008) 035503 (6).

[25] K. Zuber, *Nd double-β decay search with SNO+*, AIP Conf. Proc. **942** (2007) 101-104.

[26] W. Loveland, D.J. Morrissey, G.T. Seaborg, *Modern Nuclear Chemistry*, first ed., Wiley, New Jersey, 2006.

[27] *Uncertainty and target accuracy assessment for innovative systems using recent covariance data evaluations*, NEA status report 6410, 2008.

[28] E. Altstadt, C. Beckert, H. Freiesleben, V. Galindo, E. Grosse, A.R. Junghans, J. Klug, B. Naumann, S. Schneider, R. Schlenk, A. Wagner, F.P. Weiss, *A photo-neutron source for time-of-flight measurements at the radiation source ELBE*, Nucl. Instrum. Meth. A **34** (2007) 36-50.

[29] G. Friedlander, J.W Kennedy, E.S. Macias, J.M. Miller, *Nuclear and Radiochemistry*, third ed., Wiley, New York, 1981.

[30] P. de Marcillac, N. Coron, G. Dambier, J. Leblanc, J.P. Moalic, *Experimental detection of α-particles from the radioactive decay of natural bismuth*, Nature **422** (2003) 876-878.

[31] K. Kossert, G. Jörg, O. Nähle, C.L.V. Gostomski, *High-precision measurement of the half life of* ^{147}*Sm*, Appl. Radiat. Isot. **67** (2009) 1702-1706.

[32] N. Coron, G. Dambier, G.J. Focker, P.G. Hansen, G. Jegoudez, B. Jonson, J. Leblanc, J.P. Moalic, H.L. Ravn, H.H. Stroke, O. Testard, *A composite bolometer as a charged-particle spectrometer*, Nature **314** (1985) 75-76.

[33] E.C. Waldron, V.A. Schultz, T.P. Kohman, *Natural alpha activity of Neodymium*, Phys. Rev. **93** (1954) 254-255.

[34] W. Porschen, W. Riezler, *Natürliche Radioaktivität von Platin und Neodym*, Z. Naturforsch. **9** (1954) 701-703.

[35] W. Porschen, W. Riezler, *Sehr langlebige natürliche α-Strahler*, Z. Naturforsch. **11** (1956) 143-151.

[36] W.H. Kelly, G.B. Beard, Bull. Am. Phys. Soc. **4** (1959) 324-325.

[37] F.J. Bradley, J.D. Kurbatov, Bull. Am. Phys. Soc. **5** (1960) 20-21.

[38] A. Isola, M. Nurmia, *Alpha activity of natural neodymium*, Z. Naturforsch. **20** (1965) 541-542.

[39] J.D. Lee, *Concise inorganic chemistry*, fifth ed., Chapman & Hall, London, 1996.

[40] J.C. Bailar, H.J. Emelèus, R. Nyholm, A.F. Trotman-Dickenson, *Comprehensive inorganic chemistry*, Volume 4: Lanthanides-Transition metal compounds, first ed., Pergamon, Oxford, 1973.

[41] S. Cotton, *Lanthanide and actinide chemistry*, first ed., Wiley, West Sussex, 2007.

[42] J.C. Bailar, H.J. Emelèus, R. Nyholm, A.F. Trotman-Dickenson, *Comprehensive inorganic chemistry*, Volume 5: Actinides, first ed., Pergamon, Oxford, 1973.

[43] G.T. Seaborg, *The transuranium elements*, New Haven, Yale University Press, 1958.

[44] N. Trautmann, H. Folger, *Preparation of actinide targets by electrodeposition*, Nucl. Instrum. Meth. A **282** (1989) 102-106.

[45] J.P. Greene, A. Heinz, J. Falout, R.V.F. Janssens, *Rotating target wheel system for super-heavy element production at ATLAS*, Nucl. Instrum. Meth. A **521** (2004) 214-221.

[46] M.N. Ali, M.A. Garcia, T. Parsons-Moss, H. Nitsche, *Polymer-assisted deposition of homogeneous metal oxide films to produce nuclear targets*, Nat. Protoc. **5** (2010) 1440-1446.

[47] S. Clifford, X. Guo-ji, C. Ingelbrecht, M.J. Pomeroy, *Processes for the production of ultra-pure metals from oxide and their cold rolling to ultra-thin foils for use as targets and as reference materials*, Nucl. Instrum. Meth. A **480** (2002) 29-35.

[48] R. Grossmann, H.J. Maier, H.U. Friebel, D. Frischke, *Preparation of radioactive targets for tandem accelerator experiments by high vacuum evaporation-condensation*, Nucl. Instrum. Meth. A **480** (2002) 209-213.

[49] K. Eberhardt, W. Brüchle, Ch.E. Düllmann, K.E. Gregorich, W. Hartmann, A. Hübner, E. Jäger, B. Kindler, J.V. Kratz, D. Liebe, B. Lommel, H.-J. Maier, M. Schädel, B. Schausten, E. Schimpf, A. Semchenkov, J. Steiner, J. Szerypo, P. Thörle, A. Türler, A. Yakushev, *Preparation of targets for the gas-filled recoil separator TASCA by electrochemical deposition and design of the TASCA target wheel assembly*, Nucl. Instrum. Meth. A **590** (2008) 134-140.

[50] L.V. Drapchinsky, T.E. Kuzmina, S.M. Soloviev, *Practice of using the multiple painting method*, Nucl. Instrum. Meth. A **438** (1999) 116-118.

[51] S. Chakrabarty, B.S. Tomar, A. Goswami, V.A. Raman, S.B. Manohar, *Preparation of thin osmium targets by electrodeposition*, Nucl. Instrum. Meth. B **174** (2001) 212-214.

[52] K.M. Glover, F.J.G. Rogers, T.A. Tuplin, *Techniques used at Harwell in the preparation of stable and active nuclide targets*, Nucl. Instrum. Meth. A **102** (1972) 443-450.

[53] M.A. Garcia, M.N. Ali, T. Parsons-Moss, P.D. Ashby, H. Nitsche, *Metal oxide films produced by polymer-assisted deposition (PAD) for nuclear science applications*, Thin Soild Films, **516** (2008) 6261-6265.

[54] W. Parker, R. Falk, *Molecular plating: a method for the electrolytic formation of thin inorganic films*, Nucl. Instrum. Methods **16** (1962) 355-357.

[55] W. Parker, H. Bildstein, N. Getoff, *Molecular plating III the rapid preparation of radioactive reference samples*, Nucl. Instrum. Methods **26** (1964) 314-316.

[56] W. Parker, H. Bildstein, N. Getoff, H. Fischer-Colbrie, H. Regal, *Molecular plating II a rapid and quantitative method for the electrodeposition of rare-earth elements,* Nucl. Instrum. Methods **26** (1964) 61-65.

[57] W. Parker, H. Bildstein, N. Getoff, *Molecular plating I, a rapid and quantitative method for the electrodeposition of Thorium and Uranium,* Nucl. Instrum. Methods **26** (1964) 55-60.

[58] N. Getoff, H. Bildstein, *Molecular plating IV, a rapid and quantitative method for the electrodeposition of Plutonium,* Nucl. Instrum. Methods **36** (1965) 173-175.

[59] N. Getoff, H. Bildstein, *Molecular plating VI.* Q*uantitative electrodeposition of Americium,* Nucl. Instrum. Methods **70** (1969) 352-354.

[60] C. Ingelbrecht, A. Moens, R. Eykens, A. Dean, *Improved electrodeposited actinide layers,* Nucl. Instrum. Methods **397** (1997) 34-38.

[61] M.V. Ramaniah, R.J. Singh, S.K. Awasthi, S. Prakash, *Studies on electrodeposition of actinide elements from non-aqueous medium,* Int. J. Appl. Radiat. Is. **26** (1975) 648-650.

[62] A. Ölcer, J. Drebert, T. Reich, in: [R] Seventh International Conference on Nuclear and Radiochemistry, Budapest, Hungary, 24-29 August, 2008.

[63] N. Getoff, H. Bildstein, E. Proksch, *Molecular plating V. The influence of some experimental factors on the deposition yield,* Nucl. Instrum. Methods **46** (1967) 305-308.

[64] G. Savard, R. Janssens, *Proposed ATLAS efficiency and intensity upgrade,* ATLAS Workshop (CERN – European Center for Particle Physics – Geneva, 2009).

[65] H. Stoecker, C. Sturm, *The FAIR start*, Nucl. Phys. A **855** (2011) 506-509.

[66] S. Gales, *SPIRAL2 at GANIL: next generation of ISOL facility for intense secondary radioactive ion beams,* Nucl. Phys. A **834** (2010) 717c-723c.

[67] D. De Soete, R. Gijbels, J. Hoste, *Neutron activation analysis,* first ed., Wiley, London, 1972.

[68] G. Erdtmann, *Neutron activation analysis: techniques and relevant nuclear data*, revised and extended manuscript of a lecture held at the “International Atomic Energy Agency advanced interregional training course on sampling, sample preparation and data evaluation, for trace analysis of elements and radionuclides by nuclear and instrumental methods” at the Research Center Jülich, November 6-December 2, 1989.

[69] G.F. Knoll, *Radiation detection and measurement,* second ed., Wiley, Singapore, 1989.

[70] N. Nica, *Nuclear data sheets for A = 147,* Nucl. Data Sheets **110** (2009) 749-997.

[71] Genie 2000, *Customization tools manual*, Canberra Industries, 2009.

[72] K. Takahashi, *Progress in science and technology on photostimulable* $BaFX:Eu^{2+}$ *(X = Cl, Br, I) and imaging plates*, J. Lumin. **100** (2002) 307-315.

[73] K. Takahashi, K. Kohda, J. Miyahara, *Mechanism of photostimulated luminescence in* $BaFX:Eu^{2+}$ *(X = Cl, Br) phosphors*, J. Lumin. **31** (1984) 266-268.

[74] D. Liebe, K. Eberhardt, W. Hartmann, T. Häger, A. Hübner, J.V. Kratz, B. Kindler, B. Lommel, P. Thörle, M. Schädel, J. Steiner, *The application of neutron activation analysis, scanning electron microscope, and radiographic imaging for the characterization of electrochemically deposited layers of lanthanide and actinide elements*, Nucl. Instrum. Meth. A **590** (2008) 145-150.

[75] Fuji Photo Film Co. Ltd., *Operational guide multi-gauge software*, Version 1.0, 2004.

[76] J. Goldstein, D. Newbury, D. Joy, C. Lyman, P. Echlin, E. Lifshin, L. Sawyer, J. Michael, *Scanning electron microscopy and X-ray microanalysis*, third ed., Springer, New York, 2007.

[77] University of Torino, Solid state physics website (www.dfs.unito.it/solid/SEM).

[78] P. Eaton, P. West, *Atomic force microscopy*, first ed., Oxford University Press, New York, 2010.

[79] Asylum Research website (www.asylumresearch.com/MFP-3D).

[80] B. Bhushan, *Handbook of nanotechnology*, second ed., Springer, Würzburg, 2007.

[81] California Institute of Technology, Molecular materials research center website (mmrc.caltech.edu/XPS).

[82] D. Briggs, M.P. Seah, *Practical surface analysis – by Auger and X-ray photoelectron spectroscopy*, Wiley, Chichester, 1988.

[83] CasaXPS, *User's Manual*, Casa Software Ltd., 2013.

[84] G.C. Smith, *Surface analysis by electron spectroscopy – measurement and interpretation*, Plenum Press, New York, 1994.

2. Toward large-area targets for “TRAKULA”

A. Vascon[1], Ch.E. Düllmann[1,2,3], K. Eberhardt[1], B. Kindler[4], B. Lommel[4], J. Runke[2]

[1]Institute of Nuclear Chemistry, Johannes Gutenberg University Mainz, 55099 Mainz, Germany

[2]Nuclear Chemistry Department, GSI Helmholtzzentrum für Schwerionenforschung GmbH, 64291 Darmstadt, Germany

[3]Helmholtz Institut Mainz, Johannes Gutenberg University Mainz, 55099 Mainz, Germany

[4]Target Laboratory, GSI Helmholtzzentrum für Schwerionenforschung GmbH, 64291 Darmstadt, Germany

Published in:

Nuclear Instruments and Methods in Physics Research A **655** (2011) 72-79.

This paper is a contribution to the proceedings of the 25th World Conference of the International Nuclear Target Development Society (INTDS), held September 12-17, 2010, at TRIUMF, Vancouver, Canada.

Abstract

TRAKULA (**Tra**nsmutationsrelevante **k**ernphysikalische **U**ntersuchungen **l**anglebiger **A**ktinide, i.e., nuclear physical investigations of long-lived actinides with relevance to transmutation) is a joint research project of the German Federal Ministry of Science and Education (BMBF) on nuclear physics investigations with modern scientific, technological and numerical methods. Experiments concerning the transmutation of radioactive waste are a central topic of the project. For this, large-area samples ($\geq$ 40 cm^2) of $^{235,238}U$ and $^{239,242}Pu$ compounds are required for the calibration of fission chambers and for fission yield measurements. Another topic within the project requires large-area targets for precise measurements of the half-life, $t_{1/2}$, of very long-lived α-particle emitters like ^{144}Nd ($t_{1/2} \approx 2 \cdot 10^{15}$ y). Here, we report on electrodeposition tests with Gd and Nd (used as chemical homologues of the actinides), which were performed to find optimal deposition conditions for small-area targets that should be applicable to future large-area targets.

The layers were produced by molecular plating. A new stirring technique, ultrasonic stirring, was adopted and found to be suitable for producing large-area targets. Moreover, two different current densities (namely 0.7 mA/cm^2 and 1.4 mA/cm^2) were studied and found appropriate for target preparation. Characterization of the layers with different analytical techniques played a major role in these studies to gain a deeper understanding of the deposition process itself: neutron activation analysis and γ-spectroscopy were used for yield measurements, radiographic imaging for homogeneity studies, scanning electron microscopy for morphology studies and atomic force microscopy for roughness studies. According to the obtained results, a new electrochemical cell for the production of large-area targets was designed.

PACS: 29.25.Pj; 81.15.Pq; 82.45.-h; 28.65.+a

Keywords: Large-area target, Electrodeposition, Characterization of target

2.1 Introduction

The civilian use of nuclear energy for electricity production produces long-lived radioactive waste, whose radiotoxicity is dominated by plutonium and other minor actinides. New nuclear reactor types like the generation IV reactors with a closed fuel cycle will produce significantly smaller amounts of long-lived radioactive waste than earlier models. While this may lead to a smaller increase in the amount of nuclear waste, the challenges to a safe storage over very long times remain. Therefore, the transmutation of long-lived isotopes into shorter-lived ones, via bombardment with fast neutrons as delivered from a generation IV reactor, is being studied as one possibility to reduce the storage time of radioactive waste.

The knowledge of precise cross sections for nuclear reactions with fast neutrons is necessary for the development of generation IV reactors. In particular, precise data for inelastic neutron scattering on reactor materials (iron) and fission cross sections for plutonium and minor actinides are needed. For this reason, TRAKULA (**Tra**nsmutationsrelevante **k**ernphysikalische **U**ntersuchungen **l**anglebiger **A**ktinide, i.e., nuclear physical investigations of long-lived actinides with relevance to transmutation) started in fall 2009 as a joint research project of the German Federal Ministry of Science and Education (BMBF). Among the different partners of this collaboration, the Institute of Nuclear Chemistry of the Johannes Gutenberg University (JGU) Mainz plays the key role for the preparation of monoisotopic targets of ^{235}U, ^{238}U, ^{239}Pu, and ^{242}Pu, which will be used for measuring of the neutron induced fission cross sections, which are relevant for transmutation. Furthermore, also within the project, targets of the long-lived α-emitter ^{144}Nd will be produced. All these targets must be circularly shaped large-area targets ($\geq$ 40 cm^2) and must meet specific requirements of stability, homogeneity, roughness, and thickness. Especially, the lowest possible roughness is required for all the targets. Moreover, due to the small amounts in which many actinide isotopes are available, all steps involved in target preparation and characterization have to be optimized to be performed with the highest yield possible. Among the different techniques frequently applied for target preparation, e.g., Physical Vapour Deposition (PVD), Chemical Vapour Deposition (CVD) and Electrochemical Deposition (ED), the last one is usually used at JGU for the production of lanthanide and actinide targets with areas mostly ranging from 0.3 to 3 cm^2 [1,2]. Applying this technique to Gd and Nd (used as chemical homologues of the actinides) and characterizing the small-area targets produced with different analytical techniques, we searched for optimal deposition conditions that can be expected to be applicable to large-area targets as well. Using the obtained results from this research, we designed a new electrochemical cell for large-area samples.

The present paper reports on the target preparation and characterization methods (Section 2.2), the results concerning the optimization process (Section 2.3), and describes the layout of the new electrochemical cell (Section 2.4).

2.2 Experimental

2.2.1 Target preparation

Electrochemical deposition of lanthanide and actinide elements from organic solutions is referred to as Molecular Plating (MP) [2-7]. Ti-foils of 5 µm thickness were used as backing material for the deposition. These foils were produced by cold rolling and were pinhole-free. They were pre-cleaned with 6 M HCl, water, and isopropanol. For the MP process applied here, the lanthanide compound in the nitrate form was dissolved in 0.1 M HNO_3 to a concentration of ≈ 25 mg/ml with regard to the lanthanide. Two different procedures were followed to produce targets: (i) an aliquot of 100 µl of the stock-solution was mixed with 1 ml isopropanol, and transferred into the electrochemical cell, which was then filled up with 24 ml isobutanol (inactive MP); (ii) an aliquot of 100 µl of the stock solution was irradiated in the TRIGA Mainz research reactor, which produced a solution that contained a radioactive tracer of the element to be plated (Gd: ^{153}Gd, $t_{1/2}$ = 239.47 d; Nd: ^{147}Nd, $t_{1/2}$ = 10.98 d). This irradiated lanthanide compound solution was then used for the MP (active MP). Figure 2-1 shows a view of the MP cell with a design as proposed by Haba et al. [8]. Originally, our cell was used for the preparation of banana-shaped targets for Super Heavy Elements (SHE) studies at GSI [1]. The dimension of the targets that were produced was 3 cm × 1 cm. The plating solution was stirred by means of either a magnetic stirrer (Variomag Compact) operated at 1000 rotations per minute (rpm) or a quartz tip ultrasonic stirrer (Bandelin Sonopuls HD 2070) operated at 30% power pulse. Molecular Plating was carried out at a constant temperature of 14°C by applying two different constant currents: 2 mA and 4.2 mA, yielding current densities, respectively, of 0.7 mA/cm^2 and 1.4 mA/cm^2.

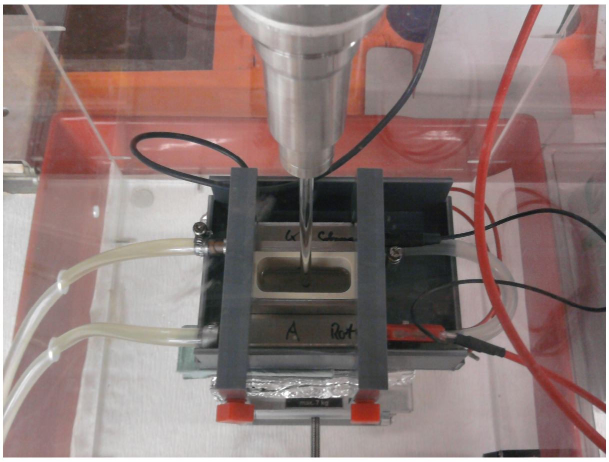

Figure 2-1 View of the cell used for molecular plating.

2.2.2 Target characterization

The deposition yield of the MP process applied was determined by an indirect and a direct method, respectively: Neutron Activation Analysis (NAA) and γ-spectroscopy. NAA was used after inactive MPs. This analytical technique, performed at the TRIGA Mainz Research Reactor, was used to determine the residual concentration of the lanthanide element in the supernatant solution after neutron irradiation in the reactor and measurement via γ-spectroscopy of a standard sample and an aliquot of the supernatant solution itself (indirect yield measurement) [9]. Gamma-spectroscopy was used after active MPs. This technique employed a high-purity germanium detector (HPGe) (GEM series HPGe Detector Model No. GEM 23158 P-Plus, ORTEC Company) to measure the active samples (direct yield measurement). To obtain quantitative data, reference sources with known amounts of the tracer were prepared. They consisted of filter papers with the same geometry as the targets, soaked with the tracer-containing solution. To avoid any kind of contamination inside the γ-spectrometer, the active samples were sealed before being inserted into the sample holder.

The homogeneity of the radioactive targets was inspected by using Radiographic Imaging (RI), using a FUJIFILM FLA 7000 equipped with reusable imaging plates (IP) and a 650 nm laser for the reading process. The amount of emerging luminescence light during this process is converted to an arbitrary unit that is proportional to the amount of radiation exposed within a single record [10]. To verify the homogeneity of the target, the image was overlaid by a grid of square spots with an area of 0.25 mm^2 each. The spatial resolution for γ-emitting nuclides was < 200 μm as determined by Liebe et al. [9].

The morphology of the targets was studied by using a Scanning Electron Microscope (SEM) (Philips XL30), operated at 20 kV. Secondary electrons were detected, magnification factors of 150×, 500×, 1000×, and 2500× were used.

The surface roughness of the targets, i.e., the measure of the texture of the surface quantified by the vertical deviations of the real surface from its ideal form, was investigated by using an Atomic Force Microscope (AFM) (MFP 3D, Asylum Research). For these investigations, a high-resolution image of a 15 × 15 μm^2 representative section of the target surface was recorded. For each 15 × 15 μm^2 section, a square mask of variable dimensions was used to determine the surface roughness as a root mean square (RMS) value. The AFM used cantilevers with a resonance frequency of 283 kHz for imaging in the AC mode (tapping mode).

2.3 Results and discussion

2.3.1 Gd-targets

2.3.1.1 Comparison between magnetic and ultrasonic stirring at low current density

In initial steps towards the production of large-area targets for the TRAKULA project, we were building up on well established methods that are successfully used for the preparation of smaller area targets. One critical aspect is the mixing of the plating solution. Magnetic stirring (MS) is the mixing technique usually applied at our institute for target preparation. It is a suitable and effective technique for the production of small-area targets. Unfortunately, considering large-area targets, such a technique loses its suitability because magnetic stirrers for these operations mandate large volumes of solution to be stirred: several hundreds of ml. Problems associated with such large volumes are that they are disadvantageous for the recovery from the supernatant solution of rare and expensive isotopes, like ^{242}Pu, in case of incomplete depositions, they are difficult to cool down, and they require laborious and slow operations for the extraction of the prepared target from the electrochemical cell. For these reasons, ultrasonic stirring (US) was tested with respect to its potential suitability as an alternative to MS. In the case of US, the mixing is obtained via ultrasonic waves emitted by a small-diameter quartz tip slightly inserted in the solution, which allows to build cells of moderate volumes even for the required large-area targets. Our main concern about this technique was that the energy released by the ultrasonic waves could destroy or damage the fresh layer deposited during the plating process. The deposition yield, homogeneity, morphology, and roughness of the layers produced with both stirring techniques were investigated to compare the suitability of the two methods. These tests were performed with small-area targets (dimension: 3 cm × 1 cm). For these reasons, by means of both MS and US, active and inactive MPs were used to produce Gd-targets applying a low constant current of 2.0 mA, (yielding a current density of 0.7 mA/cm^2), for a deposition time of 3 h. In this case, direct and indirect yield measurements gave deposition yields of about 96% for both stirring techniques applied.

The homogeneity of the active Gd-targets was inspected using RI. Figures 2-2 (a) and (b) show the normalized 3D graphs of the active Gd-targets obtained with magnetic (a) and ultrasonic (b) stirring. Apparently, both techniques yield homogeneous layers.

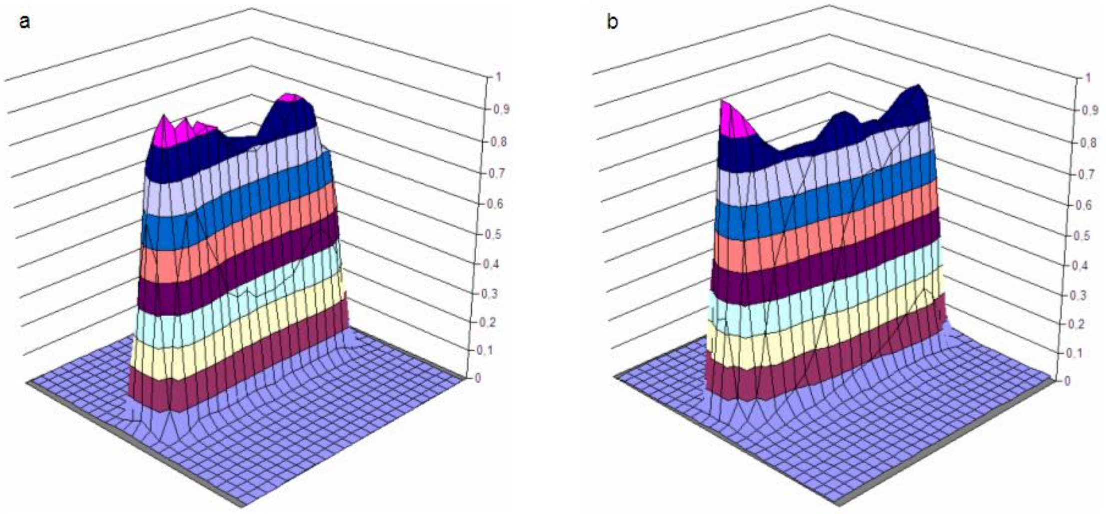

Figure 2-2 Normalized RI 3D graphs of the active Gd-targets obtained at low current density (0.7 mA/cm^2) applying MS (a), and US (b).

Morphological investigations of the inactive Gd-layers were realized by means of SEM. Figures 2-3 (a) and (b) show 150× magnification factor images of Gd-targets obtained via MS (a) and via US (b). At this magnification, both targets show a laminar texture with significant furrows originating from the drying process in air. Figure 2-3 (b) shows evident surface defects (outgrowths) generated by the defects of the substrate Ti-foil: these substrate defects act as preferential nucleation sites of the element during the deposition process. However, they do not affect the quality of the layers with respect to our applications.

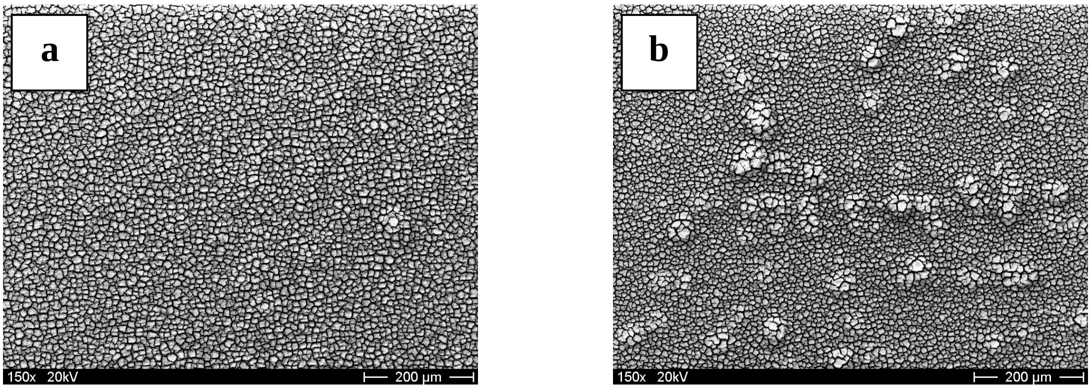

Figure 2-3 150× magnification factor SEM images of the Gd-targets obtained at low current density (0.7 mA/cm^2) applying MS (a), and US (b).

The surface roughness of the inactive Gd-targets was measured with an AFM. For Gd-targets produced with both, MS and US, the surface roughness values are of the order of 110 nm. The areas of the surface islands, as inferred from AFM analysis for both the targets, range from 5 × 5 to 10 × 10 µm^2. Figures 2-4 (a) and (b) show 15 × 15 µm^2 recorded sections of the surfaces of Gd-targets obtained with MS (a) and with US (b). The red squares represent the areas in which the roughness of the islands constituting the surface was evaluated.

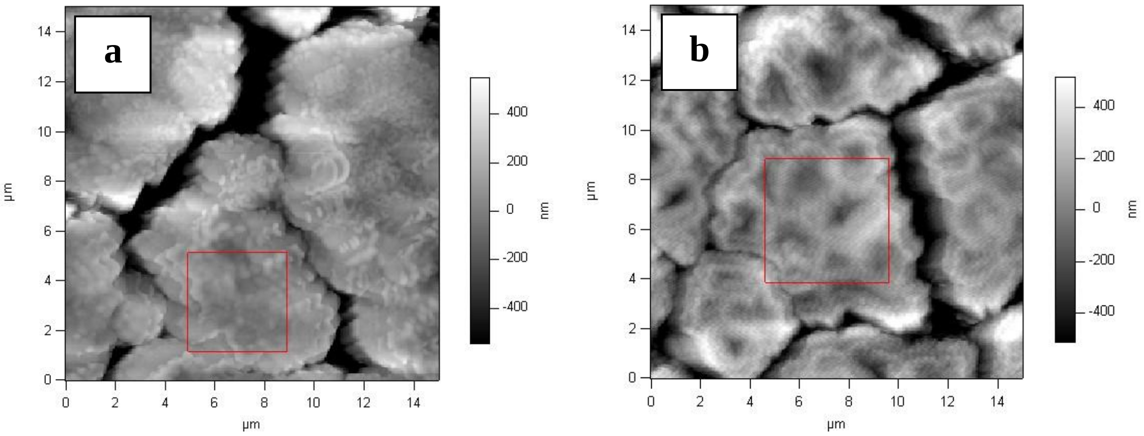

Figure 2-4 15 × 15 µm^2 AFM recorded sections of the surfaces of the Gd-targets obtained at low current density (0.7 mA/cm^2) applying MS (a), and US (b).

The analysis of all these different parameters shows an evident agreement among the results obtained for the targets produced by means of both, MS and US, and eliminates any kind of concern regarding the destruction of the fresh layer by the ultrasonic waves, as evidenced by the very uniform and stable layers that were obtained. Therefore, ultrasonic stirring is considered to be a valuable equivalent to magnetic stirring in the production of small-area targets.

The positive aspects, especially the small solution volume, of US renders this technique promising for the production of large-area targets.

2.3.1.2 Application of ultrasonic stirring at high current density

The current density applied in the experiments described in Section 2.3.1.1, i.e., 0.7 mA/cm^2, turned out to be very effective with regards to several investigated properties, i.e., deposition yield, surface homogeneity, morphology, and roughness. In separate experiments, we doubled the current density to 1.4 mA/cm^2 and characterized the obtained targets with the techniques reported in Section 2.2.2 to investigate the influence of the current density. Active and inactive MPs were used to produce Gd-targets applying a constant current of 4.2 mA for a deposition time of 3 h, and were stirred with US. Direct and indirect yield measurements gave deposition yields of about 93%. Due to the higher applied current density, a faster deposition process was expected. Indeed, the deposition yield approached 93% already after 2 h. Nevertheless, to allow a direct comparison to the low current density measurements, plating times of 3 h were chosen for these tests, too.

The homogeneity of the active Gd-targets was verified with RI. The morphology was studied with SEM and showed a laminar texture similar to that described in Section 2.3.1.1.

The surface roughness of the inactive targets was measured with an AFM. For these higher current density Gd-targets the surface roughness value is about 120 nm, similar to that of the targets prepared at the low current density. The surface islands have areas that range from 5 × 5 to 10 × 10 µm^2, again similar to those obtained at the low current density.

Overall, taking into account both the deposition yields and the surface roughnesses, a current density of 0.7 mA/cm^2 appears favorable for the TRAKULA project. A value of 1.4 mA/cm^2 should not be exceeded for effective target preparations.

Table 2-1 summarizes the conditions applied for the deposition and the results obtained from the characterization of the targets produced for these Gd-tests.

Table 2-1 Experimental conditions and results obtained for the tests with Gd-targets on Ti-backings. The plating time was always 3 h.

Stirring technique	Current [mA]	Current density [mA/cm^2]	Deposition yield [%]	Surface roughness (RMS) [nm]	Island dimension [µm^2]
magnetic stirring	2.0	0.7	96	110	5 × 5 – 10 × 10
ultrasonic stirring	2.0	0.7	96	110	5 × 5 – 10 × 10
ultrasonic stirring	4.2	1.4	93	120	5 × 5 – 10 × 10

2.3.2 Nd-targets

2.3.2.1 Application of ultrasonic stirring at low and high current density

Based on the results obtained in 2.3.1.1 and 2.3.1.2, Nd-targets were produced at current densities of 0.7 mA/cm^2 and 1.4 mA/cm^2. The deposition time was 3 h, US was used. Direct and indirect yield measurements gave slightly different deposition yields for the different current densities applied: about 99% for 0.7 mA/cm^2, about 96% for 1.4 mA/cm^2.

The homogeneity of the active Nd-targets was verified using RI and found to be similar to that of the Gd-targets (cf. Figures 2-2 (a) and (b)).

Morphological investigations of the inactive deposited Nd-layers were performed with SEM. Figures 2-5 (a) and (b) (500× magnification factor) show respectively: (a) the image of a 0.7 mA/cm^2 target, (b) the image of a 1.4 mA/cm^2 target.

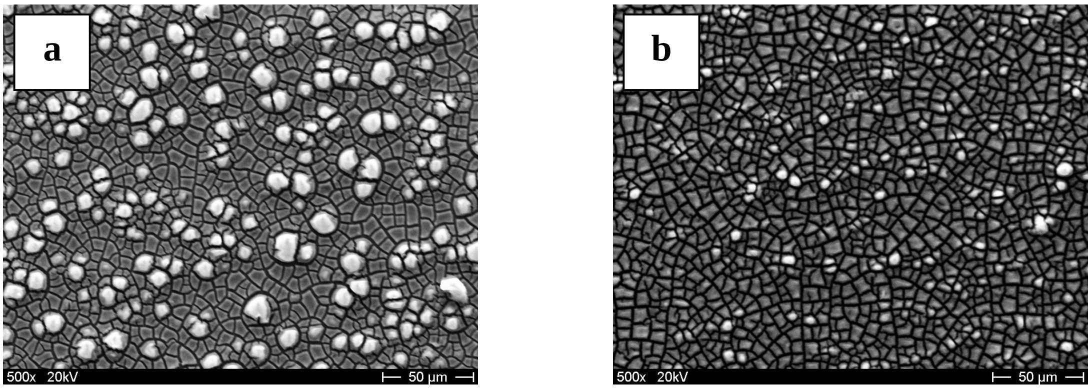

Figure 2-5 500× magnification factor SEM images of the Nd-targets obtained at low current density (0.7 mA/cm^2) (a), and high current density (1.4 mA/cm^2) (b), applying US.

Both images show a laminar texture with significant furrows originating from the drying process in air as in the case of Gd. The main difference between these SEM images and the SEM images recorded for the Gd-targets, Figures 2-3 (a) and (b), is found in the surface defects (white outgrowths, bigger for the 0.7 mA/cm^2 target, and smaller for the 1.4 mA/cm^2 target), which appear to be spot-like. This is probably due to different growth mechanisms of the layers.

For both, the 0.7 mA/cm^2, as well as the 1.4 mA/cm^2 Nd-targets, the surface roughness value as measured with an AFM is of the order of 100 nm. The areas of the surface islands range from 5 × 5 to 10 × 10 µm^2, similar to those observed on the Gd-targets. Figures 2-6 (a) and (b) show the recorded sections of the Nd-target surfaces obtained with low (a) and high current density (b). The areas analyzed for the surface roughness are indicated by the red boxes.

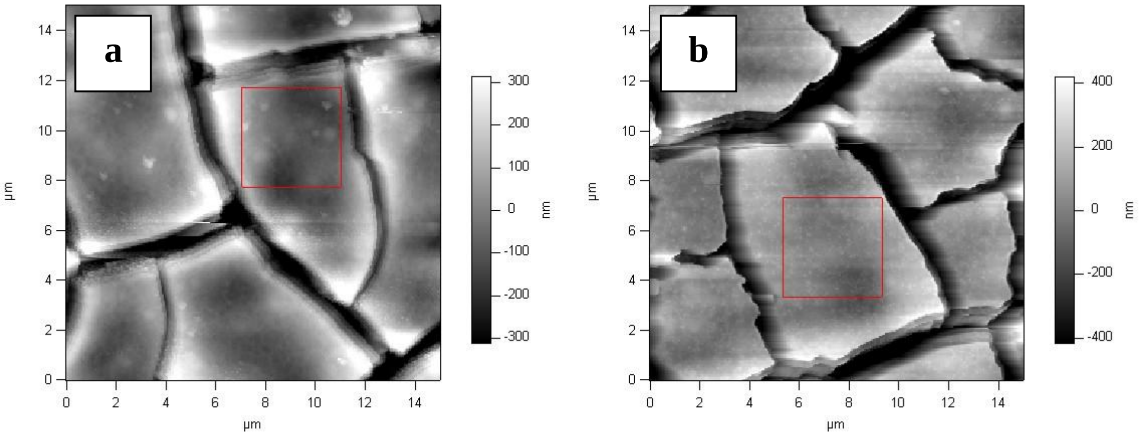

Figure 2-6 15 × 15 µm^2 AFM recorded sections of the surfaces of the Nd-targets obtained at low current density (0.7 mA/cm^2) (a), and high current density (1.4 mA/cm^2) (b), applying US.

The results obtained from this investigation show that the optimized deposition conditions found for the Gd-plating are suitable for the Nd-plating as well. In particular, the higher yields obtained and the low roughness values measured are a good starting point for the production of large-area targets of Nd.

Table 2-2 summarizes the experimental conditions and the obtained results for the Nd-targets.

Table 2-2 Same as Table 2-1, but for Nd-targets on Ti-backings. The plating time was always 3 h. Only ultrasonic stirring was applied.

Current [mA]	Current density [mA/cm^2]	Deposition yield [%]	Surface roughness (RMS) [nm]	Island dimension [µm^2]
2.0	0.7	99	100	5 × 5 – 10 × 10
4.2	1.4	96	100	5 × 5 – 10 × 10

2.3.3 Time-resolved progress of the plating process

During the deposition of Gd and Nd at a constant current, stirred with US, the evolution of the voltage over time was recorded (see Figure 2-7). The voltages are initially decreasing due to the high starting concentration of the ions in solution, they then reach a minimum and afterwards exhibit an increasing trend. The minimum is reached after about 2 h (≈ 135 min) for both the curves recorded at 2.0 mA, and after about 1 h (≈ 65 min) for both the curves recorded at 4.2 mA. The different times at which the minima occur are most probably directly related to the different kinetics of the plating processes involved: longer times for slower kinetics (low constant currents) and smaller times for faster kinetics (high constant currents). Obviously, the effects of these different kinetics are reflected in the slopes of the decreasing and increasing trends. Working at constant currents, an increase in the resistance during the plating process is the only obvious reason for a voltage increase.

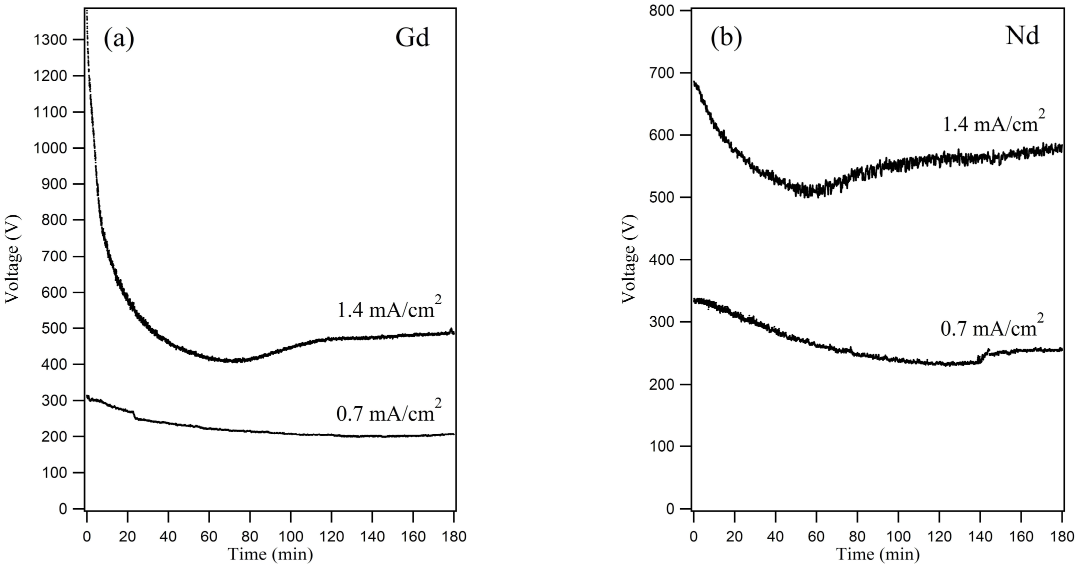

Figure 2-7 Evolution of the voltage over time for Gd (a), and Nd (b), recorded applying US at low and high current density (0.7 mA/cm^2 and 1.4 mA/cm^2).

To gain a better understanding of this process a time-resolved study of the deposited layers was performed. To this end, a total of 12 different Nd-targets were prepared at low costant current of 2.0 mA, corresponding to a current density of 0.7 mA/cm^2. The first target was plated for 15 min, the second one for 30 min, and the subsequent ones for increments of 15 min longer, up to 180 min for the target that was plated the longest. SEM characterization of these 12 targets shows that at the beginning of the deposition (15 min, Figure 2-8 (a)) the growing process starts mainly on the substrate Ti-foil defects (the so called “defect-decoration” process, typical of defective substrate surfaces). After longer deposition times, Figures 2-8 (b)-(d) show that 3D crystallites (3D islands) grow on top of predeposited bidimensional overlayers [11] (some of the growing 3D islands are underlined with dashed white circles in the figures). Based on these results, our hypothesis is that the growth mechanism is Stranski-Krastanov-like. In the future, this hypothesis will be checked by a more detailed set of experiments and an AFM analysis.

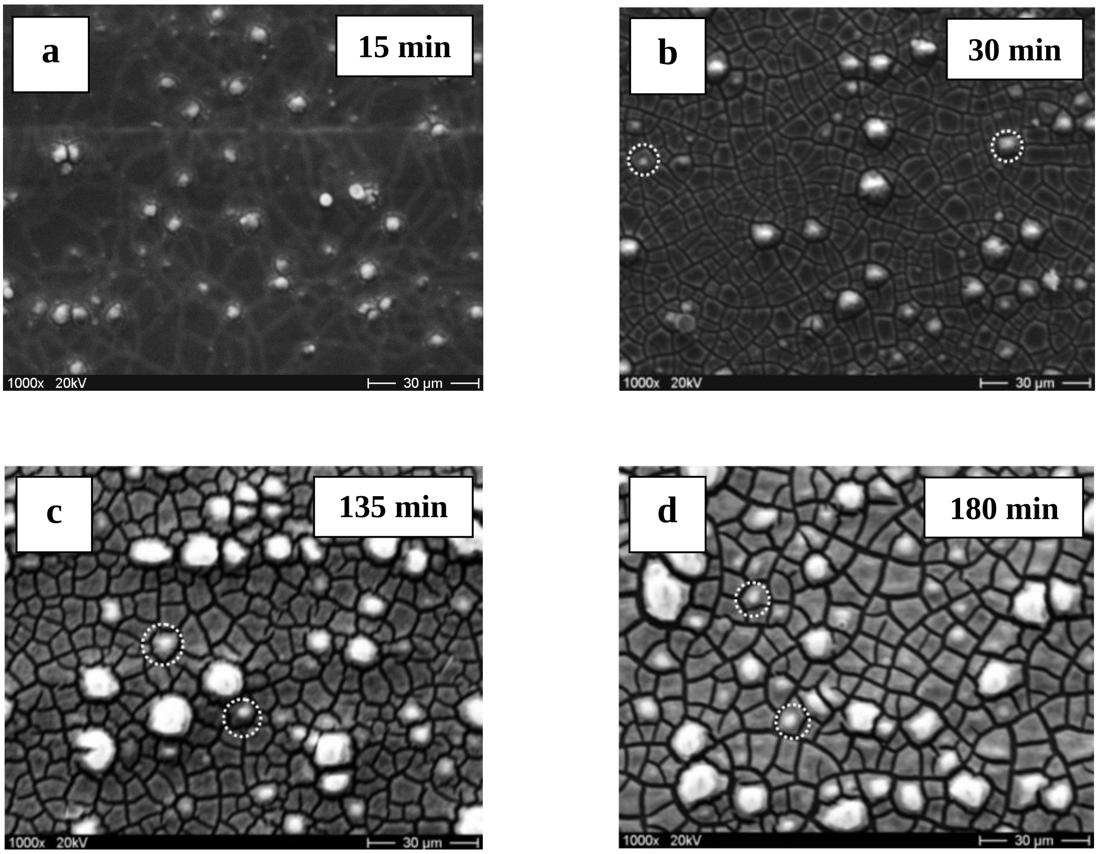

Figure 2-8 1000× magnification factor SEM images of the Nd-targets produced at 15 min intervals to cover a total deposition time of 180 min at low constant current of 2.0 mA: (a) 15 min, (b) 30 min, (c) 135 min (minimum of the curve), (d) 180 min. The dashed white circles underline some of the 3D islands growing on the surface of the deposited layer.

To obtain an understanding of the increase in the resistance, we decided to perform experiments at constant currents of 2.0 mA and 4.2 mA, characterizing the targets obtained after deposition times corresponding to the minima of the curves, by means of AFM. The obtained images are shown in Figures 2-9 (a) and (b), which show respectively: (a) a 15 × 15 μm^2 recorded section of the low current density Nd-target, (b) a 15 × 15 μm^2 recorded section of the high current density Nd-target.

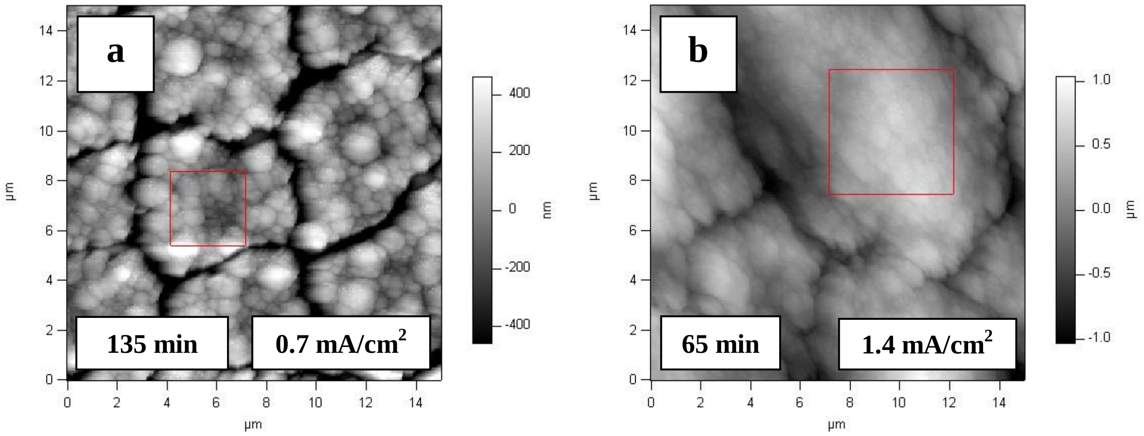

Figure 2-9 15 × 15 µm^2 AFM recorded sections of the surfaces of the Nd-targets obtained at low current density (0.7 mA/cm^2) (a), and high current density (1.4 mA/cm^2) (b), after deposition times corresponding to the minima of the curves.

Both these targets show typical coarse grains which give a very porous top microstructure that is totally different from that shown in Figures 2-6 (a) and (b) and discussed in Section 2.3.2.1 for Nd-targets obtained with low and high current density after deposition times of 3 h. In that latter case, almost smooth surfaces were obtained. At times corresponding to the minima of the curves, surface roughness measurements instead gave values of about 220 nm and 360 nm respectively for the low current density and the high current density Nd-targets. According to these results, our working hypothesis regarding the increase of the resistance during these plating processes is that the ions remaining in the solution after the minimum (10-13% of the initial ions as inferred from direct and indirect yield measurements) progressively tend to fill the pores of the surface, lowering the roughness of the layers, but increasing at the same time their insulating nature. This would explain the increase in the resistance from the minimum until the end of the process. Further experiments to better verify this hypothesis are under way.

2.4 Layout of the new electrochemical cell

The experimental results discussed in the previous sections showed that two different current densities (i.e. 0.7 mA/cm^2 and 1.4 mA/cm^2) are suitable for effective target preparation, and, moreover, that US is a promising stirring technique, also for the production of large-area targets. This last result turned out to be of especially striking importance in the design of the new electrochemical cells needed for the preparation of large-area targets, since it allowed designing them such that the inner volume can easily be varied to test how different distances between the electrodes affect the quality of the layer.

Figure 2-10 (a) shows a view of the main components of the new electrochemical cell to be built for large-area circular targets. Figure 2-10 (b) shows a schematic view of the whole cell as assembled.

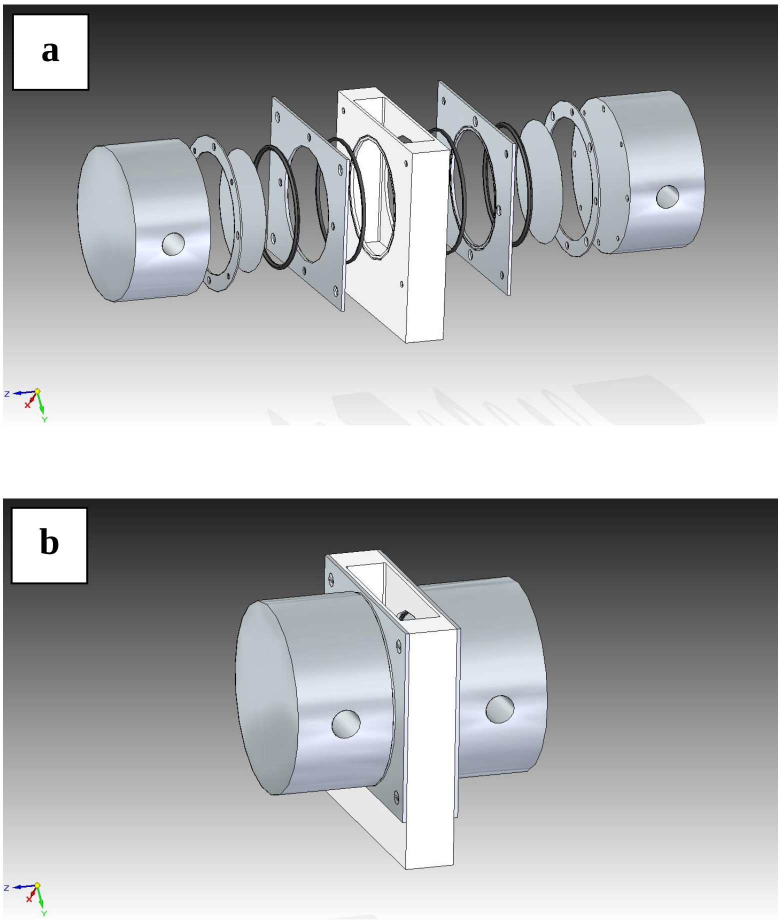

Figure 2-10 (a) Main components of the new electrochemical cell designed; from left to right: cylindrical Ti-block (electrode), circular Ti-frame, circular Ti-backing foil, Viton O-ring, rectangular Ti-frame, Viton O-ring, PEEK-cell, Viton O-ring, rectangular Ti-frame, Viton O-ring, circular Ti-backing foil, circular Ti-frame, cylindrical Ti-block (electrode). (b) Assembled cell.

According to the circular shape of the targets and in order to get homogeneous electric fields, both, the cathode and the anode have been designed as cylindrical Ti-blocks, which can be water-cooled. On one side of both electrodes a circular Ti-frame is screwed. In the case of the cathode, this frame holds a 50-µm thick circular Ti-backing foil perfectly in the center of the electrode during the deposition process. At the end of the deposition, this frame can be unscrewed to easily remove the target avoiding mechanical stress, which would be dangerous for the layer stability. At the anode, the circular frame also keeps the Ti-backing foil centered. However, the foil is used only as an interchangeable system of protection of the anode from impurities. A Viton O-ring is used to define the area of deposition of the cathode. For both, the cathode and the anode, this same O-ring serves as a means of sealing between the electrodes and the rectangular Ti-frame. This frame connects the electrode assembly with the cell. For this reason, another Viton O-ring is used to seal the rectangular frame to the cell. The cell is made of PEEK and acts as a container for the alcohol solution.

2.5 Summary

According to the requirement of the production of large-area targets ($\geq 40\ \text{cm}^2$) for the TRAKULA project, constant current-MP tests were performed to find optimal deposition conditions for small-area targets that are likely applicable as well to large-area targets. These tests were based on the use of Gd and Nd as chemical homologues of the actinides. The targets were characterized by means of direct and indirect yield measurement, RI, SEM and AFM. A new stirring technique, ultrasonic stirring, was adopted and found superior to mechanical stirring, especially for the production of large-area targets. Deposition at two different current densities (i.e. 0.7 mA/cm^2 and 1.4 mA/cm^2) was studied and both conditions were found to be suitable for target preparation. Investigation of the trend of the voltage curves recorded during the plating processes was made. Two working hypotheses were given: one about the Nd-growth mechanism at 2.0 mA (i.e. Stranski-Krastanov growth mechanism), the other about the rise in resistance during the deposition. According to the results obtained from these tests, a new electrochemical cell for the production of large-area targets was designed.

Acknowledgements

The authors would like to thank H. Adam from the institute of physical chemistry of the Johannes Gutenberg University Mainz for his assistance with the AFM measurements and the staff of the TRIGA Mainz for performing the irradiations. We acknowledge financial support by the Research Center “Elementary Forces and Mathematical Foundations” (EMG). One of us (A.V.) aknowledges financial support from the German Federal Ministry of Science and Education (BMBF) under contract number 02NUK013E.

References

[1] K. Eberhardt et al., Nucl. Instrum. Meth. A **590** (2008) 134.

[2] K. Eberhardt et al., in: J.L. Duggan, I.L. Morgan (Eds.), AIP Conference Proceedings, vol. **576**, (2001) p. 1144.

[3] W. Parker et al., Nucl. Instrum. Methods **16** (1962) 355.

[4] W. Parker et al., Nucl. Instrum. Methods **26** (1964) 55.

[5] W. Parker et al., Nucl. Instrum. Methods **26** (1964) 61.

[6] N. Getoff et al., Nucl. Instrum. Methods **36** (1965) 173.

[7] B.W. Filippone et al., Nucl. Instrum. Meth. A **243** (1986) 41.

[8] H. Haba et al., TASCA05 Workshop, www-w2.gsi.de/tasca05.

[9] D. Liebe et al., Nucl. Instrum. Meth. A **590** (2008) 145.

[10] Fuji Photo Film Co., Ltd, Operational Guide Multi-Gauge Software, Version 1.0, 2004.

[11] M. Paunovic, M. Schlesinger, Fundamentals of Electrochemical Deposition, second ed., Wiley, New Jersey, 2006.

3. Elucidation of constant current density molecular plating

A. Vascon[1], S. Santi[2], A.A. Isse[2], T. Reich[1], J. Drebert[1], H. Christ[3], Ch.E. Düllmann[1,4,5,]
K. Eberhardt[1,5]

[1]Institute of Nuclear Chemistry, Johannes Gutenberg University Mainz, 55099 Mainz, Germany
[2]Department of Chemical Sciences, University of Padova, 35131 Padova, Italy
[3]Institute of Physical Chemistry, Johannes Gutenberg University Mainz, 55099 Mainz, Germany
[4]SHE Chemistry department, GSI Helmholtzzentrum für Schwerionenforschung GmbH, 64291 Darmstadt, Germany
[5]SHE Chemistry research section, Helmholtz Institute Mainz, 55099 Mainz, Germany

Published in:

Nuclear Instruments and Methods in Physics Research A **696** (2012) 180-191.

Abstract

The production of thin layers by means of constant current or constant voltage electrolysis in organic media is commonly known as molecular plating. Despite the fact that this method has been applied for decades and is known to be among the most efficient ones for obtaining quantitative deposition, a full elucidation of the molecular plating is still lacking. In order to get a general understanding of the process and hence set the basis for further improvements of the method, constant current density electrolysis experiments were carried out in a mixture of isopropanol and isobutanol containing millimolar amounts of HNO_3 together with $[Nd(NO_3)_3{\cdot}6H_2O]$ used as a model electrolyte. The process was investigated by considering the influence of different parameters, namely the electrolyte concentrations (i.e., $Nd(NO_3)_3{\cdot}6H_2O$: 0.11, 0.22, 0.44 mM, and HNO_3: 0.3, 0.4 mM), the applied current (i.e., 2 mA and 6 mA), and the surface roughness of the deposition substrates (i.e., a few tens to several hundreds of nm). The response of the process to changes of these parameters was monitored recording cell potential curves, which showed to be strongly influenced by the investigated conditions. The produced layers were characterized using γ-ray spectroscopy for the evaluation of Nd deposition yields, X-ray photoelectron spectroscopy for chemical analysis of the surfaces, and atomic force microscopy for surface roughness evaluation. X-ray photoelectron spectroscopy results clearly indicate that Nd is present only as Nd^{3+} on the cathodic surface after molecular plating. The results obtained from this characterization and some basic features inferred from the study of the cell potential curves were used to interpret the different behaviours of the deposition processes as a consequence of the applied variables.

Keywords: thin films, neodymium, molecular plating, γ-ray spectroscopy, atomic force microscopy (AFM), X-ray photoelectron spectroscopy (XPS)

3.1 Introduction

One of the most widely applied methods for the production of thin and uniform layers to be used as targets for, e.g., accelerator and reactor science is based on the so called Molecular Plating (MP) technique. This name was coined by Parker and Falk [1] to denote electrodeposition from an organic medium, either in the constant current or in the constant voltage mode. The electrochemical cells have always been just two-electrode cells, i.e., cathode and anode, but no reference electrode. Moreover, since the required target thicknesses are usually in the range of µg/cm^2-mg/cm^2 and the areas of the deposits can span several square centimeters (according to the particular beam diameters), the concentrations of the electrolytes inside the cells are usually very small. Despite the limitation of using two-electrode cells, MP has been successfully applied since its introduction, half a century ago, for the production of, e.g., lanthanide and actinide targets [2-6], and nowadays targets produced by MP are widely used, e.g., for atomic and nuclear spectroscopy, nuclear reaction studies, or nuclear measurements [7-11]. The method is well-known to have many desirable properties, like a quantitative deposition yield of the produced layers, which usually show acceptable uniformity and good stability to the bombardments with intense particle beams [11]. Despite MP to be widely used, there are, however, rather few attempts reported where a characterization of the layers by standard analytical techniques was performed [12,13], and a detailed elucidation of even some main features of the process is still largely lacking. Work has focused rather on gaining empirical evidence on how to further improve the properties of the produced layers. Nonetheless, there is nowadays the common feeling that to increase the efficiency of the method to yet improve the obtained targets, e.g., with respect to radiation hardness, and before stepping to alternative target production techniques [14,15], it is highly desirable to reduce the knowledge gap between MP and well established electrochemical methods via an investigation and elucidation of such electrodepositions. For this reason, following a previous publication [16], an extensive investigation of the molecular plating process was carried out: constant current density electrolysis experiments in organic media using a neodymium salt as a model electrolyte were performed. Electrolyte concentration, applied current and surface roughness of the deposition substrates were varied to investigate the process. Cell potential curves were recorded to monitor the response of the process to the variables and several analytical techniques were applied to characterize the produced layers. The results of these measurements were used to interpret the different behaviours of the MPs. Elucidation of the process including a theoretical description of important basic features of constant current density MP is presented.

3.2 Experimental details

3.2.1 Deposition cells

Two different types of cells were used: a deposition cell [17] for the production of banana-shaped targets [11] for superheavy element (SHE) studies at the GSI

Helmholtzzentrum für Schwerionenforschung (GSI), Darmstadt, Germany (Cell A, Figure 3-1a), and a second cell producing round deposits, more suitable for the used characterization techniques (Cell B, Figure 3-1b).

Cell A is characterized by a central PEEK body where the electrolytic solution is inserted. The anode is made of a Ti block onto which a 47 µm-thick Pd foil is glued. The cathode is made of two Ti blocks which close an Al mask onto which a 5 µm-thick Ti foil is glued. The Pd and Ti foils are 3 cm^2 large. The set-up is screwed together and sealed using silicone sealing. The distance between the electrodes is 2.8 cm. Cell B has a central PEEK body as well. The anode is a Ti block covered by a circular 47 µm-thick Pd foil, while the cathode is a Ti block covered by a circular 50 µm-thick Ti foil fixed by a PEEK ring. The areas of the Pd and Ti foils are both 9 cm^2. The set-up is screwed together and sealed using Viton O-rings. A top-sealing is possible using a Ti frame. The distance between the electrodes is 2.8 cm. Anodes and cathodes of both cells were cooled at a constant temperature (T = 16 °C) using water-cooled Ti blocks in physical contact with the electrodes.

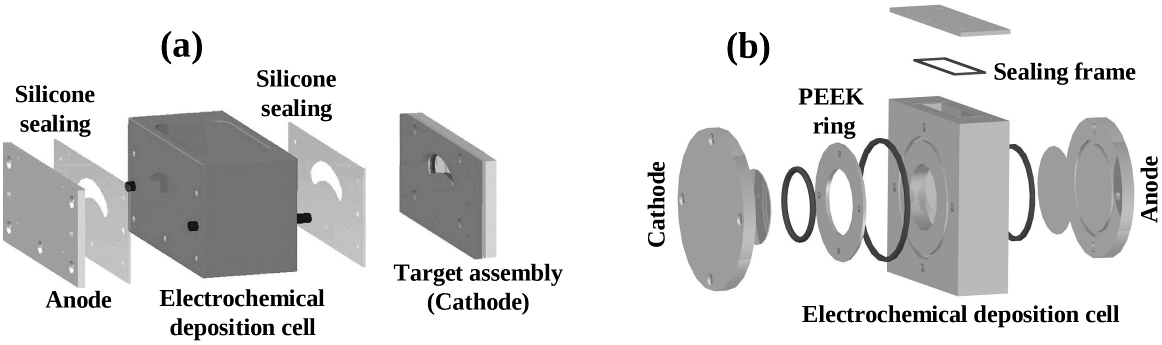

Figure 3-1 Schemes of (a) Cell A, (b) Cell B; (a) from left to right: Ti anode, silicone sealing, PEEK cell, silicone sealing, cathode assembly. (b) From left to right: Ti cathode, Ti foil, Viton O-ring, PEEK ring, Viton O-ring, PEEK cell, Viton O-ring, Pd foil, Ti anode; top: Ti frame, silicone sealing.

3.2.2 Molecular plating at constant current density

Before any deposition, both the anode (Pd foils) and the cathode (Ti foils) were cleaned with 6 M HCl (1 × 3 mL washing), demineralized water (3 × 3 mL washings), and isopropanol (1 × 3 mL washing). For the MP processes with Cell A, 0.243, 0.486, and 0.972 g of $Nd(NO_3)_3{\cdot}6H_2O$ (Alfa Aesar) were dissolved into 20 mL 0.1 M HNO_3, while for the MP with Cell B, 0.338, 0.675, and 1.350 g of $Nd(NO_3)_3{\cdot}6H_2O$ were dissolved in the same volume of acid. In this way, solutions of three different concentrations were obtained. From each solution an aliquot of 100 µL was added to a mixture of 1 mL isopropanol (Fisher Chemical) and 24 mL isobutanol (Applichem) in the case of Cell A, and to a mixture of 1 mL isopropanol and 34 mL isobutanol in the case of the Cell B. This yielded three different solutions of Nd^{3+} in the used cell; these are referred to as low concentration (LC, 0.11 mM), medium concentration (MC, 0.22 mM) and high concentration (HC, 0.44 mM). In the case of Cell A the concentration of HNO_3 was 0.4 mM, while it was 0.3 mM in the case of Cell B. In both cells the plating solutions were stirred by means of a quartz tip ultrasonic stirrer (Bandelin Sonopuls HD 2070) operated at 30% power pulse. MP experiments were carried out for 3 hours at 16 °C by applying two different constant currents: 2 mA (Cell A) and 6 mA (Cell B). The current density, 0.7 mA/cm^2, was the same in both cases.

3.2.3 Deposition substrates

The deposition substrates used in the present work are listed in Table 3-1.

Table 3-1 Deposition substrates used for the MPs performed with Cell A and Cell B.

Substrate type	Cell	Production technique
Ti1	A	cold rolling
Ti2	A	cold rolling
Ti3	B	rolling
Ti4	B	etching
Ti5	B	magnetron sputtering

All the substrates used for deposition in Cell A were 5 µm-thick Ti foils from Advent (Ti1) and Lebow (Ti2) produced via cold-rolling. A second set of experiments aimed at studying the influence of the substrate surface roughness. Therefore, the substrates used for deposition in Cell B were produced with different roughness: medium (Ti3), high (Ti4), and low roughness (Ti5). Ti3 was a circular 50 µm-thick Ti foil cut from a bigger rolled foil (Goodfellow). Ti4 was obtained by etching a Ti3 foil with concentrated HCl (~36%) for 45 min under IR lamp. Ti5 was produced by magnetron sputtering a 300-µm thick mechanically-polished Si wafer with 100 nm metallic Ti.

3.2.4 Conductivity tests

Conductivity tests were performed using an Inolab Cond 720 conductometer connected to a TetraCon 325 standard conductivity cell. The measurements were performed in stirred 0.4 and 0.3 mM HNO_3 solutions, i.e., the acid solutions typically contained in Cell A and Cell B, respectively. These solutions were prepared using the mixed solvent isopropanol/isobutanol as described in Section 3.2.2.

3.2.5 Atomic Force Microscopy (AFM) studies

The surface roughness of the deposition substrates, i.e., the measure of the texture of a surface quantified by the vertical deviations of a real surface from its ideal planar form, was investigated by using Atomic Force Microscopy (AFM) (Veeco Dimension 3100 and MFP 3D Asylum Research).

As regards the deposition foils used in Cell A, circular samples of Ti1 and Ti2 foils were cut with different diameters: 7, 10, 13, 16, and 19 mm. These samples were investigated before and after the cleaning procedure with HCl, water and isopropanol, using AFM in tapping mode and recording three (15 × 15) μm^2 images, three (1 × 1) μm^2 images and three (0.2 × 0.2) μm^2 images. For each sample of a certain diameter, the surface roughness of each of these image sizes was determined as the average root mean square value ($\mathrm{R\overline{M}S}$) of the RMS values obtained for each of the three images of a certain size. The final surface roughness of each of these image sizes was determined for both Ti1 and Ti2 foils as the arithmetic mean over all the circular samples of all the $\mathrm{R\overline{M}S}$ values evaluated for that particular image size. This systematic analysis was applied both before and after the cleaning procedure.

As regards the deposition foils used in Cell B, they were analyzed by tapping mode AFM, recording ten (5 × 5) μm^2 images and one (25 × 25) μm^2 image for each of the foils. From each of the (5 × 5) μm^2 images two RMS values were evaluated using a (1.5 × 1.5) μm^2 mask in two different positions inside the image. From each of the (25 × 25) μm^2 images, instead, twenty RMS values were evaluated using (1.5 × 1.5) μm^2 masks in twenty different positions of the image. The final surface roughness value of each of the image sizes was evaluated for each Ti foil as the arithmetic mean of all the RMS values measured for that specific image size. This systematic analysis was applied both before and after the cleaning process.

Adopting the same procedure described for the analysis of the deposition foils used in Cell B, an AFM investigation of air-dried MC targets produced using Ti1, Ti2, Ti3, Ti4, and Ti5 foils was performed. An AFM analysis of air-dried HC, MC and LC targets produced using only Ti5 foils was also performed. In both investigations, the final surface roughness value of each sample was evaluated as the arithmetic mean of all the measured RMS values ($\mathrm{R\overline{M}S}$). It has to be pointed out that because all the prepared samples showed surfaces with troughs (i.e., cracks which destroy the surface homogeneity creating smaller island-like areas in the layer), the RMS values were evaluated using (1.5 × 1.5) μm^2 masks only in the trough-free areas (i.e., the islands).

This is justified, because the troughs do not belong to the surface and hence do not define the real roughness of the deposited layers.

3.2.6 X-ray Photoelectron Spectroscopy (XPS) studies

The XPS characterization of the samples was performed using Al K_α and Mg K_α radiations. The X-ray source was operated at 10 kV anode voltage and a current of 10 mA. The pass-energy of the hemispherical energy analyzer was 50 eV. The pressure inside the ultra-high vacuum chamber was in the range of $(1.2\text{-}2.0)\cdot 10^{-9}$ mbar. The analyzed samples were the cathode (Ti3 foil) and the anode of Cell B after a MC experiment. At the end of the deposition time, Cell B was top-sealed and inserted into a glove-box, where an inert environment was assured by a constant Ar pressure (0.5 mbar, $O_2 < 1$ ppm, $H_2O < 1$ ppm). The cell was opened, the solvent extracted, and the cathode and anode foils were dried. Drying in an inert environment allowed performing a chemical surface analysis with unaltered products of reduction and oxidation obtained during the plating process. The samples were then sealed in special air-tight containers and transported under Ar atmosphere to the XPS spectrometer for the analysis. A special lock chamber filled with Ar was used to introduce the samples into the spectrometer: hence they were never exposed to air. After the first surface investigation, both samples underwent two ten-minute sputtering cycles using 4 kV Ar^+ ions (i.e., total sputtering time: 20 min). After each ten-minute sputtering cycle, the surface of the samples was analyzed by XPS.

By fitting the XPS spectra, the binding energies and peak areas of the XPS lines of interest were determined. As it was not the aim of the present work to perform a detailed chemical surface analysis of the deposits, but mainly to understand, which elements can be found on the electrodes after a constant current density MP, the individual components of the XPS lines obtained by peak fitting were not analyzed in detail. The reported spectra are therefore shown without multicomponent fitting analysis. For the cathode deposit that was analyzed before sputtering, the measured binding energies were corrected for the surface charging using the C 1s line of hydrocarbons with a binding energy of 285.0 eV [18]. After sputtering, the imprecise fittings of the 285.0 eV peaks required the use of a higher binding energy peak (ca. 289 eV) present in the same C 1s spectra to correct for the surface charge effect. For the anode deposit, instead, the correction of the binding energies was realized both before and after sputtering using only the C 1s line at 285.0 eV. The experimental uncertainty of the binding energies is ± 0.1 eV.

3.2.7 Gamma-ray spectroscopy studies

Gamma-ray spectroscopy was used after MP of Nd solution containing radioactive ^{147}Nd tracer. For this, an aliquot of 100 µL of the stock solution was irradiated with thermal neutrons in the TRIGA research reactor of Mainz University, producing in this way a solution that contained a radioactive tracer of the element to be plated (Nd: ^{147}Nd, β^-, $t_{1/2}$ = 10.98 d, E_γ = 91 keV). For this technique a high-purity germanium detector (HPGe) (GEM series HPGe Detector Model No. GEM 23158P-Plus, ORTEC Company) was employed to measure the active samples and to determine the deposition yield of the MP process. To obtain quantitative data, reference sources with known amounts of the tracer were prepared. They consisted of filter papers with the same geometry as the targets, soaked with the tracer-containing solution. To avoid any kind of contamination of the γ-spectrometer, the active samples were sealed with plastic foils before insertion into the sample holder. The yield values evaluated at the different times of interest were always obtained as the average value calculated from three distinct γ measurements.

3.3 Experimental results and analysis

3.3.1 Analysis of the conductivity tests

The conductivity (χ) measured for the 0.4 mM HNO_3 solution (Cell A acid solution) was 2.8 ± 0.1 µS/cm. The conductivity measured for the 0.3 mM HNO_3 solution (Cell B acid solution) was instead 2.0 ± 0.1 µS/cm. To evaluate the solution resistances in Cells A and B, the expression $R = \rho \cdot l/S$ was applied, where ρ is the resistivity of the system (i.e., the inverse of the conductivity), l is the distance between the electrodes, and S is the surface area of the electrodes [19]. For Cell A, where $\rho = 357 \pm 13$ kΩ·cm, $l = 2.8 \pm 0.01$ cm, $S = 3 \pm 0.1$ cm^2, the cell resistance is 333 ± 12 kΩ. For Cell B, instead, where $\rho = 500 \pm 25$ kΩ·cm, $l = 2.8 \pm 0.01$ cm, $S = 9 \pm 0.1$ cm^2, the cell resistance is 156 ± 8 kΩ. Cell A has a higher cell resistance than Cell B. If Ohm's first law, $V = RI$, where R is the cell resistance and I is the applied current, can be considered valid for the investigated MPs, then the previously calculated solution resistances can be used to estimate the contribution of the ohmic drop to the overall cell potential. For Cell A (I = 2 mA) the obtained value of V is ca. 660 V, whereas for Cell B (I = 6 mA) it is ca. 930 V. Both values are quite close to the experimentally recorded values (Cell A ca. 500 V, Cell B ca. 900 V).

3.3.2 AFM analysis

The results of the AFM analysis of the Ti1 and Ti2 foils described in Section 3.2.5 are summarized in Table 3-2, both before and after the cleaning procedure.

Table 3-2 Average root mean square values obtained after the AFM analysis of the Ti1, Ti2, Ti3, Ti4, and Ti5 foils.

Before cleaning	**Scan size (µm^2)**	**Ti1 R$\overline{\mathrm{M}}$S (nm)**	**Ti2 R$\overline{\mathrm{M}}$S (nm)**	**Ti3 R$\overline{\mathrm{M}}$S (nm)**	**Ti4 R$\overline{\mathrm{M}}$S (nm)**	**Ti5 R$\overline{\mathrm{M}}$S (nm)**
	(0.2 × 0.2)	1.4 ± 0.5	0.52 ± 0.16	-	-	-
	(1 × 1)	5.5 ± 0.8	2.4 ± 0.6	-	-	-
	(15 × 15)	29 ± 3	20.1 ± 1.8	-	-	-
	(5 × 5)	-	-	26 ± 7	330 ± 100	5.8 ± 2.7
	(25 × 25)	-	-	23 ± 8	330 ± 110	3.9 ± 0.5

After cleaning	**Scan size (µm^2)**	**Ti1 R$\overline{\mathrm{M}}$S (nm)**	**Ti2 R$\overline{\mathrm{M}}$S (nm)**	**Ti3 R$\overline{\mathrm{M}}$S (nm)**	**Ti4 R$\overline{\mathrm{M}}$S (nm)**	**Ti5 R$\overline{\mathrm{M}}$S (nm)**
	(0.2 × 0.2)	0.93 ± 0.12	0.63 ± 0.11	-	-	-
	(1 × 1)	4.5 ± 0.6	2.5 ± 0.9	-	-	-
	(15 × 15)	31 ± 3	20.6 ± 2.2	-	-	-
	(5 × 5)	-	-	21 ± 5	350 ± 140	14.9 ± 2.6
	(25 × 25)	-	-	24 ± 7	340 ± 140	12.8 ± 0.7

The results shown in Table 3-2 clearly demonstrate that Ti1 foils are rougher than Ti2 foils both before and after the cleaning procedure. The cleaning does not affect their R$\overline{\mathrm{M}}$S values.

The results of the AFM analysis of the Ti3, Ti4 and Ti5 foils described in Section 3.2.5 are summarized in Table 3-2 as well. They clearly indicate that the three deposition foils used in Cell B have very different surface roughness, around one order of magnitude of difference one from the other. The Ti4 foil is the roughest one, Ti3 has an intermediate roughness, while Ti5 is the smoothest foil, whose roughness is slightly increased after the cleaning procedure.

The results of the AFM analysis of the air-dried MC targets produced using Ti1, Ti2, Ti3, Ti4, and Ti5 foils are summarized in Table 3-3. They clearly demonstrate that rougher deposition foils grow rougher layers, the smoothest ones being the Ti2-grown MC layer in Cell A, and the Ti5-grown MC layer in Cell B.

Table 3-3 Average root mean square values obtained after the AFM analysis of the MC targets produced using Ti1, Ti2, Ti3, Ti4, and Ti5 foils.

Cell	**Deposition substrate**	**Scan size (μm^2)**	**Surface roughness R$\overline{\text{M}}$S (nm)**
A	**Ti1**	**(5 × 5)**	91 ± 24
		(25 × 25)	92 ± 16
	Ti2	**(5 × 5)**	67 ± 26
		(25 × 25)	75 ± 23
B	**Ti3**	**(5 × 5)**	150 ± 40
		(25 × 25)	190 ± 70
	Ti4	**(5 × 5)**	443 ± 140
		(25 × 25)	1100 ± 500
	Ti5	**(5 × 5)**	22 ± 13
		(25 × 25)	22 ± 13

The results of the AFM analysis of the air-dried HC, MC and LC targets produced using Ti5 foils are summarized in the (25 × 25) μm^2 images shown in Figure 3-2. Figure 3-2a shows the HC target, Figure 3-2b the MC target, and Figure 3-2c the LC target. In the investigated areas, only HC and MC targets show to have surface troughs.

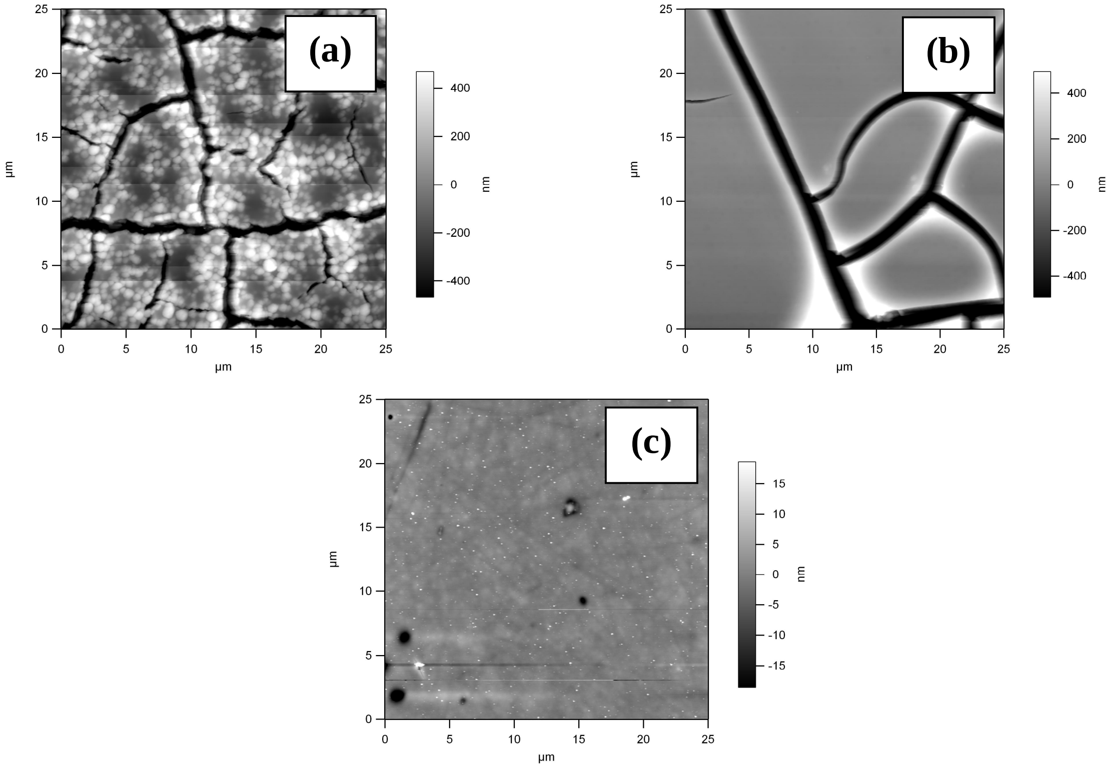

Figure 3-2 (25 × 25) μm^2 AFM images of the HC (a), MC (b), and LC (c) targets obtained using Ti5 foils.

Respecting that $\mathrm{R\overline{M}S}$ values were obtained by limiting the analysis to trough-free areas of the layer, Figure 3-2 clearly demonstrates that the HC target, with its evident surface outgrowths (i.e., white spots in Figure 3-2a), is the roughest target. The LC target is instead the smoothest one. The average root mean square values of the AFM analysis are reported in Table 3-4.

Table 3-4 Average root mean square values obtained after the AFM analysis of the HC, MC and LC targets produced using Ti5 foils, including only trough-free areas.

Target	**Scan size (μm^2)**	**Surface roughness $\mathrm{R\overline{M}S}$ (nm)**
HC	**(5 × 5)**	150 ± 30
	(25 × 25)	150 ± 30
MC	**(5 × 5)**	22 ± 13
	(25 × 25)	22 ± 13
LC	**(5 × 5)**	2.0 ± 1.6
	(25 × 25)	6 ± 3

3.3.3 XPS analysis

The XPS analysis of the deposit obtained on the Ti3 cathode of Cell B after 3 h MP from MC solution at a constant current density showed the presence of the following elements: C, O, Pd, and Nd. The corresponding XPS signals were: C 1s, O 1s, Pd 3d, Nd 3d, and Nd 4d. Ti signals were not detected, indicating that the deposited layer is thick. Nd 3d spectra were recorded using a Mg K_{α} radiation to avoid the interference of oxygen Auger lines present in the same binding energy region. Figure 3-3 shows the spectra of Nd 3d (a), Pd 3d (b), and C 1s (c) before sputtering (indicated as 0 min sputtering in the figure) and after 10 min and 20 min sputtering with Ar^+ ions. Table 3-5 shows the ratios of the total peak areas Nd 3d/C 1s, Pd 3d/C 1s, and O 1s/C 1s after 0, 10, and 20 min sputtering.

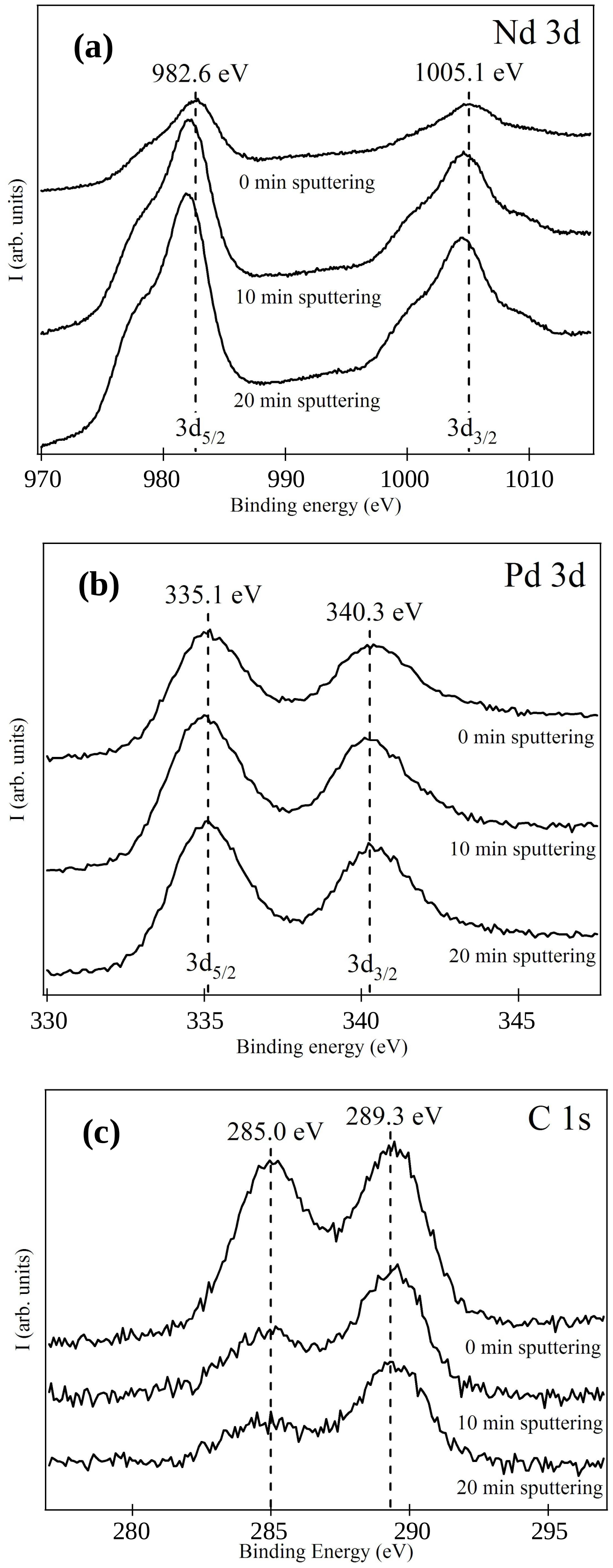

Figure 3-3 XPS spectra of the cathode deposit obtained after 3 h plating: (a) Nd 3d, (b) Pd 3d, and (c) C 1s before sputtering (indicated as 0 min sputtering in the figure), after 10 min sputtering, and after 20 min sputtering with Ar^+ ions. Identical offsets were applied between the spectra of each figure.

Table 3-5 Ratios of the peak areas Nd 3d/C 1s, Pd 3d/C 1s, and O 1s/C 1s after 0, 10, and 20 min sputtering.

Ratios of XPS peak areas	0 min sputtering	10 min sputtering	20 min sputtering
Nd 3d/C 1s	18	58	91
Pd 3d/C 1s	1.4	3.3	4.2
O 1s/C 1s	5	10	14

The measured binding energy of Nd $3d_{5/2}$ in the surface layer equals 982.6 eV (Figure 3-3a) and can be compared to the literature value of 983.1 eV [18] for Nd^{3+}. Therefore, Nd is present as Nd^{3+} in the investigated deposited layer (possibly as carboxylate, oxide, or hydroxide).

As regards the Pd 3d spectra reported in Figure 3-3b, the comparison between the experimental Pd $3d_{5/2}$ binding energy of 335.1 eV and the literature value for metallic Pd (Pd $3d_{5/2}$ = 335.1 eV [18]) indicates that Pd is deposited as metal during the MP process.

The C 1s spectra reported in Figure 3-3c show the presence of two components: the C 1s peak at 285.0 eV is aliphatic carbon of the mixed isopropanol/isobutanol solvent. The peak at ca. 4.3 eV higher binding energy (i.e., 289.3 eV) was attributed, according to literature, to possible C(O)OR -ester- (289.5 eV [18]), or COOM -metal carboxylate- (289.0 eV [18]) groups formed during the plating process, or to CO_3^{2-} (289-290 eV [18]) impurities present in the solvent. The hypothesis of C(O)OR or COOM groups formed during MP is supported by the XPS analysis of a Ti3 foil, which was treated as follows: it was inserted into the glove-box, cleaned with HCl, H_2O and isopropanol, immersed into an isopropanol/isobutanol solution, and then dried. The spectrum (reported in the Supplementary Material, Figure A.1) showed no peak at ca. 289 eV, but only the aliphatic C 1s peak of the solvent at 285.0 eV. Hence the solvent undergoes electrolysis during the MP process and is likely oxidized.

All the spectra of Figure 3-3 and the data given in Table 3-5 show that as long as the sputtering of the surface proceeds, the intensities of the Nd 3d and Pd 3d signals increase, while the C 1s intensity decreases. Particularly, they change most significantly during the first 10 min of sputtering. As regards the decrease of the C 1s intensity, it is evident that the 285.0 eV component is removed more easily than the 289.3 eV one. The 285.0 eV line originates from physisorbed solvent on the surface of the deposit, while the 289.3 eV line is due to chemisorbed species arising from solvent electrolysis. Of course, according to these trends, the ratios Nd 3d/C 1s and Pd 3d/C 1s are bound to increase with sputtering time (see Table 3-5). The same is verified for the ratio O 1s/C 1s. In particular, the ratio Nd 3d/C 1s will be the fastest growing one because of the higher amount of Nd present in the system. These trends show very clearly that the obtained target is characterized by an outer layer of solvent which covers the Nd and Pd deposit.

The XPS analysis of a Ti3 MC target, obtained with a plating time of 30 minutes, showed that after small deposition times only Nd is deposited on the cathode and is covered by a solvent layer. No signals of Pd were found. Figure 3-4 shows the spectra of Nd 3d (a) and C 1s (b) before sputtering and after 10 and 20 min sputtering with Ar^+ ions.

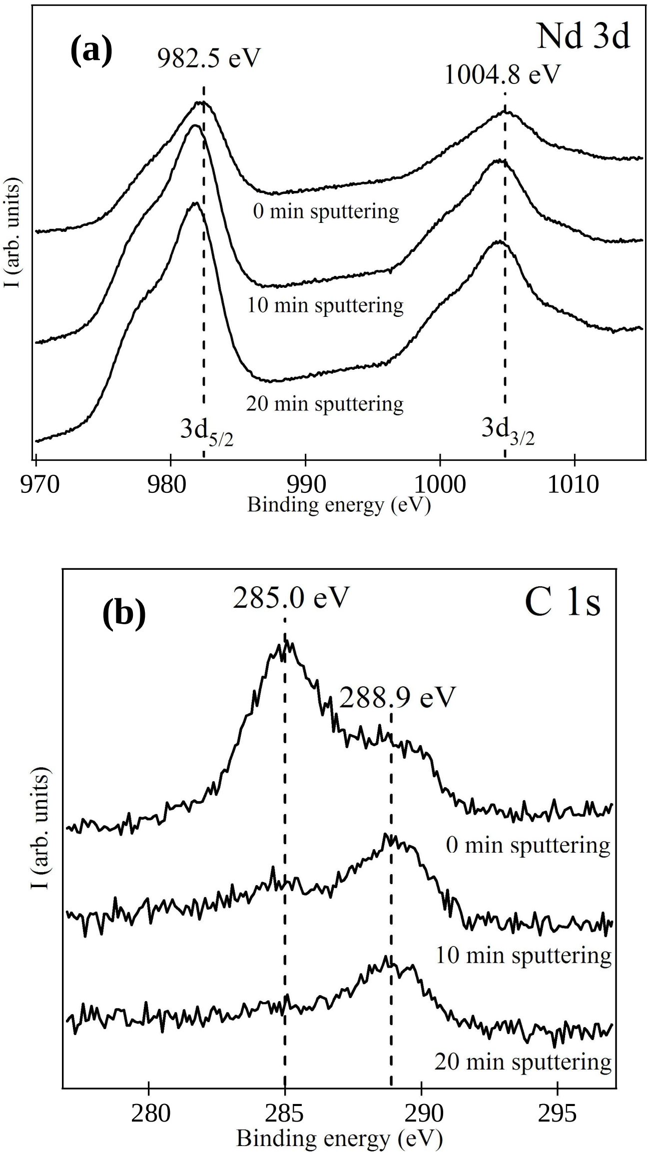

Figure 3-4 XPS spectra of the cathode deposit obtained after 30 min plating: (a) Nd 3d, and (b) C 1s before sputtering (indicated as 0 min sputtering in the figure), after 10 min sputtering, and after 20 min sputtering with Ar^+ ions. Identical offsets were applied between the spectra of each figure.

From Figure 3-4 it is once more evident that as long as the sputtering proceeds, the Nd 3d signal increases, while the C 1s intensity decreases. Particularly, the higher binding energy component of the C 1s spectra (i.e., 288.9 eV) results to be smaller than the same one reported in Figure 3-3c, where the intensity ratio to the 285.0 eV component was almost 1:1 before sputtering. This suggests that after small deposition times, the electrolysis of the solvent, which occurs in parallel with the plating of the Nd ions, is still small if compared to its contribution to the constant current density plating process realized with longer (i.e., 3 h) deposition times. Moreover, the almost unchanged intensity of the 289 eV component after sputtering indicates again its strongly chemisorbed nature, suggesting a possible complex formation with Nd atoms. If this is the case, the ca. 289 eV component would match COOM groups -metal carboxylate- formed during the plating process.

The comparisons between the C 1s spectra in Figures 3-3c and 3-4b, and the comparisons between the Pd 3d spectra in Figure 3-3b show no chemical shifts before and after sputtering. Small shifts of 0.5 eV after sputtering were observed only for the Nd 3d spectra reported in Figures 3-3a and 3-4a: this could indicate the presence of several Nd^{3+} species in the topmost surface layer.

As regards the XPS analysis of the Pd anodic surface of Cell B after the 3 h-long MP, the detected elements were: C and Pd. The corresponding XPS signals were: C 1s, Pd 3d, and Pd 3p. No N 1s signal of the NO_3^- ions deriving from the dissolution of $Nd(NO_3)_3 \cdot 6H_2O$ was observed. Figure 3-5 shows the spectra of Pd 3d (a), and C 1s (b) before sputtering, and after 10 min sputtering with Ar^+ ions. The spectra after 20 min sputtering were identical to those after 10 min sputtering.

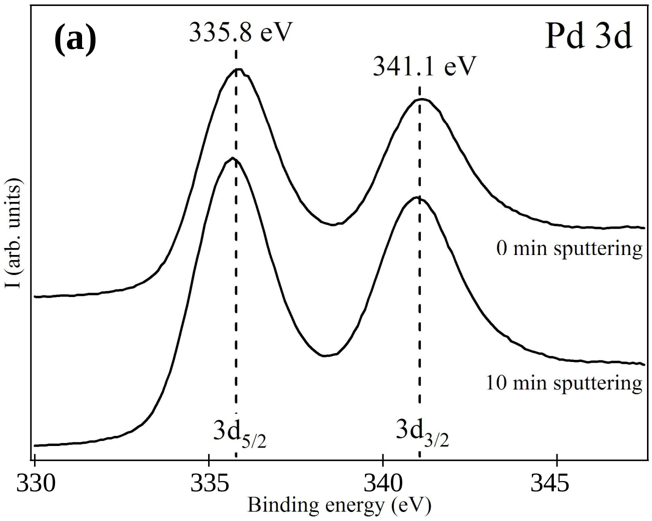

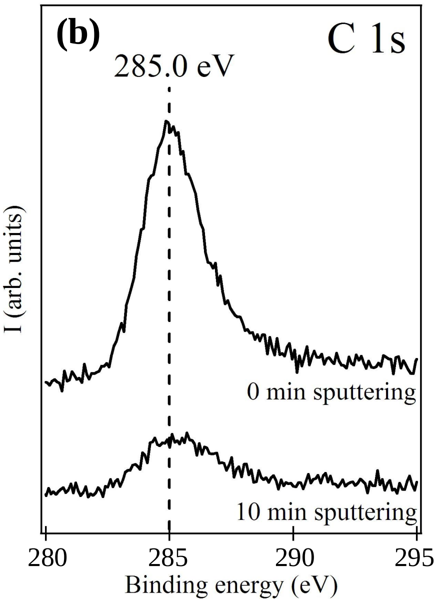

Figure 3-5 XPS spectra of the anode deposit obtained after 3 h plating: (a) Pd 3d, (b) C 1s before sputtering (indicated as 0 min sputtering in the figure), and after 10 min sputtering with Ar^+ ions. Identical offsets were applied between the spectra of each figure.

Figure 3-5 shows very clearly that as long as the sputtering proceeds the Pd 3d signal increases, while the C 1s intensity decreases. This proves that, as in the case of the cathode deposit, the metal is covered by a layer of organic molecules. In addition, the presence of only the aliphatic C 1s peak of the solvent at 285.0 eV and of metallic Pd (Pd $3d_{5/2}$ = 335.8 eV) indicates that no chemical reaction products are present on the anode: the solvent layer may just be physisorbed on the Pd surface. To prove this hypothesis, the XPS analysis of a Pd foil before electrolysis was realized: the foil was cleaned with HCl, H_2O, and isopropanol, dried in air, and then analyzed. In this case a solvent layer can only be physisorbed on the Pd surface. The detected XPS signals were: C 1s, Pd 3d, and Pd 3p. The spectra of Pd 3d, and C 1s before and after 10 min sputtering (reported in the Supplementary Material, Figures A.2 and A.3) are identical to those of Figure 3-5, showing again that the Pd 3d intensity increases during the sputtering, while the C 1s intensity decreases. Hence, the solvent layer on the anode was just physisorbed on the foil after its removal from the cell and drying. For this reason it can be said that no reaction products were found on the anode surface.

3.3.4 Molecular plating performed with Cell A

MP on Ti1 and Ti2 foils was performed with 0.22 mM Nd salt solutions (MC) and 0.4 mM HNO_3, applying a constant current of 2 mA for 3 hours on a deposition area of 3 cm^2 (current density 0.7 mA/cm^2). In Figure 3-6a the cell potential curves recorded using Ti1 and Ti2 foils as deposition substrates are compared. Both curves show the same behaviour: after an initial increase within the first few minutes, the cell potential strongly decreases within 85 min (dashed line), and then slightly increases with an inflection point at around 120 min.

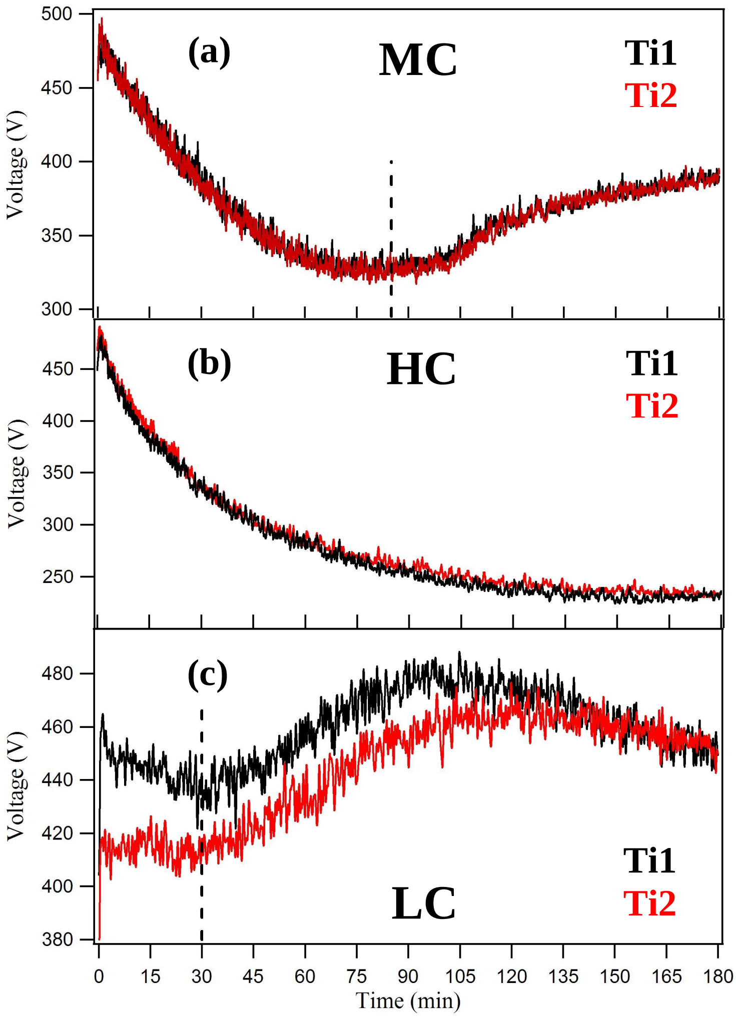

Figure 3-6 Cell potential vs time curves of molecular plating using Ti1 and Ti2 foils and recorded with (a) medium concentration [MC], (b) high concentration [HC] and (c) low concentration [LC] Nd salt. No offsets were applied between the curves.

Applying the same current density, MPs were also performed with 0.44 mM (HC) and 0.11 mM (LC) Nd salt solutions to investigate the influence of the Nd concentration. The cell potential curves obtained with the two different Ti foils display a similar behaviour: at the higher concentration (Figure 3-6b), after an initial increase, a large drop in cell potential is evident till the end of the deposition process (180 min); the cell potential approaches a constant value at around 230 V at the end of the experiment. At the lower concentration (Figure 3-6c), the cell potential curves obtained using Ti1 and Ti2 cathodes display several common features: after an initial increase, the cell potential slightly decreases within 30 min (dashed line), afterwards it increases, reaching a maximum value at around 105 min. Additional cell potential vs time curves from repetitions performed as reproducibility tests are reported in the Supplementary Material (Figures A.4-A.9) and confirm that the data shown in Figure 3-6 are typical.

By comparing the curves recorded at different concentrations of Nd salt (Figure 3-6), we notice that the cell potential profile is very sensitive to the Nd^{3+} concentration. In addition, the curves obtained with Ti1 and Ti2 foils display no significant difference in cell potential behaviour, despite the different surface roughness of the deposition substrates employed in the molecular plating (see Table 3-2).

3.3.5 Molecular plating performed with Cell B

MPs on Ti3, Ti4 and Ti5 foils were performed using solutions with 0.22 mM Nd salt (MC) and applying a 6 mA constant current for 3 hours on a deposition area of 9 cm^2 (current density 0.7 mA/cm^2). The cell potential curves obtained for the three electrodes (Figure 3-7a) display similar behaviour: after the initial increase, the cell potential decreases within 45 min (dashed line), and then increases to a maximum value. In the case of Ti3 and Ti5 substrates the maximum forms a wide plateau, ranging from around 90 min to 120 min, with the maximum located at around 110 min. In the case of Ti4 foils, instead, the formed plateau shows its maximum at around 75 min. After the maximum, all of the cell potential curves tend to slightly decrease with time. Figure 3-7b shows the variations of the cell potential with time during MP in 0.44 mM Nd salt solutions (HC). Again the three substrates display similar behaviour: after the initial increase (zoom in Figure 3-7b), the cell potential strongly decreases within 80 min (dashed line) and then slightly increases. Under the same conditions, the cell potential profiles recorded during the molecular plating with 0.11 mM Nd salt solutions (LC), display similar behaviour: after the initial increase, the cell potential decreases exponentially within 20 min (no minimum is present), and then decreases almost linearly with time with a very small slope (Figure 3-7c). Repeated cell potential vs time curves as reproducibility tests are reported in the Supplementary Material (Figures A.10-A.18) and confirm that the data shown in Figure 3-7 are typical.

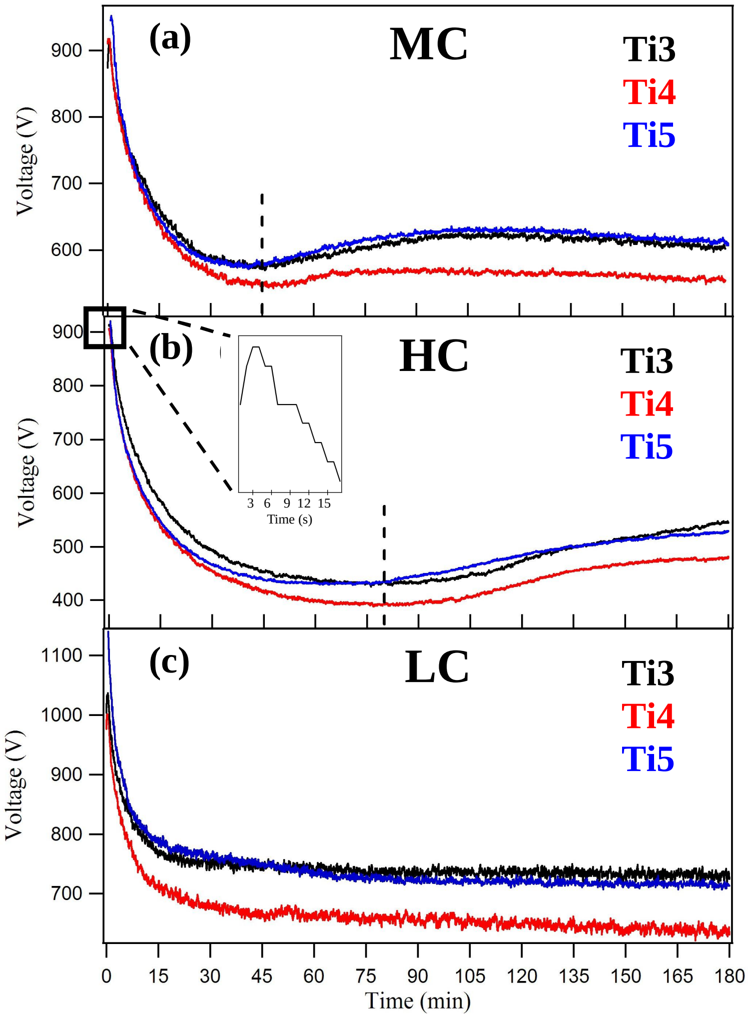

Figure 3-7 Cell potential vs time curves of molecular plating using Ti3, Ti4 and Ti5 foils and recorded with (a) medium concentration [MC], (b) high concentration [HC] and (c) low concentration [LC] Nd salt. No offsets were applied between the curves.

As already observed with Cell A, by comparing the curves recorded at different concentrations of Nd salt (Figure 3-7), we notice that the cell potential profile is very sensitive to the Nd salt concentration. Furthermore, at the same concentration of Nd salt, the curves obtained by using Ti3 and Ti5 foils do not display different cell potential behaviour, despite the different surface roughness of the deposition substrates (see Table 3-2). Differently, all the curves obtained by using the roughest substrate, i.e., the Ti4 foil, clearly show a lower cell potential trend.

A blank experiment without [$Nd(NO_3)_3 \cdot 6H_2O$] was realized with Cell B on Ti3 foil using 0.3 mM HNO_3 in isopropanol/isobutanol to verify the crititical influence of the presence of the Nd salt. The comparison between the cell potential curve recorded for this experiment and the MC Nd salt Ti3 curve clearly indicates that the cell potential decrease is due to the plating process of Nd (Figure 3-8).

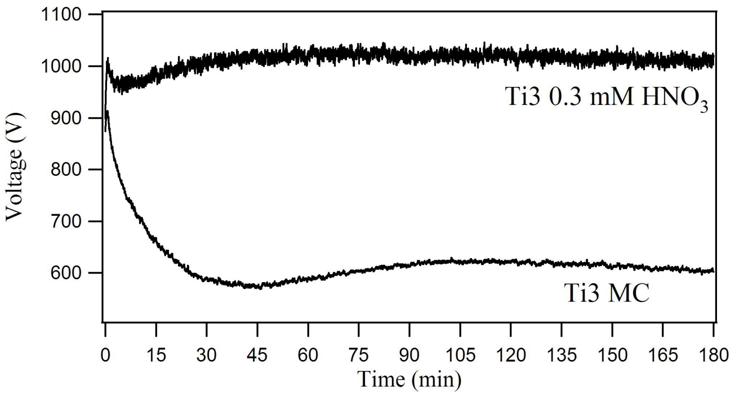

Figure 3-8 Comparison between the curves obtained using Ti3 foil and recorded without Nd salt (upper curve) and with a MC Nd salt solution (lower curve).

It is interesting to notice that, even when only the acid is present, the curve displays a minimum at around 5 min, but during the overall experiment the cell potential is higher than that observed in the presence of the Nd salt.

3.3.6 Molecular plating on a smaller deposition area in Cell B

Minima in the cell potential profiles obtained with Cell A and Cell B are given in Table 3-6. They occur at different times, although the same current density (0.7 mA/cm^2) was used.

Table 3-6 Minima time positions of the MC, HC and LC Nd salt cell potential curves recorded using Ti1, Ti2, Ti3, Ti4, and Ti5 foils.

Cell A (2mA/3cm^2)	**Cathode**	**MC minimum position (min)**	**HC minimum position (min)**	**LC minimum position (min)**
	Ti1	85	180	30
	Ti2	85	180	30

Cell B (6mA/9cm^2)	**Cathode**	**MC minimum position (min)**	**HC minimum position (min)**	**LC minimum position (min)**
	Ti3	45	80	-
	Ti4	45	80	-
	Ti5	45	80	-

The minima in the cell potential vs time curves obtained with Cell B (I = 6 mA, cathode area = 9 cm^2) occurred earlier than those recorded using Cell A (2 mA, 3 cm^2).

A plot of time position of the cell potential minima vs concentration is reported in Figure 3-9. A linear correlation of the time positions of the minima with the initial Nd concentration is found for both cells, suggesting that the position of the cell potential minima is directly correlated with the initial Nd concentration.

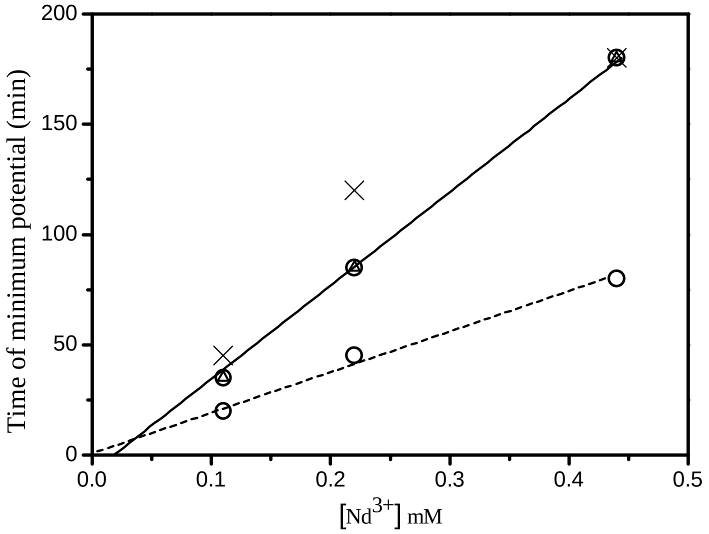

Figure 3-9 Plot of time positions of the cell potential curve minimum vs initial Nd concentration. Cell A with Ti1 and Ti2 cathode, current 2 mA, area 3 cm^2, 0.4 mM HNO_3 (dashed line, open circles). Cell B with Ti3, Ti4 and Ti5 cathodes, current 6 mA, area 9 cm^2, 0.3 mM HNO_3 (solid line, open circles); current 2 mA, 3 cm^2, 0.3 mM HNO_3 (crosses); current 2 mA, 3 cm^2, 0.4 mM HNO_3 (open triangles).

In order to get insights into these time differences and to verify this hypothesis, experiments at the three different Nd salt concentrations, i.e., LC, MC and HC, were carried out in Cell B using a Ti3 cathode having the same area as those used for MPs in Cell A. Also the applied current was identical to that of the experiments in Cell A. The circular deposition area of these foils was reduced to 3 cm^2 using a mask. A constant current of 2 mA was applied for 3 hours. The curves (Figure 3-10, higher voltage curves) display a general behaviour resembling that obtained with Cell A (Figure 3-6). Indeed, they all show much longer time positions of the minima than the cell potential curves recorded with Cell B but with 6 mA of constant current and a deposition area of 9 cm^2. Despite these similarities, it has to be noticed that the time positions of the minima (solid lines, Figure 3-10) of the potential profiles obtained for the MC and LC Nd^{3+} solutions in the present experiment (120 and 45 min, respectively) do not correspond to those of the Ti1 and Ti2 curves (85 and 30 min, respectively). These discrepancies are likely due to the different acid concentrations. In fact, HNO_3 concentration in Cell A was 0.4 mM, while it was 0.3 mM in Cell B.

Further experiments with Cell B were realized using 0.4 mM HNO_3 (Figure 3-10, lower voltage curves). The lower voltage curves of Figure 3-10 and the plot of Figure 3-9 show very clearly that the discrepancies noted above have been eliminated: the time positions of the minima in the MC and LC Nd ion experiments (dashed lines in Figure 3-10a and c) match with those found using Cell A (85 and 30 min, respectively).

Besides the different minima positions, it is evident that the cell potential curves recorded in the presence of 0.4 mM HNO_3 display cell potential values lower than those obtained with 0.3 mM acid.

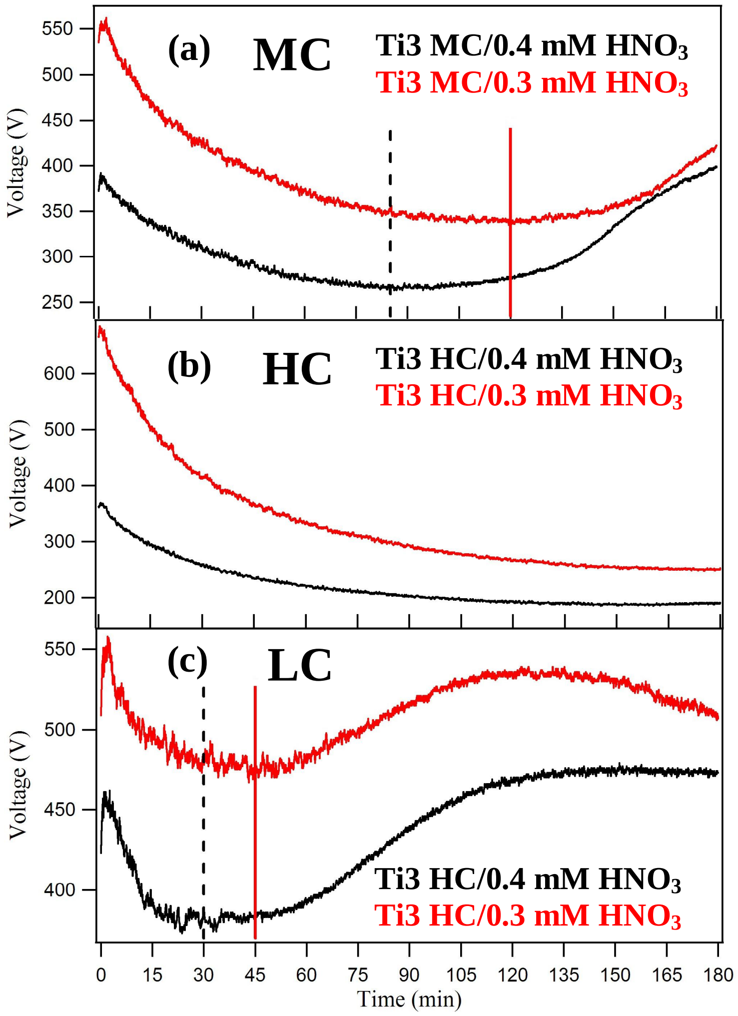

Figure 3-10 Cell potential vs time curves using a Ti3 foil with 3 cm^2 deposition area and 2 mA constant current, recorded in the presence of 0.3 mM or 0.4 mM HNO_3, for (a) 0.22 mM [MC], (b) 0.44 mM [HC] and (c) 0.11 mM [LC] Nd salt solutions.

3.3.7 Deposition yield evaluation of the molecular plating realized using Cell B

The deposition yields of the molecular plating processes were determined by depositing ^{147}Nd tracer-containing Nd and analyzing the activity of the produced layer by γ-ray spectroscopy. Experiments performed with active and inactive MC, HC and LC Nd salt solutions using Ti3 as deposition foil (see Supplementary Material, Figures A.19-A.21) show the cell potential behaviours of the active and inactive Nd salt solutions to be almost identical, indicating that the radiolysis of the solution induced by the β- and γ-radiation can be neglected.

The deposition yields (Table 3-7) were evaluated as average values at the characteristic times of the cell potential curves recorded at the different Nd salt concentrations, using Ti3, Ti4, and Ti5 cathodes in Cell B. As characteristic times, the end of the deposition process (180 min) and the occurrence of minima (if present) and maxima in the cell potential profiles were chosen.

Table 3-7 Average deposition yield values measured at different times for the MC, HC, and LC Nd salt experiments using Ti3, Ti4, and Ti5 foils.

Experiment	**Time (min)**	**Ti3 yield value (%)**	**Ti4 yield value (%)**	**Ti5 yield value (%)**
MC	45	83.7 ± 2.2	89.2 ± 2.0	71 ± 3
	75	-	98.5 ± 1.2	-
	90	98.3 ± 1.1	-	93.2 ± 2.7
	180	95.6 ± 2.7	99.6 ± 0.4	98.7 ± 0.8
HC	80	87 ± 3	86 ± 5	84.5 ± 2.0
	180	97 ± 4	98.3 ± 1.6	95 ± 5
LC	20	66 ± 3	66 ± 3	71 ± 6
	180	99.1 ± 0.9	98.3 ± 1.7	98.1 ± 0.9

As regards the MC Nd salt experiments, after only 45 min the deposition yield is already very high, over 70%. The highest yield is obtained with the Ti4 foils and the lowest one with the Ti5 foils. At 90 min the yield values approach 100%. Notably, by using the Ti4 cathode, only 75 min of deposition are sufficient to obtain a deposition yield almost identical to the final one.

Experiments at higher Nd concentration (HC) show that there is no real spread in yield values at the time of minimum cell potential (80 min) as in the case of the MC Nd salt experiments, and that all the values are similar and high. At the end of the deposition process, almost all the yield values approach 100% (see Table 3-7). These high yields are in line with earlier observations and confirm that MP is ideally suited for quantitatively depositing Nd, which represents many trivalent elements like the lanthanides and the late actinides. Concerning the lower Nd concentration measurements (LC), the times at which the deposition yields were evaluated are the end of the process (180 min) and the time corresponding to a major change in the slope of the cell potential curves (20 min), because no minimum is found in these experiments. The yield values after 20 min are similar and quite high (> 65%) if one considers the relatively short elapsed time. At the end of the deposition process, all yield values approach 100% (see Table 3-7).

3.3.8 Kinetics of molecular plating

Kinetic measurements were obtained by determining the deposition yield values with γ-ray spectroscopy as described in Section 3.2.7. The experiments were carried out in Cell B, using 0.22 mM (MC) Nd salt, and Ti3 foils as deposition substrate. The first step of this set of experiments was the preparation of an active Nd solution, i.e., a solution containing the radioactive tracer ^{147}Nd. Twelve targets were then produced by electrolysis of aliquots of 100 μL at different deposition times: the first after 15 min and the subsequent ones after increments of 15 min up to 180 min. The γ-measurements of the 12 targets gave the deposition yields reported in Figure 3-11.

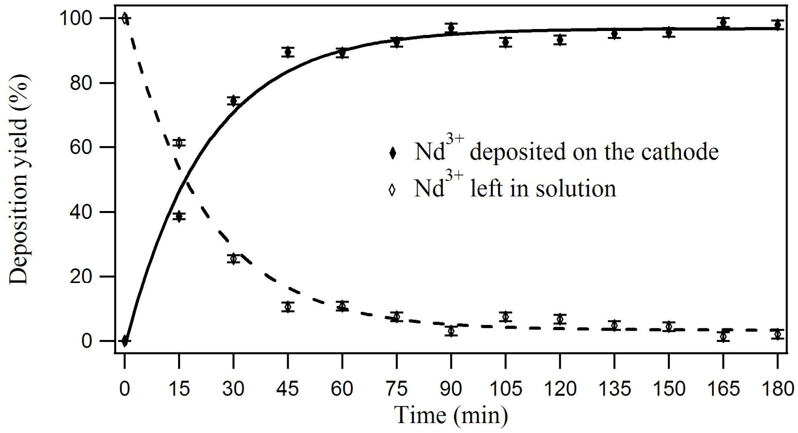

Figure 3-11 Fitting of the percentage yield values calculated directly after γ-measurement (solid curve) and after subtraction from the 100 % yield value (dashed curve).

To obtain the trend of the Nd^{3+} depletion with time, the differences between the 100% yield value and the percentage yield values evaluated at each time were calculated. The depletion curve obtained by fitting such calculated values (Figure 3-11, dashed black curve) shows an exponentially decreasing behaviour $y = y_0 + A\exp[-(x - x_0)/\tau]$ consistent with the integrated form of a first order kinetics [20], where y_0, A and τ are coefficients used for the fit and x_0 is a constant. The fitting plot of the ln[Nd]$_t$ shows a straight line with a negative slope as expected for a first order decay (see Supplementary Material, Figure A.22). Thus, the MP of the Nd^{3+} ions at the cathode follows a first order kinetic law with consequent integrated rate law $[\mathrm{Nd}]_t = [\mathrm{Nd}]_0 \exp(-kt)$, where $[\mathrm{Nd}]_t$ is the concentration of the Nd ions left in solution at the time *t*, $[\mathrm{Nd}]_0$ is the initial concentration of the metal ion and *k* is the rate constant of the process.

3.3.9 Evaluation of charge consumption for Nd plating

The quantities of charge (*Q*) effectively consumed in the MP process of Nd from MC solutions were calculated using the results obtained in the previous yield measurements. This can be done on the basis of Faraday's laws on electrolysis, $m = (MQ)/(zF)$, where *m* is the mass of the substance deposited on the electrode, *M* is its molecular mass, *Q* is the quantity of charge associated to the charge carriers which pass through the solution, *z* is the valence of the ions of the substance, and *F* is the Faraday constant (96485 C/mol) [19]. Working at constant current *I*, the total charge passed at a certain time *t* inside the cell is $Q = I \cdot t$. Evaluating *m* from γ-ray spectroscopy, the values of *Q* for Nd plating were calculated as a function of time from 15 up to 180 min. The difference between this charge and the total one is attributed to the electrolysis of solution components other than Nd^{3+}, especially the solvent. Figure 3-12 shows the plots of the calculated charges, in terms of percentages of the total charge, as a function of time. Both curves show exponential trends. It is important to notice that the contribution of the Nd ions to the charge consumption is generally low, from (15.9 ± 0.9)% at the beginning of the process (15 min), to (3.4 ± 1.4)% at the end of the process (180 min).

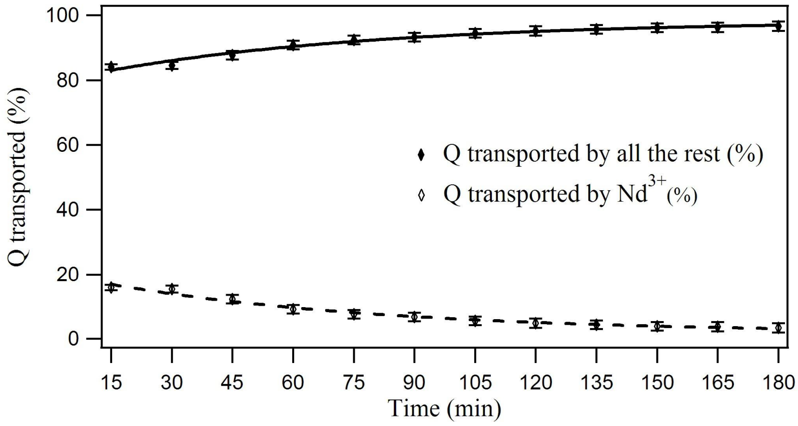

Figure 3-12 Fitting of the percentage charge quantity values for Nd ions (dashed curve), and the percentage charge quantity values for all the other charge carriers inside the cell (solid curve).

3.4 Discussion

The electrolytic solutions used in all the experiments described in Section 3.3 are usually defined as complex electrolytic solutions, i.e., solutions where different ions are contemporarily dissolved. The electrolytes present in our electrolytic solutions, $Nd(NO_3)_3 \cdot 6H_2O$ and HNO_3, are strong electrolytes. Moreover, they are both present in very small concentrations ranging from 0.11 up to 0.44 mM for $Nd(NO_3)_3 \cdot 6H_2O$, and from 0.3 to 0.4 mM for HNO_3. Thus, both the electrolytes inside the solution are reasonably totally dissociated. All the ions deriving from these dissociations contribute, according to their mobility, to the current flow inside the cell. If we consider only the cathode of the system, the XPS results shown in Section 3.3.3 clearly indicate that Nd is present as Nd^{3+} on the layer deposited after molecular plating. In addition, reduction of H^+ originating from HNO_3 and H_2O occurs. This conclusion can be inferred also from the results shown in Section 3.3.6, especially looking at the curves of the Figures 3-10a and c, where it is evident that an increase in HNO_3 concentration (from 0.3 to 0.4 mM) lowers the cell potential trends of the curves and shifts the minima of the curves to lower time values. Moreover, because of the undivided cells used, the oxidation of the Pd anode creates Pd ions which are reduced at the cathode, as proved by the XPS Pd 3d lines (Figure 3-3). Nevertheless, the reduction of these ions does not start at the beginning of the deposition process as follows from the XPS analysis of the 30-min plating time samples, which showed no indication of Pd. Finally, at the very high cell potential values applied during all MPs, electrolysis of the solvent occurs, as suggested by the C 1s spectra recorded via XPS analysis of the deposited surfaces.

The flux J_i of an electroactive species towards an electrode, i.e., the moles of the *i*th species per unit of surface of the electrode and per unit of time, is expressed by the Nernst-Planck equation. For a one-dimensional flux, this is $J_i(x) = -D_i \frac{\partial C_i}{\partial x} - \frac{z_i F}{RT} D_i C_i \frac{\partial \Phi}{\partial x} + C_i v(x)$ [21], where $-D_i \frac{\partial C_i}{\partial x}$ represents the diffusive term, $-\frac{z_i F}{RT} D_i C_i \frac{\partial \Phi}{\partial x}$ the migration term, and $C_i v(x)$ the convective term; D_i, C_i and z_i are the diffusion coefficient, the concentration and charge number of the *i*th species, respectively, Φ the Galvani potential, and v the convective velocity. In a MP experiment, the description of the flux of an electroactive species reaching the cathode involves all three terms. The migration term has to be taken into account because no support electrolyte is present in solution. The convective term has to be considered since the solutions are constantly mixed by ultrasonic stirring.

Once the current has been fixed for a certain constant current density MP, the ionic flux towards an electrode is constant. In a MP cell, where different electroactive species are deposited, the total ionic flux will be the sum of the fluxes of all electroactive ions involved in the plating process. An increase (or decrease) of the concentration of one of the electroactive species inside the cell solution, increases (or decreases) the corresponding flux of its ions towards the cathode, but the total flux stays constant. In the case of the HC, MC and LC experiments performed with both Cells A and B, the flux of Nd ions was then the highest in the HC experiments and the lowest in the LC experiments. This means that a higher Nd^{3+} concentration yields a higher number of Nd^{3+} ions per unit cathode area and unit time. This may explain why HC targets were found to be rougher than both MC and LC targets, as reported in Table 3-4 and shown by the AFM images in Figure 3-2. A higher number of ions reaching the cathode per unit area and unit time will not find place and time to organize themselves in an orderly fashion and hence will promote a disordered layer growth. The opposite will happen with a lower number of ions.

All cell potential curves reported in Section 3.3 show a steep increase for a short time at the very beginning of each deposition process. A likely explanation for such an increase is that constant current density MPs, implying electrolysis, create a high polarization of the electrodes, which causes a change in cell potential inside the electrochemical system and hence a starting increase in all the recorded curves.

The shape of the cell potential curves strongly depends on the concentrations of the electrolytes present in solution. Changing the concentrations of $Nd(NO_3)_3{\cdot}6H_2O$ (LC, MC and HC), and/or HNO_3 (0.3 and 0.4 mM) tends to change not only the cell potential trends (lower cell potential at higher concentrations) but also the time positions of the cell potential minima. It is then evident that there must be a relationship between cell potential and electrolyte concentrations. A simple relationship can be obtained if the cell potential is mainly controlled by the ohmic drop IR, or in other words, if Ohm's first law can be applied to the systems. When a current passes through an electrochemical cell, the overall cell potential is given by the difference between the equilibrium potential of the two semi-reactions occurring at the cathode and anode, plus a series of overpotentials (e.g., activation, concentration, crystallization, etc.) characteristic of the electrode reaction and the ohmic drop due to the solution resistance. If the process occurs in a highly resistive medium (i.e., very low electrolyte concentration and/or low conductivity medium) the ohmic drop may dominate the overall cell potential. This seems to be the case in the systems studied here. In fact, in both Cell A and Cell B the total electrolyte concentration (< 1 mM) was at least two orders of magnitude smaller than those typically used in electrochemical systems. On the other hand, both cells have shown extremely high (500-1000 V) cell potentials, not compatible with the usual overpotential values involved in electrode reactions.

This assumption was checked for both Cell A and Cell B, evaluating the *IR* contribution from the values of the cell resistances *R* and the applied constant currents (Section 3.3.1). In both cases, the calculated *IR* values were close to the experimental cell potentials measured at different $Nd(NO_3)_3 \cdot 6H_2O$ and HNO_3 concentrations, clearly indicating that in all experimental conditions *V* is dominated by the ohmic drop. Since the current is transported by all the ions present in solution, the conductivity depends on the total concentration of the electrolytes. Neglecting all other contributions except *IR*, the cell potential can be easily expressed as $V = j \cdot l \cdot 10^3 \sum_i \frac{1}{\nu_i \cdot c_i \cdot \Lambda_i}$, where *j* is the applied current density, *l* is the distance between the electrodes, and ν_i, c_i and Λ_i are the number of equivalents, concentration and equivalent conductivity of any *i*th electrolyte, respectively. This expression explains why at higher electrolyte concentrations lower cell potential trends are observed (and vice versa). From such an expression, however, it does not yet follow why minima are observed in almost all of the cell potential curves shown in Section 3.3. Nonetheless, it is significant to notice that the yield measurements performed in the experiments with Cell B always showed the different minima of the recorded cell potential curves to correspond to almost complete depletion of Nd^{3+} ions. This result was especially well shown by the MP kinetics derived in Section 3.3.8 and can help to understand why lower time minima were observed with lower Nd salt concentrations, while higher time minima were observed with higher Nd salt concentrations. Specifically, as reported in Table 3-6 and clearly shown in Figure 3-9, HC experiments, characterized by Nd salt concentrations twice as high as in the MC experiments, have time positions of the minima almost twice those of the MC experiments. Conversely, LC experiments, characterized by Nd salt concentrations half those of the MC experiments, have time positions of the minima almost half those of the MC experiments (except for the LC experiments in Cell B where no significant minimum was found). In fact, once a certain constant current has been fixed inside a cell, the depletion kinetics of Nd ions is fixed as well (even if different Nd salt concentrations imply different Nd ion fluxes to the cathode). For this reason, with a double amount of Nd ions, the almost complete depletion of such ions will be reached at times almost the double of the times of the MC experiments. Conversely, with half the amount of Nd ions, almost complete depletion of such ions will be reached at times about half those of the

MC experiments. In the same perspective, if a comparison is made between the experiments realized with Cell A and Cell B where the current density was the same, but the applied constant currents were different, it can be explained why the time positions of the minima of the cell potential curves recorded with Cell A are always higher than those recorded with Cell B. A lower constant current (2 mA, Cell A) will imply a slower depletion kinetics of the Nd ions, while a higher constant current (6 mA, Cell B) will imply a faster depletion kinetics of the same ions.

All cell potential curves recorded during constant current density MPs realized with Cell A and Cell B also proved to have shapes strongly influenced by the surface roughness of the electrodes, as shown by the different behaviours of the curves recorded using different cathodes. Deposition substrates with different surface roughness were indeed used in all MPs realized with both Cells A and B. In the experiments performed using Cell A, where Ti1 and Ti2 foils had similar surface roughness, no differences in the cell potential curve behaviours were noted among all curves recorded at the different Nd salt concentrations (HC, MC and LC). In the experiments performed using Cell B, instead, the foils Ti3, Ti4, and Ti5 had different surface roughness. No significant differences in cell potential behaviour were noted for the LC, MC and HC cell potential curves recorded using Ti3 and Ti5 foils. The main difference was instead shown by the curves recorded using Ti4 foils: all these curves, in fact, showed a lower cell potential trend at each of the Nd salt concentrations. This fact can be explained considering the expression for the cell resistance, i.e., $R = \rho \cdot l/S$, where l/S is the inverse of the cell constant. With smooth electrodes like Ti1, Ti2, Ti3, and Ti5 the exposed surface area, i.e., the real surface, is not significantly different from the geometric surface. Instead, in the case of highly rough surfaces like Ti4 (see Table 3-2), the real surface area is much larger than the geometric one. This causes the cell constant (S/l) to increase and the solution resistance ($R=\rho\cdot l/S$) to decrease, resulting in a decrease of the cell potential, according to Ohm’s first law.

3.5 Conclusion

In order to understand and improve the molecular plating technique for the production of targets to be applied in nuclear science, several constant current density MPs were performed using Nd as model element. The variables chosen for these investigations were: concentration of the electrolytes, applied current, and surface roughness of the deposition substrates. The influence of changes in these variables on the deposition processes was monitored recording cell potential vs time, and the obtained deposits were analyzed using γ-ray spectroscopy, XPS, and AFM.

In the complex electrolytic solutions used to perform the MPs, the electroactive species involved in the cathodic processes were Nd^{3+} and H^+ ions deriving from the dissociations of the starting strong electrolytes. Additional electroactive species were proved to be Pd ions from the oxidation of the Pd anode, as well as the electrolyzed mixed solvent. Noteworthy, XPS results clearly show that, after MP, Nd is deposited on the cathodic surface as derivatives of Nd^{3+}, possibly as carboxylate, oxide or hydroxide. This important outcome, that elucidates the fate of Nd^{3+} after MP, is reasonable on the basis of the high negative value of the Nd^{3+}/Nd standard redox potential ($E° = -2.323$ V), typical of lanthanide cations [22].

The cell potentials in the investigated systems were found to be mainly affected by the solution resistance. An expression which relates cell potential with conductance and hence electrolyte concentration was therefore derived. This approach allows for explaining the cell potential trends recorded using different concentrations of the electrolytes. We notice that the performed yield measurements always showed an almost complete depletion of the Nd ions at the minima of the different cell potential curves. This result was especially well shown by the derived first order kinetics of the MP. According to these experimental results, reasonable explanations were given to the recorded trends of the cell potential curves when different Nd salt concentrations and different currents are applied during the investigated MPs. However, our derived expression is not sufficient to fully interpret the reasons leading to the minima in the cell potential curves.

The trends of the cell potential curves were found to be also influenced by the roughness of the deposition substrates, because this implies different cell constants. Moreover, the roughness of the starting substrates, together with the initial concentration of the electrolyte to be plated, proved to strongly influence the final surface roughness of the MP-grown layers.

Our work, which exploits a variety of analytical techniques and combines this with a theoretical approach on the MP process, has yielded a better understanding of important basic features of constant current density MP.

Acknowledgements

The authors would like to thank the staff of the TRIGA Mainz for performing the irradiations, the GSI target laboratory for providing the ADVENT and LEBOW Ti foils, and Dr. T. Lauer for performing the coating of the Si wafers. A. Vascon would like to thank Fu-Kai Chang from the Institute of Mathematics of Mainz University for the fruitful discussions had together. Moreover A. Vascon would like to acknowledge financial support from the German Federal Ministry of Science and Education (BMBF) under Contract number 02NUK013E.

3.6 Appendix A. Supplementary Material

Figure Captions:

Figure A.1 C 1s XPS spectrum of a Ti 3 foil, inserted into the glove-box, cleaned with HCl, H_2O and isopropanol, immersed into an isopropanol/isobutanol solution and then dried.

Figure A.2 XPS spectra of the washed and air-dried Pd foil: Pd 3d before sputtering (indicated as 0 min sputtering in the figure), and after 10 min sputtering with Ar^+ ions.

Figure A.3 XPS spectra of the washed and air-dried Pd foil: C 1s before sputtering (indicated as 0 min sputtering in the figure), and after 10 min sputtering with Ar^+ ions.

Figure A.4 Voltage vs Time curves recorded as reproducicility tests in the MC Nd salt MPs realized using Ti1 foils. The minimum of the curves is indicated by a vertical dashed blue line.

Figure A.5 Voltage vs Time curves recorded as reproducicility tests in the MC Nd salt MPs realized using Ti2 foils. The minimum of the curves is indicated by a vertical dashed blue line.

Figure A.6 Voltage vs Time curves recorded as reproducicility tests in the HC Nd salt MPs realized using Ti1 foils.

Figure A.7 Voltage vs Time curves recorded as reproducicility tests in the HC Nd salt MPs realized using Ti2 foils.

Figure A.8 Voltage vs Time curves recorded as reproducicility tests in the LC Nd salt MPs realized using Ti1 foils. The minimum of the curves is indicated by a vertical dashed blue line.

Figure A.9 Voltage vs Time curves recorded as reproducicility tests in the LC Nd salt MPs realized using Ti2 foils. The minimum of the curves is indicated by a vertical dashed blue line.

Figure A.10 Voltage vs Time curves recorded as reproducility tests in the MC Nd salt MPs realized using Ti3 foils. The minimum of the curves is indicated by a vertical dashed blue line.

Figure A.11 Voltage vs Time curves recorded as reproducility tests in the MC Nd salt MPs realized using Ti4 foils. The minimum of the curves is indicated by a vertical dashed blue line.

Figure A.12 Voltage vs Time curves recorded as reproducility tests in the MC Nd salt MPs realized using Ti5 foils. The minimum of the curves is indicated by a vertical dashed blue line.

Figure A.13 Voltage vs Time curves recorded as reproducility tests in the HC Nd salt MPs realized using Ti3 foils. The minimum of the curves is indicated by a vertical dashed blue line.

Figure A.14 Voltage vs Time curves recorded as reproducility tests in the HC Nd salt MPs realized using Ti4 foils. The minimum of the curves is indicated by a vertical dashed blue line.

Figure A.15 Voltage vs Time curves recorded as reproducility tests in the HC Nd salt MPs realized using Ti5 foils. The minimum of the curves is indicated by a vertical dashed blue line.

Figure A.16 Voltage vs Time curves recorded as reproducility tests in the LC Nd salt MPs realized using Ti3 foils.

Figure A.17 Voltage vs Time curves recorded as reproducility tests in the LC Nd salt MPs realized using Ti4 foils.

Figure A.18 Voltage vs Time curves recorded as reproducility tests in the LC Nd salt MPs realized using Ti5 foils.

Figure A.19 comparisons between Ti3 cell potential curves recorded using active and inactive MC Nd salt solutions.

Figure A.20 comparisons between Ti3 cell potential curves recorded using active and inactive HC Nd salt solutions.

Figure A.21 comparisons between Ti3 cell potential curves recorded using active and inactive LC Nd salt solutions.

Figure A.22 $\ln[\mathrm{Nd}]_t$ values against time (dashed black line).

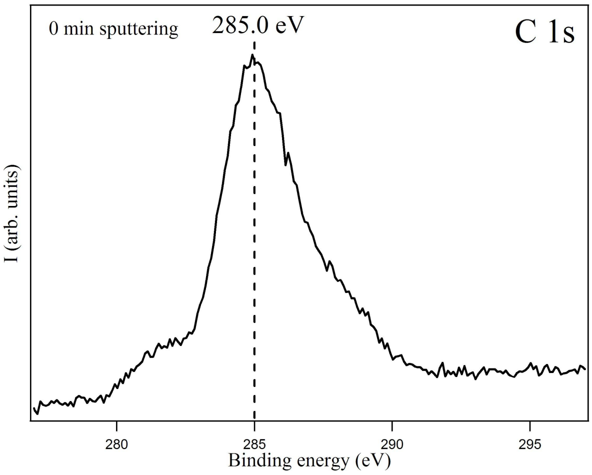

Figure A.1

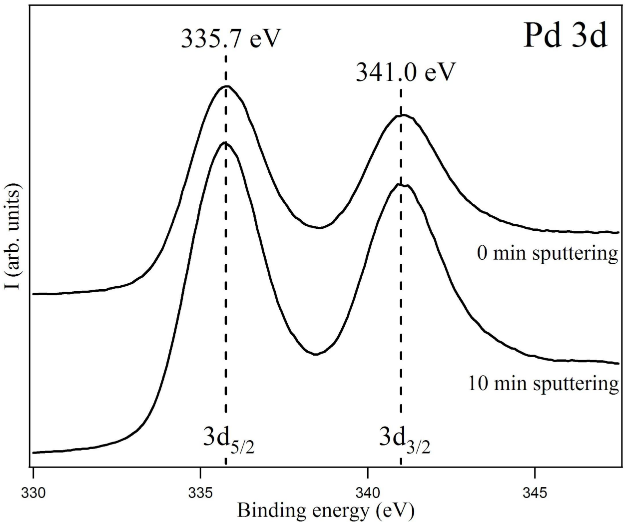

Figure A.2

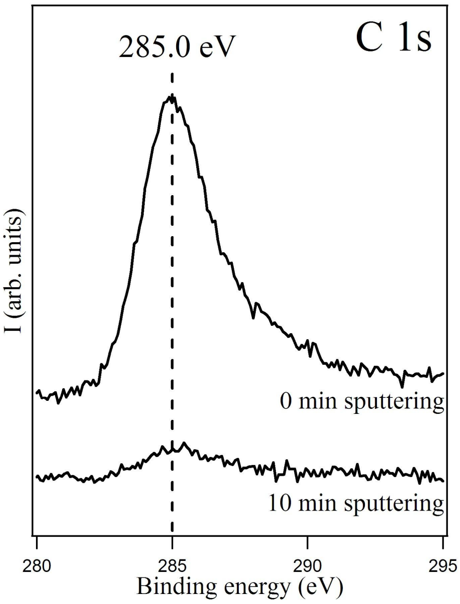

Figure A.3

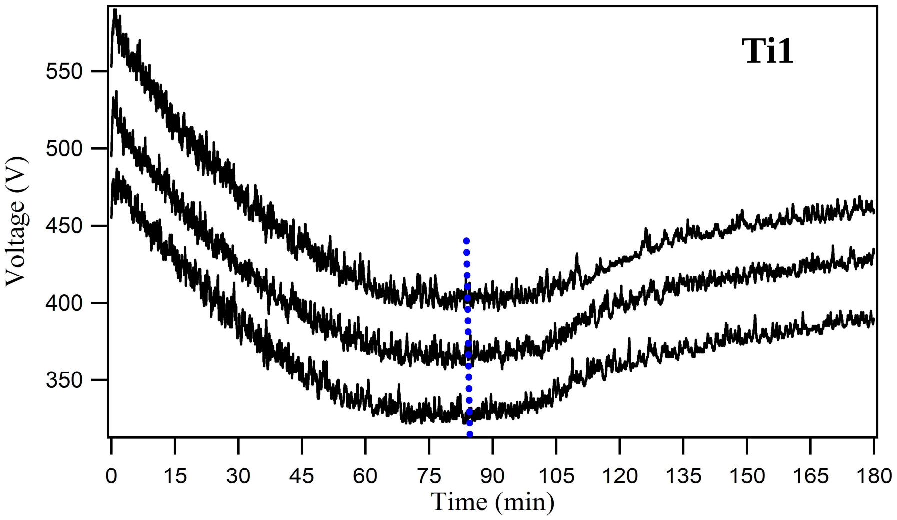

Figure A.4

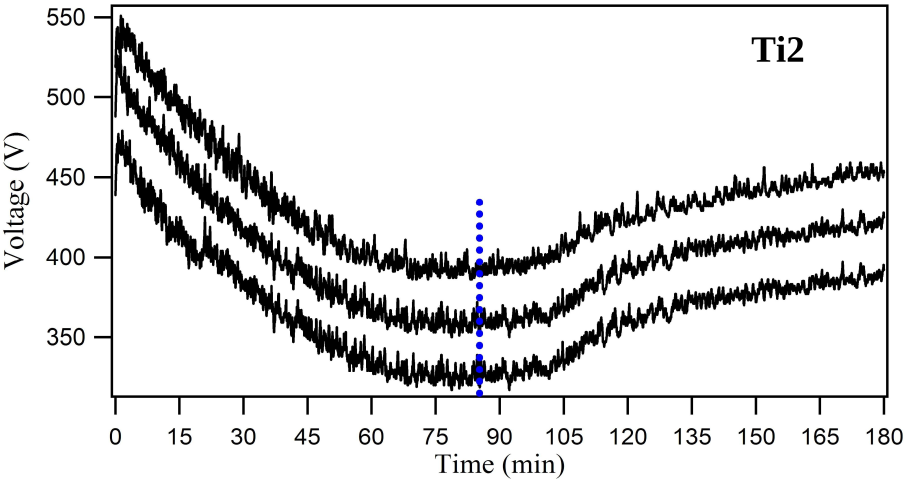

Figure A.5

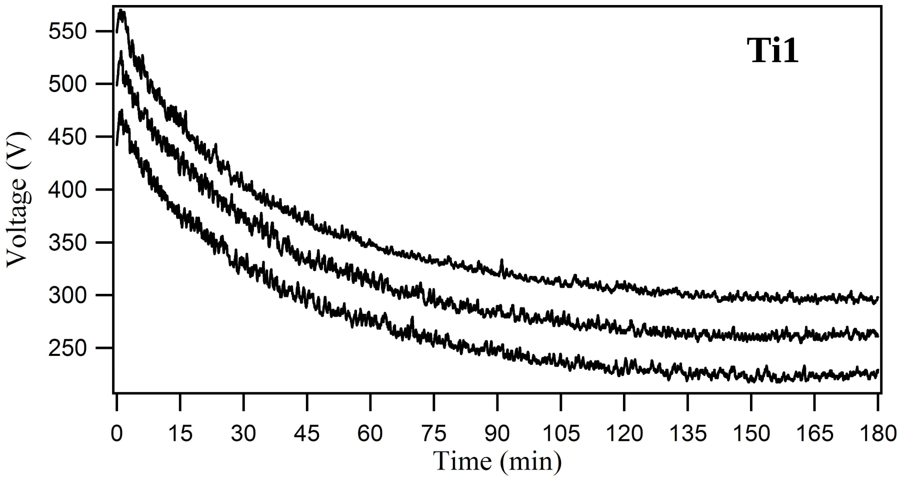

Figure A.6

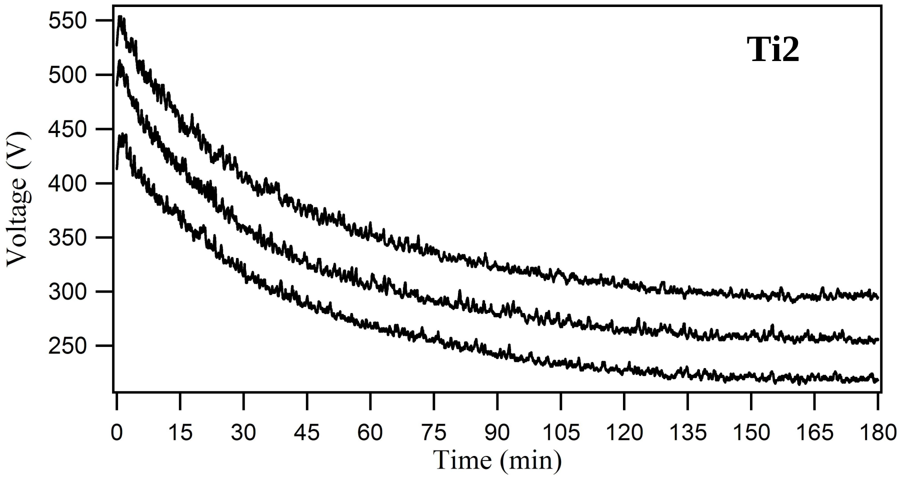

Figure A.7

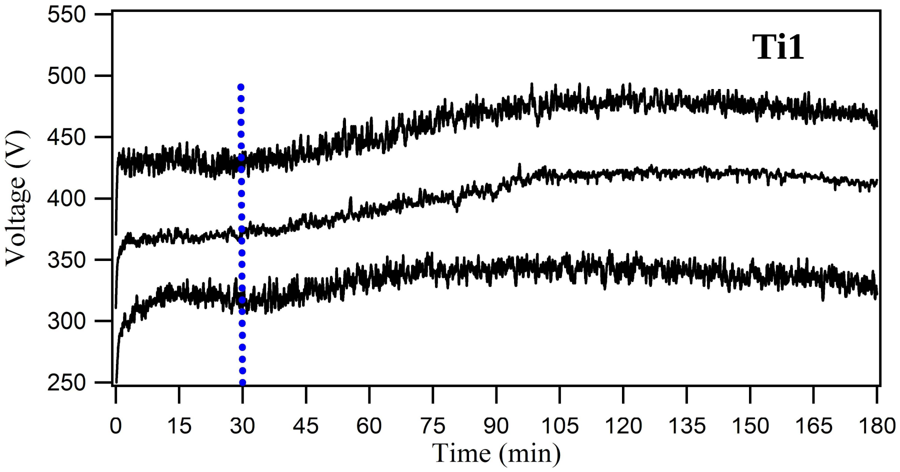

Figure A.8

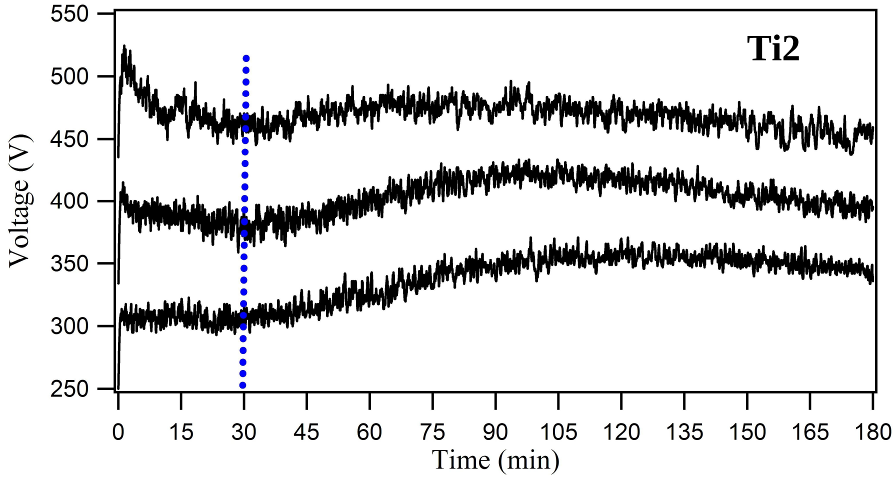

Figure A.9

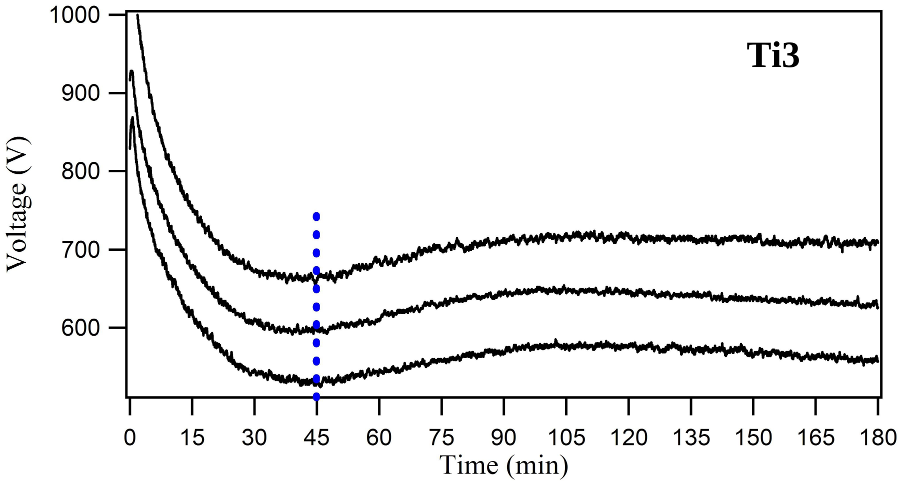

Figure A.10

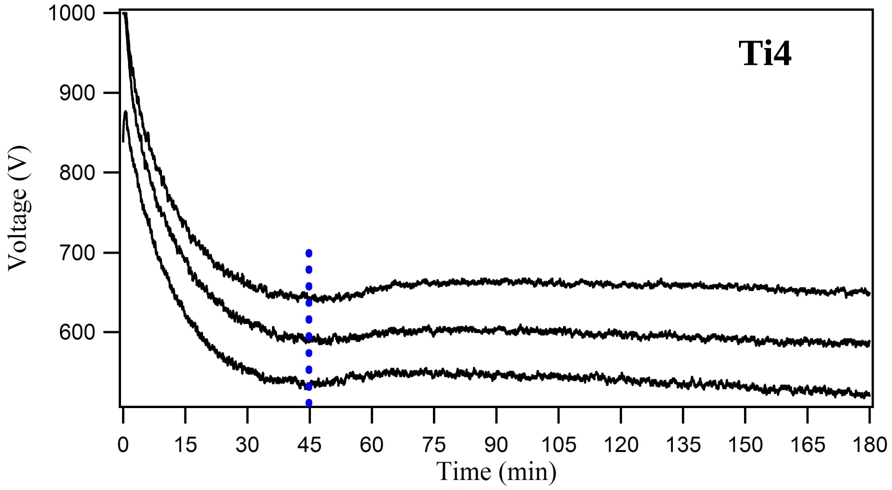

Figure A.11

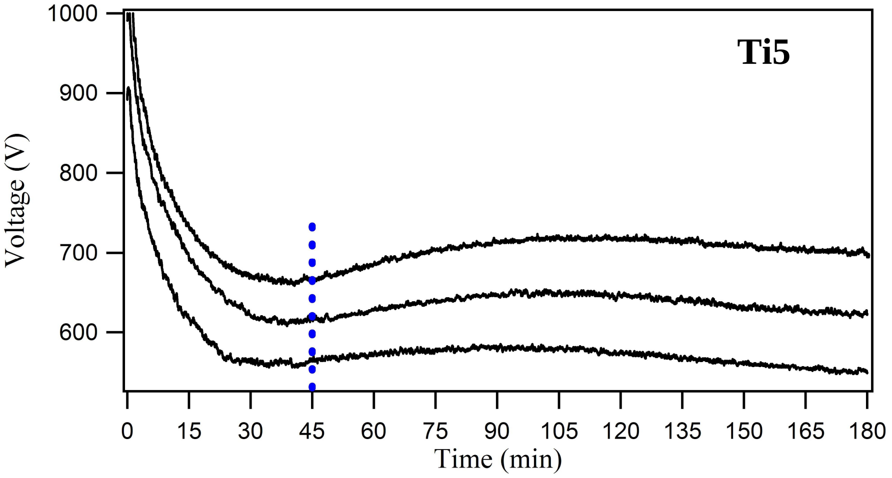

Figure A.12

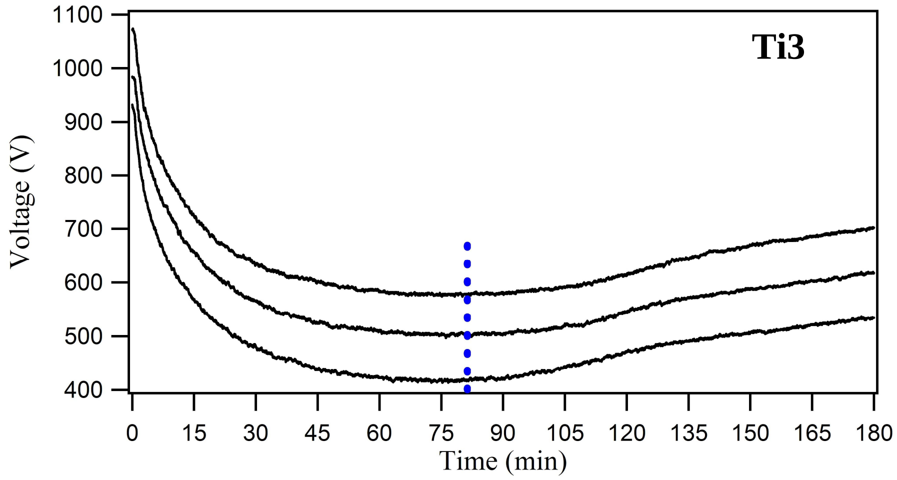

Figure A.13

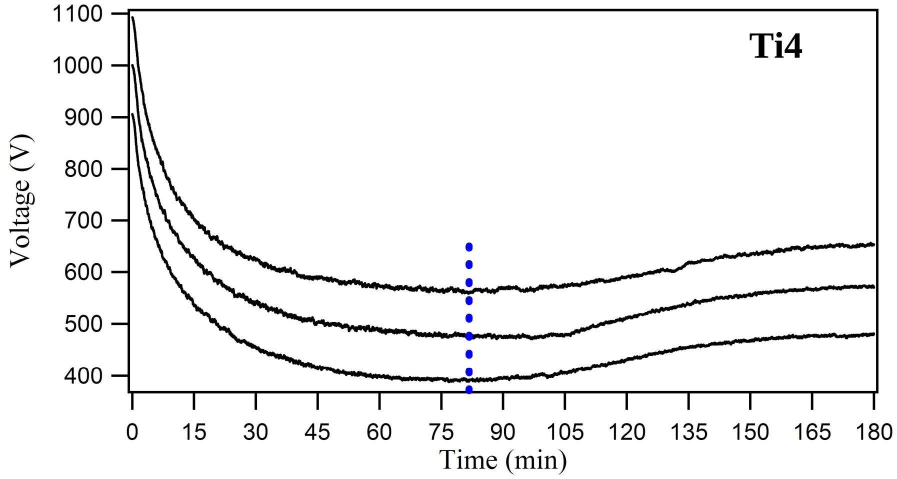

Figure A.14

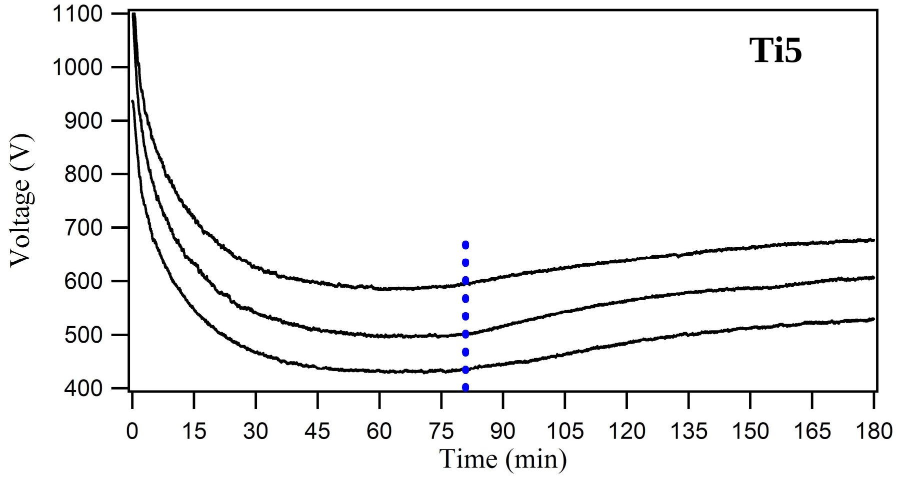

Figure A.15

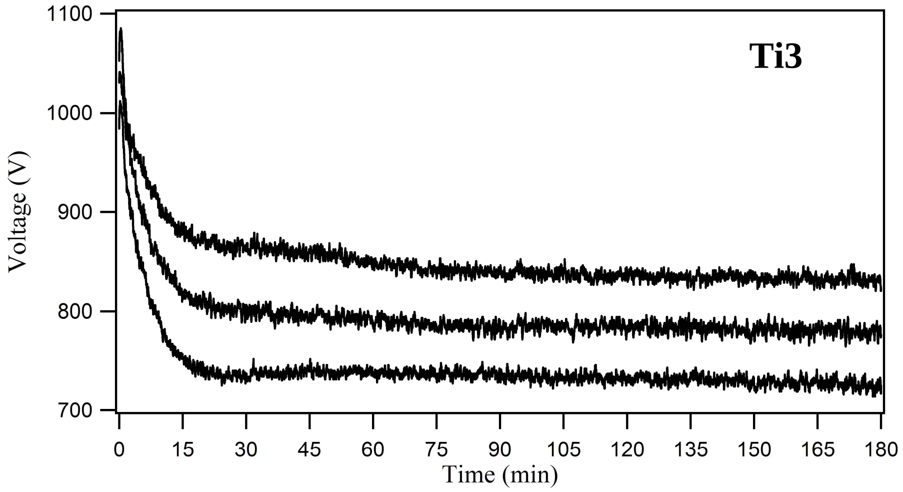

Figure A.16

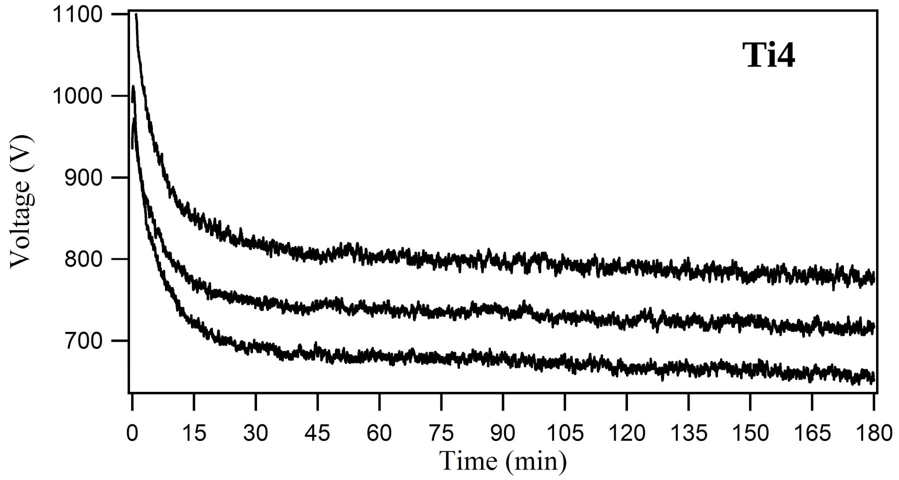

Figure A.17

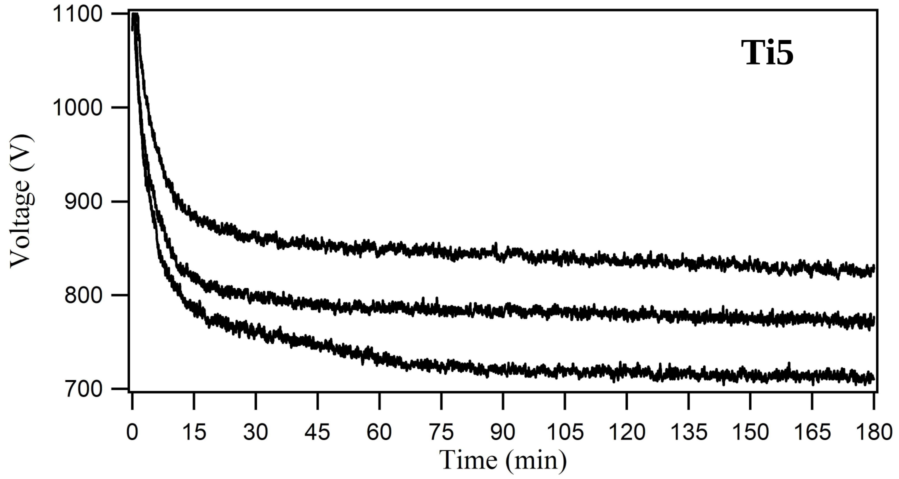

Figure A.18

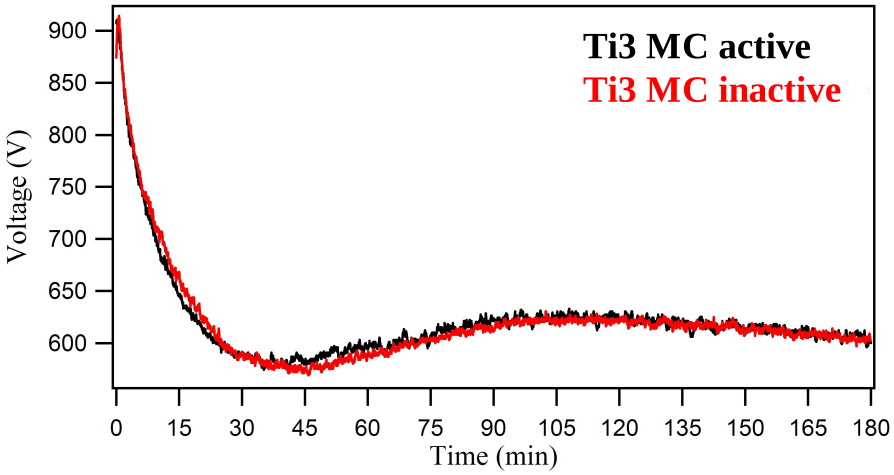

Figure A.19

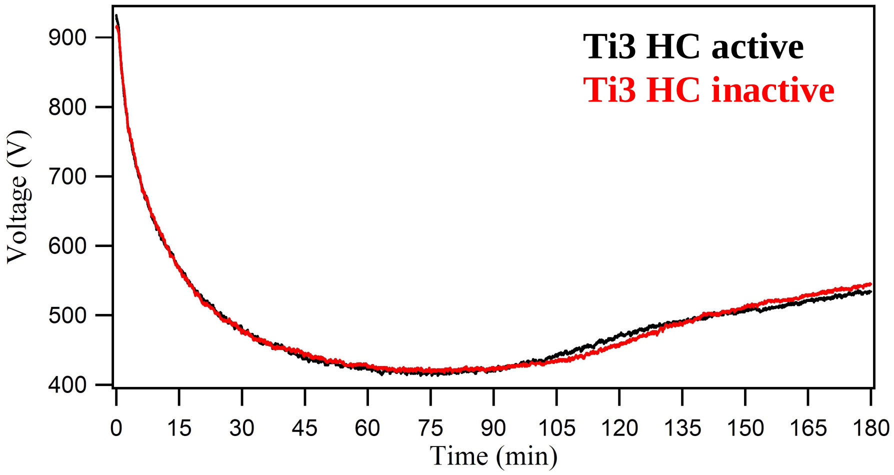

Figure A.20

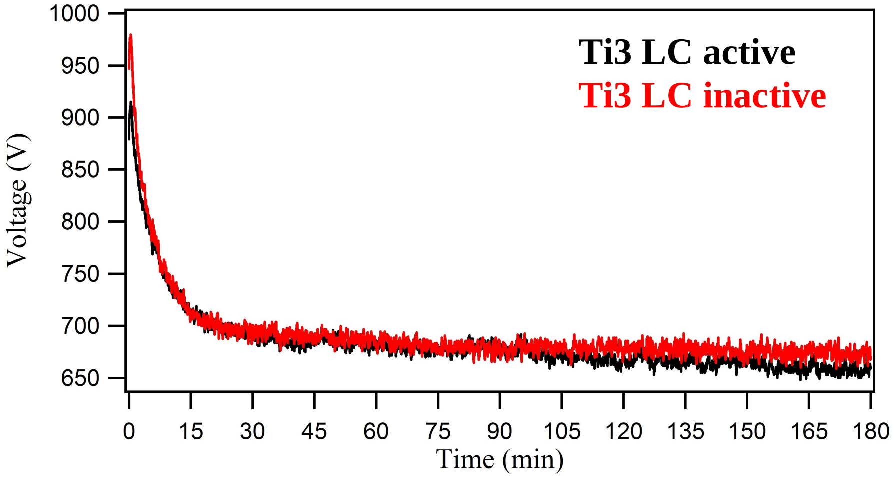

Figure A.21

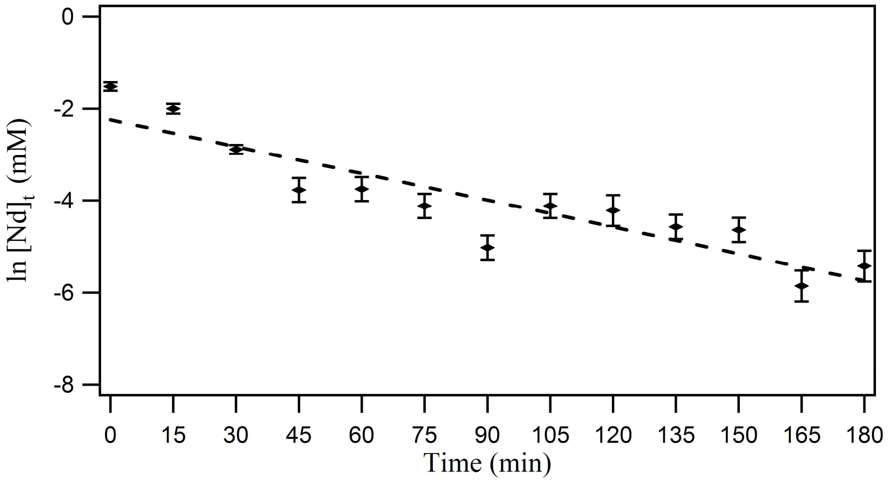
0
-2
-4
-6
-8
ln [Nd]$_t$ (mM)
0
15
30
45
60
75
90
105
120
135
150
165
180
Time (min)

Figure A.22

References

[1] W. Parker, R. Falk, Nucl. Instrum. Methods **16** (1962) 355-357.

[2] W. Parker, H. Bildstein, N. Getoff, Nucl. Instrum. Methods **26** (1964) 55-60.

[3] W. Parker, H. Bildstein, N. Getoff, H. Fischer-Colbrie, H. Regal, Nucl. Instrum. Methods **26** (1964) 61-65.

[4] W. Parker, H. Bildstein, N. Getoff, Nucl. Instrum. Methods **26** (1964) 314-316.

[5] N. Getoff, H. Bildstein, Nucl. Instrum. Methods **36** (1965) 173-175.

[6] N. Getoff, H. Bildstein, Nucl. Instrum. Methods **70** (1969) 352-354.

[7] A. Becerril-Vilchis, A. Cortès, F. Dayras, J. De Sanoit, Nucl. Instrum. Meth. A **369** (1996) 613-616.

[8] N. Trautmann, H. Folger, Nucl. Instrum. Meth. A **282** (1989) 102-106.

[9] B.W. Filippone, M. Wahlgren, Nucl. Instrum. Meth. A **243** (1986) 41-44.

[10] J.E. Evans, R.W. Lougheed, M.S. Coops, R.W. Hoff, E.K. Hulet, Nucl. Instrum. Methods **102** (1972) 389-401.

[11] K. Eberhardt, W. Brüchle, Ch.E. Düllmann, K.E. Gregorich, W. Hartmann, A. Hübner, E. Jäger, B. Kindler, J.V. Kratz, D. Liebe, B. Lommel, H.-J. Maier, M. Schädel, B. Schausten, E. Schimpf, A. Semchenkov, J. Steiner, J. Szerypo, P. Thörle, A. Türler, A. Yakushev, Nucl. Instrum. Meth. A **590** (2008) 134-140.

[12] S. Sadi, A. Paulenova, P.R. Watson, W. Loveland, Nucl. Instrum. Meth. A **655** (2011) 80-84.

[13] P.R. Watson, W. Loveland, P.M. Zielinski, K.E. Gregorich, H. Nitsche, Nucl. Instrum. Meth. B **226** (2004) 543-548.

[14] Q.X. Jia, T.M. McCleskey, A.K. Burrell, Y. Lin, G.E. Collis, H.Wang, A.D.Q. Li, S.R. Foltyn, Nat. Mater. **3** (2004) 529-532.

[15] M.A. Garcia, M.N. Ali, T. Parsons-Moss, P.D. Ashby, H. Nitsche, Thin Soild Films, **516** (2008) 6261-6265.

[16] A. Vascon, Ch.E. Düllmann, K. Eberhardt, B. Kindler, B. Lommel, J. Runke, Nucl. Instrum. Meth. A **655** (2011) 72-79.

[17] H. Haba, D. Kaji, T. Takabe, H. Kikunaga, RIKEN, Accel. Prog. Rep. **39** (2006) 109.

[18] C.D. Wagner, W.M. Riggs, L.E. Davis, J.F. Moulder, G.E. Muilenberg, Handbook of X-Ray Photoelectron Spectroscopy, Perkin-Elmer Corporation, Physical Electronics Division, Eden Prairie, Minn. 55344 (1979).

[19] S. Glasstone, An Introduction to Eletrochemistry, first ed., Litton Educational Publishing, Inc., New York, 1942.

[20] K. J. Laidler, Chemical Kinetics, third ed., Prentice Hall, New York, 1987.

[21] P. Atkins, J. De Paula, Atkins' Physical Chemistry, seventh ed., Oxford University Press, Oxford, 2002.

[22] CRC Handbook of Chemistry and Physics, 87th ed., D. R. Lide Ed., 2006.

4. Fundamental aspects of molecular plating and production of smooth crack-free Nd targets

A. Vascon[1], S. Santi[2], A.A. Isse[2], T. Reich[1], J. Drebert[1], H. Christ[3], K. Eberhardt[1,5], Ch.E. Düllmann[1,4,5]

[1]Institute of Nuclear Chemistry, Johannes Gutenberg University Mainz, 55099 Mainz, Germany
[2]Department of Chemical Sciences, University of Padova, 35131 Padova, Italy
[3]Institute of Physical Chemistry, Johannes Gutenberg University Mainz, 55099 Mainz, Germany
[4]SHE Chemistry Department, GSI Helmholtzzentrum für Schwerionenforschung GmbH, 64291 Darmstadt, Germany
[5]SHE Chemistry Research Section, Helmholtz Institute Mainz, 55099 Mainz, Germany

Accepted for publication in:

Journal of Radioanalytical and Nuclear Chemistry (2012).

This paper is a contribution to the proceedings of the 26th World Conference of the International Nuclear Target Development Society (INTDS), held August 19-24, 2012, in Mainz, Germany.

Abstract

A general understanding of the molecular plating process was obtained recently, which serves as a first step towards further improvements of the method aiming, for example, at the production of smooth, crack-free targets for nuclear physics applications. Constant current density electrolysis experiments were performed in organic media containing the model electrolyte [$Nd(NO_3)_3 \cdot 6H_2O$]. The process was investigated by considering influences of the electrolyte concentration (0.11, 0.22, 0.44 mM), the surface roughness of the deposition substrates (a few tens of nm), and the plating solvent (an isopropanol/isobutanol mixture, and N,N-dimethylformamide). The response of the process to changes of these parameters was monitored by recording cell potential curves and by characterizing the obtained deposits with γ-ray spectroscopy, X-ray photoelectron spectroscopy, and atomic force microscopy. By changing the solvent from isopropanol/isobutanol mixtures to N,N-dimethylformamide, we have succeeded in producing smooth, crack-free Nd targets.

Keywords: thin layers, neodymium, molecular plating, γ-ray spectroscopy, X-ray photoelectron spectroscopy (XPS), atomic force microscopy (AFM)

4.1 Introduction

Molecular Plating (MP) is one of the most widely applied methods for the production of thin layers to be used as sources of stationary nuclei, i.e., targets, for accelerator and reactor science. The term of molecular plating was coined by Parker and Falk [1] to denote either a constant current or a constant voltage electrodeposition in an organic medium. The method is well-known to quickly produce deposits of acceptable uniformity and adherence with quantitative yield [2,3]. Despite the wide use of MP, few are the attempts reported where a microscopic characterization of the layers was performed [4,5], investigating for example the common effect of cracking of the produced surfaces [6]. Moreover, an exhaustive elucidation of even some main features of the process is still largely lacking. To date, the focus of MP experiments has almost exlusively been on empirically improving the produced layers. In this situation we have chosen a systematic approach, studying basic features of MP with the aim of reducing the knowledge gap between MP and well established electrochemical methods, and to exploit the better insight to further increase the efficiency of the method and to improve the obtained targets. An extensive investigation of the molecular plating process was hence carried out by performing constant current density electrolysis experiments in organic media, where a neodymium salt was used as a model electrolyte [7]. Electrolyte concentration and surface roughness of the deposition substrates were varied to investigate the process. In addition, we report here on experiments where the solvent was changed from isopropanol/isobutanol mixtures to N,N-dimethylformamide (DMF). Cell potential curves were recorded to monitor the response of the process to the variables and a theoretical description of important basic features of constant current density MP was formulated. Several analytical techniques were applied to characterize the produced layers and the results were used to define the best parameters to produce smooth and crack-free Nd targets. A full account of our studies including further MPs under conditions not described in this article can be found in [7]. Here, we rather present some of the most interesting aspects of this work and give new results on experiments in DMF. These will be presented in more detail in a forthcoming publication [8].

4.2 Experimental

4.2.1 Target production

All constant current density MPs were performed in a cell (see Figure 3-1 in [7]) characterized by a central polyether ether ketone (PEEK) body where the electrolytic solution was inserted. The Ti anode of the cell was covered by a circular Pd foil, and the Ti cathode by a circular Ti foil. The Pd anode and Ti cathode had an area of 9 cm^2, and they were in physical contact with water-cooled Ti blocks used to maintain a constant temperature (T = 16 °C). Two different Ti foils, hereafter called Ti-A and Ti-B, were used as backing material for the MPs. These foils had different surface roughnesses, which, after the cleaning procedure, were: 24 ± 7 nm for Ti-A, and 12.8 ± 0.7 nm for Ti-B. Ti-A was a circular 50 µm-thick Ti foil cut from a bigger foil (Goodfellow). Ti-B was produced by coating a 300-µm thick mechanically-polished Si wafer onto which 100 nm of metallic Ti were sputtered. For more details about the MP cell and the deposition substrates we refer to [7].

Before any deposition, both the Pd anode and the cathode (Ti foils) were cleaned with 6 M HCl, water, and isopropanol. For the MPs, solutions with three different concentrations were prepared dissolving increasing amounts of $Nd(NO_3)_3 \cdot 6H_2O$ in 0.1 M HNO_3. From each solution an aliquot of 100 µL was added to a mixture of 1 mL isopropanol (Fisher Chemical) and 34 mL isobutanol (Applichem), or to 35 mL of N,N-dimethylformamide -DMF- (Merck), finally obtaining three different solutions of Nd^{3+} in both solvents. These solutions are referred to as low concentration (LC, 0.11 mM), medium concentration (MC, 0.22 mM) and high concentration (HC, 0.44 mM). Inside the cell the concentration of HNO_3 was 0.3 mM and the solutions were stirred by means of a quartz tip ultrasonic stirrer (Bandelin Sonopuls HD 2070) operated at 30% power pulse, which was previously shown to be as efficient as mechanical stirring [6]. MP experiments were carried out for 3 hours by applying a constant current of 6 mA. The current density was 0.7 mA/cm^2.

4.2.2 Target characterization

The surface roughness of the deposited layers, i.e., the measure of the texture of a surface quantified by the vertical deviations of a real surface from its ideal planar form, was investigated by using Atomic Force Microscopy (AFM) (MFP 3D Asylum Research). AFM investigations were performed in air and in liquid.

The AFM analysis was the same for all the produced targets: (5 × 5) μm^2 and (25 × 25) μm^2 images were recorded for each target and (1.5 × 1.5) μm^2 masks were used to evaluate root mean square (RMS) values in different positions inside the images. For those samples which showed surfaces with cracks, the RMS values were evaluated using masks only in the crack-free areas, as the cracks do not belong to the surface and hence do not define the real roughness of the deposited layers. The final surface roughness value of each of the image sizes was evaluated as the arithmetic mean of all the RMS values (i.e., $\overline{\mathrm{RMS}}$). More details about the AFM analysis can be found in [7].

A chemical surface characterization of a Ti-A sample after an isobutanol/isopropanol MC experiment was performed using X-ray Photoelectron Spectroscopy (XPS). Al K_α and Mg K_α radiations were employed. The X-ray source was operated at a 10 kV anode voltage and a current of 10 mA. The pass-energy of the hemispherical energy analyzer was 50 eV. The pressure inside the ultra-high vacuum chamber was in the range of (1.2-2.0)$\cdot 10^{-9}$ mbar. At the end of the deposition time, the cell was top-sealed and inserted into a glove-box, where an inert environment was assured by a constant Ar pressure (0.5 mbar, O_2 < 1 ppm, H_2O < 1 ppm). The solvent was extracted from the cell and the sample dried. Drying in an inert environment allowed performing a chemical surface analysis with unaltered products of reduction and oxidation obtained during the plating process. After the first surface investigation, the sample underwent two ten-minute sputtering cycles using 4 kV Ar^+ ions. After each ten-minute sputtering cycle, the surface of the sample was analyzed by XPS. By fitting the XPS spectra, the binding energies of the XPS lines of interest were determined. The experimental uncertainty of the binding energies is ± 0.1 eV.

The deposition yield of the MP process was determined via γ-ray spectroscopy (GEM series HPGe Detector Model No. GEM 23158 P-Plus, ORTEC Company). This technique was used after MP of Nd solution containing radioactive ^{147}Nd tracer. For this, an aliquot of 100 μL of the stock solution was irradiated with thermal neutrons in the TRIGA research reactor at the Institute of Nuclear Chemistry at the University of Mainz; the irradiation produced a solution that contained a radioactive tracer of the element to be plated (Nd: ^{147}Nd, β^-, $t_{1/2}$ = 10.98 d, E_γ = 91 keV). To obtain quantitative data, reference sources with known amounts of the tracer were prepared. Absolute yields were evaluated at different times of interest as the average value calculated from three distinct γ-ray measurements.

4.3 Results and discussion

MPs on Ti-A and Ti-B foils were performed using isopropanol/isobutanol solutions containing 0.22 mM Nd salt (MC) and applying a current density of 0.7 mA/cm^2 for three hours. Despite the different surface roughness of the two deposition substrates, the obtained cell potential curves display a similar behaviour (Figure 4-1a): after an initial increase within the first few minutes, the cell potential decreases within 45 min (dashed line), and then increases to a maximum value. The maximum is not very pronounced but forms a wide plateau, ranging from around 90 min to 120 min, with the highest value located at around 110 min. After the maximum, the two cell potential curves tend to slightly decrease with time. The cell potentials display again similar behaviour during MP in 0.44 mM Nd salt solutions (HC) (Figure 4-1b): after the initial increase (zoom in Figure 4-1b), the cell potential strongly decreases within 80 min (dashed line) and then slightly increases. Similar behaviour of the cell potential profiles was also recorded during the molecular plating with 0.11 mM Nd salt solutions (LC): after the initial increase, the cell potential decreases exponentially within 20 min (no minimum is present), and then decreases almost linearly with time (Figure 4-1c).

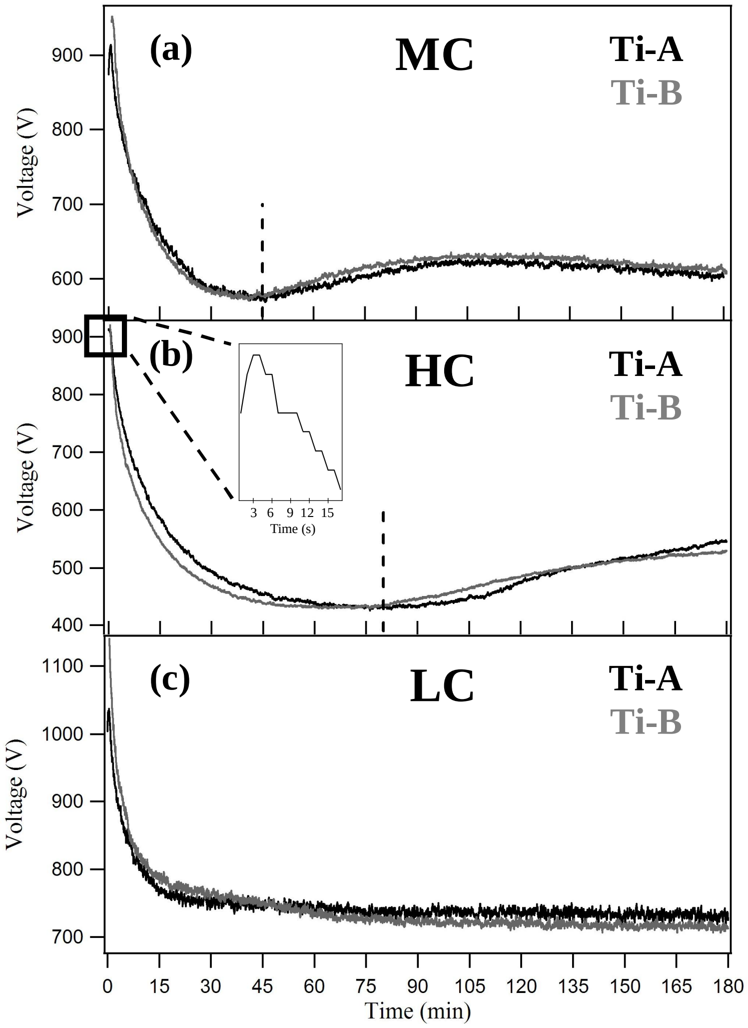

Figure 4-1 Cell potential *vs.* time curves recorded for the molecular platings performed with: (a) medium concentration [MC], (b) high concentration [HC] and (c) low concentration [LC] Nd salt in isopropanol/isobutanol mixture. Ti-A and Ti-B foils were used. No offsets were applied between the curves.

By comparing the curves recorded at different concentrations of Nd salt, it can be noticed that the cell potential profile is very sensitive to the Nd^{3+} concentration. It is then evident that there must be a relationship between cell potential and electrolyte concentration, as both cell potential trends (lower cell potential at higher concentrations) and time positions of the cell potential minima are changed by the different Nd^{3+} concentrations. A simple relationship can be obtained if the cell potential is mainly controlled by Ohm's first law, $V = IR$. The validity of this approach was verified by cell resistance measurements, which are described in detail in [7]. Neglecting all other contributions except *IR*, the cell potential can then be easily expressed as $V = j \cdot l \cdot 10^3 \sum_i \frac{1}{\nu_i \cdot c_i \cdot \Lambda_i}$, where *j* is the applied current density, *l* is the distance between the electrodes, and ν_i, c_i

and Λ_i are the number of equivalents, concentration and equivalent conductivity of any *i*th electrolyte, respectively. This expression explains why at higher electrolyte concentrations lower cell potential trends are observed (and vice versa), but it does not explain why minima are observed in almost all of the recorded cell potential curves. Nonetheless, the yield measurements performed via γ-ray spectroscopy always showed the different minima of the recorded cell potential curves to correspond to an already very advanced depletion of Nd^{3+} ions (see Table 4-1). Deposition yields approaching 100% were recorded after 3h deposition times. We refer to [7] for a more exhaustive elucidation of the electrochemistry of constant current density MP.

Table 4-1 Average deposition yield values measured at different times for the MC, HC, and LC Nd salt experiments using Ti-A, and Ti-B foils.

Experiment	Time (min)	Ti-A yield value (%)	Ti-B yield value (%)
MC	45	83.7 ± 2.2	71 ± 3
	180	95.6 ± 2.7	98.7 ± 0.8
HC	80	87 ± 3	84.5 ± 2.0
	180	97 ± 4	95 ± 5
LC	20	66 ± 3	71 ± 6
	180	99.1 ± 0.9	98.1 ± 0.9

A XPS analysis of a deposit obtained on the Ti-A cathode after 3 h MP from MC solution showed the presence of the following elements: C, O, Pd, and Nd. The corresponding XPS signals were: C 1s, O 1s, Pd 3d, Nd 3d, and Nd 4d. Pd signals derive from the oxidation of the Pd anode during MP. Ti signals were not detected, indicating that the deposited layer is thick. Nd 3d spectra were recorded using a Mg K_α radiation to avoid the interference of oxygen Auger lines present in the same binding energy region. Figure 4-2 shows the spectra of Nd 3d (a), and C 1s (b) before sputtering and after 10 min and 20 min sputtering with Ar^+ ions.

The measured binding energy of Nd $3d_{5/2}$ in the surface layer is 982.6 eV (Figure 4-2a) and can be compared to the literature value of 983.1 eV [9] for Nd^{3+}. This indicates that Nd is not reduced during MP, but rather maintained as Nd^{3+}, and deposited in the layer possibly as carboxylate, oxide, or hydroxide. This outcome is reasonable on the basis of the high negative value of the Nd^{3+}/Nd standard redox potential ($E° = -2.323$ V), typical of lanthanide cations [10].

The C 1s spectra reported in Figure 4-2b show the presence of two components: the C 1s peak at 285.0 eV is aliphatic carbon of the mixed isopropanol/isobutanol solvent. The peak at 289.3 eV can be attributed, according to literature, to COOM -metal carboxylate- (289.0 eV [9]) groups formed during the plating process. We conclude that the solvent undergoes electrolysis during the MP process.

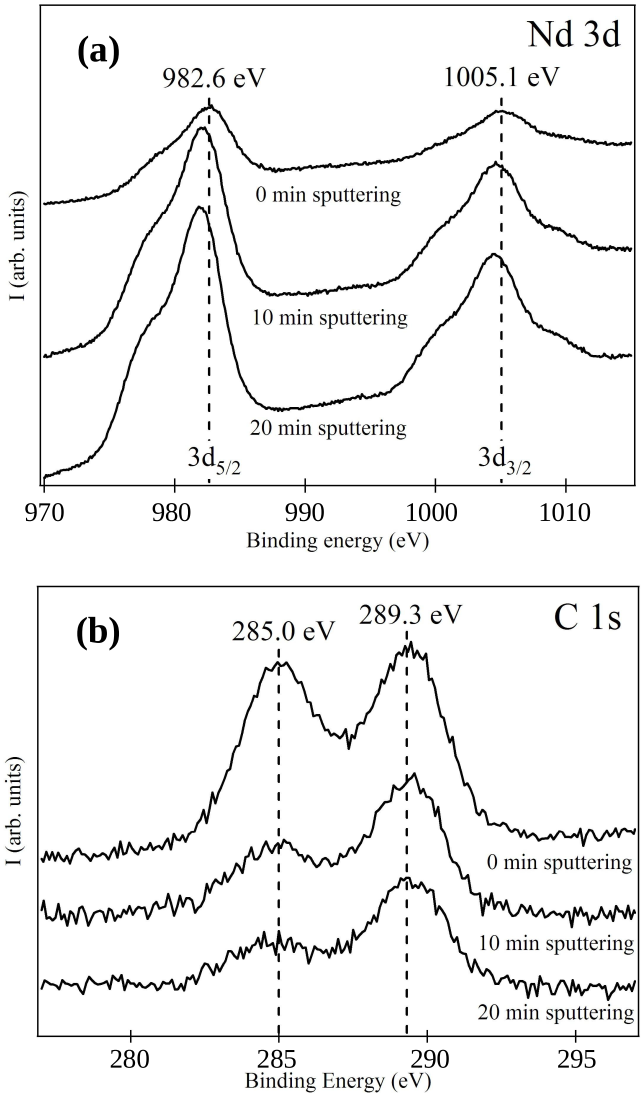

Figure 4-2 XPS spectra of the Ti-A cathode deposit obtained after 3 h plating in isopropanol/isobutanol mixture: (a) Nd 3d, and (b) C 1s before sputtering (indicated as 0 min sputtering in the figure), after 10 min sputtering, and after 20 min sputtering with Ar^+ ions. Identical offsets were applied between the spectra of each figure. (Reprinted from Nuclear Instrum. Methods A Vol. 696, A. Vascon et al., Elucidation of constant current density molecular plating, pages 180-191, Copyright (2012), with permission from Elsevier).

By comparing the trends of the spectra of Figure 4-2, it is clear that the intensity of the Nd 3d signal increases during sputtering of the surface, while the C 1s intensity decreases. As regards the decrease of the C 1s intensity, it is evident that upon sputtering the 285.0 eV component is removed more easily than the 289.3 eV one. The 285.0 eV line originates from physisorbed solvent on the surface of the deposit, while the 289.3 eV line is due to chemisorbed species arising from solvent electrolysis. These trends show that the obtained target is characterized by an outer layer of solvent which covers the Nd deposit. A detailed analysis of all the performed XPS investigations can be found in [7].

The AFM analysis of the samples was perfomed on the Ti-A and Ti-B MC targets produced using the mixed solvent isopropanol/isobutanol and the current density 0.7 mA/cm^2. Figure 4-3 shows the (25 × 25) μm^2 images of the Ti-A MC target (a), and of the Ti-B MC target (b). The $\overline{\text{RMS}}$ values of the AFM analysis are reported in Table 4-2.

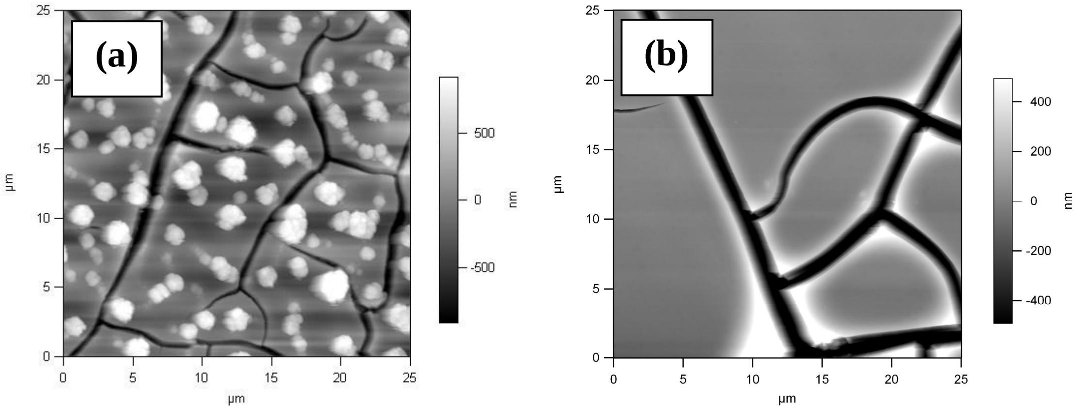

Figure 4-3 (25 × 25) μm^2 tapping-mode AFM images of the MC targets produced using the mixed solvent isopropanol/isobutanol on Ti-A (a) and Ti-B (b) deposition substrates. (Figure 4-3 (b): reprinted from Nuclear Instrum. Methods A Vol. 696, A. Vascon et al., Elucidation of constant current density molecular plating, pages 180-191, Copyright (2012), with permission from Elsevier).

Table 4-2 Average root mean square values obtained after the AFM analysis of the MC targets produced using Ti-A, and Ti-B foils.

Deposition substrate	**Scan size (μm^2)**	**Surface roughness $\overline{\text{RMS}}$ (nm)**
Ti-A	**(5 × 5)**	150 ± 40
	(25 × 25)	190 ± 70
Ti-B	**(5 × 5)**	22 ± 13
	(25 × 25)	22 ± 13

The image of Figure 4-3a shows very clearly that the layer grown on the Ti-A substrate presents evident surface outgrowths (i.e., white spots in the figure). These are absent in the case of the layer grown on the smoother deposition substrate, i.e., Ti-B, (see Figure 4-

3b). Recalling that $\overline{\mathrm{RMS}}$ values were obtained by limiting the analysis to crack-free areas of the layers, the data reported in Table 4-2 confirm what is observed in Figure 4-3, showing that the rougher deposit is the one grown on the rougher substrate, i.e., Ti-A, while the smoother deposit is the one grown on the smoother substrate, i.e., Ti-B. These results suggest that for the production of very smooth targets, deposition substrates that are as smooth as possible are advantageous.

Despite the achievement of a reduced surface roughness of the layers, both images of Figure 4-3 show the presence of severe cracking of the produced surfaces. We tested whether these cracks were a result of the plating process or if they developed afterwards, during the drying of the produced samples. For this, AFM images of a MC Ti-A target produced using the mixed isopropanol/isobutanol solvent were taken immediately after the end of the plating process, but with the solvent still present (Figure 4-4a) and once the liquid was removed and the target dried in air for a few minutes (Figure 4-4b). From the absence of cracks in Figure 4-4a we conclude that these are not associated with the MP, but develop during the post-deposition phase, i.e., during the drying of the targets.

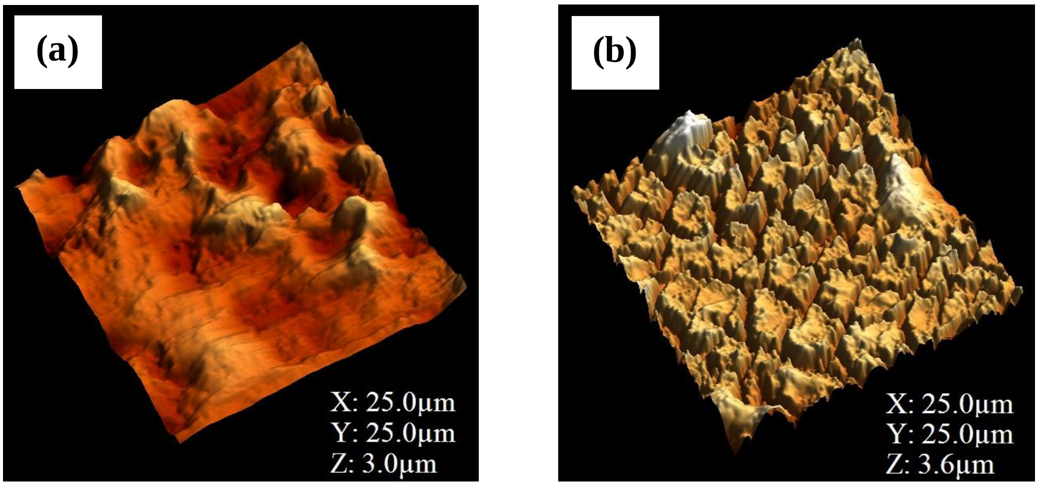

Figure 4-4 3D (25 × 25) μm^2 AFM images of the MC target produced using Ti-A and isopropanol/isobutanol solvent before (a) (i.e., contact-mode AFM analysis in liquid), and after (b) (i.e., tapping-mode AFM analysis in air) solvent removal and drying. Both images were elaborated using the WSxM 5.0 version developed by Nanotech Electronica [12]. (Reprinted from Nuclear Instrum. Methods A Vol. 714, A. Vascon et al., Smooth crack-free targets for nuclear applications produced by molecular plating, pages 163-175, Copyright (2013), with permission from Elsevier).

This observation, together with the fact that the produced targets contain solvent (see Figure 4-2b), opened a possibility to study whether a change of the solvent, away from the traditional mixture of isopropanol and isobutanol, towards a less volatile solvent, would allow production of crack-free targets. The use of DMF (boiling point, Bp = 153.0°C [11], compared to isopropanol, Bp = 82.2°C [11], and isobutanol, Bp = 107.66°C [11]) allowed production of crack-free targets. The layers produced using DMF with Ti-A and Ti-B as deposition substrates were characterized by means of AFM. Figure 4-5 shows the (25 × 25) μm^2 images of the Ti-A MC target (a), and of the Ti-B MC target (b).

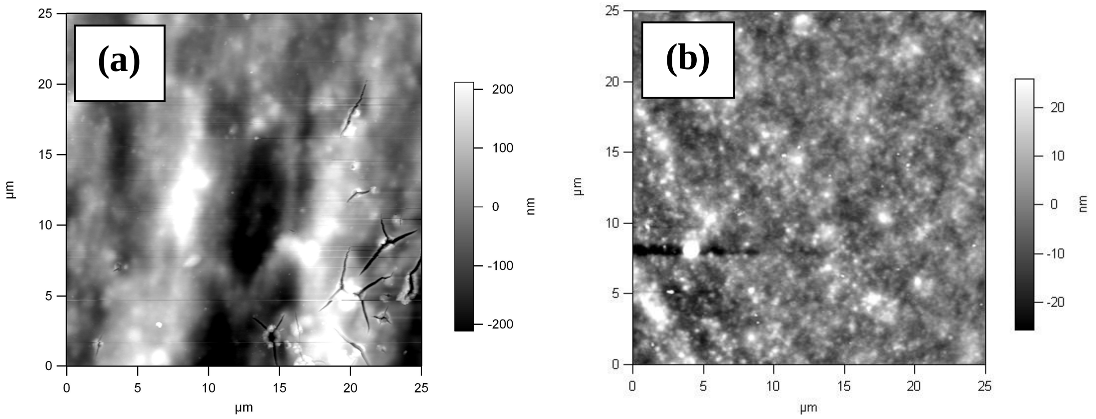

Figure 4-5 (25 × 25) μm^2 AFM tapping-mode images of the MC targets produced using the DMF solvent and applying Ti-A (a) and Ti-B (b) deposition substrates. (Figure 4-5 (a): reprinted from Nuclear Instrum. Methods A Vol. 714, A. Vascon et al., Smooth crack-free targets for nuclear applications produced by molecular plating, pages 163-175, Copyright (2013), with permission from Elsevier).

Interestingly, the sample shown in Figure 4-5a features almost no cracks, except for those mostly deriving from the surface defects (i.e., white outgrowths in the figure). In addition, as proved by Figure 4-5b, the use of Ti-B as deposition substrate not only reduces the surface roughness, as shown by the one-order of magnitude smaller RMS range (compare Figures 4-5a and b), but also eliminates completely the cracks in the layer. Ultimately, the combined use of the Ti-coated Si wafer and less volatile DMF solvent yields smooth and crack-free Nd targets. A full account of the experiments with solvents other than isopropanol/isobutanol will be given in [8].

4.4 Conclusions

To elucidate some main features of the MP process, several constant current density MPs were performed in order to better understand and to improve the technique. Neodymium was used as the model electrolyte for the experiments. The variables chosen for these investigations were: concentration of the electrolyte, surface roughness of the deposition substrates, and plating solvent. The influence of changes in these variables on the deposition processes was monitored recording cell potential *vs.* time, and the obtained deposits were analyzed using γ-ray spectroscopy, XPS, and AFM.

As detailed in [7], the cell potentials recorded during the performed constant current density MPs are mainly affected by the solution resistance. An expression relating cell potential with conductance and hence electrolyte concentration was therefore derived. This expression explains the cell potential trends recorded using different electrolyte concentrations, but it does not yet allow for interpreting the reasons leading to the minima in the cell potential curves. However, we notice that the performed yield measurements always showed an advanced depletion of the Nd ions already at the times of the minima of the different curves.

The XPS investigation of the produced targets showed that Nd is not reduced during the MP process, but rather deposited on the cathodic surface as derivatives of Nd^{3+}, possibly as carboxylate, oxide or hydroxide. This outcome is reasonable on the basis of the typically high negative values of the standard redox potentials of the lanthanide cations. Moreover, XPS proved that the produced targets are made up of both physisorbed as well as chemisorbed solvent. The presence of products of chemisorption, i.e., metal carboxylate groups, shows that the solvent undergoes electrolysis during the MP process. This contradicts the initial interpretation of Parker and Falk in [1], where MP was described as an electrodeposition with no electrolytic dissociation occurring during the passage of current.

Finally, the AFM investigation of the targets showed that smooth layers can be grown only using smooth deposition substrates. Moreover, the MP production of smooth and crack-free layers proved to be possible only when smooth substrates like Ti-coated Si wafer, and low-volatility plating solvents like DMF are used. The cracking of the surfaces seems to be connected to the drying process in air of the samples. Investigations to give reasonable explanations for these results are still underway and will be presented in a future publication [8].

Acknowledgements

The authors thank the staff of the TRIGA Mainz for performing the irradiations, and Dr. T. Lauer for performing the coating of the Si wafers. A. Vascon acknowledges financial support from the German Federal Ministry of Science and Education (BMBF) under Contract number 02NUK013E.

References

[1] Parker W, Falk R (1962) Nucl Instrum Methods 16:355-357

[2] Trautmann N, Folger H (1989) Nucl Instrum Meth A 282:102-106

[3] Eberhardt K, Schädel M, Schimpf E, Thörle P, Trautmann N (2004) Nucl Instrum Meth A 521:208-213

[4] Sadi S, Paulenova A, Watson PR, Loveland W (2011) Nucl Instrum Meth A 655:80-84

[5] Watson PR, Loveland W, Zielinski PM, Gregorich KE, Nitsche H (2004) Nucl Instrum Meth B 226:543-548

[6] Vascon A, Düllmann ChE, Eberhardt K, Kindler B, Lommel B, Runke J (2011) Nucl Instrum Meth A 655:72-79

[7] Vascon A, Santi S, Isse AA, Reich T, Drebert J, Christ H, Düllmann ChE, Eberhardt K (2012) Nucl Instrum Meth A 696:180-191

[8] Vascon A, Santi S, Isse AA, Kühle A, Reich T, Drebert J, Eberhardt K, Düllmann ChE (2012) submitted to Thin Solid Films

[9] Wagner CD, Riggs WM, Davis LE, Moulder JF, Muilenberg GE (1979) Handbook of X-ray photoelectron spectroscopy. Perkin-Elmer Corporation, Physical Electronics Division, Eden Prairie, Minn. 55344

[10] Lide DR Ed. (2006) CRC Handbook of Chemistry and Physics, 87th edn.

[11] Izutsu K (2002) Electrochemistry in nonacqueous solutions. Darmstadt, Germany

[12] Horcas R, Fernandez JM, Gomez-Rodriguez J, Colchero J, Gomez-Herrero AM, Baro W (2007) Rev Sci Instrum 78:013705-1

5. Smooth crack-free targets for nuclear applications produced by molecular plating

A. Vascon[1], S. Santi[2], A. A. Isse[2], A. Kühnle[3], T. Reich[1], J. Drebert[1], K. Eberhardt[1,4], Ch.E. Düllmann[1,4,5]

[1]Institute of Nuclear Chemistry, Johannes Gutenberg University Mainz, 55099 Mainz, Germany
[2]Department of Chemical Sciences, University of Padova, 35131 Padova, Italy
[3]Institute of Physical Chemistry, Johannes Gutenberg University Mainz, 55099 Mainz, Germany
[4]SHE Chemistry Research Section, Helmholtz Institute Mainz, 55099 Mainz, Germany
[5]SHE Chemistry Department, GSI Helmholtzzentrum für Schwerionenforschung GmbH, 64291 Darmstadt, Germany

Published in:

Nuclear Instruments and Methods in Physics Research A **714** (2013) 163-175.

Abstract

The production process of smooth and crack-free targets by means of constant current electrolysis in organic media, commonly known as molecular plating, was optimized. Using a Nd salt, i.e., [$Nd(NO_3)_3 \cdot 6H_2O$], as model electrolyte several constant current density electrolysis experiments were carried out to investigate the effects of different parameters, namely the plating solvent (isopropanol and isobutanol mixed together, pyridine, and N,N-dimethylformamide), the electrolyte concentration (0.11, 0.22, 0.44 mM), the applied current density (0.17, 0.3, 0.7, and 1.3 mA/cm^2), and the surface roughness of the deposition substrates (12 and 24 nm). Different environments (air and Ar) were used to dry the samples and the effects on the produced layers were investigated. The obtained deposits were characterized using γ-ray spectroscopy for determining Nd deposition yields, X-ray photoelectron spectroscopy for chemical analysis of the produced surfaces, radiographic imaging for surface homogeneity inspection, atomic force microscopy for surface roughness evaluation, and scanning electron microscopy for surface morphology investigation. The results allowed identifying the optimum parameters for the production of smooth and crack-free targets by means of molecular plating. The smoothest layers, which had an average RMS roughness of ca. 20 nm and showed no cracks, were obtained using 0.22 mM [$Nd(NO_3)_3 \cdot 6H_2O$] plated from N,N-dimethylformamide at current densities in the range of 0.3-0.7 mA/cm^2 on the smoothest deposition substrate available.

Keywords: smooth crack-free targets, molecular plating, neodymium, γ-ray spectroscopy, atomic force microscopy (AFM), X-ray photoelectron spectroscopy (XPS)

5.1 Introduction

Targets are an essential component in experimental nuclear science as a source of stationary nuclei, e.g., for atomic and nuclear spectroscopy or nuclear reaction studies [1-3]. Generally, targets should be chemically pure, uniform, homogeneous, crack-free over the area of interest, and well adherent to the deposition substrate. Among the several techniques available to prepare thin layers to be used as nuclear targets [4-8], molecular plating (MP) is one of the most effective and most successfully applied ones [9,10]. This technique, based on the electrodeposition of the element of interest from an organic medium either in the constant current or in the constant voltage mode, is usually chosen because of the possibility to quickly produce deposits of acceptable uniformity and adherence with quantitative yield. Recently Garcia et al. [11,12] applied polymer assisted deposition (PAD), developed by Jia et al. [13] as an alternative method to prepare thin films of metal oxides, to produce nuclear targets. PAD has been claimed to yield targets with better uniformity and homogeneity than MP. In the present work, we demonstrate that thanks to an improved understanding of the electrochemistry of MP and to more extensive surface science investigations [14,15], which showed that the roughness of the films depends on variables like deposition substrate and electrolyte concentration, targets prepared via MP can be also very uniform and homogeneous, as smooth and crack-free layers can be produced.

5.2 Experiments and results

5.2.1 Deposition cell

The cell used for the MPs is characterized by a central PEEK body where the electrolytic solution is inserted [14]. The anode and the cathode are both Ti blocks covered by a Pd foil and a Ti foil, respectively. Each of the two electrodes has an area of 9 cm^2. The distance between the electrodes is 2.8 cm. The cathode was designed to be easily removed from the cell and to be used for liquid AFM investigations. Figure 5-1 shows the cathode of the cell: a Ti block covered with a circular Ti foil fixed with a PEEK ring. A constant temperature of 16 °C was maintained in the cell by water-cooling the Ti blocks, which were in physical contact with the electrodes.

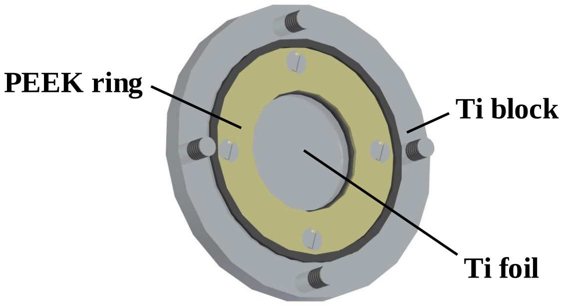

Figure 5-1 3D drawing of the cathode assembly: a Ti block covered with a circular Ti foil fixed with a PEEK ring. The cathode assembly is part of the molecular plating cell.

5.2.2 Solvents used for molecular plating

Different solvents were used to perform the MPs: isopropanol, isobutanol, pyridine, and N,N-dimethylformamide (DMF). Isopropanol and isobutanol were always used together as a mixture (3% isopropanol, 97% isobutanol), hereafter referred to as IP+IB. Table 5-1 shows some physical properties of relevance of the used solvents [16].

Table 5-1 Some physical properties (at 25°C) of the solvents used for the MPs [16].

Solvent	Bp (°C)	Viscosity (cP)	Conductivity (Sm/cm)	Relative permittivity
Isopropanol (IP)	82.2	2.044	6×10^{-8}	19.9
Isobutanol (IB)	107.7	3.910	2×10^{-8}	17.9
Pyridine	115.3	0.884	4×10^{-8}	12.9
N,N-dimethylformamide (DMF)	153.0	0.802	6×10^{-8}	36.7

The data reported in Table 5-1 show DMF to have the highest boiling point, conductivity, and relative permittivity; its viscosity is instead the lowest one. Pyridine has the lowest relative permittivity, a viscosity approaching that of DMF and a boiling point quite close to the one of the IP+IB mixture. The physical properties of the IP+IB mixture can be approximated to those of pure isobutanol, which makes up 97% by volume of the mixture. IP+IB has the highest viscosity and the lowest conductivity.

5.2.3 Deposition substrates

The deposition substrates used in the present work are listed in Table 5-2. Their surface roughnesses, evaluated by AFM (see Section 3.2.5 in [14]) after the cleaning procedure, are reported as average root mean square values ($\overline{\mathrm{RMS}}$). To facilitate comparison of the results reported here and previously in [14], we keep the labelling of our substrate types as in [14].

Table 5-2 Deposition substrates used for the MPs and their average surface roughness values ($\overline{\mathrm{RMS}}$) determined by AFM.

Substrate type	Production technique	$\overline{\mathrm{RMS}}$ (nm)
Ti3	rolling	24 ± 7
Ti5	magnetron sputtering	12.8 ± 0.7

Ti3 was a circular 50 μm-thick Ti foil cut from a bigger foil (Goodfellow). Ti5 was produced by coating a 300-μm thick, mechanically polished Si wafer with 100 nm metallic Ti. The substrates used for deposition in the cell had different surface roughnesses: larger, corresponding to a more defective surface (Ti3, Figure 5-2a), and smaller, corresponding to a less defective surface (Ti5, Figure 5-2b).

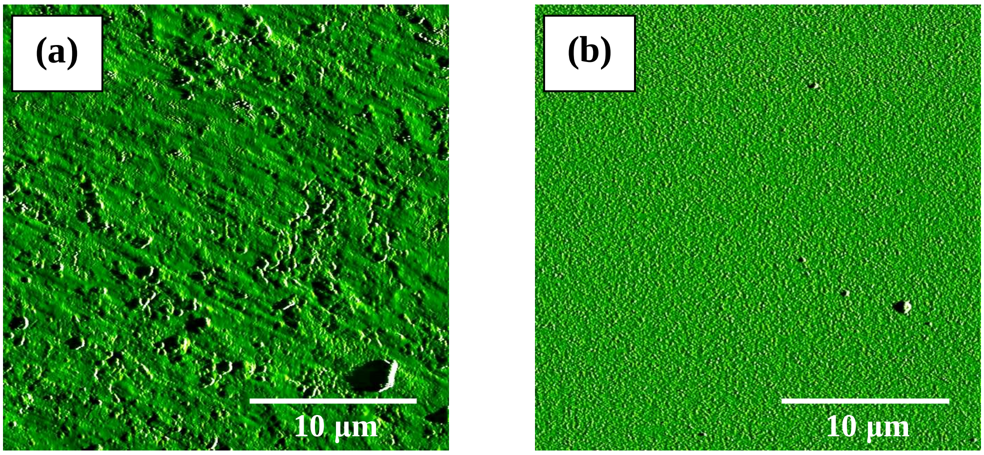

Figure 5-2 (25 × 25) µm^2 amplitude AFM images of the Ti3 (a) and Ti5 (b) deposition substrates.

5.2.4 Molecular plating at constant current density

Before any deposition, both the anode (Pd foil) and the cathode (Ti foil) were cleaned with 6 M HCl (1 × 3 mL washing), water (3 × 3 mL washings), and isopropanol (1 × 3 mL washing). Only Ti5 substrates were cleaned using HCl with a lower concentration (i.e., 0.6 M) in order to avoid corrosion-induced increase in surface roughness, as verified in [14]. For the MPs, 0.338, 0.675, and 1.350 g of [$Nd(NO_3)_3 \cdot 6H_2O$] were dissolved in 20 mL 0.1 M HNO_3 to give final solutions of three different concentrations. From each solution an aliquot of 100 µL was added to a mixture of 1 mL isopropanol (Fisher Chemical) and 34 mL isobutanol (Applichem), or to 35 mL of pyridine (Merck) or DMF (Merck), finally yielding three different solutions of Nd^{3+} in the cell; these are referred to as low concentration (LC, 0.11 mM), medium concentration (MC, 0.22 mM), and high concentration (HC, 0.44 mM). In the cell the concentration of HNO_3 was 0.3 mM. The plating solutions were stirred by means of a quartz tip ultrasonic stirrer (Bandelin Sonopuls HD 2070) operated at 30% power pulse. MP experiments were always carried out for 3 h by applying a constant current of 6 mA, corresponding to a current density of 0.7 mA/cm^2. Three-hours long MPs were also performed by testing different constant currents, i.e., 1.5, 3, or 12 mA. The corresponding current densities were 0.17, 0.3, and 1.3 mA/cm^2 (Table 5-3).

5.2.5 Atomic force microscopy (AFM) studies

5.2.5.1 Experiments

The surface roughness of the deposited layers, i.e., the measure of the texture of a surface quantified by the vertical deviations of a real surface from its ideal planar form, was investigated by using atomic force microscopy (AFM) (MFP 3D Asylum Research). AFM investigations were performed in air and in liquid.

The tapping-mode AFM analysis in air was the same for all the produced targets: ten (5 × 5) μm^2 and one (25 × 25) μm^2 images were recorded for each target. From each of the ten (5 × 5) μm^2 images two root mean square (RMS) values were evaluated using a (1.5 × 1.5) μm^2 mask in two different positions inside the image. From each of the (25 × 25) μm^2 images, twenty RMS values were evaluated using (1.5 × 1.5) μm^2 masks in twenty different positions of the image. In the case of samples presenting surfaces with cracks, the masks were used only in the crack-free areas, as the cracks do not belong to the surface and hence do not define the real roughness of the deposited layers. The final surface roughness value of each of the image sizes was evaluated for each target as the arithmetic mean of all the RMS values measured for that specific image size (i.e., $\overline{\mathrm{RMS}}$).

5.2.5.2 Results

5.2.5.2.1 Layer-growth studies from DMF solution

The growth mechanism of the layers was studied as a function of plating time by measuring the $\overline{\mathrm{RMS}}$ of air-dried targets. Twelve targets were produced using different deposition times: the first target was produced after 15 min plating and the subsequent ones after increments of 15 min up to 180 min. The targets were prepared using a 0.22 mM Nd salt (i.e., MC), Ti5 deposition substrates, at a current density of 0.7 mA/cm^2, and DMF as plating solvent. The growth study was restricted to DMF because it showed very promising results, as we briefly reported in [17] where some preliminary tests with this solvent were described.

In Figure 5-3 the $\overline{\mathrm{RMS}}$ trends of the growing layer show an almost constant behaviour (average value ca. 14 nm) during the whole period of deposition (3 h): the surface roughness does not undergo major variations. This is in contrast to similar studies performed in IP+IB on rougher substrates, where the roughness during layer growth increased by a factor of 2-5. Moreover, all the AFM images recorded for this layer-growth study showed no surface cracking. See for example the (5 × 5) μm^2 image of the deposit grown for 180 min shown in Figure 5-4. The analysis of such images and the evaluated constant $\overline{\mathrm{RMS}}$ trends suggest that the layer growing on the Ti5 cathode during a MC plating experiment performed in DMF follows a Frank-van der Merwe mechanism (layer-by-layer growth mechanism).

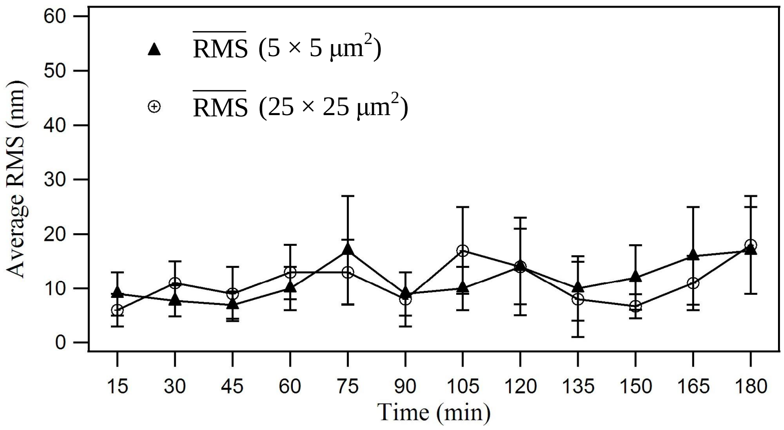

Figure 5-3 $\overline{\mathrm{RMS}}$ *vs* time trend of the layer-growth study of the air-dried targets produced using 0.22 mM Nd salt with DMF and Ti5 deposition substrates.

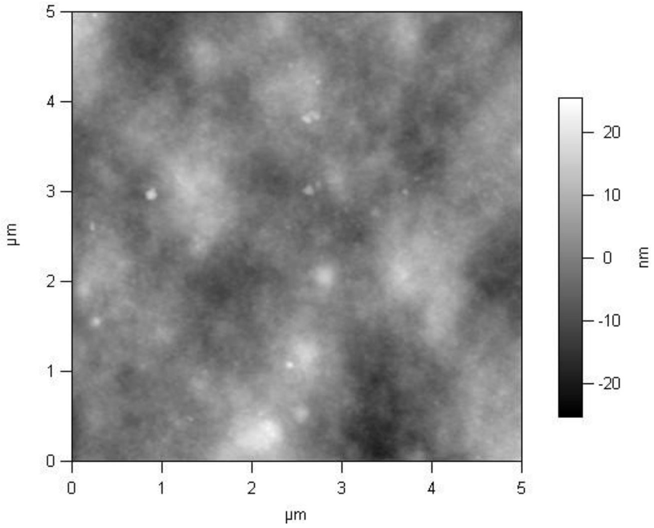

Figure 5-4 Layer-growth studies from DMF solution. (5 × 5) µm^2 topography AFM image of the sample plated for 180 min using Ti5 substrate and MC plating solution in DMF.

5.2.5.2.2 Influence of the plating solvent and of the drying environment

AFM studies in air were performed on targets produced from MC solution, after drying for one month either in air or in a glove-box where an Ar inert environment was maintained. The solvents used for the platings were IP+IB, pyridine, and DMF; the deposition substrates were Ti3 foils. The $\overline{\mathrm{RMS}}$ values of the analysis are reported in Table 5-3.

Table 5-3 Overview of relevant molecular plating parameters. Average root mean square ($\overline{\text{RMS}}$) values obtained from the AFM analyses of the samples investigating the influence of plating solvent, drying environment, electrolyte concentration, and current density on the surface roughness of the produced layers.

Substrate type	Solvent	Drying environment	Concentration	Current density (mA/cm^2)	Scan size (µm^2)	$\overline{\text{RMS}}$ (nm)
Ti3	Pyridine	Air	MC	0.7	(5 × 5)	242 ± 140
					(25 × 25)	372 ± 190
Ti3	Pyridine	Ar	MC	0.7	(5 × 5)	320 ± 160
					(25 × 25)	350 ± 180
Ti3	IP+IB	Air	MC	0.7	(5 × 5)	150 ± 40
					(25 × 25)	190 ± 70
Ti3	IP+IB	Ar	MC	0.7	(5 × 5)	140 ± 60
					(25 × 25)	180 ± 80
Ti3	DMF	Air	MC	0.7	(5 × 5)	61 ± 24
					(25 × 25)	130 ± 40
Ti3	DMF	Ar	MC	0.7	(5 × 5)	52 ± 23
					(25 × 25)	110 ± 50
Ti5	DMF	Air	HC	0.7	(5 × 5)	70 ± 21
					(25 × 25)	79 ± 14
Ti5	DMF	Air	MC	0.7	(5 × 5)	17 ± 8
					(25 × 25)	18 ± 9
Ti5	DMF	Air	LC	0.7	(5 × 5)	17 ± 3
					(25 × 25)	18 ± 8
Ti5	DMF	Air	MC	0.17	(5 × 5)	110 ± 35
					(25 × 25)	130 ± 25
Ti5	DMF	Air	MC	0.3	(5 × 5)	10 ± 4
					(25 × 25)	12 ± 5
Ti5	DMF	Air	MC	1.3	(5 × 5)	70 ± 30
					(25 × 25)	80 ± 22

Table 5-3 clearly demonstrates that, independently of the chosen drying environment, the roughest samples are those obtained using pyridine, whereas those produced in DMF are the smoothest. No differences in $\overline{\text{RMS}}$ values within experimental uncertainties were found for each kind of sample dried in air or in Ar. The analysis of the recorded AFM images showed that samples characterized by cracking of the layers present surface troughs regardless of whether they were dried in air or Ar.

Figure 5-5 shows a (25 × 25) μm^2 image of the DMF sample after drying in the inert environment.

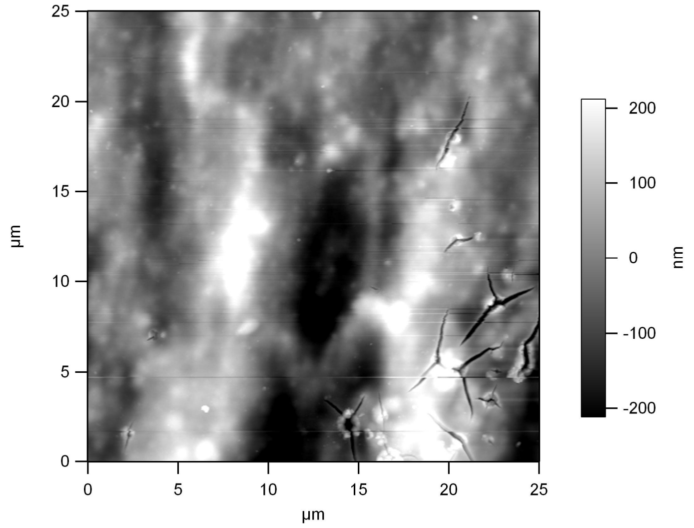

Figure 5-5 Influence of the plating solvent and of the drying environment. (25 × 25) μm^2 topography AFM image of the sample produced using MC plating solution, Ti3 substrate, DMF, and dried in an Ar inert environment.

Unlike the pyridine and IP+IB layers, characterized by severe surface cracking (see, e.g., Figure 4-3a in [17] for targets made from IP+IB on Ti3 substrates), the DMF sample shows almost no cracks, except for those mostly arising from the surface defects (i.e., white outgrowths in Figure 5-5).

5.2.5.2.3 Influence of the electrolyte concentration

Air-dried HC, MC, and LC targets produced using Ti5 as deposition substrates and DMF as plating solvent were investigated in air. The results of the analysis reported in Table 5-3 show that the HC target is much rougher than the MC and LC targets, which have identical roughness. Moreover, Table 5-3 shows that DMF MC targets prepared on Ti5 substrates are smoother than the same targets prepared on Ti3 foils.

We notice that the recorded AFM images revealed no cracks in the surfaces of the HC, MC, and LC targets plated from DMF.

5.2.5.2.4 Influence of the current density

AFM analyses in air were performed on air-dried MC targets produced using different constant current densities, namely 0.17, 0.3, and 1.3 mA/cm^2. Ti5 was used as deposition substrate, and DMF as plating solvent. The $\overline{\text{RMS}}$ values of the analysis are reported in

Table 5-3, whereas the corresponding (25 × 25) μm^2 images of the deposits are shown in Figure 5-6.

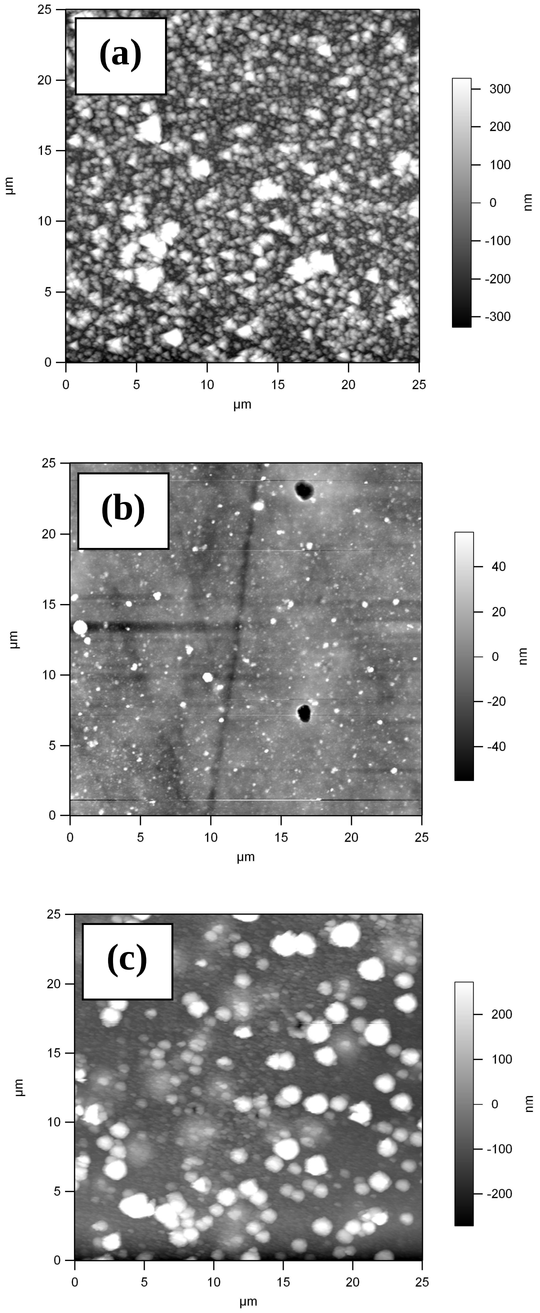

Figure 5-6 Influence of the current density. (25 × 25) μm^2 topography AFM images of samples produced using MC plating solution in DMF and a Ti5 substrate; deposits obtained after galvanostatic electrolysis at current densities of 0.17 mA/cm^2 (a), 0.3 mA/cm^2 (b), or 1.3 mA/cm^2 (c).

Table 5-3 shows that only the intermediate current density of 0.3 mA/cm^2 gives $\overline{\text{RMS}}$ values similar to those recorded for the 0.7 mA/cm^2 experiments. Both higher (i.e., 1.3 mA/cm^2) and lower (i.e., 0.17 mA/cm^2) constant current densities result in much rougher final deposits. In particular, the roughest deposit is obtained with 0.17 mA/cm^2. These results are well evidenced by the (25 × 25) μm^2 images of the 0.17 and 1.3 mA/cm^2

samples shown in Figure 5-6, where both surfaces present evident outgrowths (i.e., white spots in the figures), which are bigger in the case of the targets made at 1.3 mA/cm^2, but not covering the entire analyzed area (c), and smaller but spread over the entire surface in the case of the targets made at 0.17 mA/cm^2 (a). No surface cracks were noted for any of the investigated samples prepared with DMF.

5.2.5.2.5 Liquid AFM study from IP+IB solution

Figure 5-7 shows the results of a liquid AFM study (already briefly reported in [17]), which was performed on a MC target produced using Ti3 as deposition substrate, and IP+IB as plating solvent. At the end of the deposition, the cell was top-sealed, the anode was removed, and the solvent was extracted till only the cathode surface was covered by liquid. Then, the PEEK body of the cell was removed, leaving the cathode deposit covered in liquid: an AFM analysis in contact mode was performed recording one (25 × 25) μm^2 image (Figure 5-7a). After the liquid was removed from the cathode assembly and the target dried, a tapping-mode AFM analysis was performed and a (25 × 25) μm^2 image was recorded (Figure 5-7b). Both images were elaborated using the WSxM 5.0 version developed by Nanotech Electronica [18].

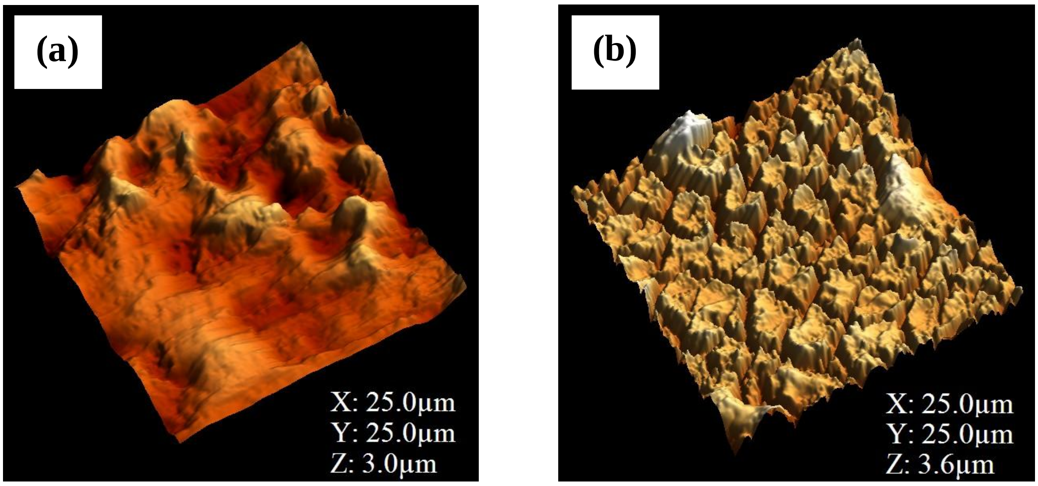

Figure 5-7 Liquid AFM study from IP+IB solution. 3D (25 × 25) μm^2 topography AFM images of the target produced using Ti3 and MC plating solution in IP+IB before (a) and after solvent removal and drying (b).

The 3D AFM images of Figure 5-7 indicate that the cracking of the surfaces develops after the removal of the liquid and the drying of the deposited layer.

5.2.6 Scanning electron microscopy (SEM) studies

5.2.6.1 Experiments

The morphology of the targets was studied using scanning electron microscopy (SEM) (Philips XL30). The microscope was operated at 20 kV. The pressure inside the vacuum chamber was 5 mPa. Backscattered and secondary electrons were detected. A magnification factor of 1000× was used.

5.2.6.2 Results

Figure 5-8 shows 1000× SEM images of three MC samples produced using the following deposition substrates and plating solvents: (a) Ti3 and pyridine, (b) Ti3 and DMF, (c) Ti5 and DMF. All samples were air-dried. Among the several SEM images recorded, these particular ones were chosen for display here because of the important surface morphology information they convey.

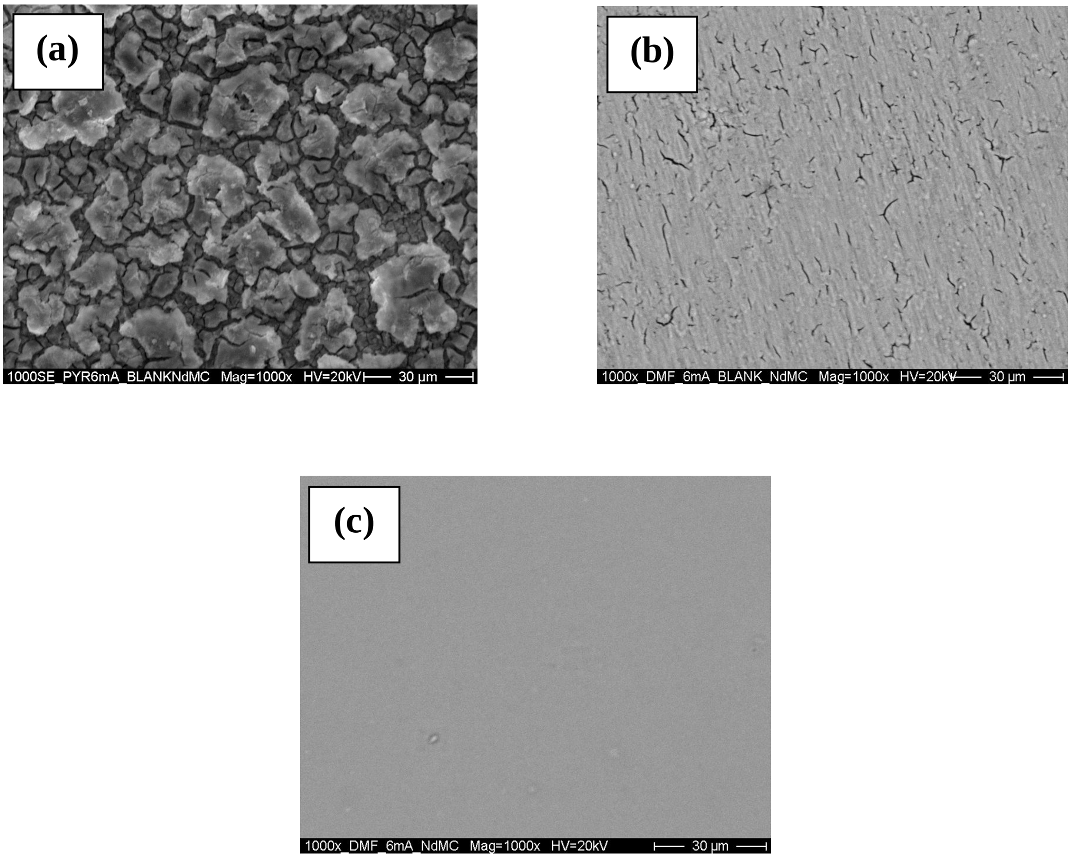

Figure 5-8 Influence of substrate surface roughness and plating solvent. 1000× SEM images of the air-dried samples produced using MC plating solution and the following substrate/solvent systems: (a) Ti3/pyridine, (b) Ti3/DMF, (c) Ti5/DMF.

Figure 5-8a shows a large-area image of an air-dried pyridine MC target. The surface of the sample suffers from severe cracking and it is visibly rough.

Figures 5-8b and c show an important effect of the deposition substrate (Ti3 *vs* Ti5) on the surface morphology of the deposits. These images indicate that MC targets prepared using DMF and a Ti3 substrate (Figure 5-8b) exhibit cracks in the layer, caused mainly by the grown surface defects, as already shown in Figure 5-5. If, instead, a smoother deposition substrate is used, i.e., Ti5, MC targets produced using DMF (Figure 5-8c) show no surface cracks (see also Figure 5-4). In constrast, MC experiments using IP+IB (see Figure 3-2b in [14]) or pyridine showed the presence of cracks in the deposited layers also when Ti5 substrates were used.

5.2.7 Radiographic imaging (RI) studies

5.2.7.1 Experiments

Radioactive targets were produced by performing MPs of Nd solutions containing a radioactive tracer of the element to be plated (Nd: ^{147}Nd, β^-, $t_{1/2}$ = 10.98 d, E_γ = 91 keV). The tracer was produced in a neutron capture reaction (n,γ) on ^{146}Nd present in the used Nd of natural isotopic composition (^{nat}Nd) by irradiating an aliquot of 100 μL of the stock solution with thermal neutrons in the TRIGA Mainz research reactor. The homogeneity of such targets was inspected by using radiographic imaging (RI), employing a FUJIFILM FLA 7000 equipped with reusable imaging plates and a 650 nm laser for the reading process. To verify the homogeneity of the target, the image was overlaid by a grid of square spots with an area of 0.25 mm^2 each. The spatial resolution for γ-emitting nuclides was < 200 μm [19].

5.2.7.2 Results

Figure 5-9a shows the 3D graph of a sample obtained using IP+IB as plating solvent and Ti3 as deposition substrate. Figure 5-9b displays the graph of a sample obtained using DMF and Ti5.

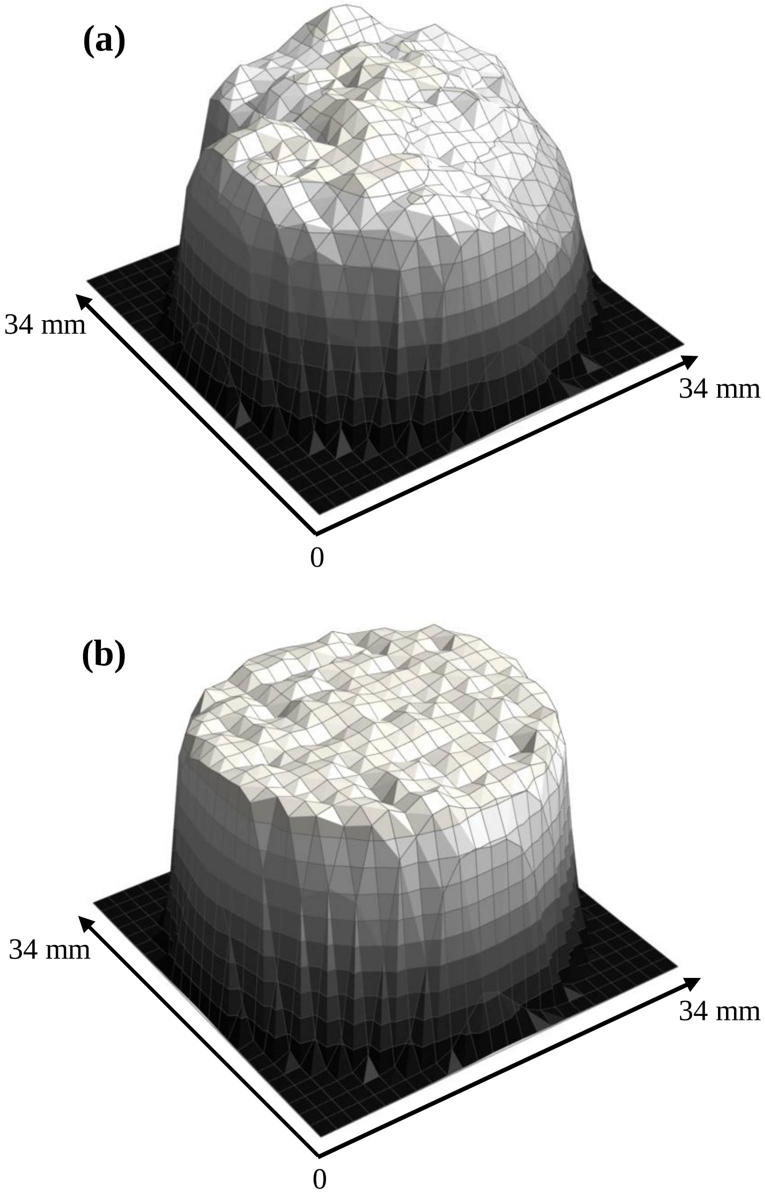

Figure 5-9 Influence of substrate surface roughness and plating solvent. RI 3D graphs of samples produced using MC plating solution and the following substrate/solvent systems: (a) Ti3/IP+IB, (b) Ti5/DMF.

The images show a definite improvement in surface homogeneity of the deposited layers once DMF is chosen as plating solvent and Ti5 as deposition substrate. Experiments showed that better homogeneity of the surfaces is achieved also when DMF is used instead of pyridine in the preparation of MC targets on Ti3 foils.

5.2.8 X-ray photoelectron spectroscopy (XPS) studies

5.2.8.1 Experiments

X-ray photoelectron spectroscopy (XPS) was used to perform the chemical surface characterization of the samples by applying Al K_α and Mg K_α radiations. The X-ray source was operated at 10 kV anode voltage and a current of 10 mA. The pass-energy of the hemispherical energy analyzer was 50 eV. The pressure inside the ultra-high vacuum chamber was in the range of $(1.2\text{-}2.0)\cdot10^{-7}$ Pa. The analyzed samples were six MC targets produced using IP+IB, pyridine, and DMF as plating solvents, and Ti3 foils as deposition substrates. Two targets were produced in each solvent; one was dried in air, while the other was dried inside a glove-box, where an inert environment was assured by a constant Ar pressure (50 Pa below atmospheric pressure, $O_2 < 1$ ppm, $H_2O < 1$ ppm). We refer to [14] for details about the drying procedure in an inert environment and the subsequent XPS analysis. Drying in different environments was investigated to probe whether reactive or inert environments like, respectively, air or Ar cause different surface chemical reactions to take place, the products of which might be identified by XPS.

After the first surface investigation, the samples underwent 10 min sputtering using 4 kV Ar^+ ions, followed by further XPS analysis.

The binding energies of the XPS lines of interest were determined by fitting the recorded XPS spectra. The analyses were performed using the CasaXPS software (version 2.3.15), with which the background was subtracted adopting the Shirley algorithm, and the peaks were fitted using the Gaussian/Lorentzian product formula. As the aim of the present work was mainly to investigate the surface chemistry of the samples after drying in different environments, a detailed chemical surface analysis of the deposits was performed only for C, which was known from [14] to be the main element composing the outer layer of the produced samples. The C 1s spectra are therefore the only ones to be shown with multicomponent fitting analysis, which was always modelled by fixing the separations in binding energy, the intensity ratios, and the full widths at half maxima (FWHM) of the different C 1s components of IP+IB, DMF, and pyridine. For the IP+IB and DMF samples dried both in air and in Ar environment, the analysis before sputtering required correcting the binding energies for the surface charging using one of the components of the C 1s lines: the 284.9 eV component [20] for IP+IB, and the 285.8 eV component [21] for DMF. After sputtering, the imprecise fittings of the reference C 1s peaks required the use of a higher binding energy peak (ca. 289 eV) present in the same C 1s spectra to correct for the surface charge effect. For the air- and Ar-dried pyridine samples, instead, the correction of the binding energies was performed both before and after sputtering using the intense N 1s line of pyridine at 400.2 eV [22]. The experimental uncertainty of the binding energies is ± 0.1 eV.

5.2.8.2 Results

The XPS analyses of the six MC targets never showed the presence of Ti signals, indicating that all the deposited layers are thick.

The Nd analysis of the samples required the use of Mg K_α radiation to avoid an interference with the Auger lines of oxygen in the binding energy region of Nd 3d. The Nd 3d spectra of all the samples dried in Ar environment (not shown) were identical to those of the air-dried targets, except for smaller intensities of the recorded peaks.

Differences among the recorded XPS signals of the IP+IB, DMF and pyridine spectra were noted only for the C 1s lines of the air- and Ar-dried samples.

5.2.8.2.1 Samples prepared from IP+IB

The XPS analyses of the air- and Ar-dried IP+IB samples showed the presence of the following elements: C, O, Pd, and Nd. The corresponding XPS signals were: C 1s, O 1s, Pd 3d, Nd 3d, and Nd 4d. Figure 5-10 shows the spectra of Nd 3d (a) and C 1s (b) of the sample dried in air and Figure 5-10c the C 1s spectra of the sample dried in Ar environment. The model applied for the multicomponent fitting analysis of the C 1s peaks took into account only the C 1s components of isobutanol, as isopropanol corresponds to just 3% of the total volume of the solvent. According to literature [20], the C 1s components of isobutanol have binding energies at 284.9 eV, 285.0 eV, and 286.5 eV, with an intensity ratio of 2:1:1. Table 5-4 shows the ratios of the total peak areas C 1s/Nd 3d, O 1s/C 1s, and the ratios between the sum of the peaks fitting a certain spectral component and a total peak area, like the ratios reported as C 1s (ca. 285 eV)/Nd 3d, C 1s (ca. 286 eV)/Nd 3d, and C 1s (ca. 289 eV)/Nd 3d. The ratios were evaluated before and after 10 min sputtering.

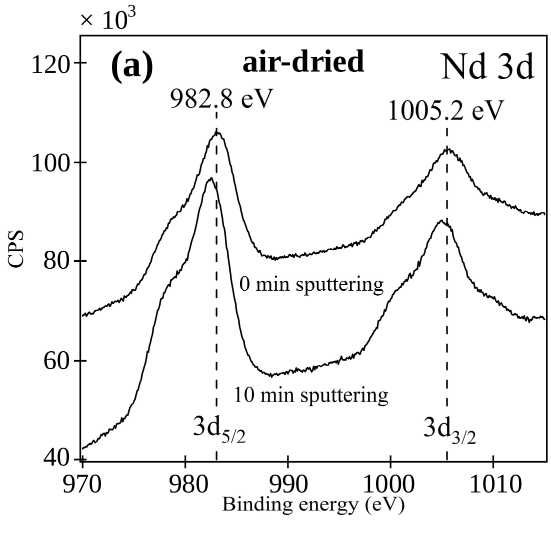

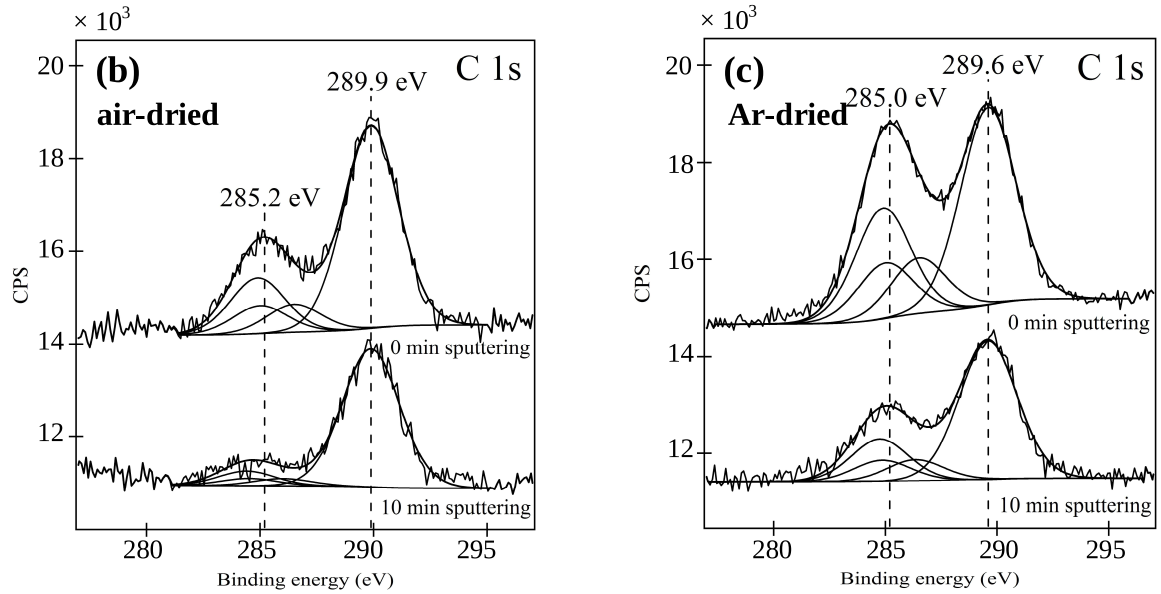

Figure 5-10 XPS spectra of samples obtained after plating on Ti3 substrates using MC plating solution in IP+IB: (a) Nd 3d (air-dried), (b) C 1s (air-dried), and (c) C 1s (Ar-dried) before sputtering (indicated as 0 min sputtering in the figure), and after 10 min sputtering with Ar$^+$ ions. Offsets were applied for clarity.

Table 5-4 Ratios of the peak areas of some of the detected elements before and after 10 min sputtering.

		Air		**Ar**	
Sample	**Ratios of XPS peak areas**	**0 min sputtering**	**10 min sputtering**	**0 min sputtering**	**10 min sputtering**
IP+IB	**C 1s/Nd 3d**	0.04	0.015	0.11	0.020
	O 1s/C 1s	6	10	4	9
	C 1s (ca. 285 eV)/Nd 3d	0.014	0.0026	0.05	0.008
	C 1s (ca. 289 eV)/Nd 3d	0.026	0.012	0.04	0.011
DMF	**C 1s/Nd 3d**	0.05	0.011	0.10	0.014
	O 1s/C 1s	6	15	5	12
	C 1s (ca. 286 eV)/Nd 3d	0.022	0.0018	0.07	0.005
	C 1s (ca. 289 eV)/Nd 3d	0.03	0.009	0.028	0.009
Pyridine	**C 1s/Nd 3d**	0.9	0.14	1.1	0.20
	O 1s/C 1s	1.3	1.4	1.2	1.4
	C 1s (ca. 286 eV)/Nd 3d	0.8	0.13	1.0	0.17
	C 1s (ca. 289 eV)/Nd 3d	0.10	0.015	0.12	0.021

The measured binding energy of the Nd 3d$_{5/2}$ peak is 982.8 eV (Figure 5-10a) and can be compared to the literature value of 983.1 eV [23] for Nd^{3+}. This indicates that Nd is present as Nd^{3+} in the deposited layer (possibly as carboxylate, oxide, or hydroxide) [14]. The C 1s spectra reported in Figures 5-10b and c show the presence of two components: the C 1s peaks at ca. 285.0 eV, which remarkably decrease upon Ar$^+$ sputtering, are due to physisorbed aliphatic carbon of the mixed isopropanol/isobutanol solvent. The peaks at the higher binding energy (i.e., 289.9 eV and 289.6 eV for air- and Ar-dried samples, respectively) can be attributed, according to literature, to COOM -metal carboxylate- (289.0 eV [23]) groups formed during the plating process, which are chemisorbed, as follows from the observation that they are not easily removed by the sputtering. This shows that the solvent undergoes electrolysis during the MP process and becomes oxidized.

For a more detailed analysis of the Nd 3d and C 1s spectra of the IP+IB samples we refer to [14].

The spectra of Figure 5-10, as well as the C 1s/Nd 3d ratios reported in Table 5-4, show that for both air- and Ar-dried samples the intensity of the Nd 3d signal increases, while that of C 1s decreases when the surface is sputtered with Ar^+ for 10 min. This result shows that the Nd deposit is covered with a layer of solvent.

A consequence of drying the samples in air can be inferred from the different intensity ratios of the two C 1s components at 0 min sputtering in Figures 5-10b and c: the 1:1 ratio of the Ar-dried sample becomes almost 1:2 after drying in air. From the analysis of the C 1s (ca. 285 eV)/Nd 3d and C 1s (ca. 289 eV)/Nd 3d ratios it is evident that while the intensity of the chemisorbed C 1s (ca. 289 eV) component is not affected by the method of drying, the physisorbed one (ca. 285.0 eV) decreases when the sample is dried in air. As a consequence more intense Nd 3d signals, hence smaller C/Nd ratios (see Table 5-4), are recorded for the air-dried sample.

5.2.8.2.2 Samples prepared from DMF

As regards the XPS analyses of the targets prepared in DMF, the spectra of both air- and Ar-dried samples showed the presence of the following elements: C, N, O, and Nd. The corresponding XPS signals were: C 1s, N 1s, O 1s, Nd 3d, and Nd 4d. No signals of Pd were detected. Figure 5-11 shows the spectra of Nd 3d (a) and C 1s (b) of the sample dried in air, and Figure 5-11c the C 1s spectra of the sample dried in Ar environment. According to literature [21], the C 1s components of DMF have binding energies at 285.8 eV, and 288.8 eV with an intensity ratio of 2:1.

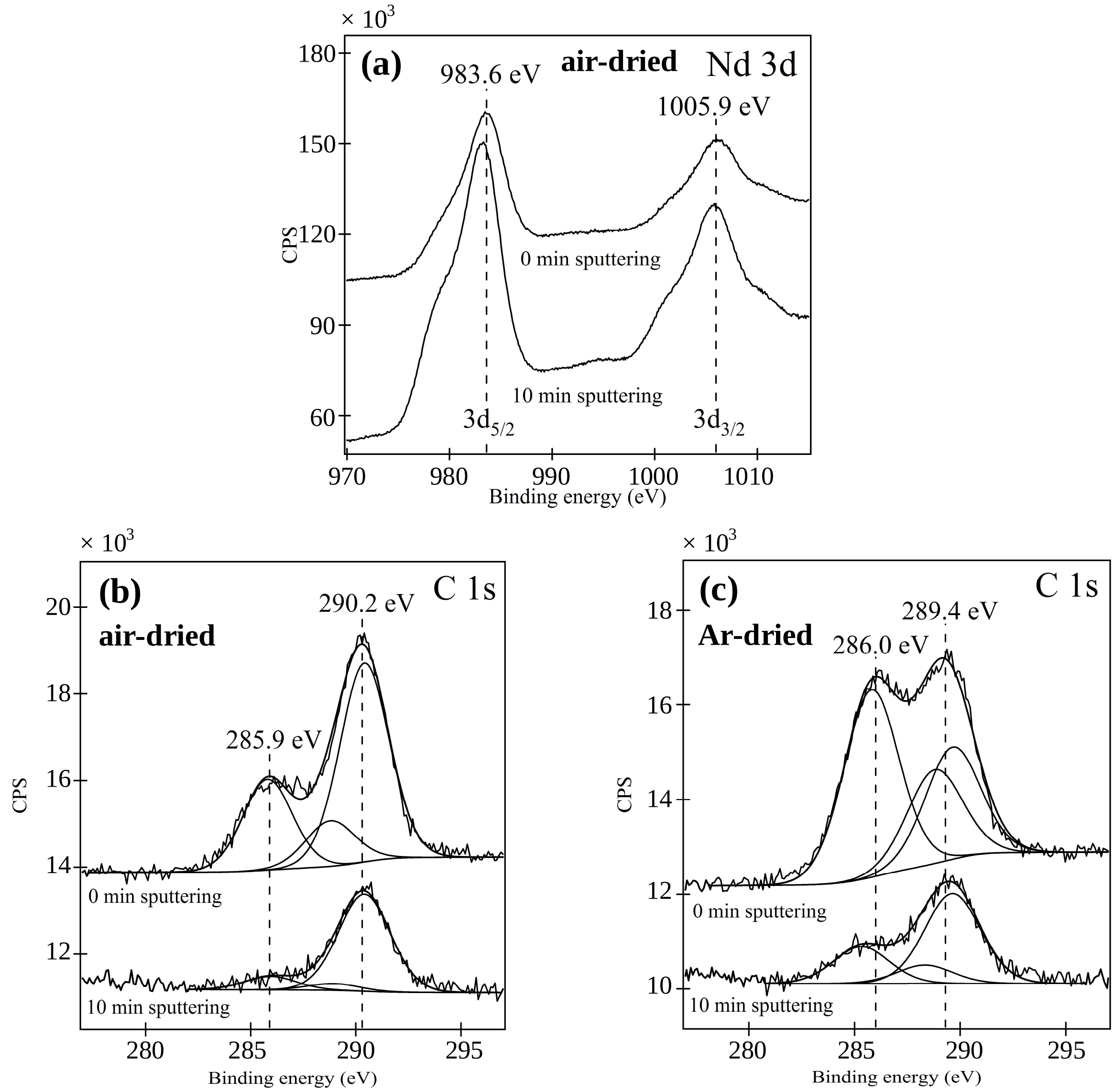

Figure 5-11 XPS spectra of samples obtained after plating on Ti3 substrates using MC plating solution in DMF: (a) Nd 3d (air-dried), (b) C 1s (air-dried), and (c) C 1s (Ar-dried) before sputtering (indicated as 0 min sputtering in the figure), and after 10 min sputtering with Ar^+ ions. Offsets were applied for clarity.

The XPS spectra of the DMF samples (Figure 5-11) are quite similar to those of the IP+IB samples (Figure 5-10). The measured binding energy of the Nd $3d_{5/2}$ peak (i.e., 983.6 eV, Figure 5-11a) confirms that Nd is deposited as Nd^{3+} also in DMF (possibly as carboxylate, oxide, or hydroxide). The C 1s spectra reported in Figures 5-11b and c show again the presence of two components: the components of the physisorbed solvent at ca. 286 eV and 289 eV, and the components of chemisorbed species at 290.2 eV in air, and at 289.4 eV in Ar environment. As in the case of IP+IB, the C 1s peak of the chemisorbed species can be attributed to possible COOM -metal carboxylate- groups formed during the plating process. The produced samples are again characterized by an outer layer of solvent which covers the Nd deposit, as indicated by the spectra of Figure

5-11, as well as by the ratios C 1s/Nd 3d reported in Table 5-4. These ratios show that, for both air- and Ar-dried samples, the intensity of the Nd 3d signal increases with sputtering time, while that of C 1s decreases.

As in the case of MPs in IP+IB, the difference between drying in air or Ar is reflected by the smaller C 1s/Nd 3d ratio in air than in Ar, i.e., 0.05 instead of 0.10 (Table 5-4). This difference is also confirmed by the larger value of the C 1s (ca. 286 eV)/Nd 3d ratio in Ar than in air. Therefore, also in the case of DMF, the 1:1 ratio of the C 1s signals of the Ar-dried sample becomes almost 1:2 after drying in air. The C 1s (ca. 289 eV)/Nd 3d ratios are very similar both in air and in Ar, indicating that the chemisorbed products are not considerably affected by drying in different environments.

5.2.8.2.3 Samples prepared from pyridine

The XPS analyses of the air- and Ar-dried pyridine samples showed the presence of the following elements: C, N, O, Pd, and Nd. The corresponding XPS signals were: C 1s, N 1s, O 1s, Pd 3d, Nd 3d, and Nd 4d. Figure 5-12 shows the spectra of Nd 3d (a) and C 1s (b) of the sample dried in air, and Figure 5-12c the C 1s spectra of the sample dried in Ar environment. According to literature [22], the C 1s components of pyridine have binding energies at 285.5 eV, 285.9 eV, and 286.3 eV, with an intensity ratio of 2:1:2.

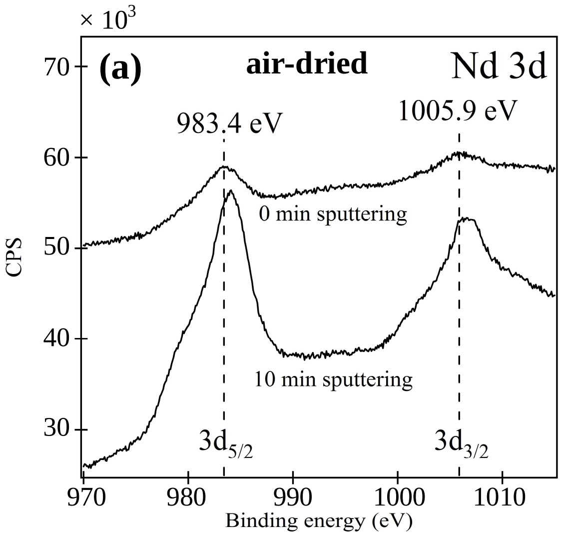

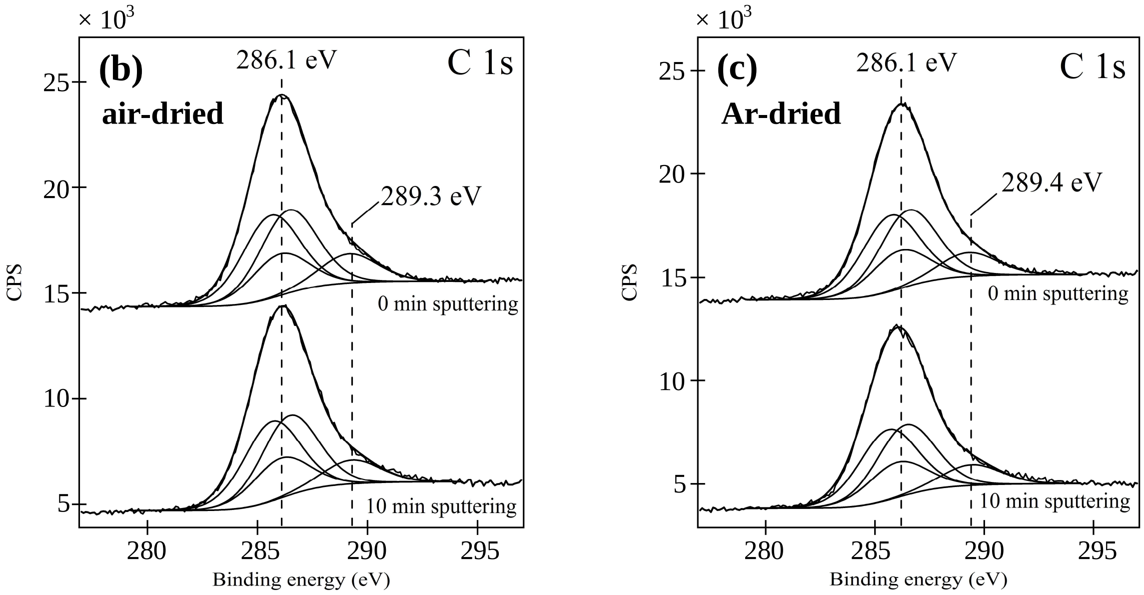

Figure 5-12 XPS spectra of samples obtained after plating on Ti3 substrates using MC plating solution in pyridine: (a) Nd 3d (air-dried), (b) C 1s (air-dried), and (c) C 1s (Ar-dried) before sputtering (indicated as 0 min sputtering in the figure), and after 10 min sputtering with Ar$^+$ ions. Offsets were applied for clarity.

The spectra of Figure 5-12a show that the Nd 3d signal before sputtering is quite low. It is much lower than the Nd 3d signals of the corresponding (unsputtered) IP+IB and DMF samples (compare Figure 5-12a with Figures 5-10a and 5-11a). As shown by Figure 5-12a and by the C 1s/Nd 3d ratios reported in Table 5-4, the intensity of the Nd 3d signal increases considerably after 10 min sputtering with Ar$^+$ ions. Therefore, the produced sample is characterized by a thicker solvent layer covering the deposit compared to IP+IB and DMF. The measured binding energy of the Nd 3d$_{5/2}$ peak (i.e., 983.4 eV, Figure 5-12a) confirms that Nd is deposited as Nd^{3+} as previously found in the case of IP+IB and DMF (possibly as carboxylate, oxide, or hydroxide). The C 1s spectra reported in Figures 5-12b and c show the presence of two components, which are visible only after multicomponent fitting analysis: the components of physisorbed pyridine at ca. 286 eV, and the components of chemisorbed species at ca. 289 eV (i.e., air: 289.3 eV, Ar: 289.4 eV). These higher binding energy components can be attributed to possible COOM -metal carboxylate- groups formed during the plating process. This indicates that the solvent undergoes electrolysis during the MP process and becomes oxidized. Nonetheless, the very small intensities of the chemisorbed components suggest that pyridine undergoes electrolysis only to a smaller degree than IP+IB or DMF.

Slight differences between drying in air or Ar are shown by the smaller C 1s/Nd 3d ratio in air (i.e., 0.9 instead of 1.1), and by the larger value of the C 1s (ca. 286 eV)/Nd 3d ratio in Ar than in air. These differences are smaller than in the case of IP+IB and DMF.

The C 1s (ca. 289 eV)/Nd 3d ratios are very similar both in air and in the Ar environment.

It has to be noticed that all the values of the ratios reported in Table 5-4 for the deposits prepared in pyridine are quite different from the corresponding values determined for IP+IB or DMF deposits, irrespective of the methods of sample drying. This follows from the large intensities of the C 1s signals in pyridine, as evidenced by the C 1s spectra reported in Figures 5-12b and c, where even after 10 min sputtering the intensities of the physisorbed components are only slightly decreased.

The comparisons between the C 1s spectra in Figures 5-10b, c, 5-11b, c, and 5-12b, c show no chemical shifts before and after sputtering. Small shifts of ca. - 0.5 eV after sputtering were observed for the Nd 3d spectra of the IP+IB and DMF samples (see Figure 5-10a for IP+IB, and Figure 5-11a for DMF). Shifts of ca. + 0.5 eV after sputtering were observed for the Nd 3d spectra of the pyridine samples (see Figure 5-12a). This could indicate the presence of different Nd^{3+} species in the topmost surface layers of the samples produced from the different solvents.

From the analysis of all the obtained XPS results, the main difference which appears to occur between samples dried in air and in a controlled inert environment, such as Ar in a glove-box, is related to the higher intensities of the peaks of the physisorbed solvent components when the drying is performed in Ar. Besides this, a slightly larger amount of O adsorbed on the surfaces of all the samples dried in air can be noticed (see O 1s/C 1s ratios in Table 5-4). Nonetheless, no strong indication for the presence of surface chemical reaction products promoted by the drying in air instead of Ar was found.

5.2.9 Molecular plating from DMF solution

5.2.9.1 Cell potential trends

Figure 5-13 shows trends of cell potential *vs* time recorded during preparation of targets, using 0.22 mM $[Nd(NO_3)_3 \cdot 6H_2O]$ solution (MC), Ti3 as deposition foil, and DMF (a) or IP+IB (b) as plating solvent. The applied constant current was 6 mA for 3 h (current density 0.7 mA/cm^2). IP+IB cell potential curves were already discussed in detail in [14].

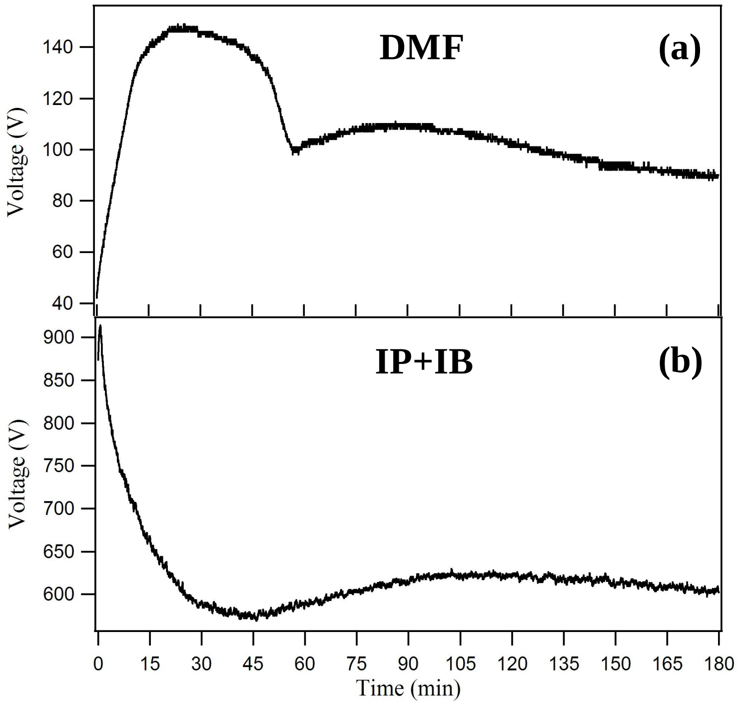

Figure 5-13 Cell potential *vs* time curves of molecular platings on Ti3 foils performed using MC plating solution in DMF (a) or IP+IB (b), and applying a constant current of 6 mA (current density 0.7 mA/cm^2).

From the comparison between the two cell potential curves, it is evident that after an increase at the beginning of the plating process, both curves decrease to a minimum value, then they increase again to reach a maximum. After this maximum, both cell potential curves tend to decrease slightly with time. The initial DMF cell potential increase is much bigger (ca. 100 V) and lasts longer than that of IP+IB, and forms a wide maximum after ca. 30 min. In the case of IP+IB the increase is only a few tens of volts and it lasts only for a few minutes at the very beginning of the deposition. The cell potential drop after the initial increase is much bigger for IP+IB (ca. 350 V) than for DMF (ca. 50 V) and the minimum is reached earlier (45 min *vs.* ca. 60 min). The minimum area is wider for IP+IB than for DMF. The second maximum is wide in both cases but it is achieved somewhat earlier in DMF (ca. 90 min) than in IP+IB (ca. 110 min). The cell potentials in DMF are much smaller than the values recorded in IP+IB.

5.2.9.2 Kinetics derived from γ-ray spectroscopy

The kinetics of the MP with DMF was studied by determining the Nd deposition yield values with γ-ray spectroscopy. A high-purity germanium detector (GEM series HPGe Detector Model No. GEM 23158 P-Plus, ORTEC Company), was used after MPs of MC Nd solutions containing radioactive ^{147}Nd tracer. To obtain quantitative data, reference sources with known amounts of the tracer were prepared. They consisted of filter papers with the same geometry as the targets, soaked with the tracer-containing solution. Twelve Ti3 targets were produced by electrolysis of aliquots of 100 μL of this solution at different deposition times: the first target after 15 min and the subsequent ones after increments of 15 min up to 180 min. The γ-measurements of the twelve targets gave the deposition yields reported in Figure 5-14, where the dashed curve fitting the open circles shows the Nd^{3+} depletion trend obtained by subtracting the deposition yield from 100%.

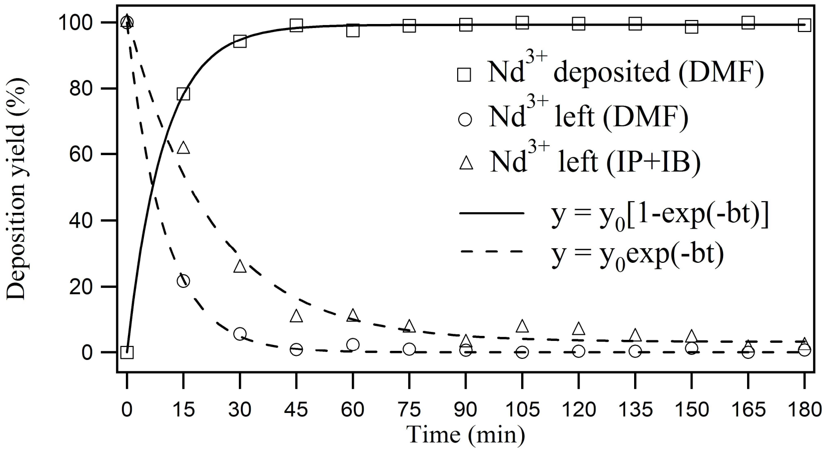

Figure 5-14 Molecular platings on Ti3 foils performed using MC plating solution in DMF or IP+IB: Nd^{3+} deposition yield (open squares) and depletion rate (open circles) in DMF, depletion rate in IP+IB [14] (open triangles); the lines are best fittings according to a first-order growth or decay. Error bars are not shown as smaller than the size of the symbols.

Nd^{3+} depletion shows an exponential decrease which can be fitted by a first-order rate law $y = y_0 \exp(-bt)$, i.e., $[\mathrm{Nd}]_t = [\mathrm{Nd}]_0 e^{-kt}$, where $[\mathrm{Nd}]_0$ and $[\mathrm{Nd}]_t$ are the initial and instantaneous concentrations of Nd^{3+} in solution, respectively, and *k* is the rate constant of the process.

For comparison Figure 5-14 shows also the Nd^{3+} depletion curve obtained during MP in IP+IB (open triangles) [14]. Both MPs follow a first-order rate law, but it is evident that the depletion kinetics is faster (i.e., *k* is larger) in DMF than in IP+IB. In particular, it is important to notice that, as in the case of IP+IB [14], the MP in DMF reaches an almost complete depletion of the Nd ions at a time corresponding to the recorded minimum (i.e., ca. 60 min) of the cell potential curve.

5.2.9.3 Conductivity measurements

The conductivity was measured using an inoLab Cond 720 conductometer connected to a TetraCon 325 standard conductivity cell. These measurements were performed only in a stirred DMF solution containing 0.22 mM $[Nd(NO_3)_3 \cdot 6H_2O]$ and 0.3 mM HNO_3. The conductivity (χ) was measured to be 46.5 ± 0.1 μS/cm. This value was used to evaluate the solution resistance, R, in the cell. The expression used for this evaluation is $R = \rho \cdot l/S$ [24], where ρ is the resistivity of the system (i.e., the inverse of the conductivity, ρ = 21.50 ± 0.05 kΩ·cm), l is the distance between the electrodes (2.80 ± 0.01 cm), and S is the surface area of the electrodes (9.0 ± 0.1 cm^2). The obtained cell resistance is 6.691 ± 0.011 kΩ. Using Ohm's first law, $V = RI$, where R is the cell resistance and I is the applied current (I = 6.00 ± 0.01 mA), the contribution of the ohmic drop to the overall cell potential was estimated to 40.15 ± 0.09 V. This value is in perfect agreement with the initial experimental value in Figure 5-13a. The cell potential during the MP process is, however, at least twice as high as the initial value. The voltage increase during the first 15 min of the electroplating is probably due to an increase of the overall resistance of the cell. Indeed, during MP the concentration of the electrolyte decreases as Nd^{3+} is deposited on the cathode, resulting in a decrease of conductivity. Also the formation and growth of the deposit, which is principally composed of Nd salts and complexes, presents an additional resistance. It appears reasonable that the cell potential observed during MPs is dominated by the ohmic drop.

5.2.9.4 Temperature measurements

Temperature measurements of the DMF plating solutions were performed using a TFK 150 thermometer connected to an inoLab pH 720 pH meter. The temperature was measured immediately before and after 3 h constant current density MP experiments at 0.17, 0.3 and 1.3 mA/cm^2. In all cases the MP experiments started after the solutions were cooled down to 16 °C. The measurements showed temperature increases of 0.4 ± 0.1 °C, 0.7 ± 0.1 °C, and 2.0 ± 0.1 °C, respectively. These results indicate that despite constant cooling during the experiments, a higher current density leads to a more pronounced temperature increase inside the system.

5.3 Discussion

Among various experimental parameters that may affect constant current density MP, two were found to be of crucial importance for the preparation of smooth and crack-free layers to be used as nuclear targets. These are the roughness of the deposition substrate and the solvent used for the platings. The different $\overline{\text{RMS}}$ values of the DMF MC targets grown on Ti3 and Ti5 substrates confirm that even small differences in surface roughness between the deposition substrates can influence the $\overline{\text{RMS}}$ of the growing layers [14]. Indeed, if the deposition substrate is rough (i.e., defective), the surface mobility of the deposited atoms will be reduced by trapping in the defects, and the produced layer will be of very low quality. Therefore, to produce smooth targets, deposition substrates as smooth as possible are required.

As regards the solvent, its importance does not only derive from being the medium in which the process is performed and hence the major factor influencing the electrochemistry of the MP, but also from the fact that the produced layers are mainly composed of physisorbed as well as chemisorbed solvent molecules. Hence, the role of the solvent in MP is twofold: it influences the electrochemistry of the process, but also the properties of the layer to be produced. Reasonable physical properties to be taken into account when choosing a solvent for MP are boiling point, viscosity, conductivity, and relative permittivity [16]. The boiling point determines the volatility of the solvent. The viscosity influences the rate of mass transfer in the solvent and is important in mass-transport controlled electrolytic processes like MP [14]. In turn, the rate of mass transfer influences the conductivity of the electrolyte solutions, which is fundamental for constant current density electrolysis experiments. Finally, the relative permittivity of a solvent has a decisive influence on the electrostatic solute-solute and solute-solvent interactions as well as on the dissolution and dissociation of electrolytes. In this study, pyridine and DMF were preferred over the more commonly used IP+IB mixture [9,10], after a careful analysis of these physical and chemical properties. All the samples produced using IP+IB, pyridine, and DMF as plating solvents and Ti3 foils as deposition substrates showed the presence of surface cracks. The liquid AFM analysis of the IP+IB sample suggested that the drying of the layer is at the basis of the surface cracking. To rule out the possibility that cracking may be connected to eventual layer-destructive chemical surface reactions occurring during the drying in air of the samples, XPS investigations were performed. The results of these investigations give no indications for the occurrence of such reactions, as air- and Ar-dried samples presented the same XPS signals. The absence of reactivity made then possible the AFM analysis in air of all these samples. These analyses confirmed the hypothesis of the drying-related nature of cracking. Indeed, the layers presenting surface cracks after drying in air also underwent cracking in Ar environment. More important than the drying environment is the boiling point of the solvent. Samples prepared in solvents with low boiling point (i.e., IP+IB and pyridine) showed the most severe surface cracking and the highest roughness. In contrast, films produced in DMF on Ti3 foils showed much smaller surface cracks and roughness. The reason why solvents with lower boiling point produce layers with severe surface cracking is very likely connected to the drying process. During drying in air, removal of solvent by evaporation implies solvent diffusion to the surface, conversion at the interface from the fluid phase to the vapour phase, and finally diffusion through the boundary layer into the distant air surrounding [25]. Because solvent evaporation diminishes the volume of the stress-free state of the coating, the current state shrinks to the maximum possible extent. Ahead of the solidification front, i.e., the front indicating the transition from liquid to solid, the shrinkage produces flow in the still liquid coating; behind, it produces in-plane stress in the solid coating because its in-plane shrinkage is frustrated by adhesion to the substrate [26,27]. The difference between the current state and the stress-free state of the coating is elastic strain to which stress is proportional via the elastic modulus (i.e., λ = *stress/strain*, where λ is the elastic modulus). Experimental and theoretical investigations [27,28] have shown that high elastic modulus and high yield-stress raise the level of stress and in-plane stress gradients, making the coatings susceptible to cracking and delamination. It is then reasonable to argue that because the high volatility IP+IB and pyridine solvents evaporate faster than the less volatile DMF (as we experimentally observed), the big volume decrease of the stress-free state of the coatings produced with such solvents will bring to a considerable difference between the current state and the stress-free one. The consequent large elastic modulus will then make these layers more likely to crack. In the “slow evaporation” regime achieved with DMF, instead, the difference between the states during the drying and the consequent elastic modulus will unlikely be as high as to create cracks. Cracking will mainly occur where a larger fragility of the layer is dictated by higher surface stress, i.e., where the surface defects have grown from the deposition foil. Once such defects are eliminated by using smoother deposition substrates, like Ti5, no cracks are observed in the surfaces of the produced DMF layers anymore. In particular, the layer growing on the Ti5 substrate during a MC plating experiment performed in DMF is assigned to follow a Frank-van der Merwe mechanism (layer-by-layer growth mechanism). In this growth mode a new layer is nucleated only after completion of the layer below and can spread over macroscopic distances creating very homogeneous surfaces, as demonstrated also by the RI studies.

The surface roughness and the morphology of the layers produced using DMF as plating solvent and Ti5 as deposition substrate can be considerably varied by changing some basic variables of the MP, like the concentration of the electrolyte to be plated and the applied current density. In the first case, the higher concentration of the electrolyte increases the flux of Nd^{3+} ions to the cathode, and hence the deposition rate onto the substrate. Because a high deposition rate causes the system to grow disorderly, the final surface roughness of the produced layer will be large [14]. In the case of the layers obtained applying different constant current densities, this simple interpretation is no longer sufficient to explain the changes observed in both roughness and morphology of the surfaces. In fact, if on the one hand, as expected, the current density of 1.3 mA/cm^2 increases the surface roughness of the layer produced with 0.3 mA/cm^2, on the other hand, the decrease to 0.17 mA/cm^2 increases the roughness even more. A possible explanation for these results comes from the fact that good epitaxial growths require not only low deposition rates, but also high surface mobility of the deposited species. In the case of the deposit obtained with the highest current density, the big outgrowths not covering the entire analyzed area may in fact suggest that the deposited species had a high surface mobility, which allowed them to condensate. In contrast, as regards the lowest current density sample, the rather small outgrowths spread over the entire surface area may indicate low surface mobility. The different mobilities could be related to the different temperatures of the substrates, which influence the ability of the deposited species to pass the activation barrier of diffusion. As the MP performed in DMF is controlled by Ohm’s first law, the preservation of a certain constant current density for a definite period of time implies the resistance of the solution to undergo several changes. If the global trend is that of an increase in the solution resistance, the temperature of the solution may increase as well, despite thermostatation of the system. As a consequence, the temperature of the cathode may also increase. This seems to be the case, as evidenced by the temperature measurements of the DMF MC solutions immediately before and after constant current density MPs at 0.17, 0.3 and 1.3 mA/cm^2. The combination of the effects of both deposition rate and surface mobility, dictated by the specific constant current density applied to the system, leads then to only few of the tested current densities being effective for defectless layer growths via MP. This is apparently the case of current densities in the range of 0.3-0.7 mA/cm^2.

Cell potential curves recorded during constant current density MPs in DMF showed to have common features with MPs in IP+IB [14]. As regards the initial increase of the potential at the beginning of the process and the different starting behaviours of the curves, we hypothesize that constant current density MPs, including electrolysis, create a high polarization of the electrodes, which causes the initial increase of the cell potential [14]. The smaller cell potential drop achieved with DMF than with IP+IB can be explained in terms of the larger conductivity of DMF. As both the constant current density MPs performed in IP+IB and DMF proved to be controlled by Ohm's first law, $V = RI$, it is easy to understand that the range of cell potential values must be smaller in DMF, because this solvent, having a larger conductivity, implies a smaller resistance. It is important to notice that in both solvents the deposition yield at the minimum of the cell potential curves is already high, with the depletion kinetics being faster in DMF than in IP+IB.

Finally, we like to stress that in none of the MPs performed from any of the used solvents metallic Nd was deposited. Rather, Nd is deposited on the cathodic surfaces as Nd^{3+} derivatives, and this is reasonable on the basis of the highly negative value of the Nd^{3+}/Nd standard redox potential ($E° = -2.323$ V [29]), typical of lanthanide cations.

5.4 Conclusion

To optimize the production of smooth and crack-free layers to be used as nuclear targets, several constant current density MPs were performed using Nd as a model element. The variables chosen for these investigations were: plating solvent, electrolyte concentration, applied current density, and surface roughness of the deposition substrate. Different environments were also used to dry the produced samples. The obtained deposits were analyzed using γ-ray spectroscopy, XPS, RI, AFM, and SEM. The results obtained from the characterization were used to identify the key parameters controlling the molecular plating of smooth and crack-free layers. The roughness of the deposition substrate and the solvent used for the platings proved to be two core factors playing a decisive role for the production of high quality layers. Surface cracking in fact occurred by means of drying only when volatile solvents and deposition substrates that were not smooth enough, were used. Different drying environments like air and Ar did not show to have any effect on the deposited layers.

Molecular platings from DMF proved to be superior over the widely performed IP+IB platings [9,10]. Indeed, despite being also governed by Ohm's first law and by similar depletion kinetics, DMF MPs performed on Ti5 substrates produced targets showing complete elimination of the surface cracks as well as high smoothness and homogeneity.

Moreover, no Pd impurities from the oxidation of the Pd anode were found on the cathode deposit when MPs were performed in DMF. The absence of such impurities may be of importance in nuclear science investigations as they could give rise to unwanted background in accelerator-based experiments.

Finally, the surface roughness and morphology of the layers produced using DMF and Ti5 substrates proved to be very sensitive to changes in, e.g., electrolyte concentration and current density.

The present work demonstrates that molecular plating can be applied to produce layers that are as smooth and crack-free as those produced by PAD, and suitable as nuclear targets. An important advantage of MP over PAD is that it is a faster deposition process, as it needs just one plating cycle to reach almost 100% deposition yield. With PAD, in contrast, coating efficiencies for one single application of ca. 33% are reported [11]; hence several deposition cycles need to be performed to obtain quantitative yields.

The results obtained in this study may also be applied for the production of smooth and crack-free lanthanide targets other than Nd, and also for the preparation of heavier actinide targets with an oxidation state of 3+ (e.g., americium and curium), for which Nd is a good model element.

Acknowledgements

The authors would like to thank the staff of the TRIGA Mainz for performing the irradiations and Dr. T. Lauer for performing the coating of the Si wafers. A. Vascon would like to thank V. Yakusheva from the GSI target laboratory for her assistance during the SEM measurements and acknowledges financial support from the German Federal Ministry of Science and Education (BMBF) under Contract number 02NUK013E.

References

[1] A. Becerril-Vilchis, A. Cortès, F. Dayras, J. De Sanoit, Nucl. Instrum. Meth. A **369** (1996) 613-616.

[2] B.W. Filippone, M. Wahlgren, Nucl. Instrum. Meth. A **243** (1986) 41-44.

[3] K.M. Glover, L. Bint, D.B. Gayther, M. King, B. Whittaker, R.A.P. Wiltshire, Nucl. Instrum. Methods **200** (1982) 151-160.

[4] S. Clifford, X. Guo-jj, C. Ingelbrecht, M.J. Pomeroy, Nucl. Instrum. Meth. A **480** (2002) 29-35.

[5] R. Grossmann, H.J. Maier, H.U. Friebel, D. Frischke, Nucl. Instrum. Meth. A **480** (2002) 209-213.

[6] L.V. Drapchinsky, T.E. Kuzmina, S.M. Soloviev, Nucl. Instrum. Meth. A **438** (1999) 116-118.

[7] S. Chakrabarty, B.S. Tomar, A. Goswami, V.A. Raman, S.B. Manohar, Nucl. Instrum. Meth. B **174** (2001) 212-214.

[8] K.M. Glover, F.J.G. Rogers, T.A. Tuplin, Nucl. Instrum. Methods **102** (1972) 443-450.

[9] N. Trautmann, H. Folger, Nucl. Instrum. Meth. A **282** (1989) 102-106.

[10] K. Eberhardt, M. Schädel, E. Schimpf, P. Thörle, N. Trautmann, Nucl. Instrum. Meth. A **521** (2004) 208-213.

[11] M.A. Garcia, M.N. Ali, T. Parsons-Moss, P.D. Ashby, H. Nitsche, Thin Soild Films **516** (2008) 6261-6265.

[12] M.A. Garcia, M.N. Ali, N.N. Chang, T. Parsons-Moss, P.D. Ashby, J.M. Gates, L. Stavsetra, K.E. Gregorich, H. Nitsche, Nucl. Instrum. Meth. A **592** (2008) 483-485.

[13] Q.X. Jia, T.M. McCleskey, A.K. Burrell, Y. Lin, G.E. Collis, H. Wang, A.D.Q. Li, S.R. Foltyn, Nat. Mater. **3** (2004) 529-532.

[14] A. Vascon, S. Santi, A.A. Isse, T. Reich, J. Drebert, H. Christ, Ch.E. Düllmann, K. Eberhardt, Nucl. Instrum. Meth. A **696** (2012) 180-191.

[15] A. Vascon, Ch.E. Düllmann, K. Eberhardt, B. Kindler, B. Lommel, J. Runke, Nucl. Instrum. Meth. A **655** (2011) 72-79.

[16] K. Izutsu, Electrochemistry in Nonaqueous Solutions, first ed., Wiley-VCH, Darmstadt, Germany, 2002.

[17] A. Vascon, S. Santi, A.A. Isse, T. Reich, J. Drebert, H. Christ, K. Eberhardt, Ch.E. Düllmann, J. Radioanal. Nucl. Chem. (2012) accepted.

[18] R. Horcas, J.M. Fernandez, J. Gomez-Rodriguez, J. Colchero, A.M. Gomez-Herrero, W. Baro, Rev. Sci. Instrum. **78** (2007) 013705-1.

[19] D. Liebe, K. Eberhardt, W. Hartmann, T. Häger, A. Hübner, J.V. Kratz, B. Kindler, B. Lommel, P. Thörle, M. Schädel, J. Steiner, Nucl. Instrum. Meth. A **590** (2008) 145-150.

[20] U. Gelius, P.F. Hedèn, J. Hedman, B.J. Lindberg, R. Manne, R. Nordberg, C. Nordling, K. Siegbahn, Phys. Scr. **2** (1970) 70-80.

[21] R.C. Gray, J.C. Carver, D.M. Hercules, J. Electron Spectrosc. **8** (1976) 343-358.

[22] D.T. Clark, R.D. Chambers, D. Kilcast, W.K.R. Musgrave, J. Chem. Soc., Faraday Trans. 2, **68** (1972) 309-319.

[23] C.D. Wagner, W.M. Riggs, L.E. Davis, J.F. Moulder, G.E. Muilenberg, Handbook of X-Ray Photoelectron Spectroscopy, Perkin-Elmer Corporation, Physical Electronics Division, Eden Prairie, Minn. 55344, 1979.

[24] S. Glasstone, An Introduction to Eletrochemistry, first ed., Litton Educational Publishing, Inc., New York, 1942.

[25] D.E. Haas, J.N. Quijada, S.J. Picone, D.P. Birnie, SPIE Proc., Sol-Gel Optics V, B. Dunn, E. Pope, H.K. Schmidt, M. Yamane, Editors, **3943** (2000) 280-284.

[26] H. Lei, L.F. Francis, W.W. Gerberich, L.E. Scriven, AIChE J. **48** (2002) 437-451.

[27] H. Radhakrishnan, Ph.D. Thesis, University of Minnesota, Minneapolis, MN, USA, 2006.

[28] J. Malzbender, G. De With, J. Mater. Sci. **35** (2000) 4809-4814.

[29] D. R. Lide (Ed.), CRC Handbook of Chemistry and Physics, 87th ed., 2006.

6. The performance of thin layers produced by molecular plating as α-particle sources

A. Vascon[1], N. Wiehl[1,2], T. Reich[1], J. Drebert[1], K. Eberhardt[1,2], Ch.E. Düllmann[1,2,3]

[1]Institute of Nuclear Chemistry, Johannes Gutenberg University Mainz, 55099 Mainz, Germany
[2]SHE Chemistry Research Section, Helmholtz Institute Mainz, 55099 Mainz, Germany
[3]SHE Chemistry Department, GSI Helmholtzzentrum für Schwerionenforschung GmbH, 64291 Darmstadt, Germany

Published in:

Nuclear Instruments and Methods in Physics Research A **721** (2013) 35-44.

Abstract

Sources for α-spectroscopy studies were prepared. Constant current density molecular plating was used to produce layers containing the α-particle emitter ^{147}Sm. Different parameters of the molecular plating process were varied, namely the plating solvent (an isopropanol/isobutanol mixture, pyridine, and N,N-dimethylformamide), the applied deposition time (90, 180, and 360 min), and the surface roughness of the deposition substrate (ca. 10, 20, and 300 nm). Using different analytical techniques, Sm deposition yields, chemical composition of the produced surfaces, surface homogeneity, roughness and morphology were investigated. Alpha spectra were recorded with a Si solid-state detector for samples belonging to the different types of characterized sources, and big differences in the peak shape and position of the peak maximum were observed, as well as significant differences in the fraction of α particles reaching the detector positioned above the samples. An explanation for the observed features is presented. The results of these studies led to the identification of the key plating parameters, namely the plating solvent and the roughness of the deposition substrate, which most affect the quality of the α spectra.

Keywords: α-particle spectroscopy, ^{147}Sm, molecular plating, atomic force microscopy (AFM), scanning electron microscopy (SEM), X-ray photoelectron spectroscopy (XPS)

6.1 Introduction

Alpha-particle sources find wide use in the nuclear sciences. Important parameters, which characterize the quality of an α-particle source, include the energy distribution of α particles of a given α line – which should be as small as possible – or the accuracy with which the absolute content of the α emitter contained in the source is known. The first feature depends critically on the quality of the thin film containing the α emitter – ideally a weight-less sample, or at least a homogeneous and smooth layer. The second feature is often evaluated from α spectroscopic measurements of the source. For this, generally a homogeneous distribution of the α emitter throughout the whole source is assumed. Among the methods to produce high-quality thin films, electrodeposition from aqueous or organic media is widely used. An example for the former is the production of Os targets to search for an α branch in ^{184}Os [1]. The latter method is commonly referred to as molecular plating (MP) [2]. It is prominently used to produce targets of long-lived transuranium isotopes for accelerator experiments in the research on superheavy elements [3]. There, in the case of α decaying isotopes like ^{249}Cf the deposition yield or total activity of the layer may be assayed by α spectroscopy [4]. Another current example, where the production of high-quality α sources is required, concerns a planned precise half-life ($t_{1/2}$) measurement of the very long-lived low energy α-emitter ^{144}Nd ($t_{1/2} = (2.65 \pm 0.37) \cdot 10^{15}$ y, $E_\alpha = 1.85$ MeV [5]), which is of interest in the context of an envisaged search for neutrinoless double-beta decay of ^{150}Nd, where ^{144}Nd is one of the unwanted background radioactivities [6]. As a first step towards the production of well-characterized Nd targets produced by MP, where the Nd content is known with high accuracy, we have recently performed systematic studies of Nd-containing layers produced by MP [7-10]. In our studies, we characterized the layers by different analytical methods (X-ray photoelectron spectroscopy, atomic force microscopy, scanning electron microscopy, or radiographic imaging) to investigate the surface chemistry, the roughness, the morphology, and the homogeneity of the produced layers. We found the plating variables to critically influence the layer properties, including the homogeneity of the Nd distribution throughout the targets, their surface roughness, and morphology. As key parameters affecting the target properties, we identified the surface roughness of the substrate onto which the target was deposited, the solvent (in our studies: N,N-dimethylformamide -DMF-, an isopropanol/isobutanol mixture -IP+IB-, and pyridine) from which the Nd was electroplated, the Nd concentration in the plating solution, and the applied current density. It turned out that in general the Nd ions contribute to less than 20% to the total current established during MPs (see Figure 3-12 in [8]), with the remainder of the current being mainly due to electrolysis of the solvent, the products of which are directly incorporated into the Nd-containing layer. Also, kinetic studies showed the Nd to deposit relatively quickly. In many cases, quantitative deposition of Nd was achieved significantly before the end of the plating process, which lasted up to several hours. Accordingly, the Nd is always covered by a Nd-free layer consisting purely of elements other than that of interest. As the energy distribution of the α particles leaving the source is determined by electronic energy loss and energy-loss straggling, such effects can be expected to directly influence the quality of the α spectra. This issue is of importance when low specific activities of very long-lived, low energy α-emitters have to be measured, because in this case, if the α-peak resolution is low, particles may be degraded to an extent that they fall within the region of electronic background and hence be lost. By careful optimization of all experimental parameters of the MP process, we recently achieved in [10] the production of very homogeneous, smooth and crack-free Nd layers.

In the current work, we focused on the properties of the α spectra obtained from samples produced 1) on substrates of different roughness, 2) from three different solvents (IP+IB, DMF, pyridine), and 3) during different deposition times. We also studied the properties of pure solvent layers, as they cover many of the targets produced by MP under these conditions, and performed MP experiments where the element of interest was absent in the plating solution. While Nd containing layers could serve as α-particle sources due to the high natural abundance of radioactive ^{144}Nd, such studies suffer from the long half-life of this isotope. To perform reasonably quick investigations of the sources, in this work Sm was preferred over Nd and ^{147}Sm (α, $t_{1/2} = (1.070 \pm 0.009) \cdot 10^{11}$ y, $E_\alpha = 2.24$ MeV [11]) was chosen as model isotope for the investigations because of its significantly shorter half-life and hence higher specific activity, and the very high precision, with which the half-life is known. We note that Sm is also a tri-valent lanthanide like Nd, and therefore its electrodeposition chemistry may be expected to be similar. To verify this assumption, and to characterize the Sm samples, several MP experiments were performed where the above mentioned parameters 1-3 were varied and the layers characterized in the same manner as the Nd layers described in [10] (Section 6.2). Alpha spectra were recorded from the different samples. From the determined amount of Sm present in the produced layers, the measured number of α particles within our detector in a given time, and the precisely known half-life of ^{147}Sm we calculated the efficiency of our source-detector setup (hereafter referred to as experimental efficiency). This efficiency was compared to the estimated geometric efficiency of our detection system, obtained using a Monte Carlo simulation (hereafter referred to as simulated efficiency). (Section 6.3). As the geometry of the source was always identical (same source- and detector diameter; same source-detector distance) the experimental efficiencies might naively be expected to be identical for all sources. This however is not the case, and the differences are likely associated with the quality of the sample and the parameters used in its preparation.

6.2 Sample production and characterization

6.2.1 Deposition cell

The cell used for the MPs was already shown and described in detail in [8]. This cell is characterized by a central polyether ether ketone (PEEK) body where the electrolytic solution is inserted. The anode and the cathode are both Ti blocks covered by circular Pd and Ti foils, respectively. Each of the two electrodes has an effective deposition area of 9.0 ± 0.1 cm^2. A constant temperature (T = 16 °C) was maintained in the cell by water-cooling the Ti blocks in physical contact with the electrodes. As was noted in [10], the temperature during plating may be slightly higher due to ohmic heating of the solution, despite the water-cooling.

6.2.2 Deposition substrates

The deposition substrates used in the present work were already described in detail in [8]. Due to the critical influence of the surface roughness on the effects studied in this work, we give in Table 6-1 their average root mean square ($\overline{\mathrm{RMS}}$) surface roughnesses, evaluated by AFM after a cleaning procedure (see Section 3.2.5 in [8]). To facilitate comparison between the results reported here and previously in [8,10], we keep the labelling of our substrate types as in [8,10].

Table 6-1 Deposition substrates used for the MPs performed and their average surface roughness values ($\overline{\mathrm{RMS}}$) determined by AFM.

Substrate type	Production technique	$\overline{\mathrm{RMS}}$ (nm)
Ti3	rolling	24 ± 7
Ti4	etching	340 ± 140
Ti5	magnetron sputtering	12.8 ± 0.7

Substrates with different surface roughness were used for deposition: medium (Ti3), high (Ti4), and low roughness (Ti5). Ti3 was a circular 50 µm-thick Ti foil cut from a bigger rolled foil (Goodfellow). Ti4 was obtained by etching a Ti3 foil with concentrated HCl (~36%) for 45 min under an IR lamp. Figure 6-1 shows an AFM image of a Ti4 substrate: the etching of the Ti foil creates evident surface defects. Ti5 was produced by magnetron sputtering a 300-µm thick mechanically-polished Si wafer with 100 nm metallic Ti. AFM images of Ti3 and Ti5 foils were already shown in Figures 5-2a and b in [10], respectively.

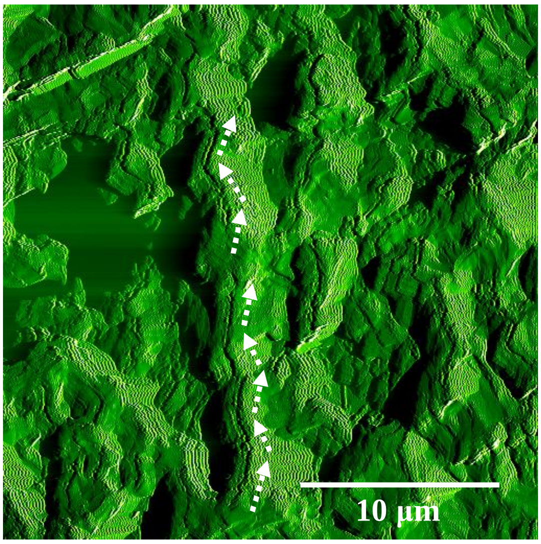

Figure 6-1 (25 × 25) μm^2 amplitude AFM image of the Ti4 deposition substrate. The dashed white arrows show some of the surface defects created by etching of the Ti3 foil.

6.2.3 Molecular plating at constant current density

Before any deposition, both the anode (Pd foil) and the cathode (Ti foil) were cleaned with 6 M HCl (1 × 3 mL washing), water (3 × 3 mL washings), and isopropanol (1 × 3 mL washing). The Ti5 foils were cleaned using HCl with a lower concentration (i.e., 0.6 M) to avoid corrosion-induced increase in surface roughness, which was observed at 6 M HCl concentration in [8]. For the MP processes, ^{147}Sm-enriched Sm_2O_3 (Isoflex USA) was used. The isotopic composition was: 0.13% ^{144}Sm, 96.4% ^{147}Sm, 2.18% ^{148}Sm, 0.53% ^{149}Sm, 0.17% ^{150}Sm, 0.36% ^{152}Sm, and 0.23% ^{154}Sm. The Sm oxide, Sm_2O_3, was transformed into the nitrate, $Sm(NO_3)_3$, via dissolution in 15 M HNO_3. The liquid was evaporated by heating under an IR lamp and the obtained solid was redissolved with 0.1 M HNO_3 to produce a Sm nitrate solution. Three Sm stock solutions were prepared following this procedure. From the solution an aliquot of 100 µL was added to a mixture of 1 mL isopropanol (Fisher Chemical) and 34 mL isobutanol (Applichem) (i.e., IP+IB: 3% isopropanol, 97% isobutanol), or to 35 mL of pyridine (Merck) or DMF (Merck), finally yielding a 0.22 mM solution of Sm^{3+} in the cell. The concentration of HNO_3 in the cell was always 0.3 mM. The plating solutions were stirred by means of a quartz tip ultrasonic stirrer (Bandelin Sonopuls HD 2070) operated at 30% power pulse. MP experiments were carried out for 90, 180 or 360 min by applying a constant current of 6 mA. The current density, 0.7 mA/cm^2, was the same in all cases. Once the MP process was over, each of the produced samples was extracted from the cell and let dry in air. The thickness of the deposits would be 125.6 ± 1.6 μg/cm^2, if 100% deposition yields were obtained.

6.2.4 X-ray photoelectron spectroscopy (XPS) studies

6.2.4.1 Experiments

The surface chemistry of the samples was investigated by using X-ray photoelectron spectroscopy (XPS) with an Al K_α radiation. The X-ray source was operated at 10 kV anode voltage and a current of 10 mA. The pass-energy of the hemispherical energy analyzer was 50 eV. The pressure inside the ultra-high vacuum chamber was in the range of $(1.2\text{-}2.0)\cdot10^{-9}$ mbar. A total of five samples was investigated. Two samples were targets produced from DMF on Ti3 foils using deposition times of 180 min, which was previously used in experiments with Nd [10], and 360 min. Only DMF was chosen as reference plating solvent for these deposits because of the excellent results previously obtained in the preparation of Nd targets [10]. The 180 min-long plated sample was produced to understand whether the surface chemistry of the Sm layers is similar or differs from the chemistry of the DMF Nd layers. A deposition time of 360 min was instead chosen to investigate potential differences in the surface chemistry of the samples when long plating times are adopted. After the initial surface investigation, these two samples underwent 10 min sputtering using 4 kV Ar^+ ions, and further XPS analyses were then performed. The other three targets were produced from Sm-free solutions to simulate and understand the electrochemistry of the MP process when no Sm^{3+} ions are present in solution anymore, i.e., when the Sm^{3+} ions have all been deposited on the cathode. These targets were produced by adding 100 μl of 0.1 M HNO_3 to the deposition cell, and then by plating for 180 min with IP+IB, DMF, or pyridine as solvents, and Ti3 foils as deposition substrates. After the first surface investigation, only the pyridine sample underwent Ar^+ sputtering.

The procedure adopted to determine the binding energies of the XPS lines of interest was identical to that described in Section 5.2.8 in [10]. As the aim of the present work was mainly to investigate the surface chemistry of the samples, a detailed chemical surface analysis of the deposits was performed only for C, which was known from [8] and [10] to be the main element composing the outer layer of the produced samples. The C 1s spectra are therefore the only ones to be shown with multicomponent fitting analysis.

6.2.4.2 Results

6.2.4.2.1 Sm samples

The XPS analyses of both Sm-containing samples showed the presence of the following elements: C, N, O, and Sm. The corresponding XPS signals were: C 1s, N 1s, O 1s, Sm 3d, and Sm 4d. The analyses never showed Ti signals (from the substrate), indicating that all the deposited layers are thick. After evaluation of the total peak areas of the detected elements, almost no difference was noted between the 180 and 360 min samples, except for the slightly larger C 1s/Sm 3d ratio of the 360 min sample (i.e., 0.05 *vs* 0.04) before Ar^+ sputtering. Figure 6-2 shows the 180 min spectra of Sm 3d (a) and C 1s (b) before sputtering (i.e., 0 min sputtering in the figure) and after 10 min sputtering with Ar^+ ions.

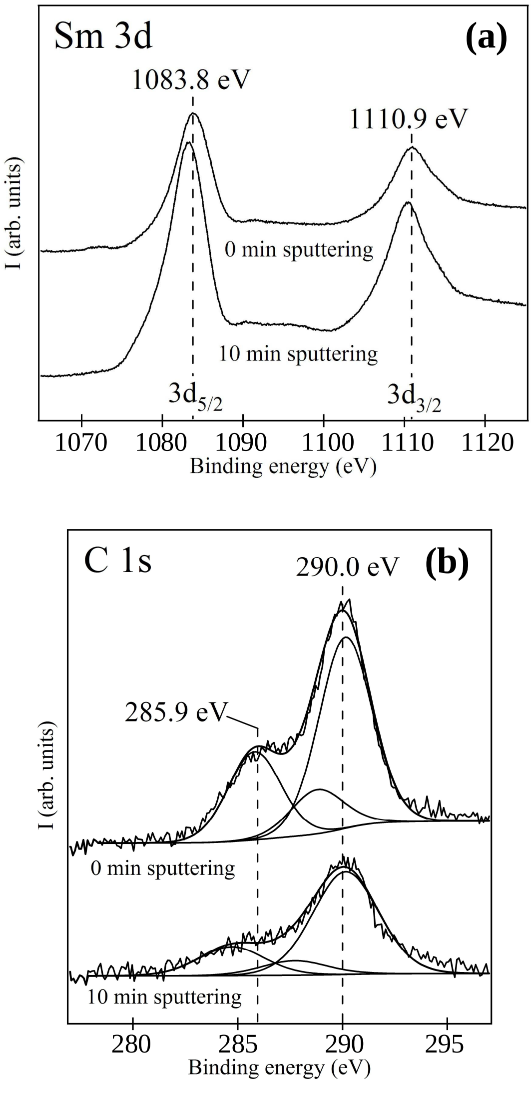

Figure 6-2 XPS spectra of the sample obtained after 180 min plating on Ti3 substrate using 0.22 mM Sm solution in DMF: (a) Sm 3d, (b) C 1s, before sputtering (indicated as 0 min sputtering in the figure), and after 10 min sputtering with Ar^+ ions. Identical offsets were applied between the spectra of each figure.

The measured binding energy of Sm $3d_{5/2}$ in the surface layer is 1083.8 eV (Figure 6-2a), which is close to the literature value of 1084.3 eV [12] for Sm^{3+}. Therefore, Sm is present as Sm^{3+} in the investigated deposited layer (possibly as carboxylate, oxide, or hydroxide), and this is reasonable on the basis of the highly negative value of the Sm^{3+}/Sm standard redox potential ($E° = -2.41$ V) [13]. A small shift of ca. - 0.6 eV after sputtering could indicate the presence of different Sm^{3+} species in the topmost surface layer of the sample. The C 1s spectra reported in Figure 6-2b show the presence of two XPS lines centered at 285.9 eV and 290.0 eV, respectively. These lines are fitted by three peaks: the peaks at ca. 286 eV and 289 eV are carbon of the DMF solvent [14]. The peak at ca. 4 eV higher binding energy (i.e., 290.0 eV) can be attributed, according to literature, to COOM -metal carboxylate- (289.0 eV [12]) groups formed during the plating process. No chemical shifts are observed after sputtering.

Both spectra of Figure 6-2 show that as long as the sputtering of the surface proceeds, the intensity of the Sm 3d signal increases, while the C 1s intensity decreases. Particularly, as regards the decrease of the C 1s intensity, it is evident that the 285.9 eV component is removed more easily than the 290.0 eV one. We attribute the 285.9 eV line to originate from physisorbed solvent on the surface of the deposit, while the 290.0 eV line is due to chemisorbed COOM species arising from solvent electrolysis. These trends clearly show the obtained sample to be characterized by an outer layer of solvent, which covers the Sm deposit. This is similar to the observation we made previously with DMF Nd samples [10], and we conclude the MP behaviour of both elements to be similar.

6.2.4.2.2 Sm-free samples

The XPS analyses of the three Sm-free samples always showed the presence of Na^+, Ca^{2+}, or K^+ ions in the investigated layers. These ions likely derive from the aqueous HNO_3 solutions used for the platings, and because of the highly negative values of their standard redox potentials, i.e., $E°_{Na+/Na} = -2.71$ V [15], $E°_{Ca2+/Ca} = -2.76$ V [15], and $E°_{K+/K} = -2.92$ V [15], they are not reduced.

The recorded C 1s spectra of the samples (not shown) were similar to those of the air-dried Nd samples produced in IP+IB, DMF, and pyridine (see Figures 5-10b, 5-11b, and 5-12b in [10], respectively). Indeed, the samples showed peaks at 285.3 eV, 285.9 eV, and 286.4 eV, which match the peaks of the physisorbed carbon of the IP+IB, DMF, and pyridine solvents investigated in Section 5.2.8 of [10], respectively. Moreover, peaks at 288.5 eV (IP+IB), 289.6 eV (DMF), and 288.4 eV (pyridine) were detected, and can be attributed to chemisorbed COOM -metal carboxylate- (289.0 eV [12]) groups formed during the plating process. Therefore, we conclude the solvents to undergo electrolysis also in the absence of Sm electrolyte.

Among all the produced samples only Sm-free IP+IB and DMF deposits showed Ti signals. In the case of the pyridine layer the absence of a Ti signal led us to perform 10 min sputtering with Ar^+ ions to check whether Ti would then appear in the spectra. Even after this sputtering time, no Ti peaks were recorded. This indicates that in the case of the sample produced from pyridine the deposited layer is much thicker than the layers obtained from DMF or IP+IB applying the same deposition times (i.e., 180 min). Table 6-2 shows the ratios of the total peak areas C 1s/Ti 2p, and the ratios between the sum of the peaks fitting a certain spectral component and a total peak area, like the ratios reported as C 1s (ca. 285 eV)/C 1s, C 1s (ca. 286 eV)/C 1s, and C 1s (ca. 289 eV)/C 1s.

Table 6-2 Ratios of the peak areas of some of the detected elements.

Sample	Ratios of XPS peak areas	Ratio value
DMF	**C 1s/Ti 2p**	0.5
	C 1s (ca. 286 eV)/C 1s	0.46
	C 1s (ca. 289 eV)/C 1s	0.54
IP+IB	**C 1s/Ti 2p**	0.4
	C 1s (ca. 285 eV)/C 1s	0.65
	C 1s (ca. 289 eV)/C 1s	0.35
Pyridine	**C 1s/Ti 2p**	-
	C 1s (ca. 286 eV)/C 1s	0.76
	C 1s (ca. 289 eV)/C 1s	0.24

Table 6-2 shows that the C 1s/Ti 2p ratio of the DMF sample is only slightly larger than the corresponding one of the IP+IB sample. This suggests the thicknesses of the deposited solvent layers to be similar. The ratios reported in Table 6-2 also show that the fraction of physisorbed solvent tends to increase from the DMF sample to the pyridine one, which is the sample with the most physisorbed solvent. This is in line with results obtained in [10], which suggested the electrochemistry of the three MP processes to be quite different.

6.2.5 Scanning electron microscopy (SEM) studies

6.2.5.1 Experiments

The morphology of the targets was studied using scanning electron microscopy (SEM) (Philips XL30). The microscope was operated at 20 kV. The pressure inside the vacuum chamber was $5 \cdot 10^{-5}$ mbar. Backscattered and secondary electrons were detected. Magnification factors of 1000× were used.

6.2.5.2 Results

Figure 6-3 shows SEM images of three samples, which were produced with a plating time of 180 min from IP+IB using the following deposition substrates: (a) Ti3, (b) Ti4, and (c) Ti5.

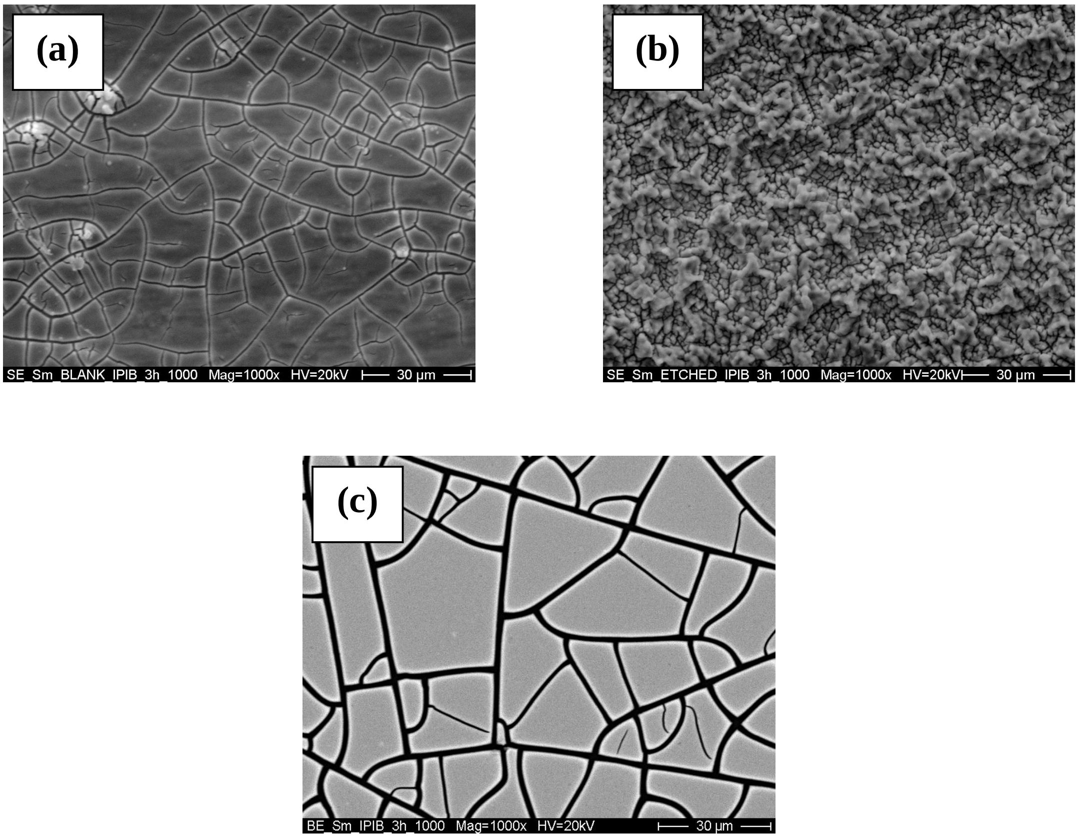

Figure 6-3 1000× SEM images of the samples produced using 0.22 mM Sm solution and IP+IB solvent on the following deposition substrates: (a) Ti3, (b) Ti4, and (c) Ti5.

The SEM images show that regardless of the different substrates used for the deposition all the samples prepared from IP+IB are characterized by severe cracking of the surfaces. The layer deposited on the Ti5 foil (Figure 6-3c) is visibly the smoothest, while the surface of the sample grown on the Ti4 substrate (Figure 6-3b) is the roughest.

Particularly, Figure 6-3b shows sharp outgrowths which indicate preferential growth of the layer along the edges of the defects created by etching of the Ti3 surface (see also Figure 6-1).

Figure 6-4 shows SEM images of the three samples that were produced with a plating time of 180 min using pyridine on a Ti5 deposition substrate (a), and DMF on Ti3 (b) or Ti5 (c) foils.

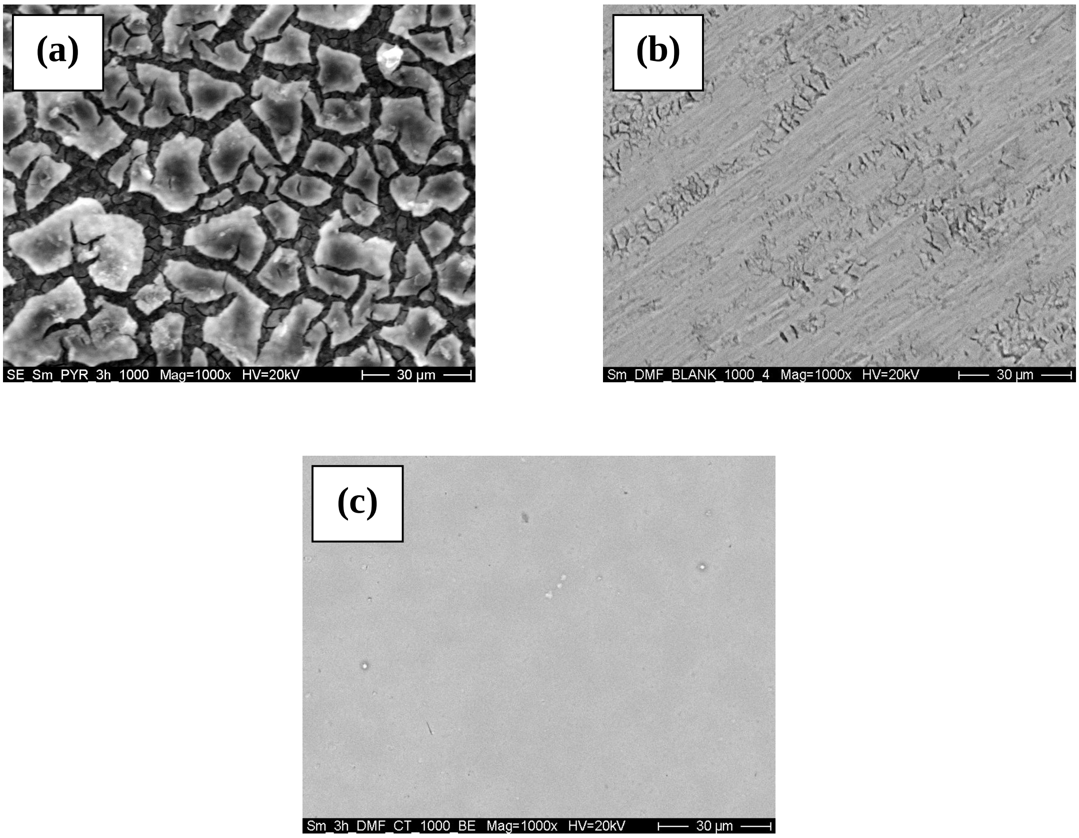

Figure 6-4 1000× SEM images of the samples produced using 0.22 mM Sm solution and the following substrate/solvent systems: (a) Ti5/pyridine, (b) Ti3/DMF, (c) Ti5/DMF.

The images of these samples are identical to Figures 5-8a, b, and c, respectively, of Nd layers investigated in [10]. The similar morphology is confirmed by pyridine samples being heavily cracked and rough (Figure 6-4a), whereas the DMF layers gain higher homogeneity and complete removal of the surface cracks upon going from the rougher Ti3 deposition substrate (Figure 6-4b) to the smoother Ti5 one (Figure 6-4c). In particular, Ti5 DMF samples plated for 90 and 360 min (not shown here) had both smooth and crack-free surfaces.

6.2.6 Atomic force microscopy (AFM) studies

6.2.6.1 Experiments

The surface roughness of the samples, i.e., the measure of the texture of a surface quantified by the vertical deviations of a real surface from its ideal planar form, was investigated by using atomic force microscopy (AFM) (MFP 3D Asylum Research). AFM investigations were performed in air aiming at verifying whether the layer growth mode defined in [10] for Nd layers is the same also for Sm layers.

The AFM analysis allowed studying the layer-growth mechanism with progressing time of the plating process using targets produced with DMF and Ti5 deposition foils. This was limited to samples produced from DMF on Ti5 foils due to the low quality of the layers grown from IP+IB or pyridine on different deposition substrates, which prevents an unambiguous assignment of the layer-growth to a specific mechanism in these cases. A total of six targets was prepared using different deposition times: the first target was produced by plating for 30 min and the subsequent ones after increments of 30 min up to 180 min. The tapping-mode AFM analysis was the same for all the targets: ten (5×5) μm^2 images were recorded for each target in ten different positions. From each of the ten images two root mean square (RMS) values were evaluated using a (1.5×1.5) μm^2 mask in two different positions inside the image. The final surface roughness value of each target was evaluated as the arithmetic mean of the twenty RMS values measured for that target (i.e., $\overline{\text{RMS}}$).

6.2.6.2 Results

Figure 6-5 shows the $\overline{\text{RMS}}$ trend of the growing layer to have an almost constant behaviour during the whole period of deposition (180 min): the surface roughness does not undergo major variations, maintaining an average value of about 10 nm.

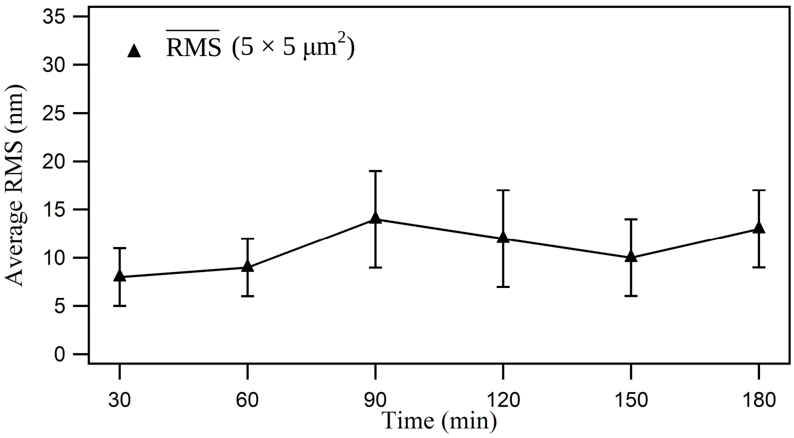

Figure 6-5 $\overline{\text{RMS}}$ *vs* time trend of the layer-growth study of the targets produced using 0.22 mM Sm salt with DMF and Ti5 deposition foils.

None of the AFM images recorded for this layer-growth study showed surface cracking. As an example, Figure 6-6 shows one (5 × 5) μm^2 image of the deposit grown for 90 min. The analysis of such images and the evaluated constant $\overline{\text{RMS}}$ trend suggest that the layer growing on a Ti5 substrate during a plating experiment performed with 0.22 mM Sm solution in DMF follows a Frank-van der Merwe mechanism (layer-by-layer growth mechanism, see Figure 6-12 in Section 6.3). This growth mechanism is the same one as that defined for Nd layers grown on Ti5 foils using DMF [10].

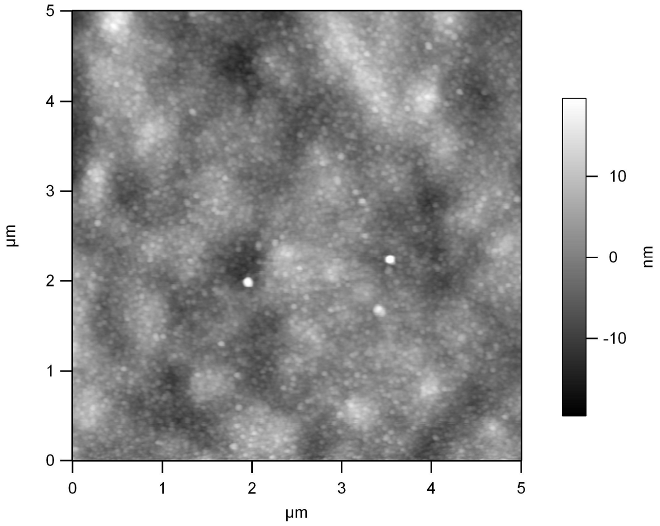

Figure 6-6 (5 × 5) μm^2 topography AFM image of the sample produced using Ti5 substrate and 0.22 mM Sm solution in DMF: deposit grown for 90 min.

For characteristic average surface roughness values of samples produced from solvents other than DMF, we refer to [10].

6.2.7 Radiographic imaging (RI) studies

6.2.7.1 Experiments

Radioactive targets were produced by performing MPs of Sm solutions containing a radioactive tracer of the element to be plated (Sm: ^{153}Sm, β^-, $t_{1/2}$ = 46.28 h [16], E_γ = 103 keV). The tracer was produced in a (n,γ) reaction on ^{152}Sm, by irradiating an aliquot of 100 μL of the stock solution with thermal neutrons in the TRIGA Mainz research reactor. The homogeneity of these targets was inspected with radiographic imaging (RI), employing a FUJIFILM FLA 7000 equipped with reusable imaging plates and a 650 nm laser for the reading process. To verify the homogeneity of the target, the image was overlaid by a grid of square spots with an area of 0.25 mm^2 each. The spatial resolution for γ-emitting nuclides was < 200 μm [17].

6.2.7.2 Results

Figure 6-7 shows the RI results of targets that were all plated for 180 min using Ti5 foils and the following solvents: pyridine (a), IP+IB (b), and DMF (c).

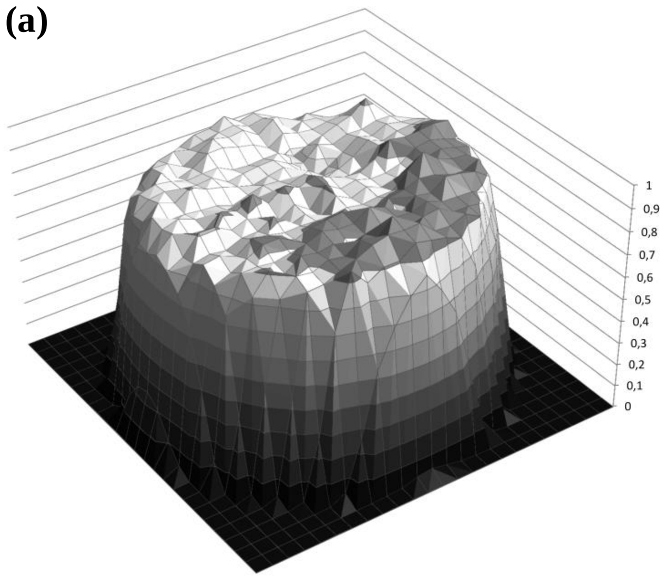

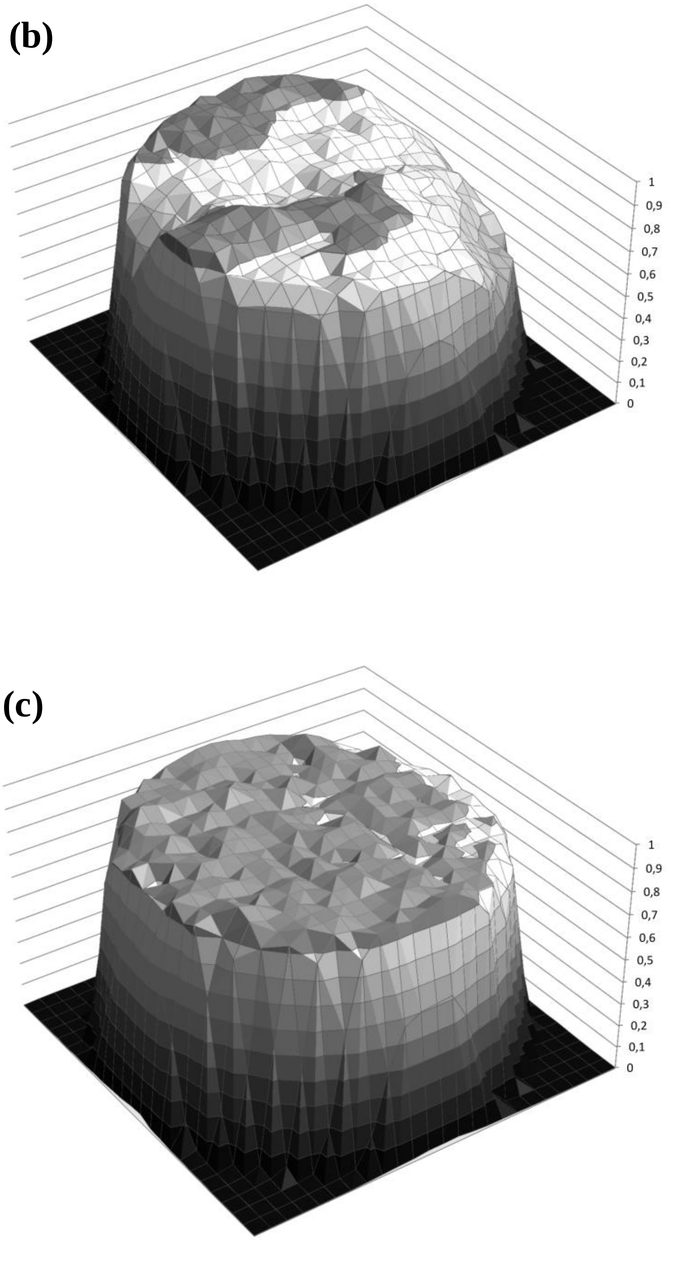

Figure 6-7 RI normalized 3D graphs of samples produced using 0.22 mM Sm solution and the following substrate/solvent systems: (a) Ti5/pyridine, (b) Ti5/IP+IB, and (c) Ti5/DMF.

Figures 6-7a and b show poor homogeneity of the produced layers, while Figure 6-7c shows that the combination of DMF and the deposition substrate Ti5 produces the most homogeneous targets.

6.2.8 Gamma-ray spectroscopy studies

6.2.8.1 Experiments

Gamma-ray spectroscopy was performed after MP of Sm solution containing radioactive ^{153}Sm tracer. A high-purity germanium detector (GEM series HPGe Detector Model No. GEM 23158 P-Plus, ORTEC Company) was used to determine the Sm deposition yield. To obtain quantitative data, reference sources with known amounts of the tracer were prepared. They consisted of filter papers with the same geometry as the targets, soaked with the tracer-containing solution. The yield values were always obtained as the average value calculated from three distinct γ-ray measurements. To avoid β^- pileup from ^{153}Sm in the low energy region (i.e., 0-1.5 MeV) of the α spectrum, the evaluation of the yields was never performed on the samples from which α spectra were recorded, but only on analog samples.

6.2.8.2 Results

In Table 6-3 we list the deposition yields obtained from the γ-ray analysis. The evaluated data clearly show the deposition yield to be quantitative for all different types of samples produced for α spectroscopy. In particular, the identical deposition yields of the DMF Ti5 samples plated for 90, 180, and 360 min suggest relatively quick depositions of the Sm^{3+} ions, as it was also observed for the Nd^{3+} ions in [10].

Table 6-3 Characteristic data of the different types of samples investigated by α-particle spectroscopy. The geometric efficiency of the α detector was calculated by Monte Carlo simulation to be (15.7 ± 0.8)%.

Exp.	Solvent	Foil	Plating time (min)	Yield* (%)	^{147}Sm layer density (μg/cm^2)	Area (counts)	FWHM (keV)	Detection efficiency (%)
A	Pyridine	Ti5	180	98.8 ± 1.1	119.6 ± 2.0	20160 ± 220	406	12.88 ± 0.24
	IP+IB	Ti5	180	99.5 ± 2.1	120 ± 3	23750 ± 190	263	15.1 ± 0.4
	DMF	Ti5	180	99.1 ± 2.2	120 ± 3	23920 ± 150	189	15.2 ± 0.4
B	IP+IB	Ti3	180	99.2 ± 1.4	120.1 ± 2.3	23370 ± 180	248	14.88 ± 0.29
	IP+IB	Ti4	180	99.8 ± 1.2	120.8 ± 2.1	20960 ± 190	152	13.26 ± 0.24
	IP+IB	Ti5	180	99.5 ± 2.1	120 ± 3	23750 ± 190	263	15.1 ± 0.4
C	DMF	Ti3	180	98.7 ± 2.8	119 ± 4	21010 ± 190	157	13.4 ± 0.4
	DMF	Ti5	180	99.1 ± 2.2	120 ± 3	22100 ± 150	169	14.1 ± 0.4
D	DMF	Ti5	90	99.9 ± 0.6	120.9 ± 1.7	21970 ± 150	163	13.89 ± 0.19
	DMF	Ti5	360	99.6 ± 1.1	120.6 ± 2.0	21510 ± 180	173	13.64 ± 0.24

* Determined by γ-ray spectroscopy of ^{153}Sm.

6.3 Alpha-particle spectroscopy investigation

6.3.1 Experiments

The α-particle spectra were obtained by measuring the produced samples (diameter: 34.0 ± 0.1 mm) with an Ortec ruggedized partially depleted Si detector (model CR-SNA-450-100), which had a diameter of 22.2 ± 0.1 mm, and a nominal resolution of 20 keV at 5.486 MeV. The detector was lodged in a vacuum chamber, coupled to a charge-sensitive preamplifier, a Canberra 2015A pulse-shaping amplifier, a Nuclear Data 579 analog-to-digital converter (ADC), and a Canberra Accuspec PC-resident multichannel analyzer (MCA). The samples were always positioned at a distance of 3.9 ± 0.5 mm from the detector and measured for counting times of 48 h. A wide-angle geometry was chosen because of the low activity of the sources. The geometric efficiency was estimated using a Monte Carlo simulation. For this, α particles originating from randomly distributed positions on a flat surface and emitted isotropically into randomly distributed directions were generated. The geometric efficiency is then the ratio of the number of α particles reaching the detector to the total number of created α particles. The simulation was performed for 10^7 particles to minimize the influence of statistical effects. The uncertainty of the simulated efficiency was estimated by calculating the efficiency for a distance sample-detector of (3.9 – 0.5) mm and a detector diameter of (22.2 + 0.1) mm as the upper value, and for a distance sample-detector of (3.9 + 0.5) mm and a detector diameter of (22.2 – 0.1) mm as the lower value. With that the simulation yields a geometric efficiency of (15.7 ± 0.8)%.

Standards for background measurement were produced by performing MPs without Sm, i.e., by adding 100 μL of 0.1 M HNO_3 to the deposition cell. For these MPs the same solvent, substrate, and deposition time were used as for the Sm sample of interest. Counting times of 48 h were adopted. The spectra were evaluated using the Genie 2000 software from Canberra. This included the evaluation of the FWHM and the areas of the ^{147}Sm peaks, as well as background subtraction between 0.6 and 2.3 MeV. We investigated this large energy region because of the pronounced low-energy tailing of the peaks of some of the investigated sources.

The samples from which α spectra were recorded were produced using different plating solvents (i.e., pyridine, IP+IB, and DMF), deposition substrates (i.e., Ti3, Ti4, and Ti5 foils), and times (i.e., 90, 180, and 360 min).

6.3.2 Results

The area and FWHM values of the ^{147}Sm peaks of the different types of samples from which α spectra were recorded are also contained in Table 6-3. We separately studied the influence of the three parameters of interest according to four experiment series. In experiment series A, we investigated the influence of the plating solvent, in series B the influence of the roughness of the deposition substrate, in series C the influence of surface cracks, and in series D the influence of the deposition time. For any given series, always the same stock solution was used: solution 1 for A and B, solution 2 for C, and solution 3 for D. Therefore, when comparing experiments from different series with each other, additional systematic differences, which we do not include in the given error bars, may be present.

6.3.2.1 Experiment A: influence of the plating solvent

Figure 6-8 shows the α spectra of Sm samples which were plated for 180 min on Ti5 substrates using pyridine, IP+IB, or DMF as plating solvents. We refer to Figures 6-4a, 6-3c, and 6-4c, respectively, and Section 6.2.5 for the morphological properties of these samples.

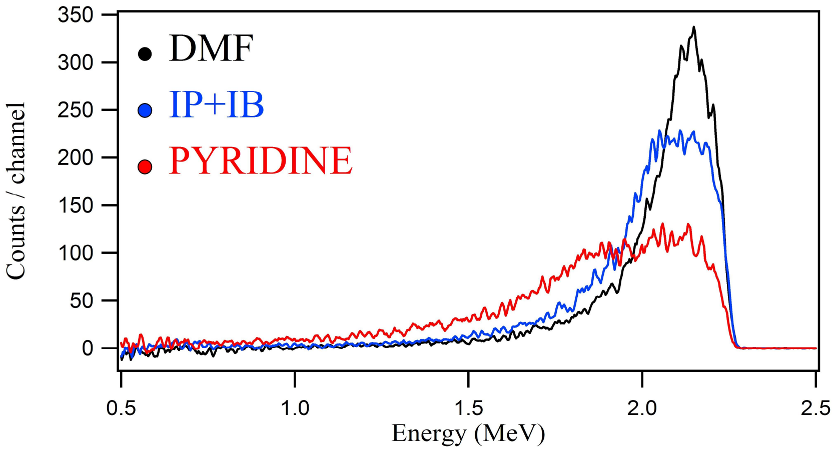

Figure 6-8 Experiment A. Alpha-particle spectra of the sources plated for 180 min on Ti5 deposition substrates using 0.22 mM Sm solution and DMF (see Figure 6-4c), IP+IB (see Figure 6-3c), or pyridine (see Figure 6-4a) as plating solvents.

Figure 6-8 and the data of Table 6-3 show that the ^{147}Sm peak resolution depends drastically on the solvent from which the layer was plated. It increases from pyridine over IP+IB to DMF. In particular, we noticed that the number of counts/channel recorded in the peak maximum increases from pyridine (ca. 100), to IP+IB (ca. 200), to the final

DMF sample (ca. 300). Moreover, the peaks of the three samples show different shapes: sharp and with only a small low-energy tail in the case of the DMF source, flat and with a pronounced low-energy tail in the IP+IB and pyridine deposits.

As regards the areas of the peaks, the data reported in Table 6-3 demonstrate that the pyridine sample is the one with the smallest number of recorded counts, i.e., ca. 15% fewer counts than the DMF and IP+IB samples, which have the same areas and layer densities within the reported error bars. The relative detection efficiency for the pyridine source is thus about 15% smaller than the efficiencies for the DMF and IP+IB sources. These experimental efficiencies, in turn, are identical within the error bars, and also in agreement with the geometric efficiency estimated by Monte Carlo simulation.

6.3.2.2 Experiment B: influence of the roughness of the deposition substrate

Figure 6-9 shows the α spectra of Sm samples which were plated for 180 min using IP+IB and Ti3, Ti4, or Ti5 deposition substrates. We refer to Figures 6-3a, b, and c, respectively, and Section 6.2.5 for the morphological properties of these samples.

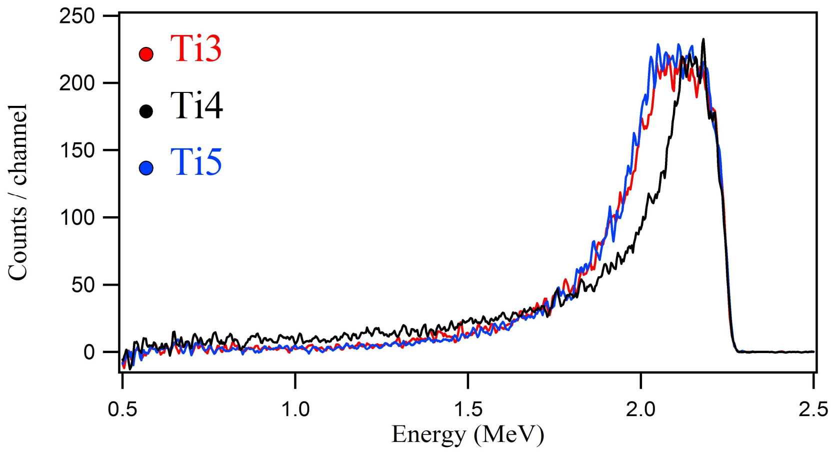

Figure 6-9 Experiment B. Alpha-particle spectra of the sources plated for 180 min using 0.22 mM Sm solution and IP+IB solvent on Ti3 (see Figure 6-3a), Ti4 (see Figure 6-3b), or Ti5 (see Figure 6-3c) deposition substrates.

Figure 6-9 as well as the data in Table 6-3 show the ^{147}Sm peaks of the layers grown on Ti3 and Ti5 substrates to yield α spectra with similar areas (within the error bars of the corresponding deposition yields) and FWHM. In the case of the layer grown on Ti4, i.e., the roughest deposition substrate, the sharpest peak is observed, but its area is the smallest among the evaluated ones. It contains ca. 10% fewer counts than the Ti3 and Ti5 samples, whose relative detection efficiencies are thus almost 10% larger than the efficiency for the Ti4 source. Moreover the Ti4 deposit shows the largest peak tailing in the low-energy region of the spectrum.

6.3.2.3 Experiment C: influence of surface cracks in the DMF samples

Figure 6-10 shows the α spectra of Sm samples which were plated for 180 min on Ti3 or Ti5 substrates using DMF as plating solvent. We refer to Figures 6-4b and c, respectively, and Section 6.2.5 for the morphological properties of these samples.

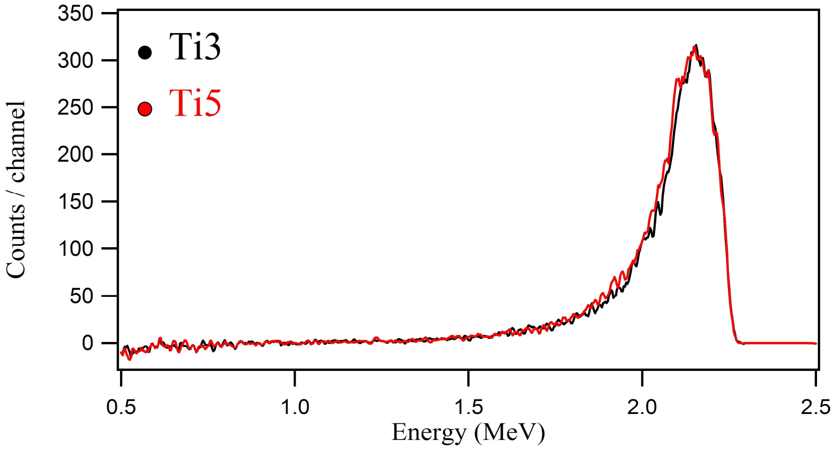

Figure 6.10 Experiment C. Alpha-particle spectra of the sources produced using 0.22 mM Sm solution and DMF on Ti3 (see Figure 6-4b) or Ti5 (see Figure 6-4c) deposition substrates.

The two spectra contained in Figure 6-10 are identical within the error bars. Consequently, the experimental detection efficiencies of the two sources are identical within the given uncertainties.

6.3.2.4 Experiment D: influence of the deposition time used to produce the DMF samples

Figure 6-11 shows the α spectra of Sm samples which were plated for 90 or 360 min on Ti5 substrates using DMF as plating solvent. We refer to Section 6.2.5 for the morphological properties of these samples.

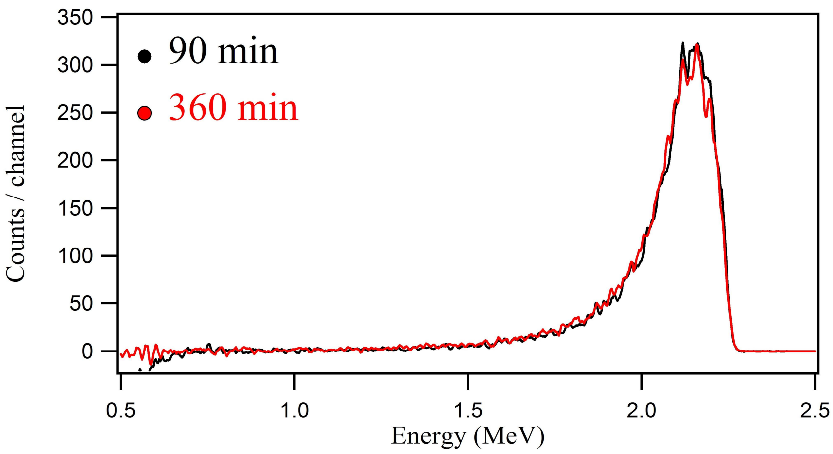

Figure 6-11 Experiment D. Alpha-particle spectra of the sources plated for 90 or 360 min using 0.22 mM Sm solution, DMF, and Ti5 deposition substrates.

As confirmed by the data of Table 6-3, both ^{147}Sm peaks of Figure 6-11 are characterized by similar resolutions and areas. The experimental detection efficiencies of the two samples are the same.

6.4 Discussion

The XPS investigations of the ^{147}Sm α-particle sources proved that because of DMF electrolysis during constant current density MP, the Sm^{3+} deposit is always covered by an outer layer of both physisorbed and chemisorbed DMF molecules. Interestingly, this solvent layer does not get much thicker after long deposition times (i.e., 360 min). This outcome can be better understood according to the results of the XPS investigations of the Sm-free DMF, IP+IB, and pyridine samples, which simulated the electrochemistry of the MP process after quantitative Sm deposition has been achieved. These samples are characterized by completely different layer thicknesses: thin and quite similar in the case of the DMF and IP+IB samples, much thicker in the case of the pyridine sample. These results suggest that the MPs performed using different solvents have very different electrochemistry, as confirmed by the evaluated ratios of physisorbed and chemisorbed C 1s components. It is then likely that according to the used solvent MP produces layers with very different growth rates, and hence thicknesses. When this plating technique is applied to produce α-particle sources, the choice of the solvent is therefore important not only because it influences layer properties like morphology and surface roughness [10], but also because it promotes a certain electrochemistry of the process which affects layer thickness in different ways. An example of electrochemistry not significantly influencing layer thickness is given by the α spectra of the samples produced on Ti5 foils applying

DMF and deposition times of 90 and 360 min (Figure 6-11). In this case the α peaks show similar resolutions and areas. Another example, showing instead electrochemistry with opposite influence, is given by the α spectra of Figure 6-8, where the ^{147}Sm peak of the Ti5 sample plated for 180 min using pyridine is characterized by fewer counts and worse resolution than the DMF and IP+IB Ti5 samples, despite having identical deposition yields. These differences are likely explained by self-absorption of the emitted α particles promoted by the thick pyridine layer grown on top of the Sm deposit during the applied plating time. Moreover, it is probable that the rough and heavily cracked surface of the pyridine sample causes varying α particle path lengths inside the layer with varying energy losses which contribute to an increased spread of the peak and its tailing. As regards instead the α spectra of the IP+IB and DMF Ti5 samples of Figure 6-8, the similar areas of the ^{147}Sm peaks are not surprising as the solvent layer thickness and deposition yields are similar. Nonetheless, the DMF peak has a better resolution than the IP+IB one. According to the SEM results, these two layers are mainly different in terms of the cracking of the produced surfaces: absent in the case of the DMF sample, quite severe and extended, instead, in the IP+IB source. It seems reasonable to argue that the cracks may play a role in favouring more scattering in the IP+IB sample than in the DMF one, hence lowering the resolution of the IP+IB peak. Despite this obvious interpretation, the α spectra of the DMF samples plated for 180 min on both Ti3 and Ti5 substrates (Figure 6-10), do not seem to confirm this as the main possible conclusion. Indeed, as the DMF sample grown on the Ti3 substrate was characterized by cracks present over the whole surface, while the Ti5 deposit was not, α spectra of such sources were compared in order to investigate the potential influence of the cracks on the investigated spectra. We realize that this may not be an ideal model, as the cracks present in the IP+IB layer are much more severe and extended than those formed in the DMF samples. Nonetheless, we chose this as the best approach to reality, and it showed that the α spectra of the DMF samples with or without cracks are similar. Therefore, the different resolutions of the IP+IB and DMF peaks do not seem to be explicable in terms of layer inhomogeneities like surface cracks, even if this cannot be totally excluded. An additional explanation may be found in the shapes of the two peaks: sharp and with only a small low-energy tail in the case of the DMF source, flat and with a pronounced low-energy tail in the IP+IB deposit. The shape of the IP+IB peak resembles that of the pyridine peak, which is probably flat because of the large source thickness. A reasonable explanation to the apparent increase of the thickness of the IP+IB sample may derive from the particular arrangement of the Sm atoms favoured by a layer growth mechanism different from the Frank-van der Merwe one followed by the DMF deposit (Figure 6-12a).

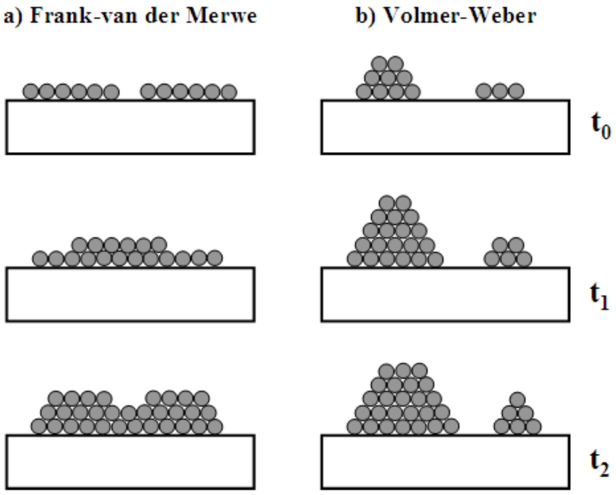

Figure 6-12 Classical layer growth mechanisms adopted from [18]: a) Frank-van der Merwe and b) Volmer-Weber.

In the Frank-van der Merwe growth mode a new layer is nucleated only after completion of the layer below [18]. Therefore, thin and homogeneous films (Figure 6-7c) can be obtained. The opposite of the Frank-van der Merwe mechanism is the Volmer-Weber growth mode (Figure 6-12b), where the nucleation of small aggregates on the substrate surface leads to the formation of three-dimensional islands, which cause the growing of rough and thick multi-layer films [18]. In the case of the IP+IB and pyridine layers, no unambiguous assignment of the layer-growth to a specific mechanism was possible. Nonetheless, from the comparison of the peak shape of the DMF α spectrum with the shapes of the IP+IB and pyridine spectra, and from the RI results, it seems reasonable to argue that layers grown on Ti5 substrates using pyridine or IP+IB solvents do not follow the same growth mechanism as that of the DMF sample. These layers may then follow a Volmer-Weber growth mechanism, or even other modes. In any case, the resolutions and areas of the α peaks shown in Figure 6-8 are affected by several variables, which may be resumed as layer thickness, layer growth mode, and layer morphology, i.e., inhomogeneities like surface cracks. In particular, the reason why the DMF sample is clearly the best produced α source is because the main variable affecting its α spectrum seems to be the followed Frank-van der Merwe growth mechanism. In the case of the IP+IB sample, instead, variables very likely influencing the recorded spectrum are both layer growth mode and layer inhomogeneities, while for the pyridine source all three variables are effective, with the thickness of the solvent layer covering the Sm deposit probably being the most important one. These variables may be more generally referred to as “layer variables”, as they influence the α spectra of the investigated samples by means of “layer effects” promoted by the particular solvents used for the MPs.

Layer effects not connected to the applied plating solvent can also be noticed in the α spectra of the IP+IB samples which were produced on Ti3, Ti4, and Ti5 deposition substrates (Figure 6-9). In this case, the α spectrum of the Ti4 sample suggests the roughness of the deposition substrate to be a layer variable, too. Despite having a deposition yield very similar to those of the Ti3 and Ti5 samples, the ^{147}Sm peak of the Ti4 source shows in fact a smaller area but a better resolution than the other IP+IB α spectra. According to literature [19], sources prepared on backings with fine scratches on their surfaces (hence quite rough) lead to smaller peak areas and also lower resolutions than those obtained from sources prepared on smooth backings. Clearly these results only partially agree with what is shown by the Ti4 α spectrum. In particular, the high resolution seems to indicate that the α particles generated inside the layer either undergo complete self-absorption, or reach the detector with almost their initial energy. Our working hypothesis to explain this anomaly is that during growth of the layer surface defects present on the deposition substrates act as preferential nucleation sites (see Figure 6-13).

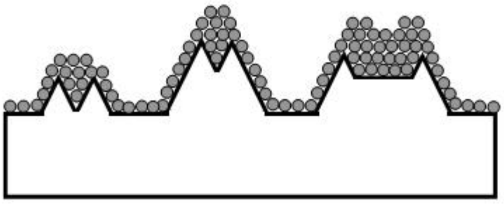

Figure 6-13 Graphical representation of the layer growth on the etched Ti4 substrate.

Indeed, as shown in Figure 6-3b, the edges of the defects of the Ti4 substrate act as preferential sites for the growth of the Sm layer, creating evident sharp outgrowths, which contain a large fraction of the deposited material and hence are the main α-particle emission regions. The particles emitted from regions other than these ones, e.g., the valleys between the outgrowths, may undergo more scattering hence creating the peak tailing in the low-energy region of the spectrum. Therefore, it is reasonable to include the roughness of the deposition substrate among the layer variables when MP is used to produce α sources with a certain solvent. In this case the substrate favours in fact a particular layer growth which also promotes layer effects influencing the spectra.

From the determined experimental efficiencies follows that indeed, layer variables of a sample affect the obtained α spectra in different ways. In some spectra, the low-energy tail is much more pronounced than in others, which is reflected also in the FWHM values reported in Table 6-3. Furthermore, also the fraction of α particles that reaches the detector depends on the properties of the sample, even if nominally all samples have the same areal density of ^{147}Sm and the same size. Non-ideal samples – like those prepared from pyridine or on the very rough substrate Ti4 – lead to detection efficiencies which are significantly smaller than in the case of, e.g., the samples prepared in DMF on ideally flat Ti5 substrates, where experimentally determined efficiency and simulated geometric efficiency are identical. Such effects should then be taken into account and studied, especially in experiments aiming at the determination of half-lives of primordial nuclides using samples produced by MP.

6.5 Conclusion

Constant current density MP was applied to produce layers containing the long lived α-particle emitter ^{147}Sm. Several samples were prepared by varying different parameters, namely the plating solvent, the applied deposition time, and the surface roughness of the deposition substrate. The sources were analyzed using γ-ray spectroscopy, RI, XPS, SEM, and AFM. The results obtained from these characterizations confirmed the prepared Sm samples and the Nd layers produced in [10] to have similar properties. Alpha spectra were recorded for samples belonging to the different types of characterized sources by using small source-to-detector distance. Under the adopted wide-angle geometry, the peak shapes were mainly determined by source effects [20]. Thanks to the different applied characterization techniques, the source effects could be categorized according to what we called “layer variables”, as variables influencing the α spectra of the samples to be investigated by means of “layer effects” promoted by specific MP parameters. In particular, two parameters were found effective for layer effects: the plating solvent and the roughness of the deposition substrate. The solvent affects thickness, morphology, and growth mode of the layer to produce, while the substrate roughness influences mainly the growth of the deposit, and only as a consequence its thickness and morphology. These layer variables proved to influence the relative detection efficiencies of the α measurements by as much as 15%. Despite this, to our knowledge these variables have not been considered so far, e.g., as systematic effects in the evaluation of half-lives determined from such measurements. In particular, computer simulations, which are frequently used to calculate counting efficiencies, often do not adequately take these effects into account.

Acknowledgements

The authors would like to thank the staff of the TRIGA Mainz for performing the irradiations, Prof. A. Kühnle for providing the AFM microscope, Dr. T. Lauer for performing the coating of the Si wafers, and V. Yakusheva from the GSI target laboratory for her assistance during the SEM measurement. A.V. acknowledges financial support from the German Federal Ministry of Science and Education (BMBF) under Contract number 02NUK013E.

References

[1] R.F. Sperlein, R.L. Wolke, J. Inorg. Nucl. Chem. **38** (1976) 27-29.

[2] W. Parker, R. Falk, Nucl. Instrum. Methods **16** (1962) 355-357.

[3] K. Eberhardt, W. Brüchle, Ch.E. Düllmann, K.E. Gregorich, W. Hartmann, A. Hübner, E. Jäger, B. Kindler, J.V. Kratz, D. Liebe, B. Lommel, H.-J. Maier, M. Schädel, B. Schausten, E. Schimpf, A. Semchenkov, J. Steiner, J. Szerypo, P. Thörle, A. Türler, A. Yakushev, Nucl. Instrum. Meth. A **590** (2008) 134-140.

[4] J. Runke, Ch.E. Düllmann, K. Eberhardt, P.A. Ellison, K.E. Gregorich, S. Hofmann, E. Jäger, B. Kindler, J.V. Kratz, J. Krier, B. Lommel, C. Mokry, H. Nitsche, J.B. Roberto, K.P. Rykaczewski, M. Schädel, P. Thörle-Pospiech, N. Trautmann, A. Yakushev, J. Radioanal. Nucl. Chem. (2012) submitted.

[5] B. Al-Bataina, J. Jänecke, Radiochim. Acta **42** (1987) 159-164.

[6] K. Zuber, AIP Conf. Proc. **942** (2007) 101-104.

[7] A. Vascon, Ch.E. Düllmann, K. Eberhardt, B. Kindler, B. Lommel, J. Runke, Nucl. Instrum. Meth. A **655** (2011) 72-79.

[8] A. Vascon, S. Santi, A.A. Isse, T. Reich, J. Drebert, H. Christ, Ch.E. Düllmann, K. Eberhardt, Nucl. Instrum. Meth. A **696** (2012) 180-191.

[9] A. Vascon, S. Santi, A.A. Isse, T. Reich, J. Drebert, H. Christ, K. Eberhardt, Ch.E. Düllmann, J. Radioanal. Nucl. Chem. (2012) accepted.

[10] A. Vascon, S. Santi, A.A. Isse, A. Kühnle, T. Reich, J. Drebert, K. Eberhardt, Ch.E. Düllmann, Nucl. Instrum. Meth. A **714** (2013) 163-175.

[11] K. Kossert, G. Jörg, O. Nähle, C.L.V. Gostomski, Appl. Radiat. Isot. **67** (2009) 1702-1706.

[12] C.D. Wagner, W.M. Riggs, L.E. Davis, J.F. Moulder, G.E. Muilenberg, Handbook of X-Ray Photoelectron Spectroscopy, Perkin-Elmer Corporation, Physical Electronics Division, Eden Prairie, Minn. 55344 (1979).

[13] T. Moeller, J.C. Bailar, H.J. Emeleus, R. Nyholm, A.F. Trotman-Dickenson, Comprehensive Inorganic Chemistry, Pergamon, Oxford, 1973.

[14] R.C. Gray, J.C. Carver, D.M. Hercules, J. Electron Spectrosc. **8** (1976) 343-358.

[15] D. R. Lide (Ed.), CRC Handbook of Chemistry and Physics, 87th ed., 2006.

[16] R.G. Helmer, Nucl. Data Sheets **107** (2006) 507-788.

[17] D. Liebe, K. Eberhardt, W. Hartmann, T. Häger, A. Hübner, J.V. Kratz, B. Kindler, B. Lommel, P. Thörle, M. Schädel, J. Steiner, Nucl. Instrum. Meth. A **590** (2008) 145-150.

[18] M. Paunovic, M. Schlesinger, Fundamentals of Electrochemical Deposition, second ed., Wiley, New Jersey, 2006.

[19] D.E. Watt, D. Ramsden, High Sensitivity Counting Techniques, MacMillan and Co., New York, 1964.

[20] A. Martìn Sànchez, A. Fernàndez Timòn, M.P. Rubio Montero, Appl. Radiat. Isot. **56** (2002) 51-55.

7. Outlook and closing remarks

The performed experiments yielded relevant improvements in the preparation of targets for nuclear investigations by means of molecular plating (MP).

MP was confirmed to be very effective for target production and smooth, crack-free layers were prepared.

The question about the suitability of MP or PAD [1] to the production of targets for the higher intensity beams of the future generation [2,3] cannot yet be answered. In principle, the removal of cracks and other aberrations from both types of targets implies a reduced tendency of the layers to break under the thermal stress of the beam and thus an increased structural rigidity. Nonetheless, significant comparisons will be possible only when these beams are made available and the first tests are performed.

Research in the MP field is interdisciplinary, involving aspects from electrochemistry, materials science, and radiochemistry. The experiments performed during the thesis have shown in fact that investigations in these fields are needed not only to improve the quality of the layers but also to interpret unexpected scientific results (see, e.g., the different recorded α spectra).

The study of the electrochemistry of MP is that of an electrodeposition process. Electrodepositions are usually carried out from aqueous solutions because of the great practical importance of water solvents and also because of the greater experimental difficulties in working with organic solutions [4]. Moreover, the performance of these depositions is always affected by several variables, which are often optimized by empirical approach [5]. MP is thus the alternate version of an already complex process, which is further complicated by the use of non-aqueous solutions and elements like, e.g., the lanthanides or the actinides, whose chemistry is rather peculiar.

The use of a reference electrode in the typical two-electrode cells of MP would facilitate the investigation of the electrochemistry by allowing the study of the processes taking place at the electrode of interest, i.e., the working electrode. Information about the species being consumed and produced at, e.g., the cathode could in fact explain how the plating evolves over time. Nonetheless, the method of measuring electrode potentials in non-aqueous solutions has not yet been well established. The most serious problem is the reference electrode; there is no primary reference electrode like the standard hydrogen electrode (SHE) in aqueous solutions and no reference electrode as reliable as the aqueous Ag/AgCl electrode. Thus, various electrodes are usually employed in practical measurements, making the comparison of potential data difficult [4]. Moreover, standard redox potentials of lanthanide and actinide elements have been mainly determined in aqueous solutions [6,7].

An additional drawback of the study of electrodepositions like MP is the common use of undivided cells, i.e., cells with no physical separation system, e.g., a porous membrane, between anode and cathode. This causes the possibility that species generated at one electrode are consumed at the other electrode and vice versa, hence significantly complicating the electrode processes – the presence of reduced Pd in the deposits of some of the performed MPs is a direct evidence of this effect.

The general complexity of MP and the difficulty of measuring electrochemical data are the main reasons why the derived expression for the cell potential at constant current density is not sufficient to interpret the experimental behaviour beyond the different voltage trends recorded with various electrolyte concentrations. If this expression had also described the evolution of the potential over time it would have probably given insight into the reasons of the minima in the curves. As this was not possible, the cell potential minima can currently be identified with only the advanced depletion of the ions of interest.

Despite the incomplete understanding of the electrochemistry underlying MP, it is worth pointing out two achievements of the performed experiments, which reshape the concept of MP itself. First of all, the original statement of no electrolytic dissociation occurring during MP [8] was disproved. Secondly, it was confirmed that the species of interest is not deposited as the chemical compound initially dissolved in solution [9,10]. The absence of the reduced element in the deposit can be explained with the unique chemistry of both lanthanide and actinide elements. Thus, the main features which led to the name “molecular plating” are wrong and the technique is rather just a common electrodeposition from an organic medium.

Much of the information about the nature of MP was obtained with characterization experiments exploiting analytical techniques used in materials science. These techniques showed to be suitable for the research in the MP field. In particular, the use of AFM in liquid environments proved to be effective to answer the question about the origin of cracking in the produced surfaces. AFM experiments in liquid would have also allowed inferring the layer growth mechanisms of the samples produced with the very volatile IP+IB and pyridine solvents. An analysis of the deposits before drying – hence in the liquid phase – would have in fact avoided the surfaces to be damaged by the cracks, thus giving the experimental proof of the correctness (or incorrectness) of the inclusion of the growth mechanism among the layer variables influencing α-spectroscopy measurements. Unfortunately, as liquid AFM investigations are very time-consuming they could be performed only on few occasions. Future experiments should exploit more this type of analysis to get direct information about the surfaces before any modification induced by the drying process.

Concerning the use of MP produced layers as α-particle sources, forthcoming investigations should be also combined with computer simulations to get a better understanding of the way the layer variables affect the experimental α spectra. The simulations could be very helpful to reproduce the behaviour of α particles emitted from sources which are characterized by, e.g., different layer thickness, growth mechanism, or morphology. The effects of the layer variables could be simulated with, e.g., Monte Carlo codes using measured values of specific properties of the sources. Important parameters are usually the thickness of the layers, their density – or eventually just the areal density – and the stoichiometry of the produced deposits. Cross-sectional SEM images of the targets [1] could be used to measure thickness values – even if not very accurately. Other, more complex but precise approaches include Rutherford scattering [11] and X-ray diffraction analysis [12]. Weighing could be also applied but only if the ratio of target weight to backing weight is not too small [11]. As regards instead the determination of the stoichiometry of the deposits, XPS could be used to evaluate the atomic ratios of the elements present in the produced layers.

The results obtained during this work open the way to the production of the lanthanide and actinide targets required within the frame of the TRAKULA project. The half-life determination of ^{144}Nd will definitely benefit from the high quality of the α sources producible with DMF and the very smooth Ti-coated Si wafers. The production of the U and Pu targets will also benefit from the controlled use of those MP parameters which have been found to influence the quality of the deposits. The electrolyte concentration, the applied current density, and the roughness of the deposition substrate will also play a role in this case. As regards instead the solvent, the optimum one might be different from DMF, which was mainly tested with the lanthanides Nd and Sm. The very special nature of U and Pu, with their higher oxidation states (+6 and +4 the most stable ones, respectively) than Nd and Sm (+3), could in fact favour MPs with completely different electrochemistry. For this reason, no model elements can be reliably used to perform deposition test experiments. U and Pu themselves have thus to be used, with all the limitations resulting from working with these radioactive elements.

With this thesis, the hope is to have started a more scientific approach to the research in the field of target preparation by means of MP. The work to be done is still a lot, but it may be rewarded with unexpected outcomes.

References

[1] M.N. Ali, M.A. Garcia, T. Parsons-Moss, H. Nitsche, *Polymer-assisted deposition of homogeneous metal oxide films to produce nuclear targets*, Nat. Protoc. **5** (2010) 1440-1446.

[2] H. Stoecker, C. Sturm, *The FAIR start*, Nucl. Phys. A **855** (2011) 506-509.

[3] G. Savard, R. Janssens, *Proposed ATLAS efficiency and intensity upgrade*, ATLAS Workshop (CERN – European Center for Particle Physics – Geneva, 2009).

[4] K. Izutsu, Electrochemistry in Nonaqueous Solutions, first ed., Wiley-VCH, Darmstadt, Germany, 2002.

[5] M. Paunovic, M. Schlesinger, Fundamentals of Electrochemical Deposition, second ed., Wiley, New Jersey, 2006.

[6] J.C. Bailar, H.J. Emelèus, R. Nyholm, A.F. Trotman-Dickenson, *Comprehensive inorganic chemistry*, Volume 4: Lanthanides-Transition metal compounds, first ed., Pergamon, Oxford, 1973.

[7] J.C. Bailar, H.J. Emelèus, R. Nyholm, A.F. Trotman-Dickenson, *Comprehensive inorganic chemistry*, Volume 5: Actinides, first ed., Pergamon, Oxford, 1973.

[8] W. Parker, R. Falk, *Molecular plating: a method for the electrolytic formation of thin inorganic films*, Nucl. Instrum. Methods **16** (1962) 355-357.

[9] M.V. Ramaniah, R.J. Singh, S.K. Awasthi, S. Prakash, *Studies on electrodeposition of actinide elements from non-aqueous medium*, Int. J. Appl. Radiat. Is. **26** (1975) 648-650.

[10] A. Ölcer, J. Drebert, T. Reich, in: [R] Seventh International Conference on Nuclear and Radiochemistry, Budapest, Hungary, 24-29 August, 2008.

[11] G. Friedlander, J.W Kennedy, E.S. Macias, J.M. Miller, *Nuclear and Radiochemistry*, third ed., Wiley, New York, 1981.

[12] A. Eisenstein, *An X-ray method for measuring the thickness of thin crystalline films*, J. Appl. Phys. **17** (1946) 874-878.